12-2017

Multiscale Mechanistic Approach to Enhance Pool Boiling Performance for High Heat Flux Applications

Arvind Jaikumar
aj4853@rit.edu

R·I·T

Multiscale Mechanistic Approach to Enhance Pool Boiling Performance for High Heat Flux Applications

by

Arvind Jaikumar

A dissertation submitted in partial fulfillment of the requirements
for the degree of Doctorate of Philosophy in Microsystems Engineering

Microsystems Engineering Program
Kate Gleason College of Engineering

Rochester Institute of Technology
Rochester, New York
December, 2017

Multiscale Mechanistic Approach to Enhance Pool Boiling Performance for High Heat Flux Applications

by

Arvind Jaikumar

Committee Approval:

We, the undersigned committee members, certify that we have advised and/or supervised the candidate on the work described in this dissertation. We further certify that we have reviewed the dissertation manuscript and approve it in partial fulfillment of the requirements of the degree of Doctor of Philosophy in Microsystems Engineering.

_____

Dr. Satish G. Kandlikar (Advisor) Date
James E. Gleason Professor, Mechanical Engineering

_____

Dr. Michael Schertzer Date
Assistant Professor, Mechanical Engineering

_____

Dr. Robert Stevens Date
Associate Professor, Mechanical Engineering

_____

Dr. Jiandi Wan Date
Assistant Professor, Microsystems Engineering

Certified by:

_____

Dr. Bruce Smith Date
Director, Microsystems Engineering Program

Abstract

Kate Gleason College of Engineering
Rochester Institute of Technology

Degree: Doctor of Philosophy **Program**: Microsystems Engineering

Authors Name: Arvind Jaikumar **Advisors Name:** Dr. Satish G. Kandlikar

Dissertation Title: Multiscale Mechanistic Approach to Enhance Pool Boiling Performance for High Heat Flux Applications

The advent of cloud computing and the complex packaging architecture of next generation electronic devices drives methods for advanced thermal management solutions. Convection based single-phase cooling systems are inefficient due to their large pressure drops, fluid temperature differences and costs, and are incapable of meeting the cooling requirements in the high power density components and systems. Alternatively, phase-change cooling techniques are attractive due to their ability to remove large amounts of heat while maintaining uniform fluid temperatures. Pool boiling heat transfer mechanism centers on the nucleation, growth and departure of a bubble from the heat transfer surface in a stagnant pool of liquid. The pool boiling performance is quantified by the Critical Heat Flux (CHF) and Heat Transfer Coefficients (HTC) which dictate the operating ranges and efficiency of the heat transfer process. In this work, three novel geometries are introduced to modify the nucleation characteristics, liquid pathways and contact line motion on the prime heater surface for a simultaneous increase in CHF and HTC.

First, sintered microchannels and nucleating region with feeder channels (NRFC) were developed through the mechanistic concept of separate liquid-vapor pathways and enhanced macroconvection heat transfer. A maximum CHF of 420 W/cm^2 at a wall superheat of 1.7 °C with a HTC of 2900 $MW/m^2°C$ was achieved with the sintered-channels configuration, while the NRFC reached a CHF of 394 W/cm^2 with a HTC of 713 $kW/m^2°C$. Second, the scale effect of liquid wettability, roughness and microlayer evaporation was exploited to facilitate capillary wicking in graphene through interlaced porous copper particles. A CHF of 220 W/cm^2 with a HTC of 155 $kW/m^2°C$ was achieved using an electrodeposition coating technique. Third, the chemical heterogeneity on nanoscale coatings was shown to increase the contribution from transient conduction mechanisms. A maximum CHF of 226 W/cm^2 with a HTC of 107 $kW/m^2°C$ was achieved. The enhancement techniques developed here provide a mechanistic tool at the microscale and nanoscale to increase the boiling CHF and HTC.

Acknowledgements

"Teamwork coming together is a beginning, keeping together is progress and working together is success" – Henry Ford

This dissertation would not be complete without the synergistic environment developed at the Thermal Analysis Microfluidics and Fuel Cell Laboratory (TAMFL) at Rochester Institute of Technology. I would like to express my sincere gratitude to my advisor, Dr. Satish G Kandlikar, for giving me the opportunity and creating a platform to express my ideas. His passion and enthusiasm for the subject motivated me at every stage of my research work. I also like to thank him for initiating and involving me in the outreach initiatives (beyond 9.8 and E-cubed fair) which had a profound impact in my life.

I would like to thank my committee members – Dr. Michael Schertzer, Dr. Robert Stevens and Dr. Jiandi Wan for being an excellent sounding board. I would like to thank all my TAMFL lab members – Dr. Rupak Banerjee, Dr. Ankit Kalani, Pruthvik Raghupathi, Isaac Perez-Raya, Alyssa Recinella, Travis Emery and Aranya Chauhan for their continued support and timely assistance without which this dissertation would not have been possible. I also like to thank Andrew Greeley, Austin Hayes and Jean-Patrick Kalumbwe for their efforts in the fabrication of the test setup. A part of this work was accomplished through collaboration with material science experts - Dr. Surendra Gupta and Dr. Anju Gupta, and I greatly appreciate their help in the successful completion of this dissertation.

I would like to thank my parents for always standing by me and supporting me in all walks of my life. Words cannot express the sacrifices they have made. Their constant encouragement and belief gave me the strength to overcome many challenges I encountered over the years.

Dedication

To Chithra Jaikumar and Jaikumar Venkatraman

Table of Contents

List of Figures

List of Tables

Nomenclature

Symbol	Description	Units/Value
B_y	Bias error	-
Ca	Capillary number	-
C_0	Distribution parameter	-
C_1	1 + cosθ	-
C_2	sinθ	-
C_l , C_{ph}	Specific heat	J/kg-K
C_{sf}	Surface-fluid factor	-
d_B	Bubble departure diameter	m
D_h	Hydraulic diameter	m
dT/dx	Temperature gradient	°C/m
E	Thermal Effusivity	$J/m^2Ks^{1/2}$
g	Acceleration due to gravity	m/s^2
h_{lv}, h_{fg}	Latent heat of vaporization	J/kg
k_{Cu}	Thermal conductivity of copper	W/m-K
L	Characteristic length	m
Nu	Nusselt number	
P_y	Precision error	-
Pr	Prandtl number	-
q″	Heat flux based on projected area	W/cm^2
Q_{ME}	Heat transferred through microlayer evaporation	W
$\dot{Q}_{TC}$	Heat transferred through transient conduction	W

r_c	Critical radius	m
r_{cmax}	Maximum critical radius of cavity	m
r_{cmin}	Minimum critical radius of cavity	m
R	Radius of a vapor bubble	m
R_a	Arithmetic mean roughness	µm
Re	Reynolds number	-
$t_{adv.}$	Advancing wetting time	s
T∞	Fluid temperature	°C
T_s	Temperature of the surface	°C
t	Bubble cycle time (without waiting time)	s
$t_{adv.}$	Advancing wetting time	s
T_1	Top thermocouple	°C
T_2	Middle thermocouple	°C
T_3	Bottom thermocouple	°C
T_{sat}	Saturation temperature of the fluid	°C
U_p	Uncertainty in the specific parameter	-
U_y	Uncertainty	-
u_{ai}	Uncertainty of measured parameter *ai*	-
V_{drift}	Drift velocity	m/s
V_{vapor}	Vapor phase superficial velocity	(m/s)
$V_{\delta o}$	Volume of microlayer corresponding to initial thickness	m^3
V_o''	Wicking rate	m/s

v	Contact line velocity	m/s
W	Jet impingement width	m
Wi	Wicking number	-
x_1	Distance between T_1 and top surface of the test chip	m

Greek Symbols

α_G	Gas void fraction	-
α_l	Thermal diffusivity	m^2/s
$\beta,\ \theta_r$	Receding contact angle	deg.
δ_t	Thermal boundary layer thickness	m
θ_D	Dynamic contact angle	-
λ_c	Critical capillary length	m
μ_l	Dynamic viscosity	Ns/m^2
ρ_V, ρ_g	Density of vapor	kg/m^3
ρ_l	Density of liquid	kg/m^3
σ	Surface tension	N/m
φ	Surface inclination angle	Deg.
Δx	Distance between thermocouples	m
ΔT_{sat}	Wall superheat	°C
ΔT_{sub}	Subcooling temperature difference	°C

List of Abbreviations

CHF	Critical Heat Flux	W/m^2
CL	Contact line	-
HTC	Heat transfer coefficient	$W/m^2°C$

Chapter 1

1. Introduction

The physical mechanisms underlying the heat transfer modes (conduction, convection, and radiation) are of prime importance to quantify the efficacy of the processes. Conduction refers to the transfer of heat in a solid or liquid when a temperature gradient exists in the stationary medium, while convection occurs between a surface and the moving fluid. Radiation heat transfer occurs in the absence of an intervening medium and is characterized by the inherent property of materials to emit electromagnetic waves and the associated energy transfer between them.

Convection based heat transfer mechanisms are attractive because of their ability to remove large amounts of heat and enable compactness. They are further classified into single-phase and two-phase heat transfer processes. Typically, single-phase energy transfer occurs through a sensible (or internal thermal) energy change in the working fluid. Two-phase heat transfer is accompanied by the latent heat transfer which induces a phase-change between liquid and vapor states (boiling or condensation). Regardless of the nature of the convection heat transfer process, the rate equation for convection is expressed as,

$$q'' = HTC\ (T_s - T_\infty) \tag{1}$$

where, q'' is the heat flux, T_s and T_∞ are the surface and fluid temperatures, HTC is the proportionality constant, called the convection heat transfer coefficient (HTC), which indicates the efficiency of the heat transfer process.

1.1. Boiling Heat Transfer

Since the latent heat of liquid is significantly greater than the sensible heat of the liquid over the allowable temperature rise of the cooling fluid, heat transfer due to phase change is substantially higher than single phase heat transfer. Boiling is a heat transfer process accompanied by phase change from liquid to vapor. It is further classified into pool and flow boiling as shown in Figure 1. Pool boiling (Figure 1a) is the boiling of a stagnant liquid over a heated surface while flow boiling is the boiling of a flowing fluid over a heated surface. In the case of pool boiling, the growth and departure of bubbles is the main reason for liquid motion while in the case of flow boiling (Figure 1b), the presence of an external force also aids in the mixing of the liquid. While flow boiling can result in high heat transfer, inherent difficulties such as flow instability and large power requirement to pump or high pressure drop make its use difficult in certain applications.

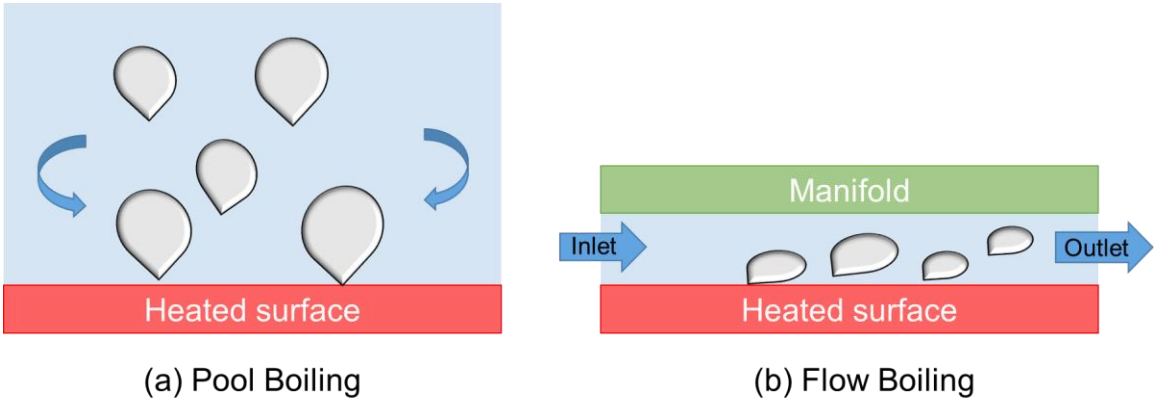

Figure 1. Schematic representation of the types of boiling (a) pool boiling and (b) flow boiling.

1.2. Pool Boiling

Pool boiling results in a phase change from liquid to vapor accompanied by bubble nucleation, growth and departure in a quiescent liquid where the fluid motion is governed by free convection or the motion of the departing bubbles. The pool boiling heat transfer

performance can be improved by using two methods; passive methods and active methods. Passive methods relate to structured heat transfer surfaces without using external power whereas active methods involve using external power, i.e. a magnetic field. Pool boiling heat transfer enhancement offers attractive cooling schemes in high powered electronic systems, refrigeration and the nuclear industry. This technique does not require any moving parts, and is highly beneficial from both thermal and cost perspectives. The main objective of these augmented surfaces is to reduce wall superheat and increase critical heat flux which offers enhanced performance over a wide operating range.

1.3. Bubble Nucleation

Entrapped gases facilitate growth of the bubble when the saturation temperature of the liquid surrounding the vapor bubble is greater than the temperature corresponding to the saturation pressure of the vapor. Figure 2 shows the different forces acting on a bubble. The two forces for static bubble are surface tension and pressure forces due to liquid and vapor.

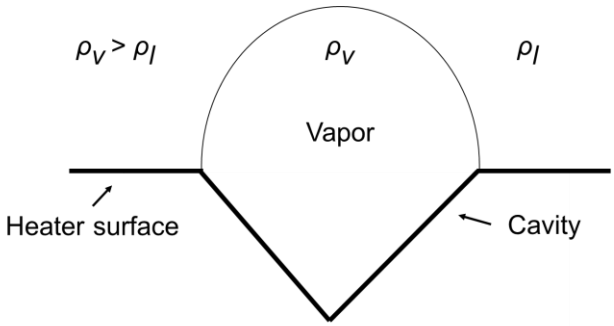

Figure 2. Schematic representation of forces acting on a bubble.

The force balance for the above configuration can be obtained as shown below,

$$\pi R^2(\rho_V - \rho_l) - 2\pi R\sigma = 0 \quad (2)$$

From the above equation, vapor pressure can be represented as,

$$\rho_V = \rho_l + \frac{2\sigma}{R} \tag{3}$$

Equation (3) shows the dependence of bubble radius on the vapor pressure. For a small bubble, the vapor pressure is high indicating that saturation temperature will be higher for a fluid at pressure, ρ_V proving that a superheat is required for a vapor bubble to grow.

The onset of nucleate boiling is characterized by a range of active nucleation sites proposed by Hsu and Graham [1] and Hsu [2]. Kandlikar and Spiesman [3] through simulations identified the thermal boundary thickness to be equal to 1.1 times the bubble radius and modified the equation proposed by Hsu [2]. In their subsequent work, Kandlikar et al. [4] modified this equation further by incorporating the effects of contact angle (receding) as shown below,

$$\{r_{cmax}, r_{cmin}\} = \frac{\delta_t \sin\theta_r}{2.2}\left(\frac{\Delta T_{sat}}{\Delta T_{sat} + \Delta T_{sub}}\right)\left[1 \pm \sqrt{1} - \frac{8.8\sigma T_{sat}\,(\Delta T_{sat} + \Delta T_{sub})}{\rho_V h_{lv} \delta_t {T_{sat}}^2}\right] \tag{4}$$

The bubble nucleation will occur when the radii lies within the range specified by Equation (4). For a smooth polished surface, higher superheats are expected to initiate nucleation. The wall superheat corresponding to the critical cavity radius is the given by,

$$\Delta T_{sat,ONB\ at\ r_c} = \frac{1.1 r_c q''}{k_l \sin\theta_r} + \frac{2\sigma \sin\theta_r\, T_{sat}}{r_c \rho_v h_{lv}} \tag{5}$$

1.4. Heat Transfer Mechanisms

Pool boiling heat transfer mechanisms center on the bubble nucleation, growth and departure from the heated surface. Three popular and well-established heat transfer mechanisms that revolve around the aforementioned bubble ebullition cycle are: (i) microlayer evaporation, (ii) transient conduction mechanism, and (iii) microconvection. Figure 3 shows the schematic of the heat transfer mechanisms and their spatial influence in the vicinity of a bubble undergoing an ebullition cycle.

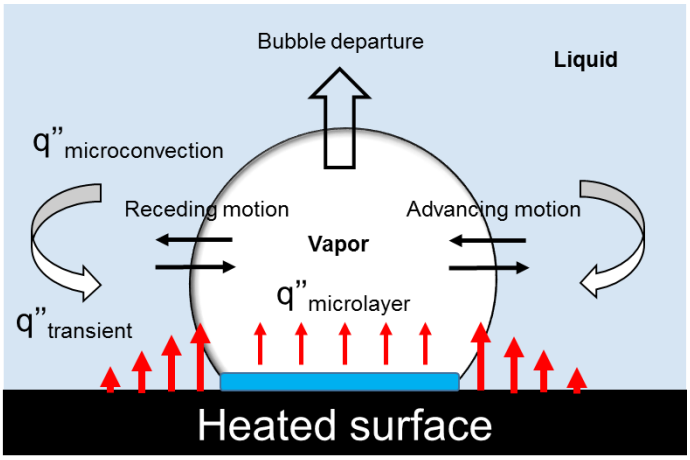

Figure 3. Heat transfer mechanisms in the influence region during bubble ebullition cycle.

Microlayer evaporation: Microlayer evaporation occurs when a thin liquid film is trapped underneath a growing bubble. This film evaporates contributing to the heat transfer. The microlayer undergoes thermal relaxation and interacts with the wall during the initial superheat conditions. Central regions of the microlayer may evaporate depending on the specific solid-fluid combinations creating dry patches. The origin of the microlayer can be traced to the pioneering work by Moore and Mesler [5], Hendricks and Sharp [6], and Cooper and Lloyd [7]. More recently, Mogaddam and Kiger [8] have shown that the microlayer contribution to the total heat flux is between 15-25% and remains constant over the heat flux range.

Evaporation of this thin film leads to a substantial increase in the bubble growth rate [9]. The total energy from the microlayer can be estimated by analyzing (i) the heat transfer from the wall during the microlayer event, and (ii) the initial sensible energy of the microlayer [8]. The thickness of the microlayer contributes to the total heat transferred during the process. Since the microlayer thickness typically measured are in the microscale

(less than 10 μm), the temperature profile within this layer is expected to be linear. The total microlayer heat transferred over the bubble cycle time can be estimated using

$$\dot{Q_{ME}} = \frac{\rho_l V_{\delta o} h_{lv}}{t} \tag{6}$$

where, $\dot{Q}_{ME}$ is the heat transferred from the microlayer, ρ_l, $V_{\delta o}$, h_{lv} and t are the liquid density, volume of the microlayer, latent heat and time, respectively.

Transient conduction: This mechanism occurs during the advancing motion of the liquid and the subsequent departure of the bubble from the heater surface. Effectively, the conduction in the liquid during replenishment and removal of liquid following the departure of the bubble is referred to as the transient conduction. The contact line velocity during the liquid advancing motion determines the efficacy of the rewetting process, and therefore the contribution from transient conduction mechanisms. Mikic and Rohsenow [10,11] and Han and Grifith [12] were the first to evaluate the transient conduction mechanisms for a bubble growing on a heater surface in pool boiling conditions.

Transient conduction occurs as the contact line sweeps over the heater surface during the advancing motion of the liquid. This motion creates the cold bulk liquid to quench the heater surface resulting in a cooling effect. The first report on this mechanism can be traced to Mikic et al. [11] where the displaced volume of the bubble was assumed to be replaced by the liquid front instantaneously. Through advanced sensor based instrumentation techniques, Demiray and Kim [13] demonstrated that the liquid front advanced gradually over the heater surface. The expression for surface heat flux per unit length can be estimated using,

$$\dot{Q}_{TC} = \int_0^x \frac{k\Delta T}{\sqrt{\pi \alpha_l x}}\, dx \tag{7}$$

where, $\dot{Q}_{TC}$ is the heat transferred through transient conduction, k is the thermal conductivity, α_l is the thermal diffusivity, and x is the distance travelled by the CL.

Microconvection: The oscillatory interface motion during bubble growth creates convective currents in the vicinity of the bubble. This convective current is effective in disturbing the thermal boundary layers creating a heat transfer enhancement. The influence region of microconvection is often estimated to be twice the bubble departure diameter. At higher heat fluxes, increased interface motion is expected to increase the contribution from microconvection. Generally, the Rohsenow [11] model, which relies on the convection induced by the generation of bubbles on the heater surface, is employed by estimating the microconvection heat fluxes in the vicinity of the bubbles,

$$\frac{C_l\,(\Delta T)}{h_{lv}} = C_{sf}\left(\frac{q''}{\mu_l h_{lv}}\sqrt{\frac{\sigma}{g\,(\rho_l - \rho_v)}}\right)^{0.33} Pr_l^{1.7} \tag{8}$$

Where C_l is the specific heat, h_{lv} is the latent heat of vaporization, μ_l is the dynamic viscosity, ρ_l and ρ_g are the liquid and vapor densities, C_{sf} is the surface-fluid factor, σ is the surface tension, and q'' is the macroconvective heat flux in their model.

1.5. Pool Boiling Curve

The pioneering work conducted by Nukiyama [14] led to the understanding of boiling heat transfer. A plot depicting the dependence of heat flux on the wall superheat to characterize boiling was achieved using a power controlled nichrome wire. The significant contribution from his work led to the identification of the following four regimes of pool boiling:

1. Free convection boiling
2. Nucleate boiling,
3. Transition boiling, and
4. Film boiling.

Figure 4 shows the schematic representation of a pool boiling curve with the four regimes and the dominant heat transfer mode in each regime.

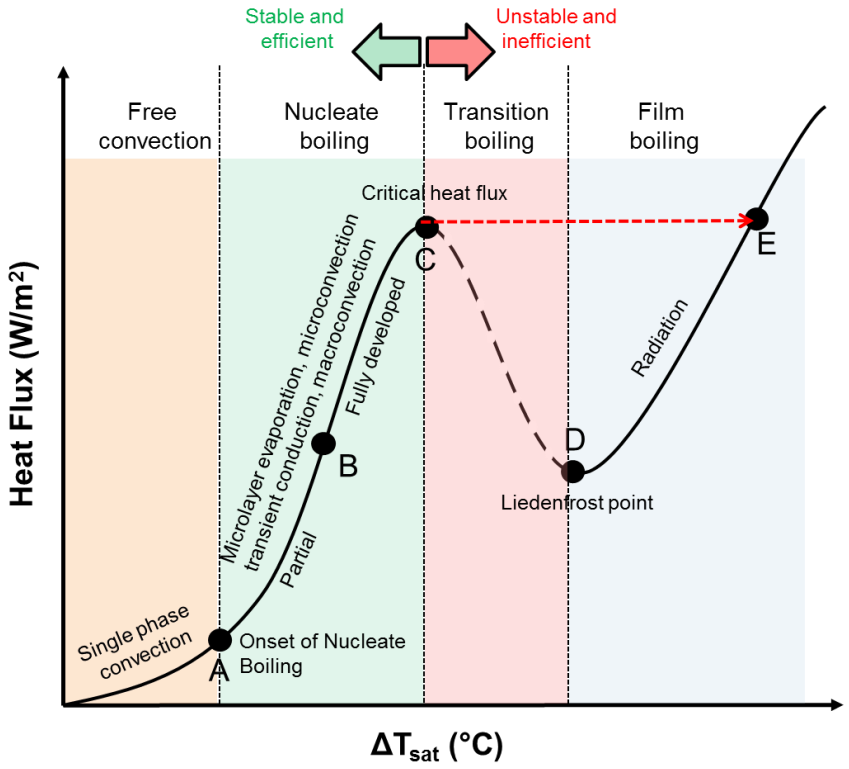

Figure 4. Pool boiling curve showing the dominant mechanisms in each regime.

Free/Natural convection boiling: When surface temperature (T_{wall}) is greater than the saturation temperature of water (T_{sat}), density of the fluid close to the surface decreases. This results in a density gradients causing the hot fluid to rise and the cold fluid to move

towards the hot surface setting up natural convective currents. Thus, heat is transferred from the surface to water via free convection. It exists in the range $\Delta T_{sat} < \Delta T_{sat,A}$.

Nucleate boiling: Nucleate boiling is accompanied by nucleation and subsequent departure of bubbles on the heated surface. $\Delta T_{sat,A}$ is referred to as the Onset of Nucleate Boiling where the first bubble nucleates. There are two distinguishable flow regimes in this region in a heat flux controlled system. This is shown as region A-C in Figure 4 and is referred to as the partial nucleate boiling. This region is characterized by isolated bubbles that form and detach from the surface. This disturbance (separation) in the vicinity of the heater surface induces a good fluid mixing increasing the HTC, with an increase in the heat flux. With further increase in the heat flux and wall superheat ΔT_{sat} increases beyond a certain value indicated by $\Delta T_{sat,B}$ where more nucleation sites become active and increased bubble formation causes bubble interference and coalescence. In the region B-C, bubbles coalesce and escape as jets or columns. This region is referred to as fully-developed nucleate boiling.

Transition boiling: This region exists in $\Delta T_{sat,C} \leq \Delta T_{sat} \leq \Delta T_{sat,D}$. The heat flux rate in the nucleate boiling is very high as a result of agitating motion of bubbles. This intense formation of bubbles results in an unstable vapor film at high heat fluxes. This film has a very low thermal conductivity as it is formed by vapor. The heat flux rate and ΔT_{sat} continues to increase as long as the agitating motion of bubbles overcomes the effects of the film. However, when the insulating effects of the film dominates the bubble agitation, the heat flux rate decreases with increasing ΔT_{sat}. In this region, the conditions oscillate between film and nucleate boiling, i.e. the film is continually forming, collapsing and

reforming. Since the thermal conductivity of the vapor film is very low compared to that of the liquid, h and q_s must decrease with increasing ΔT_{sat}.

Film boiling: It exists in the region $\Delta T_{sat} > \Delta T_{sat,D}$. The surface is completely covered by vapor film. Point D is called the Leidenfrost point where the heat flux is minimum, $q''_{min.}$ Heat transfer from the heater surface to the liquid occurs by radiation and conduction. As T_{wall} is increased, heat flux increases as h increases. Then radiation effects dominate conduction resulting in the rapid increase in heat flux with increasing ΔT_{sat}.

Nucleate boiling is widely recognized as an effective technique to dissipate heat from these devices and is the focus of the current work. CHF is the upper governing limit in the nucleate boiling regime and HTC determines the heat removing capability of the surface. The extent of enhancement of an augmented surface is determined by the degree to which its boiling curve is shifted to the top and left, which indicates high CHF and HTC when compared to a plain surface without augmentation features. This has led to widespread research for developing surface geometries to improve HTC and CHF in pool boiling that caters to a wide range of applications.

1.6. Applications

Numerous applications benefit from enhanced boiling heat transfer. Typically, the heat fluxes determine the operating ranges while the HTC's dictate the efficiency of the process. A simultaneous enhancement in both CHF and HTC is desirable for most applications, albeit some applications can still benefit from either an increase in CHF or an increase in HTC. An application specific description of the benefits of boiling heat transfer is elucidated here.

1.6.1. Electronics Cooling

The fast-paced and emerging fields, such as microelectronics, have identified advanced thermal management solutions as a critical pathway to significantly bolster the advancements in the industry [15]. With the device size and the packing architecture predicted to become complex every successive year, it is imperative that the component level heat fluxes are expected to increase significantly. Figure 5a shows the heat generation in various electronic components of different length scales. Some applications that can directly benefit from advanced thermal management solutions are high-power desktop computers, data center (server and rack level) cooling, solid-state laser diode cooling, etc. Currently, air and liquid cooling techniques are employed to meet the demand for efficient cooling of high-power density components. These techniques operate under low heat transfer coefficients or require a large volumetric flow rate to induce the required level of cooling. Cumulatively, they increase the pumping power and costs, which reduces the energy efficiency of the cooling technique. Since the latent heat of liquid is significantly greater than the sensible heat of the liquid over the allowable temperature rise of the cooling fluid, heat transfer due to phase change is substantially higher than single phase heat transfer. Figure 5b compares the heat transfer coefficients of popular cooling methods.

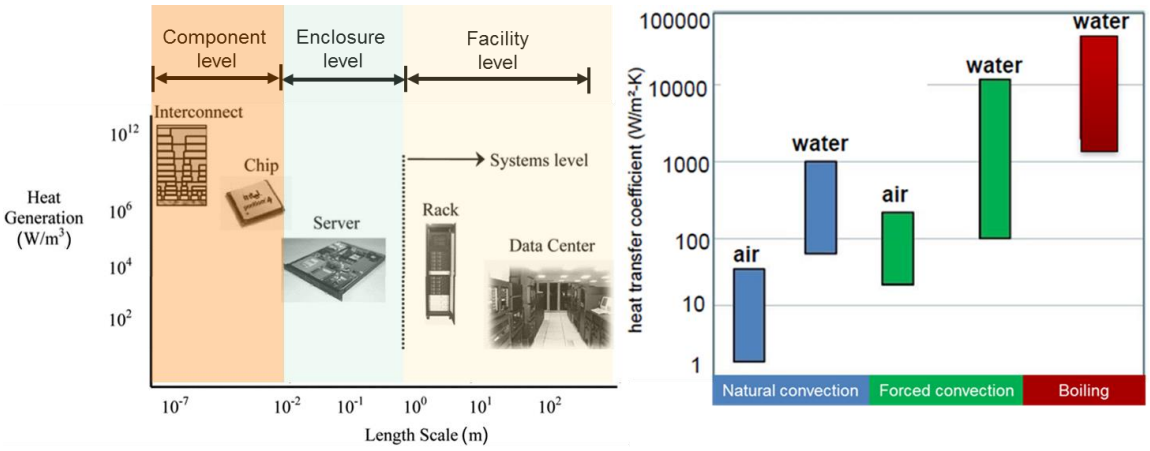

(a) Component level heat generation in data centers

(b) Typical heat transfer coefficients for popular cooling techniques

Figure 5. (a) Length scale based heat generation trends in electronics [16], (b) popular cooling methods and their respective heat transfer coefficients (Data adopted from Incropera and Dewitt [17].

1.6.2. Refrigeration and air-conditioning

Flooded evaporators employing pool boiling are at the core of numerous refrigeration systems in industrial and commercial applications. However, the operating HTCs in these chillers are considerably low, and the CHFs for refrigerants are also extremely low (~250 kW/m^2). Increasing CHF will allow a larger volumetric heat transfer rate, compact evaporators and lower refrigerant inventory. Since the refrigerant-side HTC is the dominant thermal resistance, improving boiling performance of evaporators improves the energy efficiency of the refrigeration cycle and can potentially reduce the energy costs in the US. A US Department of Energy status report [19,20] has identified that an increase in the evaporator performance has the potential to significantly impact the global energy concerns. A COP increase of 5-10% would result in annual US energy savings of $2.3-4.6 billion.

1.6.3. Reboilers

Kettle reboilers find applications in refineries, gas processing and petrochemical plants. Boilers that are used in production of electricity use extremely high steam parameters to reduce fuel consumption. These boilers encounter challenges related to the selection of heater material. Typically steel based alloys are employed, however the manufacturing costs are significantly higher and the plant operates at an efficiency of 40-45%. A critical condition in the design of the evaporators are the uniform distribution of temperature. The existing arrangement in these evaporators can be improved by carefully manipulating the liquid and vapor travel close to the tube surface through vortex generators and vapor encapsulation inhibitors.

1.6.4. Desalination

Nearly 20% of the world population is living below the acute water poverty level (500 m^3 per capita per year) [21]. Thermal desalination is a highly attractive technique to remove salts from sea water to produce water for human consumption and other agricultural applications. It overcomes the hurdles in the Reverse Osmosis process such as its high maintenance cost, water quality due to residual deposition of chlorides and bromides, and algae blooms that pose serious health hazards.

1.7. Structure of Dissertation

The dissertation is structured as follows:

Chapter 1 (Introduction): The basic concepts and underlying physical mechanisms in boiling heat transfer is its relevance to industrial applications is highlighted.

Chapter 2 (Literature Review): This section reviews the recent advances and notable contributions in enhancing pool boiling heat transfer. A historic perspective of the mechanistic evolution of surface geometries and a critical review is provided.

Chapter 3 (Experimental Details): The mechanical design and fabrication details of the basic test section components is described. The experimental procedure and protocols followed during the experimental testing is presented. Heat loss and uncertainty analysis arising from the instrumentation and testing is also explained.

Chapter 4 (Results and Discussion): The results are presented in three main sections classified based on the enhancement mechanisms and scales (i) enhanced macroconvection in microscale (200 - 400 μm) features, (ii) increased capillary wicking in microscale (40 – 60 μm) graphene composites, and (iii) modified contact line motion on nanoscale chemically inhomogeneous surfaces.

Chapter 5 (Major Accomplishments): The sections outlines the accomplishments at the micro and nanoscale and the mechanistic outcomes of tailoring surfaces with flow modulation, nucleation enhanced and capillary propelled mechanisms. The societal outcomes in industrial applications is also described.

Chapter 7 and 8: are for references and appendices, respectively.

Chapter 2

2. Literature Review

2.1. Surface Enhancement Goals

Numerous applications demand wide heat flux operating ranges and efficient heat removal processes to improve safety, reliability and functionality of the product. When translated to a boiling curve, this represents an increase in CHF accompanied by a decrease in wall superheat relative to a baseline surface as shown in Figure 6. Cumulatively, it represents a leftward shift in the boiling curve which represents the degree of enhancement achieved with a specific enhancement feature.

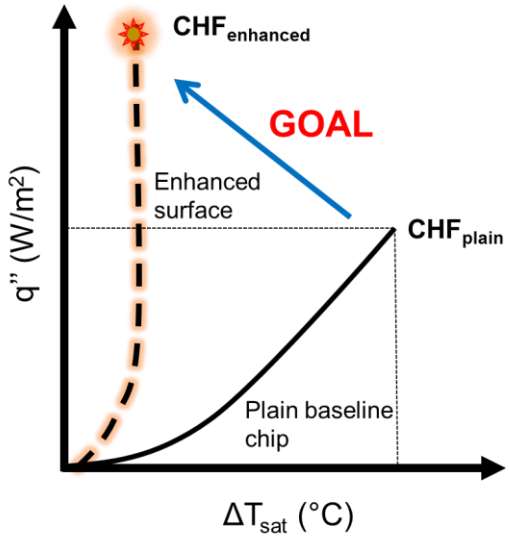

Figure 6. Schematic representation of surface enhancement goals.

2.2. Baseline Surface

The baseline surface in a number of research studies [22–25] have been defined as the surface lacking the enhancement features. Since the roughness plays a critical role in the overall boiling heat transfer performance, due consideration to the surface roughness

parameters must be given to clearly define the baseline value. In this work, a plain copper surface manufactured through a computer numerical control micromachining process with a mean arithmetic roughness (R_a) of 1.1 µm (± 0.3 µm) serves as the baseline for enhancement comparison. Alternatively, a number of heat transfer models are available to predict the CHF on plain surfaces. Amongst these models, the Kandlikar model [26] is widely accepted as it accurately captures the hydrodynamic parameters and its interaction with the solid substrate through the measurement of contact angles. This model uses a force balance on the growing bubble to predict the CHF as shown,

$$q''_{CHF} = h_{fg}\rho_g^{1/2}\left(\frac{1+cos\beta}{16}\right)\left[\frac{2}{\pi}+\frac{\pi}{4}(1+cos\beta)cos\varphi\right]^{1/2} \times \left[\sigma g\left(\rho_l-\rho_g\right)\right]^{1/4} \quad (9)$$

Equation (9) may be employed in ascertaining the experimental CHF values obtained on the plain baseline surface.

2.3. Enhancement Techniques

Pool boiling heat transfer centers on the nucleation, growth and departure of a bubble on a surface through latent heat. During this process, heat is transferred through (i) Microconvection, (ii) Microlayer evaporation, and (iii) Transient conduction. The heat transfer in each of these processes relies on the region surrounding the bubble, often referred to as the influence region. Enhancement strategies are devised to improve the local nucleation and rewetting mechanisms in this region which have resulted in significant improvements in either critical heat flux (CHF) or heat transfer coefficients (HTC).

The following classification is used to discuss the enhancement mechanisms:

- Increased surface area through extended surfaces, protrusions

- Additional nucleation sites through porosity, re-entrant cavities, microcavities
- Increased capillary wicking through porous coatings, bio-templated features, nanowires
- Wettability modifications through biphilic surfaces, nanofluids modifications
- Contact line augmentations through nanoscale and microscale ridges
- Graphene based structures

2.3.1 Increased surface area

Increasing the surface area has been one of the oldest and conventional techniques to increase the heat transfer rate. Researchers have explored rectangular fins or micro fins and tested with various fluids; all of which have resulted in increased heat transfer performance due to area enhancement. Pastuszko and Piasecka [27] experimentally studied the effect of pool boiling performance on mini fin arrays and micro cavities with water and FC-72 at atmospheric pressure. Mini fins of 0.5 mm and 1 mm and microcavities of depth 15 – 30 µm were fabricated by the spark erosion technique. Their study suggested that microcavities provided additional nucleation sites which contributed to intensification of heat flux. Furthermore, they suggested mini fins with 1 mm height provided effective boiling heat transfer intensification for water at heat fluxes higher than 70 W/cm^2. Pastuszko [28] studied the effect of fin height, pore diameters and tunnel pitch of tunnel surfaces fabricated from a 0.05 and 0.1 mm thick perforated copper foil with pore diameters of 0.3, 0.4, 0.5 mm sintered with mini fins of height 5 and 10 mm. A heat transfer coefficient of 50 $kW/ m^2\text{-}^{\circ}C$ is reported for water which was 3 – 4 times higher than smooth fins.

Rainey et al. [29] experimentally studied the effects of pressure, subcooling and non-condensable gas of microporous enhanced square copper pin fin array with FC-72 as the working fluid on nucleate boiling and CHF. Their study revealed that for saturated liquid with microporous finned surfaces, CHF values decreased linearly with increasing fin length. They attributed this effect to decreased fin tip temperatures. Furthermore, their research suggested that horizontal orientation of heater surfaces performed better than its vertical counterpart. Guglielmini et al. [30] conducted a series of studies for different geometries on square pin fin array with FC-72 as the working liquid. They concluded that longer fins performed better when the fins are uniformly spaced and also finned surfaces significantly increases heat transfer coefficient at low heat fluxes.

Concluding remarks: Increased surface area provides additional nucleation cavities and greater surface area for heat transfer. The application of tall fins with refrigerants (low HTC) is attractive but the performance with other fluids (high HTC) seems detrimental. A temperature gradient generally develops along the fin height which introduces two regimes of boiling (i) film boiling at the base of the fin, and (ii) nucleate boiling at the top. The thermal resistance also influences this effect which causes an increase in the surface temperature and a drop in the HTC. Literature shows a lack of area enhanced surfaces at the microscale which contributes to an increase in both CHF and HTC.

2.3.2 Increased nucleation sites

Porous surfaces have offered very high flux at relatively low temperature differences due to their increased surface area and availability of additional nucleation sites. Patil and Kandlikar [31] reviewed the different manufacturing techniques used to create porous surfaces for boiling heat transfer. The manufacturing techniques were classified into

sintering, electrodeposition, and advanced techniques. Their study suggested sintering to be an easy and efficient technique to obtain porous structure with electrodeposition being a viable alternative using hydrogen bubble evolution. They also listed soldering, brazing, binding with alloys, chemical vapor deposition etc. under advanced techniques.

Nakayama et al. [32,33] suggested three fundamental evaporation modes (flooded mode, suction evaporation mode and dried up mode) responsible for boiling heat transfer in porous surfaces. Suction evaporation mode is identified as an effective region to dissipate large heat flux. Webb [34] conducted a series of boiling experiments to study different geometric variables like particle diameter, coating thickness and pore size of copper porous coatings. The results indicate that a maximum boiling coefficient is obtained with a coating thickness of roughly three to four times particle diameters for highly conductive surfaces like copper but this finding does not hold true for low thermal conductivity materials like bronze. Furthermore he suggested that pore size has a significant effect over particle size. The paper also identifies the requirement to understand vapor-liquid phenomena in the pores.

Li and Peterson [35] conducted a study on porosity, pore size and thickness of sintered copper mesh structure. Their study on three pore sizes, 119.2 μm, 140 μm and 232.2 μm, suggested that a smaller pore size was better for heat transfer performance. In terms of CHF, a thicker coating increased the CHF whereas a thin coating contributed to low wall superheats. Afgan et al. [36] conducted pool boiling tests with distilled water, R-113 and ethanol on horizontal tubes to understand the effect of hysteresis. The tube was coated with sintered metal layers of spherical or dendritic particles. Boiling hysteresis was observed

for coating thickness of over 1 mm with water. It was concluded that for highly wetting liquids, hysteresis was observed for all coating thicknesses.

Bergles and Chyu [37] conducted boiling tests on porous metallic coatings to understand the effect of hysteresis. The degradation characteristics of porous surfaces are studied for commercial application of these surfaces with water and R-113. They observed that nucleation takes place within the porous matrix and these reentrant cavities are not subjected to flooding. Mudawar and Anderson [38] studied different enhancement techniques like fins, studs, grooves and vapor trapping cavities by having the heater surface in vertical orientation with FC-72 and FC-87. Heat fluxes in surplus of 100 W/cm^2 with saturated FC-72 were reported for cylindrical enhanced surfaces. They also concluded that artificial cavities larger than 0.3 mm were ineffective in lowering wall temperature.

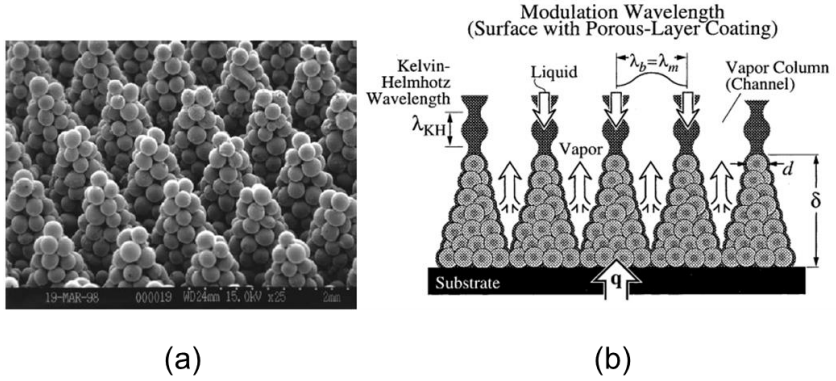

Figure 7. (a) SEM image of modulated sintered porous coatings, (b) proposed liquid-vapor pathways in structures showing vapor venting in the valleys with liquid capillary sucking through the porous hills [39].

Liter and Kaviany [39] implemented modulated porous structures to create vapor venting and artery liquid capillary action inside the porous coatings as shown in Figure 7. This arrangement was highly effective and increased the CHF by 3X. However, at higher heat fluxes, the counter-flow resistance increases due to increased nucleation activity on the

surface. This disrupts the capillary action and results in dry-out conditions. Li and Peterson [40] used sintered porous mesh of varying thickness to understand the effect of thickness as shown in Figure 8a. A CHF of 347 W/cm^2 was reported, however the wall superheat was in excess of 60 °C which is undesirable as the HTC is significantly lower. This study helped identify an optimal thickness to strike a balance between availability of additional nucleation sites and thermal resistance offered by the porous coatings. In another publication, Li et al. [41] used modulated porous coatings to reach a CHF of 450 W/cm^2 at a wall superheat of 25 °C. A maximum HTC of 200 kW/m^2°C was obtained for this surface. The sintered porous coatings were placed on a circular area (8 mm diameter, Figure 8b) and the importance of vertical and lateral liquid replenishing pathways through the porous structure were highlighted in their study.

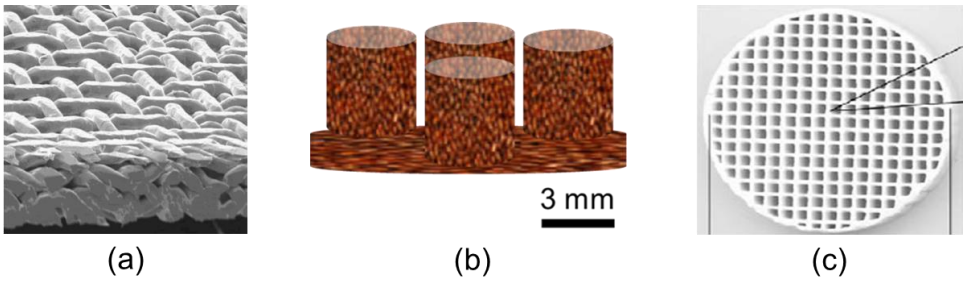

Figure 8. Porous heat transfer surfaces (a) sintered-mesh [35], (b) tall porous modulated posts [41], and (c) honey comb structures [42].

Some non-conventional techniques have been used by researchers to increase CHF. Mori and Okayuma [42] created a heat transfer surface by attaching a honeycomb structure to the heated surface and investigated the effect of height of the structure on the pool boiling performance as shown in Figure 8c. They reported a CHF of 250 W/cm^2 which was approximately 2.5 times higher than a plain surface. They identified capillary action and

reduction of flow resistance as the enhancement mechanism. However, the wall superheat reported in their study was 50 °C, which is undesirable.

Concluding remarks: This porous enhancement technique benefits from increasing the nucleation site density on the boiling surface. Consequently, the ONB occurs at lower wall superheat due to the capability of the cavities to trap gases which reduces the hysteresis effect. The liquid retention in the coatings increases the effects due to thin film evaporation (microlayer evaporation). The challenge in these surfaces is that the thermal resistance needs to be carefully weighed against the availability of additional nucleation sites. Thicker coatings increase CHF but also have higher wall superheats due to thermal resistance induced by the coating.

2.3.3 Increased evaporation through capillary wicking

The microlayer is a thin liquid film contained under a growing bubble from which evaporation occurs. Increasing the surface area occupied by the liquid film is seen as an effective way to improve the heat transfer rate. Nakayama et al. [32] used tunnel structures with pore sizes, channel heights, channel width, tunnel pitch and pore pitch ranging between 30-600 μm and achieved a heat flux of 130 W/cm^2 at a wall superheat of 4.5 °C. The bubble formed inside the tunnels exited periodically from the pores, while liquid entered from other pores.

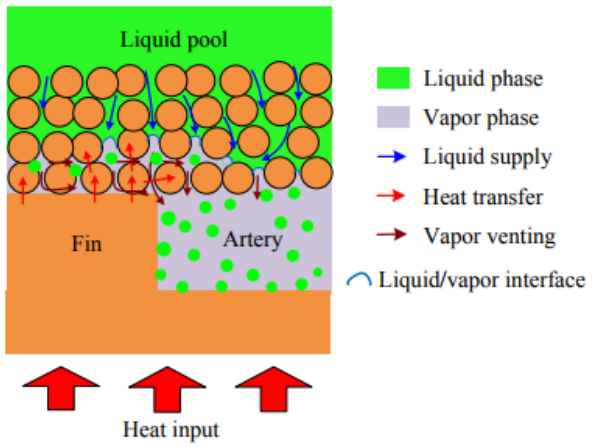

Figure 9. Porous artery structure with inverted vapor venting in the channels and liquid feed through porous coatings [43].

Bai et al. [43] used arterial structures on a circular substrate with microchannels. A porous silver-brazed plate was assembled over the microchannel as shown in Figure 9. The microchannels were employed as vapor venting routes with porous-plates structures serving as liquid feeders through capillary forces. A maximum CHF of 610 W/cm^2 at a wall superheat of 43.5 °C was obtained. Inverting the flow and using microchannels as vapor removal pathways results in extremely high wall superheats as the prime heat exchange surface is in contact with vapor. Rahman et al. [24] used bio-templated virus structures to create micropillar wick structures as shown in Figure 5a. They introduced a non-dimensional wicking number which directly correlated with the increase in CHF. A maximum CHF of 250 W/cm^2 was obtained at a wall superheat of ~30° which was attributed to the wickability of the surfaces. In a subsequent publication, Rahman et al. [44] employed bi-conductive strips and bio-templated wicking structures to improve the wettability. A maximum CHF of 307 W/cm^2 was obtained at a wall superheat of 16 °C.

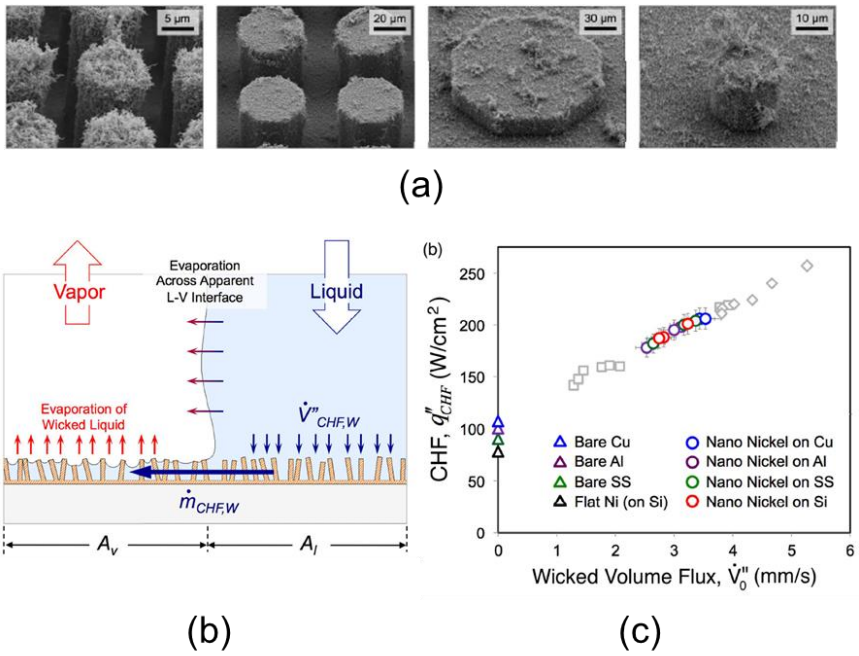

Figure 10. Capillary wicking on bio-templated nanostructures. (a) Different configurations of micro posts enhanced with nanostructures, (b) liquid-vapor interaction in the enhanced structures, and (c) Linear dependence of CHF on the wicking rate [24].

Concluding remarks: The increased evaporation from curved interfaces formed inside the wick structures contributes towards increasing the heat transfer rates. In such an arrangement, increased evaporation rates leads to excessive bubble formation leading to localized dry-spots and an increase in surface temperature.

2.3.4 Surface wettability change

Changing the surface energy through nano/microscale coatings have shown to increase the CHF. Nanoscale coatings by electrodeposition process have contributed to improved liquid wettability which has enhanced boiling heat transfer. Yao et al. [22] grew copper nanowires with 200 nm diameter and 5-10 µm height on flat copper substrate using anodized aluminum oxide templates and electrodeposition process as shown in Figure 11a. A boiling performance of 164 W/cm^2 at a wall superheat of 11 °C was reported owing the

improvement to increased heat transfer area and coupling effects of micro/nanoscale cavities which affe cted the bubble dynamics associated with pool boiling. Ahn et al. [45] deposited nano sized zircaloy-4 on a surface to decrease the contact angle of water which increased liquid wettability contributing to enhanced performance. Betz et al. [25] have shown that patterning hydrophilic regions with hydrophobic islands resulted in maximum enhancement in CHF. The patterned hydrophobic and hydrophilic surfaces are shown in Figure 11b.

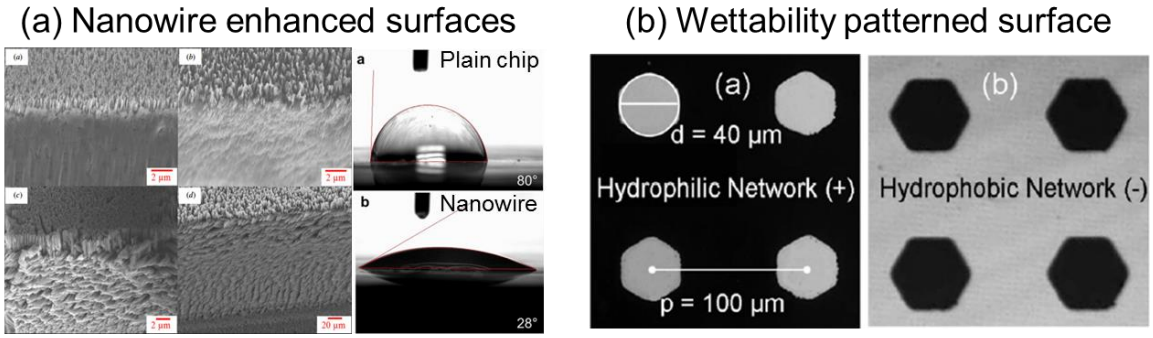

Figure 11. Nanowire enhanced surfaces [22] and Patterned hydrophobic and hydrophilic structures [25] for improved wettability.

Concluding remarks: A hydrophilic coating improves the liquid wetting while the hydrophobic coating influences the nucleation characteristics. The hydrophilic region results in cavities being flooded which causes delayed ONB while the hydrophobic regions results in dry-spots and impedes heat transfer. The challenge in these coatings is to carefully weigh out the effects of hydrophobic and hydrophilic regions on the surface.

2.3.5 Increased heat transfer from microlayer

Recently, Zou and Maroo [46,47] employed ridges as an enhancement structure and demonstrated that the fragmentation of the microlayer in the form of discrete ridges resulted in additional evaporation of the microlayer liquid film underneath the bubble. This

caused an increase in bubble growth rate and frequency leading to an increase in CHF values which was supplemented with an analytical model. Additionally, they also demonstrated that an enhancement in CHF was achieved when the microlayer thickness was less than the ridge heights which enabled partitioning of the microlayer into slabs. Figure 12 summarizes their understanding of the types of enhancements achieved on the microridge surfaces and the corresponding geometrical parameters of the ridges.

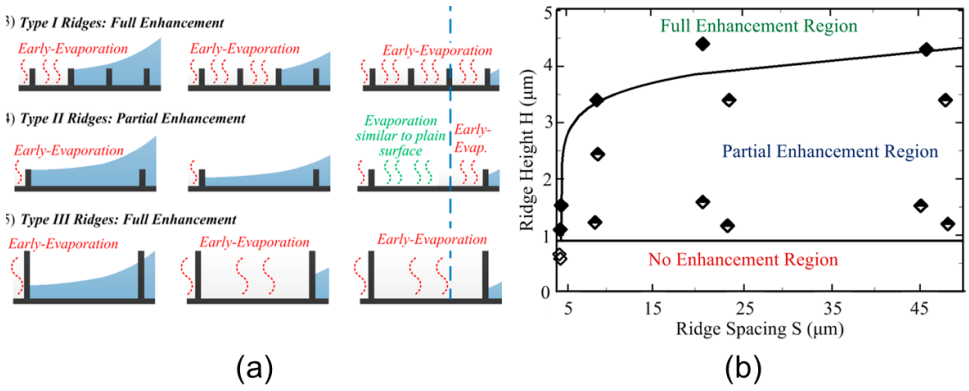

Figure 12. Microlayer evaporation from microridges. (a) Schematic representation of the types of microlayer fragmentation mechanisms, and (b) microridge geometry dependence on the type of enhancement [47].

Concluding remarks: The microlayer fragmentation results in increased evaporation rates which results in higher bubble frequencies and growth rates. However, this mechanism is effective in the absence of wicking. In addition, the structural dimensions play a critical role. A large ridge spacing results in additional effects including roughness that changes the dynamics of the underlying mechanism.

2.3.6 Contact line modifications

Interface motion and its dynamics are at the heart of numerous wetting and non-wetting applications in microfluidics, heat transfer, ink-based printing, and the purification

industry. Solid surfaces commonly employed in these applications are inherently rough due to surface features as a consequence of the manufacturing process or energetically heterogeneous due to a change in chemical composition. The roughness implicates a change in the contact angle measured along different viewing directions while the heterogeneity manifests through the motion of the contact line (CL) [48]. For surfaces with roughness features, the contact angle (and hysteresis) may take a predictable character. Consequently, the motion of the CL occurs in a stick-slip fashion when the liquid interface is advanced or receded [49,50]. The Wenzel equation successfully predicts the expected contact angles for roughened surfaces by applying a *rugosity* factor. This factor is computed as the surface area normalized over a smooth surface without roughness features, thereby providing a strategy to increase or decrease wettability of a solid surface through roughness modulation.

The wetting behavior in the chemical heterogeneity case is generally ignored since the scale of the heterogeneous irregularities is often isolated from the feature sizes and the CL at the solid-liquid-vapor/gas interface is affected only in the microscale. However, in applications that employ nanoscale coatings, the motion of the CL due to the heterogeneity induced by the chemical constituents has a significant bearing on the wetting behavior [51]. In this case, the Cassie-Baxter equation [52] may be employed in estimating the apparent CA through the known area fractions of the two constituents on the surface. Such surfaces are beneficial in driving the CL through contact angle manipulation as it traverses through different chemically constituted nanoscale patches.

Brochard [53] demonstrated the motion of the CL towards lower surface energy on a surface treated with chemical gradients and towards higher surface energies on thermally

induced gradients. Decker and Garoff [54] experimentally investigated the effects of contact angle hysteresis and CL motion on chemically heterogeneous surfaces. They demonstrated that chemical change induces a specific change in the advancing and receding angles, but not necessarily in the contact angle hysteresis. Additionally, they showed that the spatial variation of wettability influences the CL motion on the surface. Varagnolo et al. [55] showed that large wettability contrasts between hydrophobic and hydrophilic patterns on a surface reduces the effective CL speed by causing the interface to undergo a stick-slip motion. These studies indicate that the local wettability change on chemically inhomogeneous surfaces drives the CL motion.

The three-phase contact line and its dynamics significantly alter the bubble dynamics on the heater surface. The heat transfer due to the CL motion is significantly higher than the bulk heat transfer as indicated in multiple reports [56,57]. This new enhancement method was recently adopted into the family of enhancements which was made possible from the pioneering studies [56]. They observed the meniscus deformation at the contact line can affect the disjoining pressures, which is capable of enhancing the heat transfer. Recent developments through controlled two-phase experimentation techniques [8,13,58] suggest that the initial receding motion of the liquid increases the dry-spot region and drives the superheated liquid layer away from the dry-spot, thereby resulting in a lower heat transfer. On the other hand, it is shown that the advancing motion contributes efficiently by causing a gradual quenching of the region as the bubble departs which results in 3X heat transfer when compared to the receding contact line motion.

Recently, Raghupathi and Kandlikar [59] fabricated microgrooves of shallow depths to understand the contact line dynamics under saturated boiling conditions. Using high speed

imaging, they were able to demonstrate the generation of multiple contact lines for specific aspect ratios of the grooves. The schematic representation of the contact line arrangement on the microgroove surface is shown in Figure 13. The multiple contact lines increase the heat transfer proportionally, thereby resulting in ~2X increase in CHF based on the wetted area, as shown in Figure 13. When the groove heights were less than 50 µm, microlayer portioning was seen to be effective. As the heights were increased (greater than 100 µm), bubble confinement in the channels was seen to be responsible.

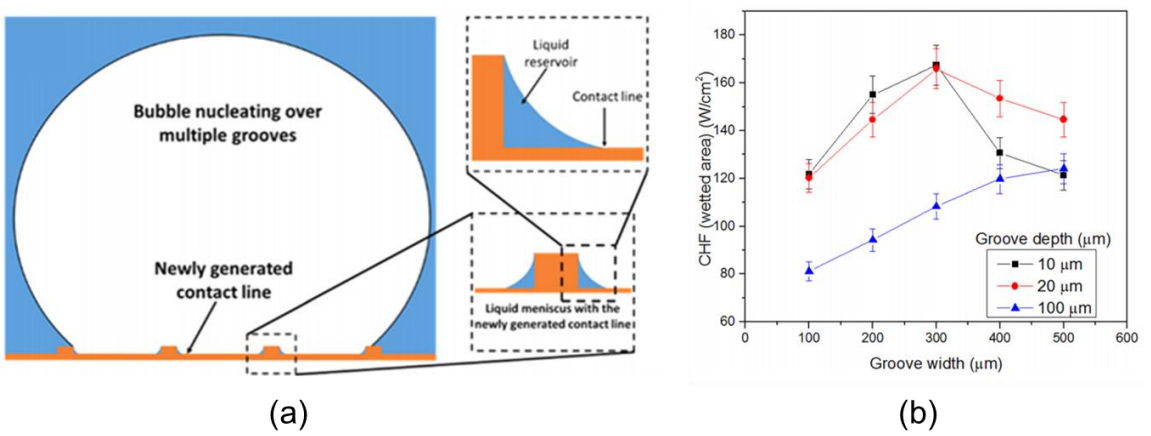

Figure 13. Microgrooves showing additional contact line formations, (b) Effect of microgroove width on the CHF based on the wetted area [59].

Concluding remarks: A critical consideration while designing surfaces with this concept is the competing influence of nucleation activity, bubble coalescence, capillary wicking and contact angles. Typically, the enhancements have been attributed entirely to the contact line mechanisms but the weighted influence of other mechanisms such as roughness augmentation and microlayer evaporation needs to be incorporated in the design of structures.

2.3.7 Graphene coated surfaces

Graphene, a two-dimensional layered material, has gathered interest in the field of heat transfer enhancement due to its thermal conductivity and wetting behaviour which makes it an active research topic. Previous research in the field of graphene as an enhancement for two-phase heat transfer coatings is mainly focused on boiling colloids and its resulting self-assembly characteristics.

Table 1. Literature summary of high performing surfaces with GO and graphene colloids

Author's	Heat flux (W/cm^2)	Enhancement mechanism
Ahn *et al.*	139	Base layer deposition
Kim *et al.*	140	Laminated film
Ahn *et al.*	158	Wetting characteristics
Park *et al.*	175	Self-assembly characteristics

Table 1 summarizes the heat flux obtained and enhancement mechanisms by boiling colloidal graphene and graphene oxide (GO). Ahn et al. [60] boiled colloidal reduced graphene oxide (RGO) to study the effect of graphene base layer deposition due to self-assembly. Kim et al. [61] experimentally investigated the effects of concentration of GO colloids on a nichrome wire heater and concluded that GO deposition on the surface forms a smooth laminated film which results in an increase in CHF. Ahn et al. [62] also conducted an experimental study to understand the effect of RGO flake aggregation on CHF on a one and two sided coating on Ni-Cr wire. Park et al. [63] further demonstrated that the nanofluids containing graphene nanosheets can be exploited to maximize CHF by the self-assembly characteristic of nanofluids. However the capillarity and surface wettability effects by boiling nanofluids are still not fully understood. Fundamental understanding of

the underlying bubble dynamics can be achieved by directly coating a GO or graphene layer on the substrate.

2.3.8 Previous relevant work at the Thermal Analysis Microfluidics and Fuel Cell Laboratory (TAMFL) at RIT

The application of separate liquid vapor pathways as a mechanistic tool has shown to yield high CHF's with a simultaneous increase in HTC. Departing bubbles are postulated to as localized pumps by directing the liquid towards the heater surface. Kandlikar [64], through his pioneering work in 2013 was the first to establish this mechanism. A contoured fin was developed to exploit the mechanism using evaporation momentum force to control the bubble trajectory on the heater surface. Bubbles were generated at the nucleation site located between the land and fin. The bubbles swept over the land regions while liquid was added through the sidewall regions of the fins (see thumbnail in Fig. 14). This mechanism resulted in a CHF of 300 W/cm^2 and a HTC of 629 $kW/m^2°C$. Cooke and Kandlikar [65] showed that open microchannels acts as reservoirs and direct liquid towards the nucleation sites. In 2014, Patil and Kandlikar [23] developed porous fin tops through a two-step electrodeposition technique and forced nucleation to occur over the fin tops with liquid addition through the channel region. Figure 14 summarizes the notable enhancements (nanowires [22], open-microchannels [66], contoured fin [64], electrodeposited fin tops [23]) developed at RIT-TAMFL from 2011 to 2014.

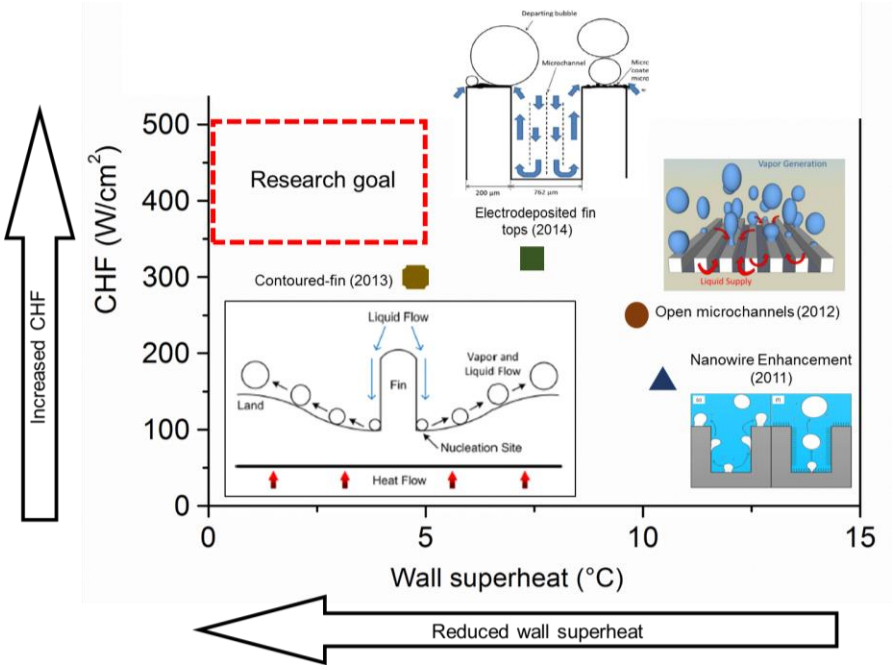

Figure 14. Performance metrics and enhancement mechanisms for surface developed at RIT-TAMFL. This plot also shows the research goals of the present work indicated by the performance metrics, i.e. CHF > 350 W/cm^2 and wall superheat < 5°C.

2.4. Research Gap

Understanding heat transfer mechanisms is crucial in developing the next generation of enhancement techniques in pool boiling. As seen from literature, surface enhancements have contributed towards identifying benchmark mechanisms, namely, additional surface area, increased nucleation activity, wickability, wettability control, and microlayer partitioning. However, these enhancements introduce challenges such as thermal resistance, and the competing nature of liquid and vapor in the vicinity of the heated surface which leads to early CHF or increased wall superheats that translates to low HTC. These techniques have resulted in CHF's of 250 W/cm^2, or the HTC's have been lower than 150 kW/m^2°C. Although the focus of the previous research study has been directed towards delaying the formation of the vapor film, the factor of safety imposed for practical

applications further lowers the operating ranges. In addition, the chaos near the heater surface makes the system unreliable and unstable.

Therefore, a research gap is identified where the enhancement in both CHF and HTC is required to improve the reliability of devices and facilitate its adoption in industries. This research work aims to achieve this by introducing a novel enhancement technique termed as *separate liquid-vapor pathways*. This work is expected to have a direct impact by reducing the size of heat exchangers and liquid inventory, while simultaneously ensuring safe and wide operating ranges. This work has direct applications in electronics cooling, refrigeration, nuclear, and distillation industries. The foundation of this mechanism can be manifested in multiple ways to further refine and improve the performance characteristics based on the specific targeted applications. For example, the separate-liquid vapor pathways over tubular surfaces (commonly employed as evaporators in refrigeration systems), can result in location-specific enhancement that can modulate the flow around different regions on the tubes.

Chapter 3

3. Experimental Details

This chapter focuses on the test section, experimental setups, instrumentation techniques, data acquisition systems and experimental procedure adopted in the research work.

3.1. Test Section

The test section used in this study was a 10 mm × 10 mm boiling surface in the middle of a square 17 mm thin copper chip as shown in Figure 15a. The heater side consisted of a 10 mm × 10 mm × 9 mm protrusion with three 0.76 mm holes drilled 3 mm apart to accommodate the thermocouples as shown in Figure 15b. The effect of contact resistance in the heat flux and surface temperature calculation were eliminated by holes drilled in the test chip. Three K-type thermocouples are inserted into these holes to read temperatures T_1, T_2 and T_3.

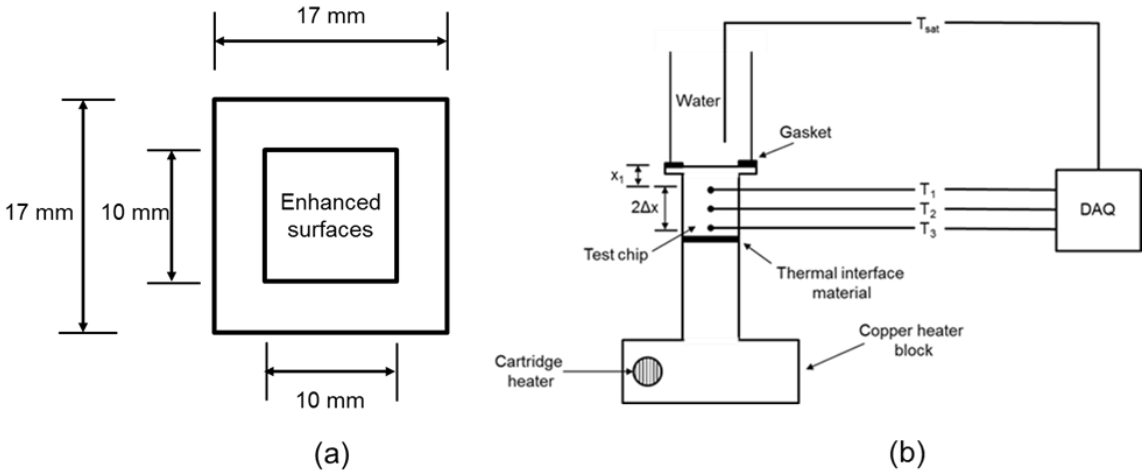

Figure 15. Copper test section details (a) boiling surface, and (b) heater assembly.

The heat flux to the test section was calculated using the 1D conduction equation,

$$q'' = -k_{Cu}\frac{dT}{dx} \tag{10}$$

The temperature gradient dT/dx was calculated using the three point backward Taylor's series approximation

$$\frac{dT}{dx} = \frac{3T_1 - 4T_2 + T_3}{2\Delta x} \tag{11}$$

where, T_1, T_2, T_3 are the temperatures corresponding to the top, middle and bottom of the test chip under study.

The boiling surface temperature was obtained by using eq. (1) and is given by,

$$T_{wall} = T_1 - q''\left(\frac{x_1}{k_{Cu}}\right) \tag{12}$$

where, T_{wall} is the boiling surface temperature and x_1 is the distance between the boiling surface and thermocouple T_1; x_1 was equal to 1.5 mm for all the test surfaces.

3.2. Experimental Setup

An open to atmosphere system and a closed loop vapor chamber system were designed and fabricated to conduct experimental tests with water and dielectric fluids, respectively. The mechanical design and CNC programming were conducted using SolidWorks and SprutCAM respectively. Conventional and Computer Numerical Control (CNC) machining processes were employed for fabricating the components associated with the setup. A detailed description of the two test setups is described below.

3.2.1. Test set-up with water as the working fluid

The schematic of the pool boiling test setup used in this study with water as the working

fluid is show in Figure 16. The main components of the test setup included: (i) test chip, (ii) water bath, and (iii) heating unit. The test chip was housed in a ceramic chip holder held on the bottom garolite plate over which a quartz glass water bath measuring 14 mm × 14 mm × 38 mm was assembled. A rubber gasket was used to seal the two contacting surfaces and it also covered the area outside the 100 mm^2 boiling surface. Additionally, this excess area was covered with Kapton® tape to prevent it from participating in heat transfer. This tape has a thermal conductivity of 0.12 W/m-K at 23°C and has been employed as a heat sealant for a wide range of industrial applications [67]. A middle garolite plate held the water bath on the upper side and was connected to the top aluminum plate by means of two stainless steel socket head cap screws. A water reservoir was mounted between the middle garolite plate and top aluminum plate to replenish water in the glass water bath. The water reservoir was sealed with rubber gaskets on all sides to ensure against leakage. The top aluminum plate was provided with two circular openings for the saturation thermocouple probe and a 60-VDC, 200 W auxiliary cartridge heater to maintain water in the reservoir at saturation by boiling it continuously.

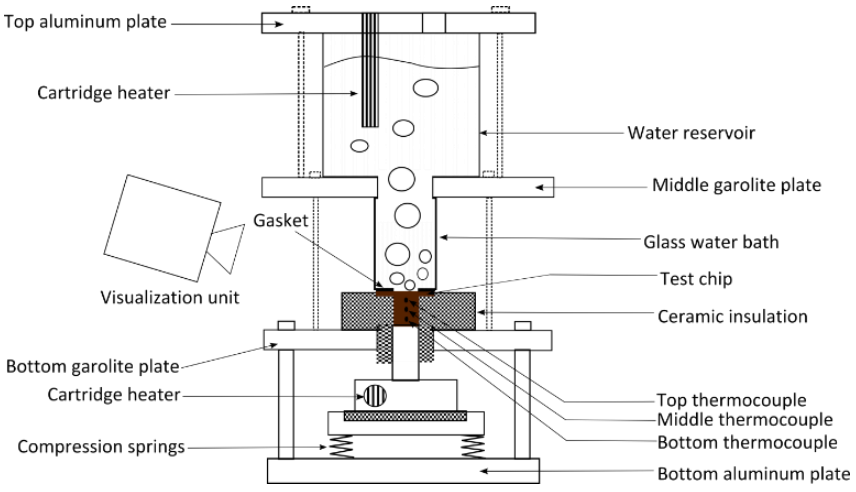

Figure 16. Schematic of experimental pool boiling test setup with water.

The bottom section of the setup consisted of four 120-VDC, 200 W capacity cartridge heaters inserted into a copper heater block similar to the heater section employed by Kalani and Kandlikar [68] in their setup. The block consisted of a truncated portion measuring 10 mm × 10 mm × 40 mm that fits into the groove on the bottom side of the ceramic chip holder. This ensured that the 10 mm × 10 mm surface of the heater is in contact with the test chip which also has a base section measuring 10 mm × 10 mm which facilitated 1D conduction from the heater to the test chip. Thus no heat spreader effect was utilized. Additionally, the copper block was housed on a ceramic sleeve to minimize heat losses. Four compression springs supported the bottom aluminum plate that provided the required degree of movement to establish contact between the test chip and the heater block and accommodate for any thermal expansion during testing. A shaft pin connected the bottom garolite plate and the work desk which ensured stability and robustness of the setup during testing.

A National Instruments (NI) cDaq-9172 data acquisition system with NI-9213 temperature module was used to record the temperature. A LabVIEWVR virtual instrument displayed and calculated the real time surface temperature and heat flux values.

3.2.1.1. Test procedure and experimental setup validation

The test setup was assembled and distilled water was allowed to stand to check against leakage. The main and auxiliary heater electrical connections were made. Each heater was powered by individual power supplies. A grafoil® paper was inserted as a thermal interface material between the heater block and the test chip to minimize contact resistance.

The power was increased in steps once the working liquid attained saturation temperature.

The temperatures were recorded when the thermocouple fluctuation was not greater than ±0.1° over a duration of 10 min. The tests were performed at atmospheric pressure conditions. The data will be collected and processed with heat loss and uncertainty corrections and presented using a traditional pool boiling curve.

Table 2. Percentage composition of elements in copper 101 [70]

Element	Percentage
As	0.0005 (max)
Cu	99.99 (min)
O	0.0005 (max)
P	0.0003 (max)
Sb	0.0004 (max)
Te	0.0002 (max)

To ensure correct assembly and working of the test section, a plain baseline copper chip (C101, oxygen free copper manufactured by Online Metals) was subjected to a boiling test with water to capture the nucleate boiling curve. The selected copper metal type meets the ASTM F-68 standards, and is used in applications where chemical stability as opposed to electrical conductivity of the copper is desired. The percentage composition of different elements is shown in Table 2. This chip was tested until CHF was achieved and further validated by comparing to the Kandlikar CHF model [71] shown in Equation (9). A receding contact angle of 43° was measured using a VCA Optima contact angle goniometer and used in the calculations for estimating the CHF in Equation (9). The experimental and theoretical values were in good agreement, with a percentage difference of less than 1.

3.2.2. Test setup with refrigerants as the working fluid

A test setup designed and fabricated by Kalani and Kandlikar [68] was used to investigate the pool boiling performance with FC-87 (Figure 17). The tests were conducted at standard atmospheric pressure. The main components of the test setup included a stainless steel

chamber, a heater assembly and a water-cooled condenser unit. The stainless steel chamber was 100 mm in diameter and contained the working liquid. Two cylindrical flanges were used to seal the cylindrical chamber on either end. O-rings were provided between the chamber and flanges to prevent leakage and to maintain the pressure in the chamber at the desired level. Openings were provided on the top flange for the refrigerant inlet, saturation thermocouple probe, vacuum port and condenser inlet and outlet connections. The condenser was connected to a water circulating bath which had a temperature range of -30 °C to 150 °C and also a flow control valve to provide the necessary flow rate. A pressure gauge was used in conjunction with the condenser flow rate/temperature control to maintain the pressure inside the chamber at the desired level.

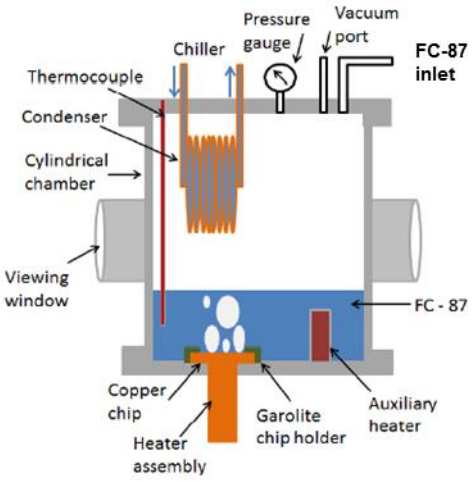

Figure 17. Schematic of pool boiling experimental setup with refrigerants as the working fluid [68].

The bottom flange consisted of an auxiliary heater (120 VDC, 200 – W) which was grooved in and also an opening for the copper heater rod to contact the test chip. The test chip was housed in a garolite casing and bolted to the bottom flange. This ensured that the test surface was held in the horizontal orientation at all times during the experiments. A

cartridge heater inserted into the copper heater rod was connected to the main power supply to supply heat to the test chips. An arctic silver Thermal Interface Material (TIM) was used between the copper heater rod and the test chip to minimize contact resistance. Three K-type thermocouples were inserted into the holes, drilled 8 mm apart, in the copper heater rod to measure the temperature gradient. A NI cDaq-9172 data acquisition system with NI-9213 temperature module was used to record temperatures.

The design of the test chip and its assembly in the garolite casing demands area outside the boiling surface which results in heat loss to the ambient air due to natural convection. A heat loss study was performed in which fiberglass insulation is made to cover the boiling surface and a single phase test is run in air to calculate the heat loss. The heat loss is plotted against the difference in temperature between the surface and ambient air. A linear line fit equation is established and the corrected heat flux is computed. The heat loss did not exceed 2 W/cm^2 for all the tested surfaces here.

3.2.2.1. Test procedure and experimental setup validation

The primary concern in any vapor chamber is to ensure complete sealing. To check for leakage, FC-87 was filled in the steel chamber and allowed to stand for a 24-hour period. After checking for leaks, the chamber was evacuated and again filled with FC-87 by opening the inlet valve to a height of approximately 60 mm above the test chip. The test section and auxiliary heaters were powered by separate power supplies.

The voltage in the power supply was increased in small increments once saturation temperature was attained. The temperatures, coolant flow rate and pressure data were logged. The data was recorded after ascertaining steady state when the thermocouple readings did not fluctuate by more than ±0.1 °C over a 10 min period. Standard atmospheric

conditions were attained inside the chamber by regulating the coolant temperature and flow rate in the circulation bath and power supplied to the heater.

A similar validation procedure to that with water is followed during testing. A plain baseline copper chip was tested with FC-87 as the working fluid to ensure correct setup and operation of the system. The contact angle measured for FC-87 was less than 5°, rendering the surface to be superhydrophilic for the specified copper-FC-87 setup. The CHF obtained was compared to the theoretical CHF obtained by using the Kandlikar CHF equation (see eq. 9).

3.3. Uncertainty Analysis

The procedure for uncertainty calculations is illustrated using the results obtained with the plain baseline copper chip. Firstly, to ensure that the heat is transferred by 1D conduction to the test surface and to ensure minimum heat loss in the measurement region, the temperature profile is mapped. Based on the Fourier law of heat conduction, the temperature profile across the test section is expected to vary linearly with distance. Figure 18 shows the temperature distribution for heat flux of 18 W/cm^2, 66 W/cm^2 and 128 W/cm^2 plotted between T_3 and T_1 for the copper plain chip surface which depicted linear progression with an R-squared value close to 1 which ensured minimal heat loss in the heat flux operating ranges and the experimental process.

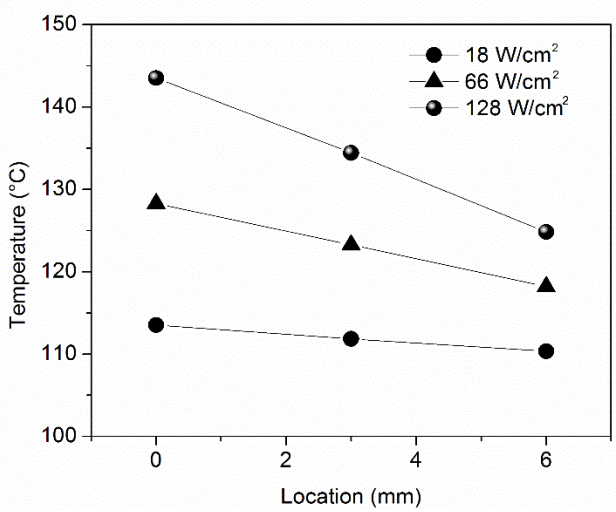

Figure 18. Temperature distribution measured at different heat fluxes measured between the bottom (T_3) and top (T_1) thermocouples.

Two main errors that arise during experimentation are the bias errors and precision errors. The bias errors arise due to errors from calibration instruments and precision errors are due to sensitivity of the testing devices. A thorough uncertainty analysis was performed, similar to Patil and Kandlikar [23] and Cooke and Kandlikar [65].

Cumulatively, the errors due to bias and precision can be expressed as,

$$U_y = \sqrt{B_y^2 + P_y^2} \tag{13}$$

where, U_y is the uncertainty or error, B_y is the bias error and P_y is the precision error. The parameters contributing to the errors are the thermocouple calibrations, thermal conductivity of copper and the distance between the thermocouple spacing on the test chip. The thermocouples were calibrated and its precision error was computed statistically to be $\pm$ 0.1 °C.

Each individual error that propagated due to measurement in temperature and also distance between thermocouple spacings are calculated using the following equation below,

$$U_p = \sqrt{\sum_{i=1}^{n} \left(\frac{\partial p}{\partial a} \times u_{ai} \right)^2} \tag{14}$$

where U_p is the uncertainty in the parameter p, and u_{ai} is the uncertainty of measured parameter a_i. The uncertainty in the heat flux can thus be expressed by the following equation.

$$\frac{U_{q"}}{q"} = \sqrt{\left[\left(\frac{U_k}{k} \right)^2 + \left(\frac{3U_{T_1} * k_{Cu}}{\Delta x * q"} \right)^2 + \left(\frac{4U_{T_2} * k_{Cu}}{\Delta x * q"} \right)^2 + \left(\frac{U_{T_3} * k_{Cu}}{\Delta x * q"} \right)^2 + \left(\frac{U_{\Delta x}}{\Delta x} \right)^2 \right]} \tag{15}$$

The computed values resulted in an uncertainty of less than 6% in CHF for all the tests reported in this study. The maximum uncertainty in wall superheat was ±0.1 °C. At low heat fluxes (less than 75 W/cm^2) the value of uncertainty was ~15%. The relatively high uncertainty was attributed to the error in the surface temperature measurements. However at CHF, which is the main region of interest, this value dropped to less than 6%, which provides good confidence in the values reported.

Chapter 4

4. Results and Discussion

4.1. Enhancement through separate liquid-vapor pathways

One of the principle challenges in designing enhanced surfaces is the chaotic and competing nature of liquid and vapor pathways in the vicinity of the heated surface. This significantly impedes the heat transfer and makes the operation of the system highly unstable and unreliable. Increased bubble generation rates increase the contribution from latent heat transfer but the rapid nucleation activity and its subsequent coalescence leads to localized dry-spots and eventual formation of a vapor film. This results in increased wall superheats and reduction in CHF which limits the efficiency of cooling. In some cases, the formation of the vapor film leads to complete thermal meltdown of the system which is undesirable. In order to overcome this challenge, separate liquid-vapor pathways are proposed to reduce the liquid-vapor counter-flow resistance near the heater surface. Through this mechanistic approach, the CHF and HTC's are expected to be increased to unprecedented levels. The efficacy of the mechanism has the potential to maintain a self-sustained convective system which is stable and reliable at higher heat fluxes, which has not been the case in previous enhancement methods. A range of microscale structures were fabricated to demonstrate the boiling performance characteristics. A detailed experimental investigation on the enhanced surfaces was conducted with distilled water and dielectric fluids at atmospheric pressure to evaluate the potential of the proposed mechanism.

4.1.1. Selective enhancement configurations on open microchannels

Open microchannels are surface enhancements to improve liquid directionality and transport mechanisms for efficient heat transfer. Typically, microchannels have a cover

plate to confine the flow within the hydraulic diameters and are referred to as closed microchannels. In this work, open microchannels refer to surfaces without the cover plate, and are shown to be extremely beneficial for pool boiling heat transfer enhancements [66]. The geometrical parameters that define an open microchannel configuration are the channel width, depth and fin width as shown in Figure 19. In this section, heat transfer mechanisms are explored by depositing porous coatings on an open microchannel with channel width 762 µm, channel depth 400 µm and fin width 200 µm. The dimensions were chosen based on the highest performing surface with open microchannels [23,66]. Three surfaces were fabricated with sintered porous coatings on: (i) entire microchannel surface (sintered-throughout), (ii) only the fin tops (sintered-fin-top), and (iii) only the channel walls (sintered-channel). Their pool boiling performance with degassed and distilled water at atmospheric pressure was experimentally obtained.

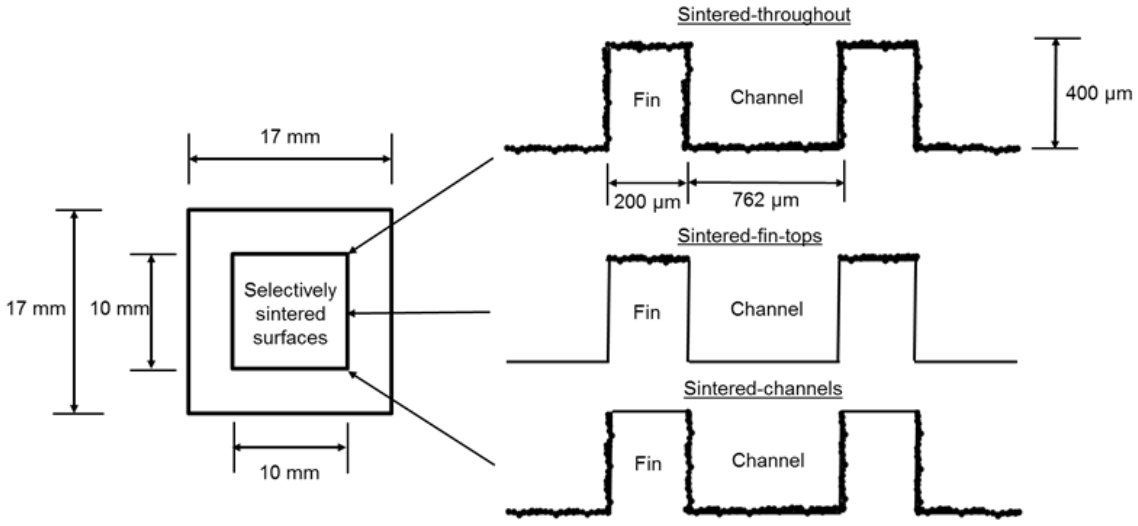

Figure 19. Heat transfer surfaces prepared with selectively coated configurations.

Open microchannels were machined on a 10 mm × 10 mm central area on the boiling surface of the copper test chip using a CNC machine. Microchannel dimensions are kept

constant for all surfaces investigated in this study, as mentioned previously. Three surfaces identified as sintered-throughout, sintered-fin-tops and sintered-channels were fabricated.

A screen printing technique was used to deposit porous coatings on the surface [72]. A fixture was fabricated to screen print uniformly on the heat transfer surface using a fine mesh (count=230). The coating mixture consisted of commercially available 3M™ copper powder with a mean particle size of 10 – 20 μm and binder oil (Nazdar 9627) mixed in a ratio of 2:1, respectively. The mixture was spread on the mesh and a transversal pass with a solid squeegee ensured a coating thickness of approximately 100 μm. Coating thickness was confirmed by laser confocal microscope images. The coated surface was then sintered at 800 °C for a duration of two hours which involved ramp up, hold and ramp down to ensure substrate bonding. Tape tests confirmed adhesion to the copper substrate. Figure 20a and b show the scanning electron microscopy (SEM) image for a sintered-fin-top surface. The SEM image suggested that the particles bonded with each other and yielded a pore size between 5-20 μm which was ideal for boiling enhancement [73]. Figure 20b showed that there were no porous deposits that seeped into the channels during the process. The SEM images suggested that this manufacturing technique is feasible to create coatings with selective enhancement. The same process was used in the sintered throughout and sintered channel geometry and the resulting morphology was identical.

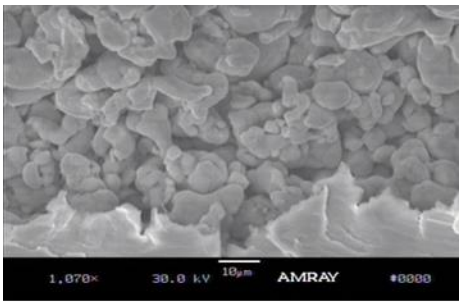

(a)

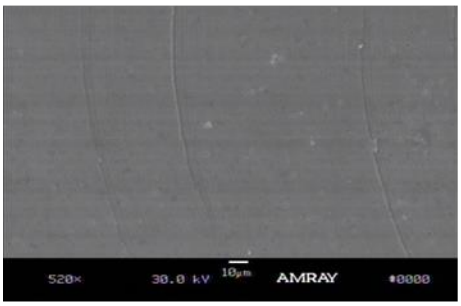

(b)

Figure 20. SEM images of sintered fin top surface with (a) porous deposits obtained on fin tops, and (b) without coatings in the channel bottom.

4.1.1.1. Pool Boiling Results with Water

Pool boiling performance of the three surfaces fabricated shown in Figure 19 were investigated in this study. The main objective of this work was to study the effect of selective porous coating on open microchannels using screen printing and sintering. To serve as a baseline for enhancement comparisons, a plain chip was tested for its boiling performance. This chip reached a CHF of 128 W/cm^2 at a wall superheat of 19.5 °C.

Two key parameters that represent the effectiveness of the augmented surfaces are the maximum heat dissipated (CHF) and the wall temperature corresponding to the CHF. Wall temperature was estimated at the top of the microchannel fin and heat flux was calculated based on the projected area. Nucleate boiling was the main region of interest in this study

and experiments were stopped as soon as CHF was reached which was indicated by a sudden spike in the temperature readout.

Figure 21 shows the pool boiling curves for sintered-throughout, sintered-fin-top and sintered-channel surfaces. The plain baseline chip data is also included in this plot. Heat flux was plotted in units of W/cm^2 which is commonly used in electronics cooling application. A CHF of 313 W/cm^2 at a wall superheat of 7.5 °C was obtained with the sintered-throughout surface. The sintered-fin-top surface reached a CHF of 257 W/cm^2 while the sintered-channel surface dissipated 303 W/cm^2 at CHF. The wall superheats for all the surfaces investigated here were under 10 °C. The uncertainty bars are shown in this plot.

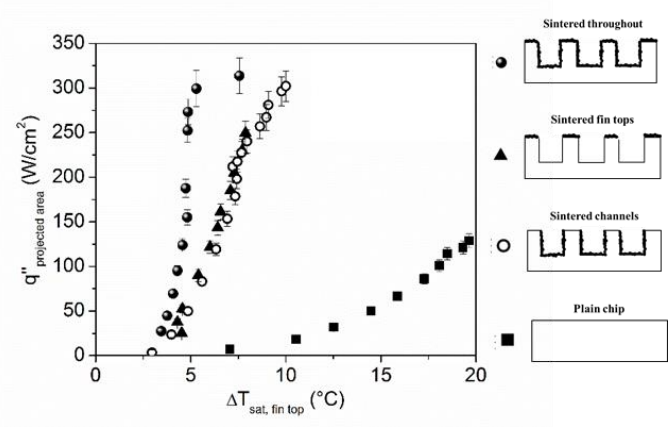

Figure 21. Pool boiling curve for sintered-throughout, sintered-fin-tops and sintered-channel surfaces with water at atmospheric conditions with wall superheat computed using fin top temperature.

There was significant enhancement in all the augmented surfaces at both low and high heat fluxes when compared to a plain chip. Amongst the enhanced surfaces, no appreciable differences in slope of the curves were noticed at low heat fluxes (less than 75 W/cm^2). However, at higher heat fluxes (in excess of 75 W/cm^2) the difference in the slopes were

more pronounced. A higher CHF was obtained for sintered-fin-tops when compared to Patil and Kandlikar [73] who reported a CHF of 242 W/cm^2 for an open microchannel fin top obtained by electrodeposition process which had the same microchannel dimensions (channel width = 762 µm, fin depth = 400 µm and fin width = 200 µm) used in this study. The results obtained suggested that the manufacturing technique also played a critical role in enhancing the pool boiling performance.

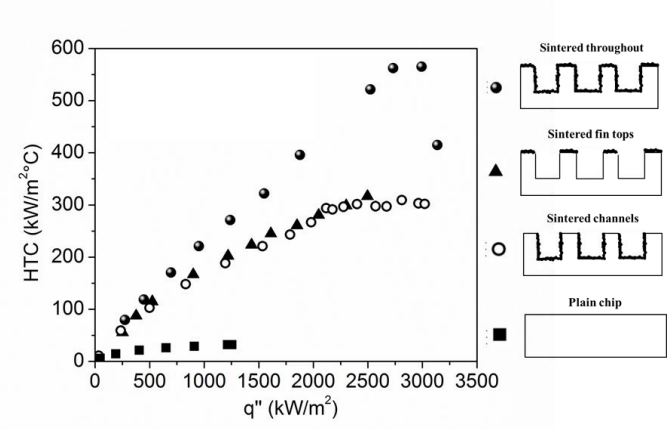

Figure 22. Heat transfer performance of selectively sintered surfaces using fin top temperature.

Figure 22 shows the variation of HTC with the heat flux. The general trend indicated that HTC increased with increasing heat fluxes although the last data marker for the sintered throughout surface showed a significant dip in the HTC value. This may be due to an overshoot in the temperature caused by rapid bubble coalescence resulting in small pockets of vapor film on the surface. These vapor film pockets impeded heat transfer and increased the wall temperature leading to CHF. The highest HTC reported in this study was 565 kW/m^2°C for the sintered-throughout surface representing an enhancement of 782% compared to a plain chip. The HTC values were in excess of 300 kW/m^2°C for all the tested surfaces here. The heat transfer performance for sintered fin tops and sintered channels had overlapping curves.

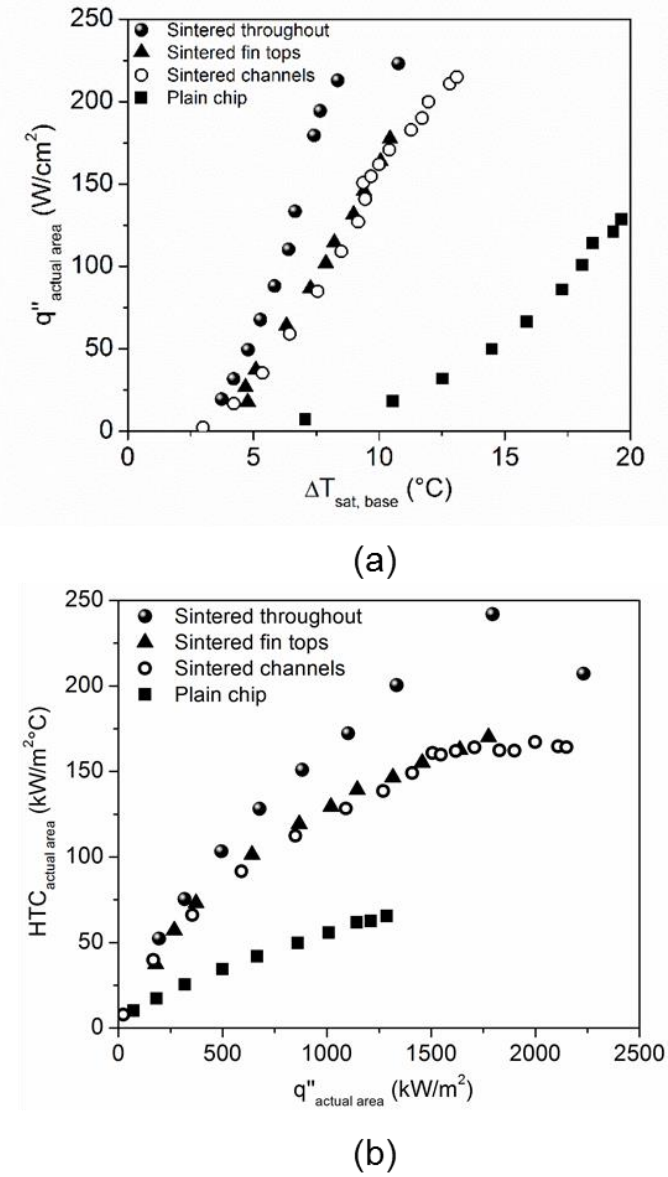

Figure 23. Normalized (a) pool boiling curve (b) Heat transfer performance using actual area and base temperature plotted for the surfaces investigated here.

The effect of additional surface area provided by the microchannel geometry can be considered through the normalized values of CHF and HTC calculated using the actual surface area of the chip. Figure 23a shows a normalized pool boiling curve with heat flux computed using the actual surface area and wall superheat corresponding to the temperature at the base of the fin. Useful information regarding the contribution of open

microchannel to the heat transfer performance can be inferred from this plot. Sintered-throughout had a CHF of 223 W/cm^2 at a wall superheat of 10.7 °C. Sintered-channels and sintered-fin-tops had a CHF of 210 W/cm^2 and 170 W/cm^2 at wall superheats of 12.8 °C and 10.4 °C, respectively. The tested surfaces performed better than the plain chip with enhancements of 74%, 64% and 32% in CHF for sintered-throughout, sintered-channels and sintered-fin-tops respectively when the actual area was considered. Similar enhancement was obtained when the heat transfer performance curve was plotted for the pool boiling curves as shown in Figure 23b. It can be concluded that microchannels aided in the convective flow of liquid and provided additional heat transfer surface area.

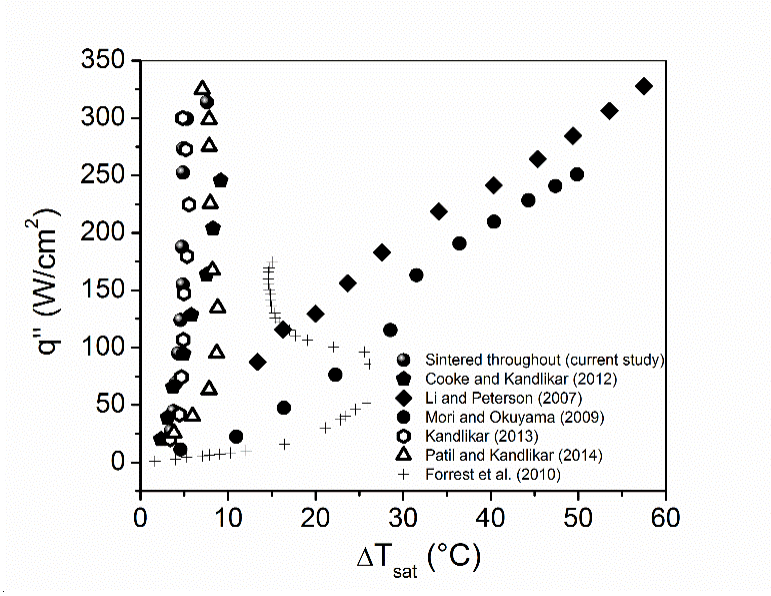

Figure 24. Pool boiling curve comparison with similar enhancements available in literature – Cooke and Kandlikar [2], Li and Peterson [13], Mori and Okayuma [14], Kandlikar [23], Patil and Kandlikar [25], Forrest et al. [27].

Pool boiling plots for the best performing chip in this study (sintered throughout) was compared with the performance plots of similar enhancement techniques available in literature [35,42,64,65,73,74] and is shown in Figure 24. The CHF value was in close

comparison to that reported by Kandlikar [64] and Patil and Kandlikar [73]. Li and Peterson [35] and Mori and Okayuma [42] have reported higher CHF values; however their wall superheats are in excess of 50 °C, which is undesirable. The wall superheat and CHF for the best performing chip in this study are 7.5 °C and 313 W/cm^2 respectively. The path traced by this curve overlaid the data for the highest performing surface reported by Patil and Kandlikar [73] which had a CHF of 325 W/cm^2.

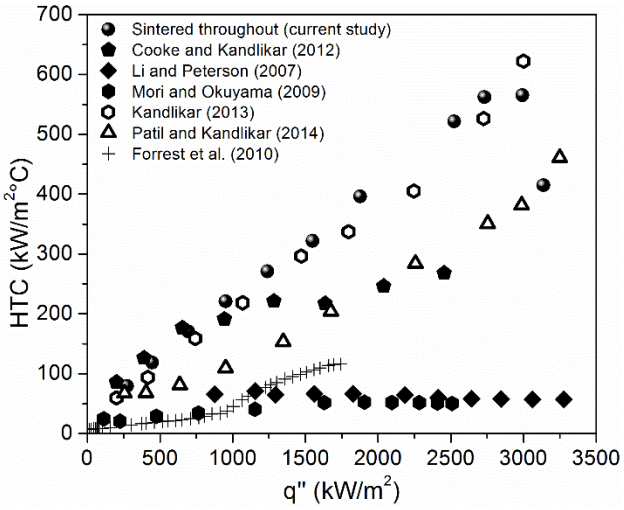

Figure 25. Heat transfer coefficient comparison with available literature Cooke and Kandlikar [2], Li and Peterson [13], Mori and Okayuma [14], Kandlikar [23], Patil and Kandlikar [25], Forrest et al. [27].

Figure 25 shows the heat transfer coefficient plots for a sintered-throughout surface and other enhancements available in literature. A close comparison can be drawn with the record heat transfer coefficient (629 kW/m^2°C) reported by Kandlikar [64] based on evaporation momentum force. Moreover, the sintered-throughout surface performed slightly better than Patil and Kandlikar [73] before reaching CHF. The HTC obtained here is amongst the best performing surfaces reported in literature.

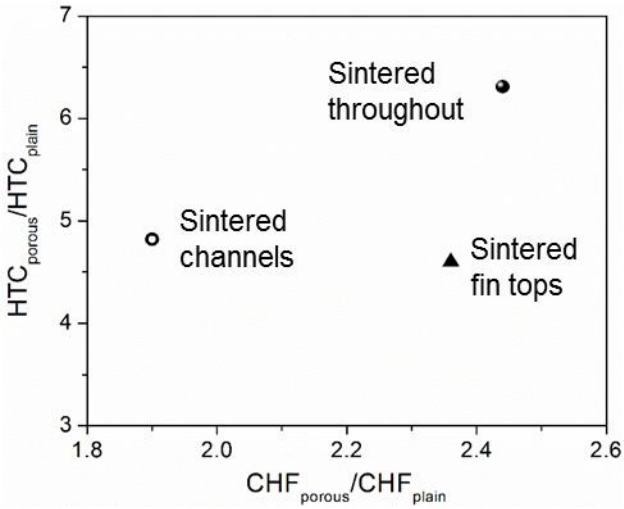

Figure 26. Degree of enhancement in HTC and CHF compared to a plain chip for the three configurations (channel width = 762 μm, channel depth = 400 μm and fin width = 200 μm) investigated here. CHF was calculated based on the projected area and wall superheat using temperature at the fin top. HTC at CHF was obtained from the CHF and the corresponding wall superheat.

Researchers have presented different methods to quantify the heat transfer enhancement. The degree of enhancement in CHF and HTC can be better understood by taking ratios of the enhanced surface to that of a plain surface as shown in Figure 26. The figure represents the enhancement achieved in HTC at the corresponding CHF values. The sintered throughout surface had a HTC which was approximately 6.5 times that of a plain chip. The tested surfaces here had over four-fold enhancement in HTC values and approximately two-fold enhancement in CHF which indicated that selective and strategic placement of nucleation sites through porous coatings significantly improved the pool boiling performance.

4.1.1.2. Heat Transfer Mechanisms

High speed images were captured using a Photron FASTCAM® at 4000 fps at low heat fluxes (~ 15 W/cm^2) to identify the location of bubble nucleation for each configuration

and to predict the liquid supply pathways. Three enhancement mechanisms were identified as follows:

1. Area Augmented Enhanced Nucleation (sintered-throughout)

Figure 27a shows the image obtained at a heat flux of 10 W/cm^2 for a sintered-throughout surface. The image suggested that the bubbles nucleated in the channels as well as fin tops. The enhanced nucleation activity in the region created chaotic liquid motion in the immediate vicinity of the bubbles. Figure 27b shows a schematic of the sintered-throughout surface showing increased bubble activity compared to a sintered-fin-top and sintered-channel. The mechanism can be better understood by studying the bubble escape route, liquid supply pathways and heat transfer enhancement as described below.

Bubble escape route: The bubble nucleation in the channels and fin-tops suggested that this configuration did not yield separate liquid-vapor pathways. However, the increased nucleation activity created chaotic motion as the bubbles departed from the surface.

Liquid supply pathways: The liquid addition to the nucleation sites in this configuration was due to the agitation created by the bubbles. The bubbles leaving the surface induced a squirt effect which propelled the bulk liquid to reach the nucleation site. Since high temperature sintering produces limited number of interconnected tunnels [31], liquid flows from the top surface of microchannels to the channel bottom region due to both capillary flow as well as liquid transport through gravity and chaotic liquid-vapor motion.

Heat transfer enhancement: This mechanism due to bubble activity increased the HTC and CHF significantly which is attributed to the increase in the availability of nucleation sites over the entire surface area of the microchannel.

2. Bubble Induced Liquid Jet Enhancement – Type 1 (sintered-fin-tops)

Figures 27c and 27d show the high speed image captured at 15 W/cm^2 and the schematic of a sintered-fin-top surface, respectively. Previously, it has been shown that selective placement of nucleation sites induces convective flow of liquid [73]. The convective liquid flow occurs through the channels and is similar to a jet impingement mechanism. The image shows that most of the nucleation occurred on the fin tops. However, the fabrication process employed generated some nucleation cavities in the channels as a result of which some bubble nucleation was observed in the channels. The mechanism can be better explained with the schematic to identify the bubble escape route, the liquid supply pathways and the heat transfer enhancement.

Bubble escape route: The schematic identifies the bubbles to emerge and escape from the fin tops. Although some bubbles were also observed in the channels, the dominant nucleation region is seen to be on the fin tops.

Liquid supply pathways: The liquid supply occurs through the channel regions. The liquid flow is governed by both capillary and wicking motion. The liquid jet enters the channel region where it impinges on the base and turn towards the fin tops to feed the nucleation sites. This observation was consistent with that reported by Patil and Kandlikar [73]. Although the manufacturing technique used in their study was different to the one used here, the vapor removal and liquid addition pathways are similar.

Heat transfer enhancement: At higher heat fluxes (in excess of 100 W/cm^2) the ability of this surface to sustain the liquid flow is key to enhance the performance. Higher surface temperature at the bottom of the channel compared to the fin top may cause additional

nucleation sites to become active in the channels which may disrupt the jet impinging mechanism contributing to decreased performance in both HTC and CHF which is observed here.

3. Bubble Induced Liquid Jet Enhancement – Type 2 (sintered-channels)

Figure 27d shows the high speed image obtained for a sintered-channel surface. In this figure, the bubbles were seen to nucleate in the channels only. This mechanism has a distinct advantage over the sintered-fin-tops configuration in generating separate liquid-vapor pathways and sustaining the flow for better enhancement.

Bubble escape route: The schematic shown in Figure 27e identifies vapor removal route from the sintered coatings inside the channels. Before departure, the bubbles are seen to grow to the channel width, trace the sidewalls of the fins and eventually depart from adjacent fin tops creating a squirt effect.

Liquid supply pathways: The liquid supply to the nucleation sites in the channels occurs through the fin top regions. The liquid flow from the fin-tops to the bottom of the channel occurs through capillary and gravity transport and also through the chaotic liquid-vapor motion as vapor leaves the channels.

Heat transfer enhancement: The main advantage of this configuration is that it can sustain the convective liquid flow at higher heat fluxes compared to the sintered-fin-tops surface. This is because the nucleation occurs in the channels which is at a higher surface temperature than the fin tops, and will not disturb the prevalent convective flow. This can further be related to the performance which shows that sintered-channels had a higher CHF and HTC compared to sintered-fin-tops.

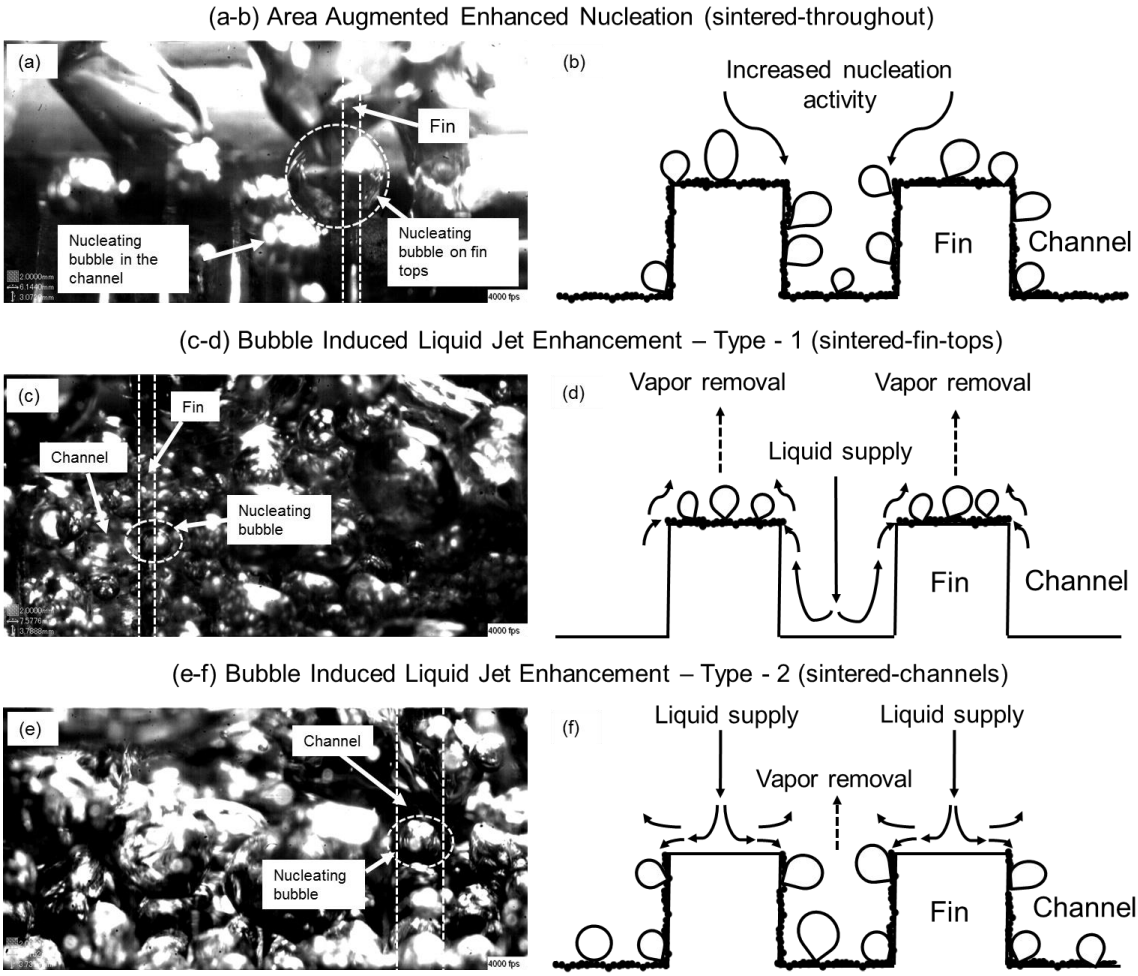

Figure 27. Bubble nucleation and schematic of liquid-vapor pathways for (a-b) sintered-throughout (c-d) sintered-fin-tops, and (e-f) sintered-channels.

Both Type-I and Type-II enhancement mechanisms are based on the enhancement due to liquid jet impingement. This is different from the other mechanisms reported by earlier investigators, such as directed bubble motion from the evaporation momentum force [64] or providing capillary pathways for liquid feed to the nucleation sites [39].

Since the channel geometry was seen to affect the boiling performance for the electrodeposited fin-top case reported by Patil and Kandlikar [73], it is expected that the performance of the other two configurations, sintered-throughout and sintered-channels,

will also be affected by changing the microchannel dimensions, such as channel width, fin width, and channel depth. The effect of channel width is evaluated in the next section.

4.1.1.3. Effect of channel width on boiling performance with water

The objective of this section is to study the effect of channel width on pool boiling performance for the three selectively sintered open microchannel configurations (i) sintered-throughout, (ii) sintered-fin-tops, and (iii) sintered-channels discussed previously. Literature has shown that channels widths over 1 mm significantly reduces the CHF [65,73]. Therefore in this study, three channel widths – 300 µm, 500 µm and 762 µm for each configuration were investigated with distilled water at atmospheric pressure. This range is selected from previous published work on open microchannel studies [66,73]. A performance summary is provided in Table 3.

Table 3. Summary of test surfaces and performance characteristics of selectively sintered configurations.

Surface	Channel width (µm)	CHF (W/cm^2)	HTC (kW/m^2°C)
Sintered-throughout	300	265	304
	500	241	410
	762	313	565
Sintered-fin-tops	300	305	308
	500	272	148
	762	249	364
Sintered-channels	300	420	2900
	500	281	599
	762	299	363

4.1.1.4. Pool boiling results and enhancement mechanisms

Pool boiling curves relating the heat flux and wall superheat are used to characterize the performance of the surfaces tested here. The focus of the current work is to understand the effect of channel width on performance for the three selectively sintered configurations.

Increased CHF and reduced wall superheat are desired for the efficient performance of the surfaces. A plain baseline chip was used for enhancement comparisons. The degree of enhancement obtained was compared with the plain baseline surface.

Sintered throughout

Figure 28a shows the schematic of a sintered throughout surface geometry. Pool boiling curves based on the projected area are shown in Figure 28b. Three channel widths tested (300 µm, 500 µm and 762 µm) and the plain chip data are included in this plot. A CHF of 313 W/cm^2 at a wall superheat of 7.5 °C was obtained for a channel width of 762 µm. The 300 µm and 500 µm channel width test chips had a CHF of 265 W/cm^2 and 241 W/cm^2 at a wall superheat of 7.9 °C and 8 °C, respectively.

Figure 28c shows the heat transfer performance plot. The general trend indicated that the HTC increased with heat flux. A maximum HTC of 304 kW/m^2°C, 410 kW/m^2°C and 565 kW/m^2°C was obtained for 300 µm, 500 µm and 762 µm, respectively. The three chips showed significant enhancement in CHF and HTC over a plain chip indicating that the combination of enhancement techniques significantly improved the performance. Closer investigation revealed that wider channels performed better than narrower channels.

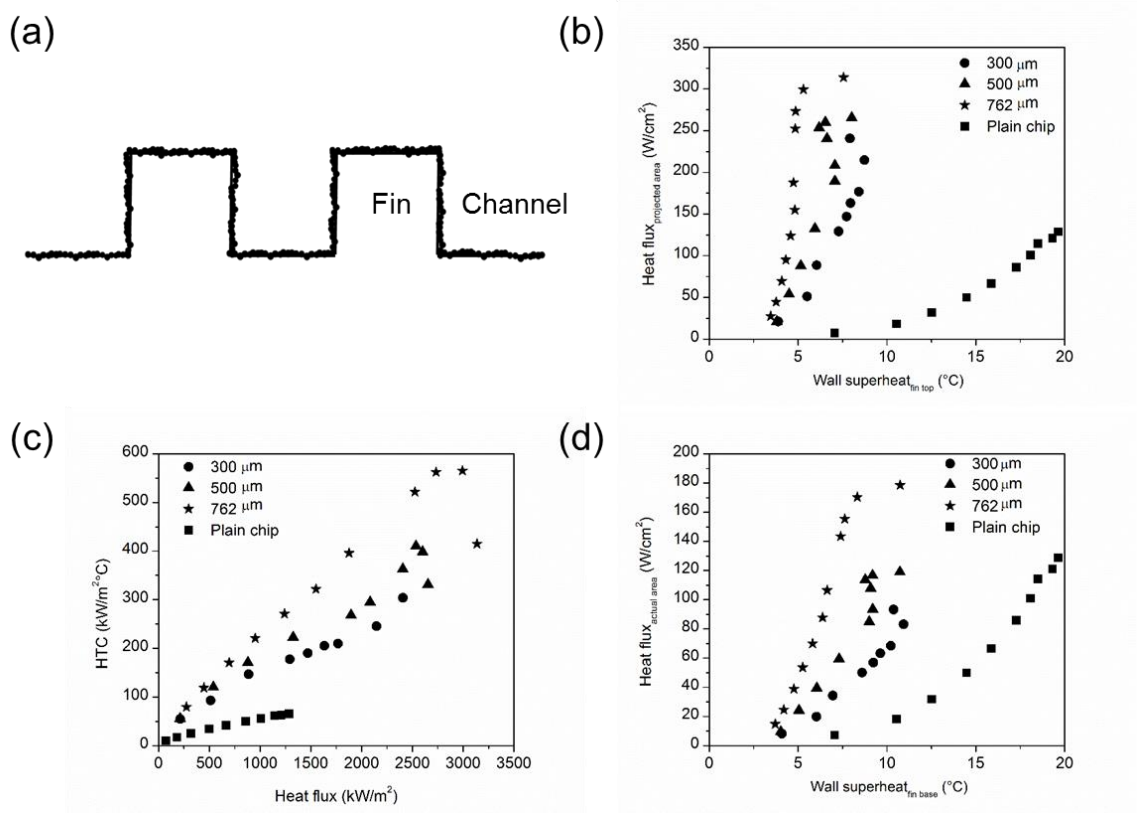

Figure 28. (a) Schematic of sintered-throughout configuration (b) Pool boiling curve for the three tested channel widths (300 µm, 500 µm and 762 µm) with distilled water at atmospheric pressure using projected area and fin top temperature. The channel depth and fin width were maintained constant at 400 µm and 200 µm, respectively. (c) HTC based on the projected area and fin top temperature for the three tested surfaces (d) Area normalized boiling curves based on the actual surface area of the fins (without considering the wetted area provided by the sintered layer) and the temperature at the fin base.

Figure 28d shows the normalized plot for the three channel widths tested here. The contribution of competing mechanisms can be understood from this plot. Area augmentation and improved liquid-vapor pathways are identified as competing mechanisms here. In the plot, the 300 µm and 500 µm channel width surfaces have area enhancement as their dominating mechanism while liquid pathways influenced by increased nucleation activity dominates in the 762 µm channel width surface. The wall

superheat is significantly reduced for all the surfaces investigated here due to availability of additional nucleation sites. The 762 μm channel width surface showed significant enhancement in CHF over other surfaces. The CHF's based on the actual area are 93 W/cm^2, 118 W/cm^2 and 178 W/cm^2 for the 300 μm, 500 μm and 762 μm channel width surfaces, respectively.

In the previous section, 'Area Augmented Enhanced Nucleation' was noted as the enhancement mechanism for the sintered throughout configuration. This mechanism essentially identifies chaotic liquid-vapor motion with liquid supply pathways generated in the normal and lateral direction as a result of this chaotic motion. However, facilitating pathways for liquid to enter the channels and feed to the nucleation sites is critical to further improve the performance. With this understanding, the effect of channel width can be explained for this configuration. Increasing the channel width results in improved liquid pathways into the channels preventing dry-out condition. A wider channel offers a larger number of liquid supply pathways to feed to the nucleation sites which is identified as the main reason for the CHF enhancement. The liquid supply pathways progressively decreases with the decreasing channel widths which is seen by the lower CHF values reported for the 500 μm and 300 μm channel widths.

In support of the above description, high speed images were captured at 4000 fps and at a low heat flux value (~15 W/cm^2) using a Photron FASTCAM®. The visual access to the heater surface is impeded by the chaotic liquid-vapor motion which made imaging difficult at higher heat fluxes. Figure 29 shows the images obtained for 300 μm and 762 μm. The images (29a and c) show that the bubbles nucleated in the channels and on the fin tops. The figure also shows the schematic (29b and d) of the proposed liquid-vapor pathways in the

two configurations based on the images captured. The schematic identifies restricted liquid pathways in the narrow channels and availability of additional liquid pathways in the wider channels. As a result, a lower CHF value is observed in the 300 µm channel width surface.

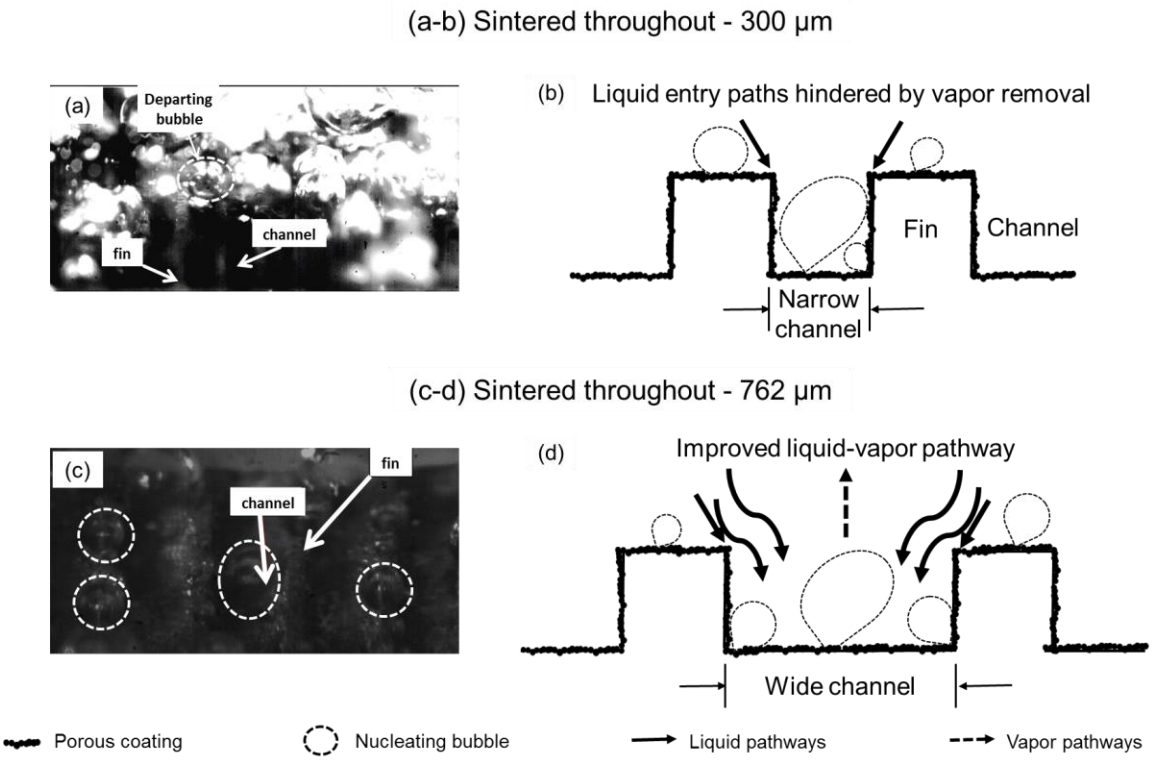

Figure 29. (a and c) Photographic image obtained for a channel width of 300 µm showing bubble nucleation on the fin tops and inside the channels (b and d) Proposed heat transfer mechanisms for narrow and wide channel widths for sintered-throughout configuration.

Sintered-fin-tops

The schematic and the scanning laser confocal microscopy image for a sintered fin-top configuration is shown in Figure 30(a). Figure 30(b) shows the boiling curves obtained for the sintered-fin-top configuration. Similar to sintered-throughout, three channel widths - 300 µm, 500 µm and 762 µm were tested. A maximum CHF of 305 W/cm^2 was achieved with a channel width of 300 µm. The CHF's for the 500 µm and 762 µm were 272 W/cm^2 and 249 W/cm^2, respectively. The trend indicates that the narrower channels perform better

than wider channels indicating that the liquid and vapor transport in this configuration is fundamentally different than the one seen in sintered-throughout.

Heat transfer performance curves are shown in Figure 30c. Maximum HTCs of 308 kW/m^2°C, 148 kW/m^2°C and 364 kW/m^2°C were obtained for the test chips with channel widths of 300 µm, 500 µm and 762 µm, respectively. A normalized plot showing the enhancement achieved is shown in Figure 30d. The CHFs based on the actual area are 118 W/cm^2, 121 W/cm^2 and 142 W/cm^2 for the 300 µm, 500 µm and 762 µm channel width test surfaces, respectively. A similar trend to sintered-throughout is observed here with area enhancement being the dominating mechanism in the 300 µm and 500 µm surfaces and the separate liquid-vapor pathways being the driving mechanism in the 762 µm surface.

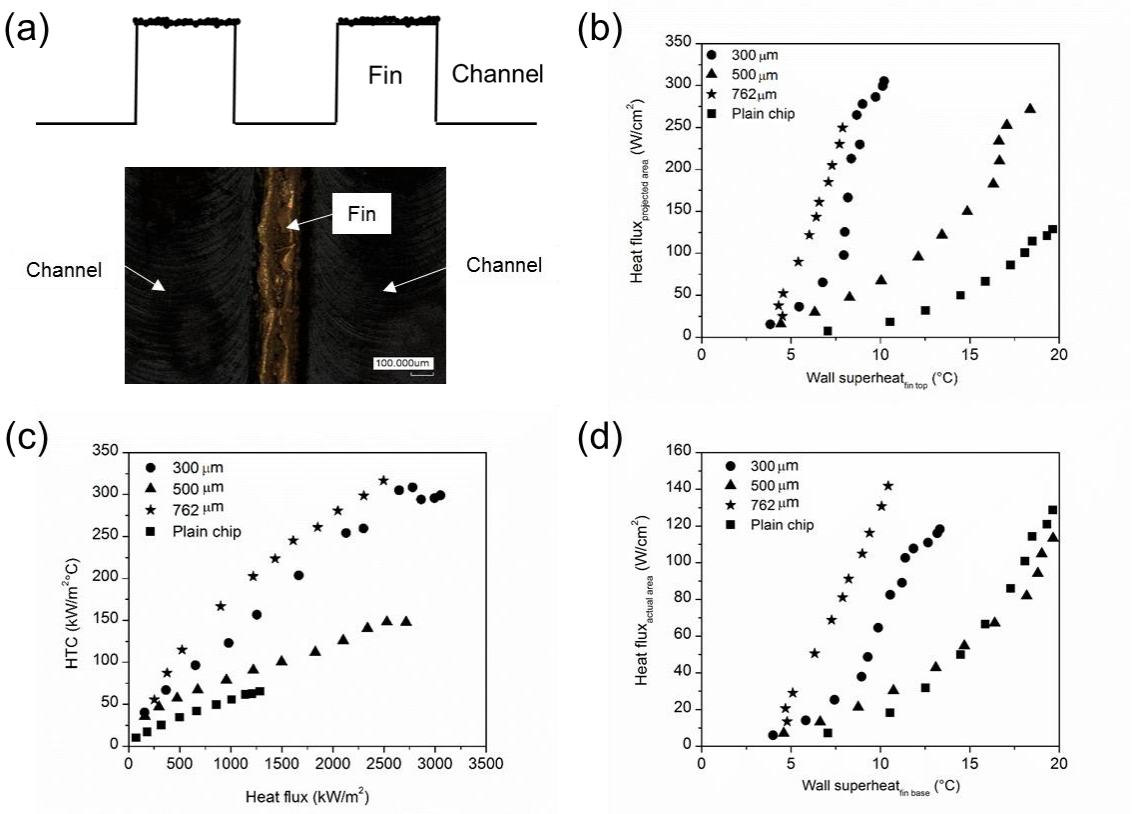

Figure 30. (a) Schematic of sintered-fin-top configuration and a scanning laser confocal image of the 762 μm channel width sintered-fin-top surface. The image shows sintered porous sintered coatings on fin tops with no deposits observed inside the channels (b) Pool boiling curves for the three tested channel widths (300 μm, 500 μm and 762 μm) with distilled water at atmospheric pressure using projected area and fin top temperature (c) HTC based on the projected area and fin top temperature for the three tested surfaces (d) Normalized boiling curve based on the actual surface area (without considering the wetted area provided by the sintered layer) and the temperature at the fin base.

Two enhancement mechanisms were seen for sintered-fin-tops and sintered-channels as they exhibit separate liquid-vapor pathways:

- Bubble Induced Liquid Jet Enhancement - Type-1 (sintered-fin-tops)
- Bubble Induced Liquid Jet Enhancement - Type-2 (sintered-channels)

In Type-1, separate liquid-vapor pathways are generated with nucleation occurring on the fin tops and subsequent liquid addition through the channel regions similar to a jet impingement mechanism. The increased CHF observed with decreasing channel widths can be attributed to the capability of the liquid to overcome the resistance after impinging on the base of the channels and ability to travel against gravity to feed the nucleation sites. In a wide channel, the capability of the liquid to overcome gravity is significantly hampered due to the increased travel length of the liquid in the channel base after impinging which results in decreased velocity and inability to feed the nucleation sites located on the fin tops. A further downside of this mechanism is that at higher surface temperatures, nucleation cavities become active in the base of the channel thereby disrupting the existing convective flow and decreasing CHF. Furthermore, the porous nucleation sites are located on the 200 μm fin width for the three channel widths tested. Since the area covered by the porous coating is significantly lower compared to sintered-throughout and sintered-channel

configurations, the wall superheats observed in this configuration set are relatively higher. Increasing the fin width has resulted in decreased performance as demonstrated by Patil and Kandlikar [73].

High speed images were taken to understand the underlying convective mechanisms. The images for the 300 μm and 762 μm channel width surfaces suggested that bubbles nucleated on the fin tops with liquid addition through the channel regions are shown in Figure 31a and c. However analyzing the mechanism further suggested that the liquid supply is affected by the channel width which subsequently affects the heat transfer performance. A wider channel as shown in Figure 31d has a longer liquid flow path after impinging on the channel base where the liquid is unable to overcome the resistance of the sidewalls of the channels to feed the nucleation sites. The liquid flow is further hampered by the nucleating bubbles in the channels at higher heat fluxes. The combined effect of increased flow length and nucleating bubbles inside the channels significantly reduces the CHF in the wider channels. The liquid flow in the narrow channel is improved as the liquid is able to impinge on the base and feed the nucleation sites. However, the nucleation in the channel regions disrupts the existing convective flow. In studying the channel widths employed here, the 300 μm channel width had a higher CHF compared to the 500 μm and 762 μm channel width test surfaces.

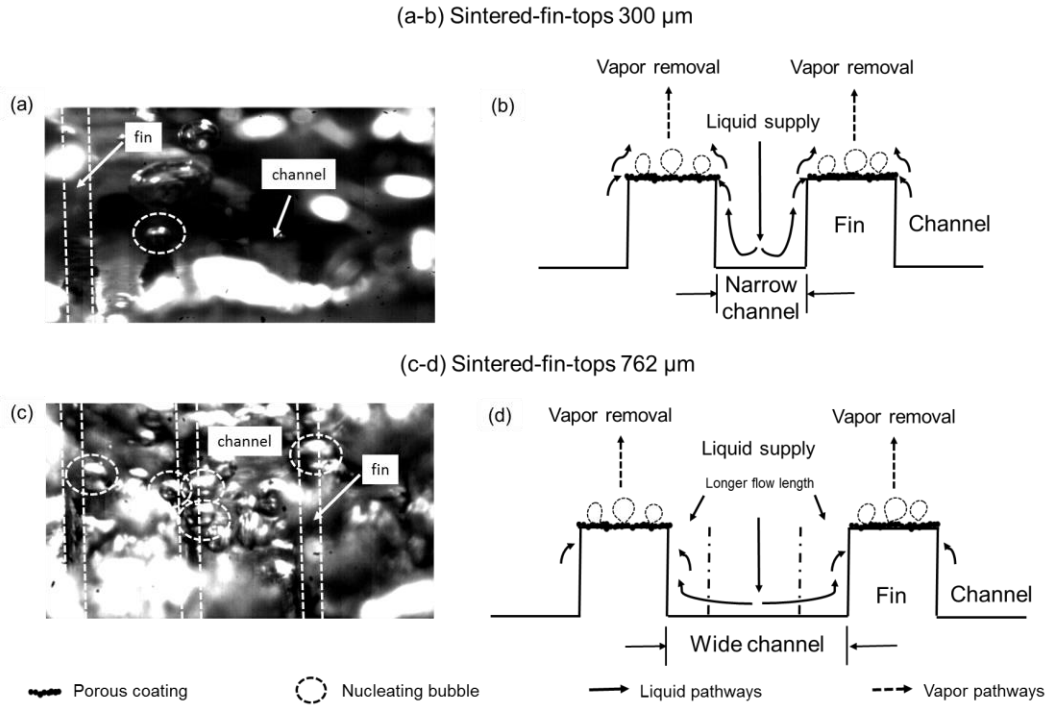

Figure 31. Photographic images and proposed heat transfer mechanisms for sintered-fin top configuration for channel widths of 300 µm and 762 µm. The different liquid flow pathways for 'Bubble Induced Liquid Jet Mechanism-Type 1' for a narrow and a wide channel are identified here.

Sintered-channels

Figure 32a shows the schematic and a confocal laser scanning microscope image of a sintered-channel configuration. In the image, porous coatings are seen in the channel base. The fin tops are plain without any porous deposits. Figure 32b shows the pool boiling curves obtained for three channel widths (300 µm, 500 µm and 762 µm) based on the projected area with sintered-channel configuration. A CHF of 420 W/cm^2 at a wall superheat of 1.7 °C was obtained for the 300 µm channel width. The 500 µm and 762 µm channel widths had CHF's of 281 W/cm^2 and 299 W/cm^2, respectively. The wall superheats for the 500 µm and 762 µm channel width surfaces were 5.2 °C and 8.4 °C, respectively. Figure 32c shows the heat transfer performance plot. The heat dissipating capability of the

surface can be established using this plot. An unprecedented maximum HTC of 2.9 MW/m^2°C was obtained for a channel width 300 µm. Although the uncertainty is very high at this value of HTC due to extremely small wall superheat and very high heat flux, it still represents a significant improvement over any other boiling surface. To the best of the authors' knowledge, this is the highest reported HTC in literature for pool boiling with water at atmospheric pressure. The 500 µm and 762 µm surfaces had a maximum HTC of 599 kW/m^2°C and 363 kW/m^2°C, respectively.

Figure 32d shows the area-normalized plot with the wall superheat based on the temperature at the base of the fin. The sintered-channel configuration yielded CHFs (based on the actual surface area) of 162 W/cm^2, 126 W/cm^2 and 172 W/cm^2 for the 300 µm, 500 µm and 762 µm channel width surfaces, respectively. The results suggest that significant enhancement is achieved based on the actual area indicating that separate liquid-vapor pathways was the driving mechanism ('Bubble Induced Liquid Jet Enhancement – Type 2') in this configuration.

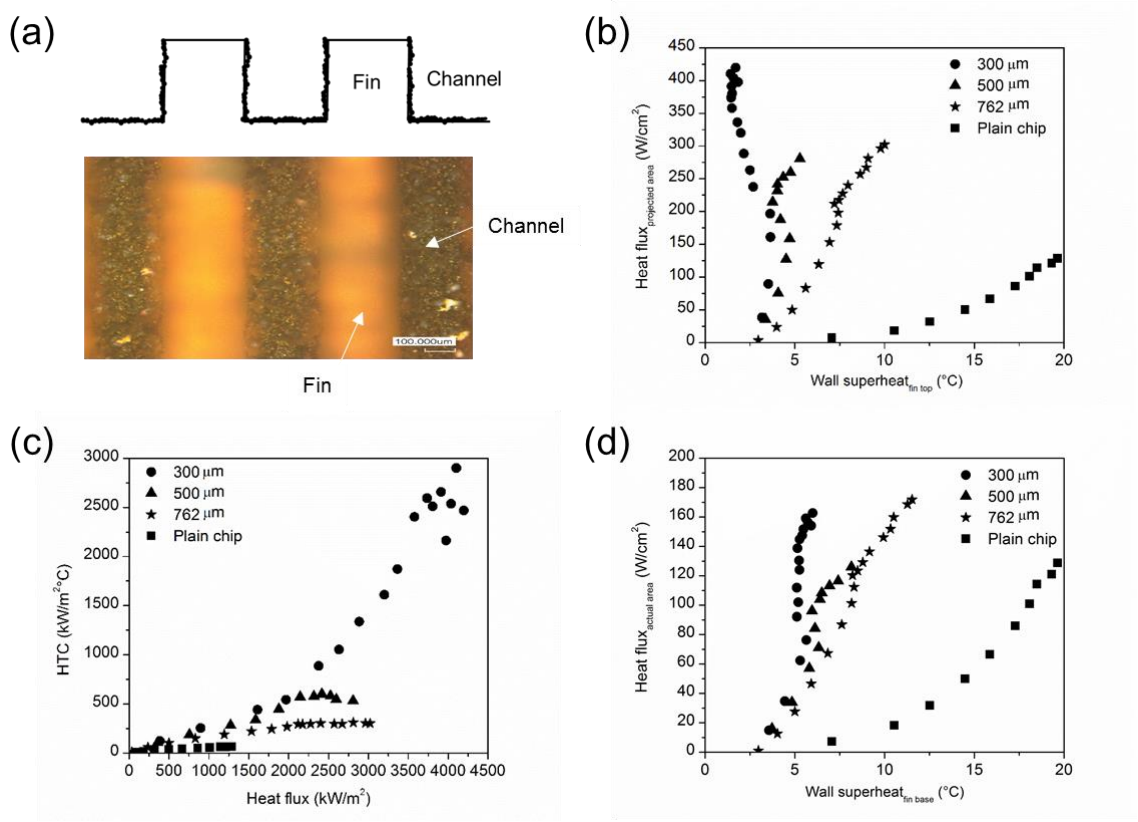

Figure 32. (a) Schematic of sintered-channel configuration with a confocal laser scanning microscopy image taken at 10X magnification (b) Pool boiling curve for the three tested channel widths (300 μm, 500 μm and 762 μm) with distilled water at atmospheric pressure using projected area and fin top temperature (c) HTC based on the projected area and fin top temperature for the three tested surfaces (d) Area normalized boiling curve based on the actual surface area (without considering the wetted area provided by the sintered layer) and the temperature at the fin base.

The key idea in the sintered-channel configuration was that the bubbles nucleated inside the channels with liquid addition through the fin top regions. The liquid transport from the fin tops to the channel bottom was governed by capillary motion (wicking inside the porous coatings) and gravitational motion. A distinct feature of this configuration is that nucleation is always favored inside the channels and the convective mechanism is sustained at higher heat fluxes making this configuration superior to other mechanisms – 'Area Augmented

Enhanced Nucleation' for sintered-throughout and 'Bubble Induced Liquid Jet Enhancement – Type 1' for sintered-fin-tops. The wall superheat is always lower at the fin top as compared to the channel surface. This prevents any adverse bubble nucleation on the fin tops that would otherwise obstruct the liquid return pathways.

However in this mechanism the jet impingement on the fin tops results in a certain fraction of liquid turning towards the bulk as against entering the channels. This can be detrimental in a wider channel as the demand for liquid supply is higher due to the increased number of nucleation sites. Since the volume of liquid supplied through the fin tops is lesser in a wider channel, the 762 µm channel width has the lowest CHF. This mechanism is different from the sintered-throughout (lacking jet impingement) as the liquid supply to the channels works in fundamentally different ways. On the other hand, a narrow channel ensures continuous supply of liquid to the nucleation sites ensuring complete rewetting until the wicking limit is reached inside the porous coatings leading to CHF. The superior rewetting mechanism coupled with sustained convective flow is critical to improve the performance as exhibited by the 300 µm channel width test chip.

High speed video images were taken to identify the liquid and vapor pathways in the 300 µm and 762 µm channel width (Figure 33a and c). Imaging was done at lower heat fluxes of ~15 W/cm^2 for both the surfaces. The images suggested that a significant number of bubbles were seen to emerge inside the channels in the 762 µm chip. The increased vapor generation rate in the wider channels demands more liquid and also serves as hindrance to the liquid supply pathways in the channel whereas the narrower channels provides improved pathways for liquid to rewet the channel efficiently. Increasing the fin width has shown to decrease the CHF [73]. A sintered-channel configuration with a fin width of 500

μm and a channel width of 300 μm was also investigated in this study to see if the same trend is observed. The CHF for this surface was 195 W/cm^2 showing a significant reduction in performance.

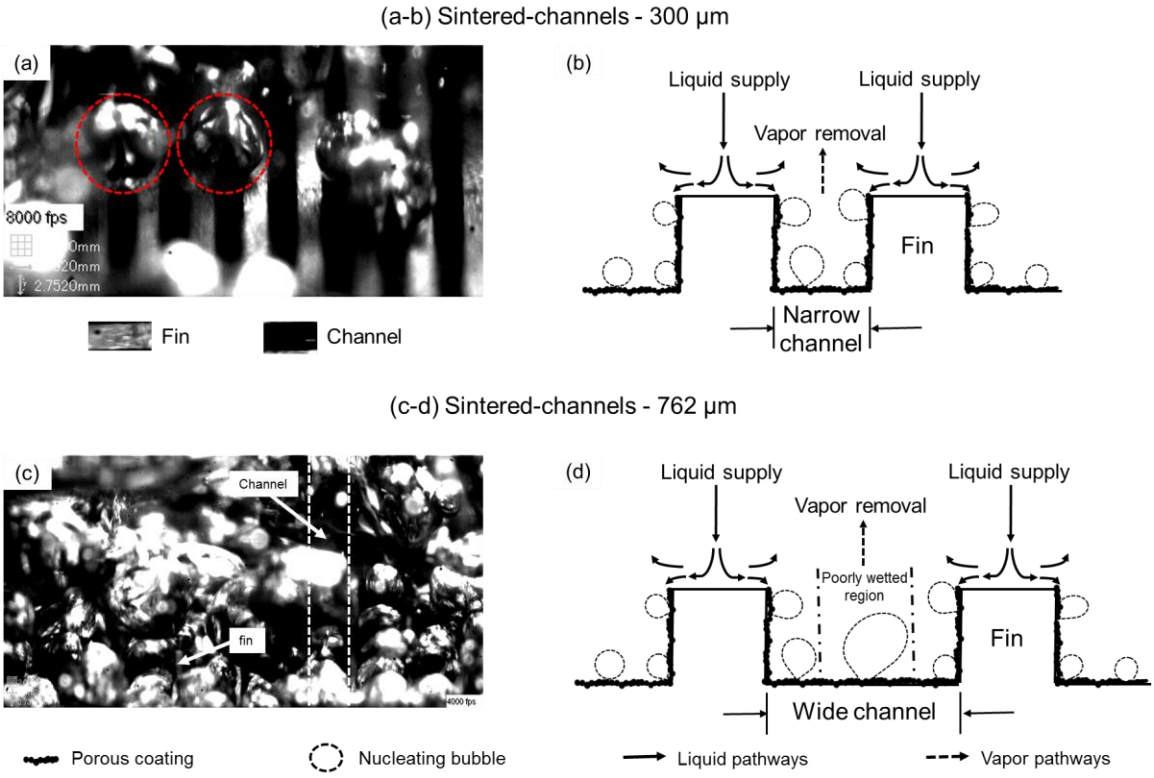

Figure 33. (a and c) High speed images showing bubble nucleation inside the channels. The 762 μm channel width surface has more number of bubbles emerging due to availability of additional nucleation sites. (b and d) Proposed heat transfer mechanisms showing jet impingement on the fin tops resulting in liquid supply to the channels for a narrow (300 μm) and wide channel (762 μm) in a sintered-channel configuration.

4.1.1.5. Enhancement mechanism comparisons

In the sintered-throughout configuration, the primary enhancement mechanism is driven by increased nucleation activity which causes liquid agitation in the immediate vicinity of the departing bubbles. The liquid supply pathways are influenced by the channel width where a wider channel is expected to supply liquid more efficiently than a narrow channel.

However there is randomness in this mechanism. The bubbles departing from the fin tops could also contribute to the liquid supply to the channels. There are no organized liquid supply and vapor removal pathways. Area enhancement and availability of additional nucleation sites dominate the mechanism of increased nucleation activity. In one such mechanistic approach in this configuration, it can be said that the liquid pathways entering the channels (i) laterally into the channels and (ii) vertically from sidewalls through wicking from the fin tops enhance the performance. In the wide channels, these pathways are more in number and increase the CHF by preventing dry-out. However any nucleation on the fin tops may further disrupt the flow of liquid into the channels. In addition, the liquid also needs to be supplied to the nucleation sites located on the fin tops which further starves this configuration of liquid supply. In a narrow channel (300 μm), the area enhancement is the highest which requires more number of liquid pathways to feed the nucleation sites. The increased nucleation activity inhibits the liquid supply leading to early CHF. However in a wider channel (762 μm) the liquid supply is sustained for a longer period due to the decreased nucleation sites compared to the 300 μm surface.

In the sintered-channel geometry, the location of porous coatings inside the channels influences bubble nucleation to occur in the channels. The liquid supply occurs through the fin tops. In such a system with separate liquid-vapor flow fields, the liquid transport to the channel regions is influenced by capillary wicking through the coatings on the sidewall regions of the channel. In a wide channel (700 μm), the capillary wicking is insufficient to wet the central regions of the channel base which results in dry-out conditions leading to early CHF. In the narrow channel (300 μm), the wetting is superior where the liquid is able to reach the channel base and feed the nucleation sites. These mechanisms at play are

significantly amplified at higher heat fluxes, which sustain the mechanism and enhance the performance.

In the sintered-fin top geometry, the enhancement mechanism is driven by liquid transport in the channels. The liquid impinges on the base of the channels similar to a jet impingement-like mechanism and forces the liquid to flow towards the nucleation sites located on the fin tops. These separate liquid-vapor pathways work differently in a narrow and wide channel. In a wide channel, the liquid flow length is larger than a narrow channel. This results in decreased flow velocity and inability of the liquid to reach the fin tops. In a narrow channel the competing mechanisms are sustained and wet the fin tops to supply liquid. However in such a setup, bubbles nucleating in the channels at higher heat fluxes create some order of randomness in the liquid supply and vapor removal pathways in both the narrow and wide channels.

4.1.1.6. Effect of electrodeposited fin tops with dielectric fluid (FC-87)

This section focuses on using chips fabricated by Patil and Kandlikar [73] and evaluating their pool boiling performance with FC-87, which is a widely-accepted fluid in the electronics cooling industry. The hypothesis of the current study is based on the superior jet impingement liquid pathways provided by microchannels and additional nucleation sites provided by porous coatings to cohesively work towards enhancing the boiling performance. The cohesive mechanism will lead to separate liquid-vapor pathways which will aid in delaying CHF by continually supplying liquid to the nucleation sites. This will help meet the electronics cooling requirement by dissipating high heat flux and also satisfying the maximum temperature limit (of around 85 °C) imposed for such applications.

Five chips with different microchannel dimensions were used to study the effects of the geometrical parameters on the boiling performance with FC-87 at standard atmospheric pressure. The dimensions of the channel width, channel depth and fin width were measured using a laser confocal microscopy and tabulated in Table 4. The focus of the current work is to evaluate the pool boiling performance with FC-87 at atmospheric pressure. A plain chip was used to compare the performance improvement. The roughness (R_a) of the plain chip was measured using a scanning laser confocal microscope at five different locations on the boiling surface and averaged to be 1.6 μm.

Table 4. Test matrix with dimensions used in this study.

Chip no:	Channel width (μm)	Channel depth (μm)	Fin width (μm)
1	300	400	200
2	400	200	200
3	400	400	200
4	762	400	200
5	762	200	200

Pool boiling tests were conducted on the test surfaces shown in Table 4. The effect of channel width and channel depth of an open microchannel configuration on the pool boiling performance is studied here. Firstly, a plain chip was tested for enhancement comparisons and it reached a CHF of 11 W/cm^2 at a wall superheat of 29 °C as shown in Figure 34. The figure also shows the pool boiling data obtained for chips 1-4. The fin widths were maintained constant and the channel width and the channel depth are the only variable parameters in these tests.

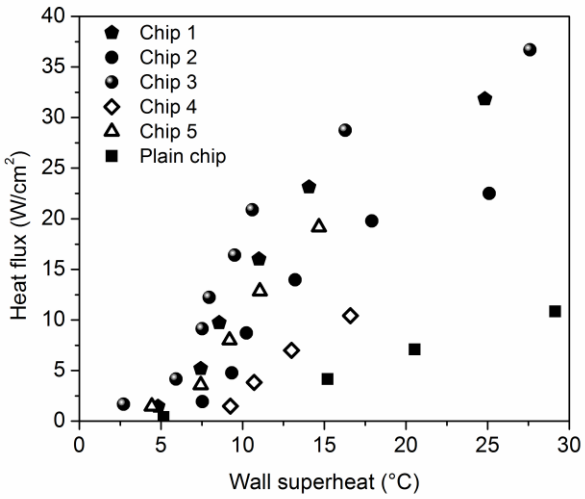

Figure 34. Pool boiling curve obtained with FC-87 at standard atmospheric pressure.

In the enhanced chips, a CHF of 37 W/cm^2 was obtained at a wall superheat of 27 °C for chip 3 which had a channel width of 400 µm, channel depth of 400 µm and fin width of 200 µm. This represented an enhancement of 270% in CHF compared to a plain chip. Chip 1 had a CHF of 31 W/cm^2 at a wall superheat of 25 °C. Chip 2, 4 and 5 had CHF's of 22 W/cm^2, 10 W/cm^2 and 19 W/cm^2 at wall superheats of 25 °C, 16 °C and 14 °C respectively. All the chips tested here showed enhancement in either CHF, HTC or both. This can be seen by the curves shifted to the left when compared to a plain chip in the pool boiling curve.

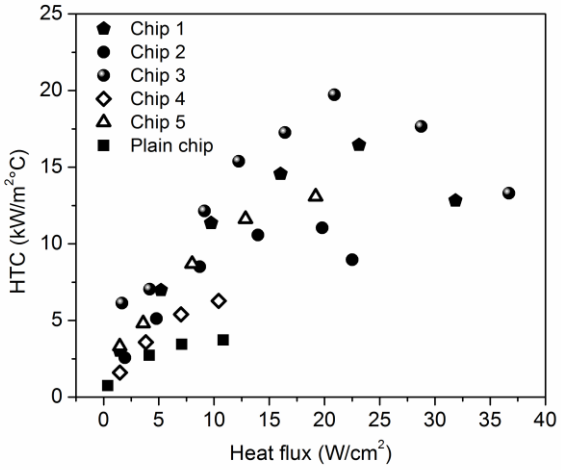

Figure 35. Heat transfer performance curve obtained for FC-87.

Figure 35 shows the pool boiling HTC for the chips tested here. In this plot, HTC is plotted on the y-axis and heat flux on the x-axis. HTC is represented in SI units of kW/m^2°C which is commonly used for performance enhancement comparisons. The effectiveness of the surface in terms of heat dissipation performance can be inferred from this plot. Chip 3 had the highest HTC of 20 kW/m^2°C before reaching CHF. The general trend indicated that HTC increased with increasing heat flux till the inflection point which is seen to be between 15 - 20 W/cm^2 for most chips and then a dip in HTC values is observed beyond this point. All the tested surfaces had a higher HTC than plain chip suggesting that the porous fin tops on open microchannels significantly improved the performance.

Effect of channel width

Two geometric parameters of open microchannels are studied here. The effect of channel width can be understood from the performance of chips 1, 3 and 4, as shown in Figure 36. In this plot, CHF is plotted on the y-axis and channel width on the x-axis to find a trend in the performance characteristics. The CHFs for chips 1, 3 and 4 indicate that there is

existence of an optimal channel width for a given channel depth and fin width. Chip 1 and chip 3 indicate that CHF increases with an increase in channel width but drops significantly for chip 4 with a wider channel.

The variation of CHF with channel width for chip 2 and chip 5 with a constant channel depth = 200 μm and fin width = 200 μm is also studied. There is no stark difference in performance of these two curves but CHF of chip 2 is slightly higher than chip 5 which fits into the trend explained previously.

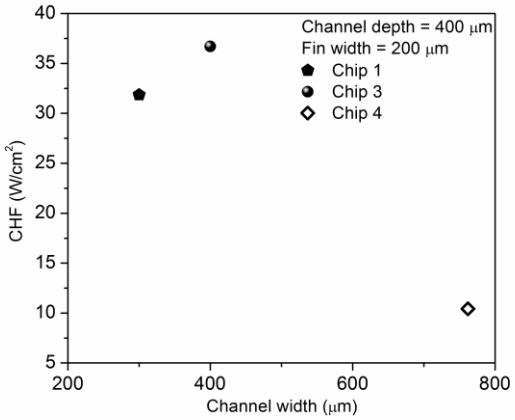

Figure 36. Effect of channel width and CHF for chips 1, 3 and 4.

Effect of channel depth

Two groups can be formed to understand the effect of channel depth. Group 1 consisted of chip 2 and 3 which had a constant channel width of 400 μm and fin width of 200 μm, and group 2 consisted of chip 4 and 5 and had a constant channel width of 762 μm and fin width of 200 μm. Group 1 suggested that the deeper channels (chip 3) performed better than the shallower channels (chip 2). Group 2 suggested the opposite was true where an increase in channel depth causes the CHF to drop significantly. This suggested that an optimum channel width to depth ratio exists for an open microchannel surface. This seems

to be dependent on the location of nucleation sites, the liquid feed mechanism to the nucleation site and the properties of the working liquid.

Figure 37 shows a high speed image obtained at a heat flux of 5 W/cm^2 obtained with a Photron FASTCAM® high speed camera at a frame rate of 4000 fps for chip 4. Similar images were obtained for chip 2 as well. The image identifies bubble nucleation on the fin tops and their subsequent rise. The liquid replenishment occurs from the liquid flow into the channel regions. This convective mechanism is similar to a jet impingement generating separate liquid and vapor pathways as shown in the schematic. At higher heat fluxes the nucleating bubble activity is intense due to availability of additional nucleation sites inside the porous coatings. This intense bubble nucleation activity enforces the liquid circulation and further reinforces the convective mechanism, which is critical to enhance the performance. However, the vigorous nucleation and bubble departure activity inhibits visual access to the heater surface at higher heat fluxes. The heat transfer performance obtained is significantly higher with a CHF as high as 37 W/cm^2 and a HTC of 20 kW/m^2°C under this mode.

This mechanism reveals that the liquid transport in the channel region governs the CHF limit for all open microchannels with porous fin tops. The capability of liquid to overcome the flow resistance offered by the microchannel walls is critical to delay CHF. There are many variables that affect the overall performance of the surfaces investigated here. However the experiments conducted suggest that the liquid flow resistance and liquid impingement effect are the two competing mechanisms. It is seen that the convective mechanisms are similar for both water [73] and FC-87 as shown here.

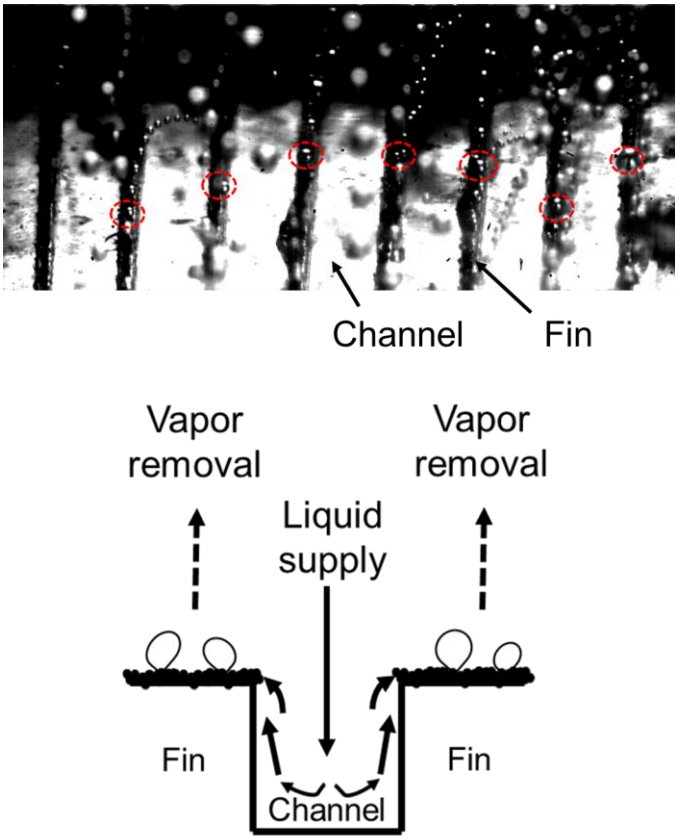

Figure 37. High-speed image of nucleation on the fin top surface (top image) and a schematic representation (bottom image) of liquid and vapor pathways for chip 4.

Further examination of the results indicated that the channel width to depth ratio is an important parameter. Chips 1 and 3 have this ratio as 1 or lesser, while it is 2 for Chip 2, 1.9 for Chip 4, and 3.8 for Chip 5. For a ratio of 1, the liquid is seen to be able to efficiently irrigate the microchannel walls. If this ratio exceeds 1, liquid may not be able to reach the bottom of the microchannels and may lead to performance deterioration. This needs to be checked in further refining the fin geometry. However, as the width/depth ratio goes above 1, liquid circulation and reduction in area enhancement start to become a concern. The performance further deteriorates with the increased flow resistance which is encountered by the liquid in the channels when the ratio is above 1. Chip 5, with the highest width/depth ratio of 3.8, yields the lowest CHF in the group of enhanced chips. While the porous

coatings provide a bubble pumping mechanism, liquid circulation and area enhancement in different microchannel configurations are important considerations in enhancing heat transfer performance. This study addresses the liquid transport concerns in an open microchannel configuration by identifying a suitable width to depth ratio of the channels.

6.2 Comparison with water

The test results obtained with FC-87 are compared with water [73]. Table 5 summarizes the test results with channel width to depth ratio being the governing factor linked to the performance. A definite trend is not observed to represent a unified understanding of the performance with FC-87 and water. However it can be seen that when the channel width/depth ratio is 1, highest performance is achieved with water as well as FC-87. For FC-87, a channel width/depth ratio of less than 1 enhances the performance. A 3.3 and 2.8 fold CHF enhancement is achieved for a ratio of 1 and 0.75 respectively. Reducing this ratio below 1 increases the available surface area, but liquid circulation is adversely affected.

Table 5. Comparison of CHF enhancement for FC-87 and water

Channel width/channel depth	$CHF_{enahnced}/CHF_{plain}$	
	FC-87	Water
0.75	2.81	2.2
1	3.36	2.56
1.9	0.9	2.2
1.72	1.72	2.1
2	2	1.89

Comparison to literature

Figure 38 shows the pool curves for some of the top performing surfaces available in literature and chip 3 used in this study with FC-87 as the working liquid. Two surface

enhancements, porous coatings and fins, were developed by Chang and You [75]. These structures had a CHF of 14 W/cm^2 and 24 W/cm^2 respectively. Mudawar and Anderson [38] developed fins that were approximately 12 mm tall and reported a CHF of 21 W/cm^2 with FC-87. Enhancement in this configuration is mainly driven by area augmentation. However, the best performing chip (Chip 3) in this study had a CHF of 37 W/cm^2 which was the highest reported CHF in literature with FC-87 at atmospheric pressure. The enhancement mechanisms can be attributed to the additional nucleation sites, liquid circulation within the microchannels, and the additional heat transfer area available over the microchannel surfaces.

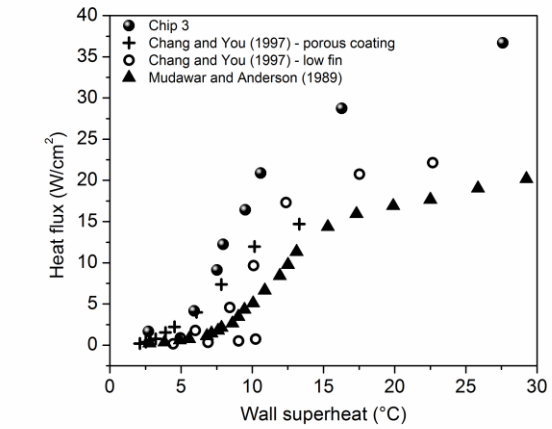

Figure 38. Pool boiling performance comparison with available curves in literature [18,38].

Patil and Kandlikar [73] proposed a mechanism in which the bubbles generated on the fin tops induced liquid circulation within the microchannels with water. This mechanism is seen to hold good for FC-87 as well based on the image shown in Figure 37 and the performance obtained. The strategic location of nucleation sites on the fin tops seems to increase the vapor generation rate with liquid supply through the channel regions of microchannels. The combination of two techniques enhances the performance by

facilitating separate liquid-vapor pathway which is identified as the key mechanism to delay CHF and increase HTC.

4.1.2. Nucleating regions with feeder channels

Bubbles departing from the nucleation sites induce a liquid flow from the bulk to the heated surface during pool boiling. Alternating the nucleating regions with non-nucleating regions facilitates separate liquid-vapor pathways for departing vapor bubbles and returning liquid. An additional enhancement through liquid feeder channels on the heater surface directing the returning liquid towards the nucleating region was implemented.

4.1.2.1. Hypothesis

At CHF, a vapor blankets the heated surface as a result of increased bubble frequency and lateral bubble coalescence, and inhibits liquid supply to the nucleation sites. In order to delay the formation of the vapor blanket and to facilitate continuous liquid supply, disjunctions in the fins are proposed to serve as liquid-vapor pathways as shown in Figure 39. The bubble departure diameter is a critical parameter which governs the lateral coalescence of bubbles and formation of separate liquid-vapor pathways [39,64]. In this study the Fritz equation is employed to calculate the bubble departure diameter,

$$d_B = 0.0208\beta \left[\frac{\sigma}{g(\rho_L - \rho_G)}\right]^{1/2} \quad (16)$$

where, β is the receding contact angle, σ is the surface tension force, g is the gravitational force and ρ_L and ρ_G are the liquid and vapor densities, respectively. It is postulated that for water boiling on a copper heater surface at atmospheric conditions the spacing between the disjunctions on the microchannel surface should approximately be equal to the departure bubble diameter given by Eq. (16) to prevent lateral coalescence. The departure bubble

diameter is calculated to be equal to 2.213 mm for $\beta = 42.5°$ and surface, $\sigma = 58.91 \times 10^{-3}$ N/m for water at 100 °C.

In the current design of the enhancement structures, the liquid supply to the nucleation sites is enhanced through feeder channels that transport liquid from the bulk toward the heater surface. The feeder channels provide a pathway on the heater surface for the liquid to flow uninterrupted towards the nucleation regions. Figure 39 shows a schematic of the test surface in which nucleation occurs in the nucleating region (NR) channels which are separated by a bank of feeder channels (FC). This arrangement is referred to as Nucleating Regions with Feeder Channels (NRFC). The NR channels serve as the preferential vapor generation and removal pathway with liquid addition through the FCs. Nucleation is seen to occur preferentially at the intersection of the nucleating region and the feeder channels. As the separate liquid vapor pathways are established at higher heat fluxes, any nucleation occurring in the feeder channels is suppressed by the flow of cooler liquid returning from the bulk.

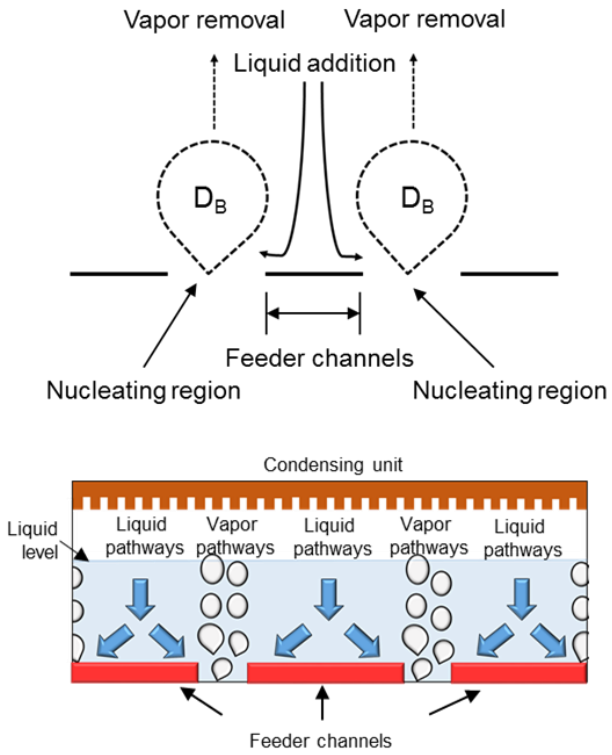

Figure 39. Top - Schematic showing the liquid supply and vapor removal pathways for a NRFC configuration. The spacing between NR channels was derived based on Fritz equation. Bottom - A cartoon showing the proposed liquid and vapor pathways for the NRFC configuration.

The spacing between the NR channels were derived from the departure bubble diameter information using Fritz equation (Eq. 16). However, this was used as a guidance. The optimum spacing may be different because of deviations in departure bubble diameter due to effects arising from localized geometry and heat flux levels. An optimum spacing for specific heater surface and fluid may be obtained through experiments. Therefore, four chips with NRs separated by 4.75 mm, 3 mm, 2.125 mm and 1.6 mm respectively were fabricated as shown in Figure 40. The feeder and nucleating microchannels (rectangular cross-section) were fabricated using a CNC machine on a 10 mm × 10 mm area on the boiling surface of the chip. Table 6 shows the microchannel dimensions used in the study.

The effect of NR spacings are investigated for their pool boiling performance with water at atmospheric pressure.

Table 6. NRFC dimensions

Microchannel parameter	Fin width	FC width	NR channel width	FC and NR channel depth
Value (μm)	200	500	500	400

.

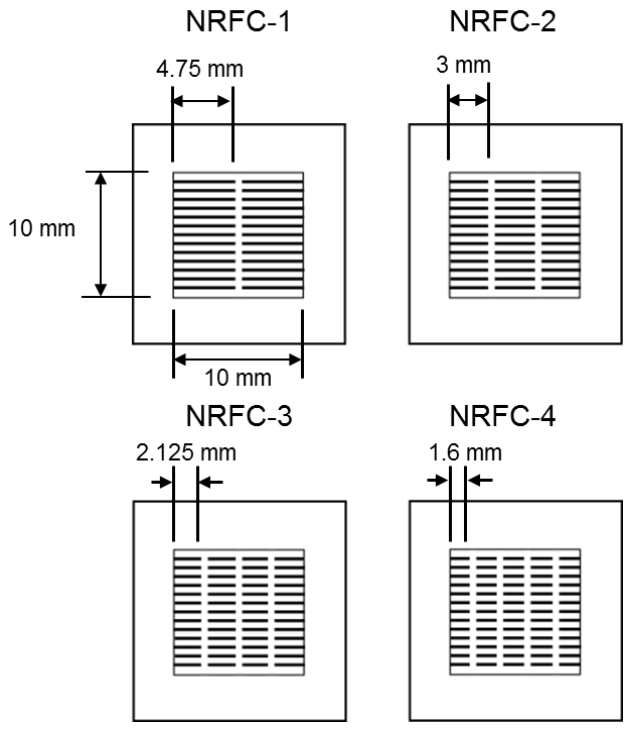

Figure 40. Test chips used in this study.

4.1.2.2. Pool boiling results with water

The results are presented in a pool boiling curve which relates the heat flux and the wall superheat. The wall superheat is defined as the difference between the surface temperature of the chip and the saturation temperature of the fluid. The surface temperature is calculated as the temperature at the top of each microchannel chip. Also, a heat transfer performance

plot showing the heat transfer coefficient versus the heat flux provided a clear comparison with a plain chip.

Firstly, distilled water was boiled on a plain chip to serve as the baseline for all enhancement comparisons. Figure 41 shows a comparison of pool boiling curves for four NRFC chips with 1 to 4 NR channels and the plain chip. All the test chips were tested until they reached CHF. The CHF and wall superheat values are tabulated in Table 7. It is seen that NRFC-3 was the best performing chip with a CHF of 394 W/cm^2 at a wall superheat of 5.5 °C which translated to an enhancement of 209% in CHF compared to a plain chip. NRFC-1, 2 and 4 had CHFs of 350 W/cm^2, 285 W/cm^2 and 252 W/cm^2 at wall superheats of 13.1 °C, 11 °C and 14.9 °C respectively. The corresponding performance with open microchannels as reported by Cooke and Kandlikar [65] was 244 W/cm^2. From a simplistic approach, although the area enhancement was reduced in the NRFC configurations compared to the open microchannels, the performance was enhanced which suggested that separate-liquid vapor pathways assisted with liquid feed channels was the driving mechanism for the enhancement as against the area augmentation.

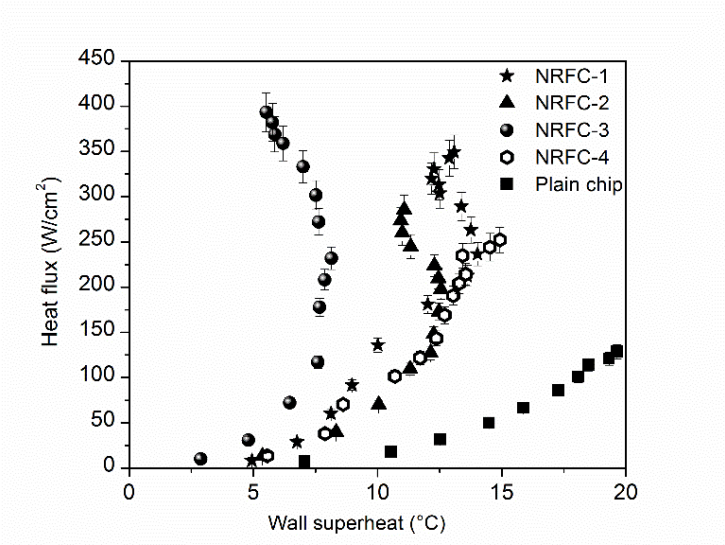

Figure 41. Pool boiling curves for NRFC surfaces with water at atmospheric pressure plotted using the 1 cm^2 projected area and the fin top temperature.

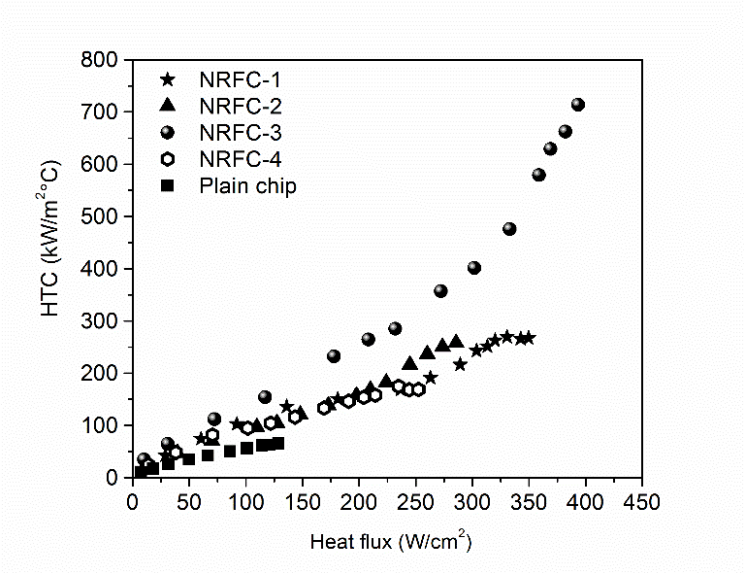

Figure 42. Heat transfer coefficient comparison for the NRFC surfaces using fin top temperature.

Figure 42 shows the variation of HTC plotted against heat flux. At CHF, HTCs of 267 kW/m^2°C, 257 kW/m^2°C and 168 kW/m^2°C were observed for NRFC-1, 2 and 4, respectively. NRFC-3 had the best performance with a HTC of 713 kW/m^2°C representing an exceptional enhancement of 996% in HTC at CHF over a plain chip.

Table 7: Test matrix and results

Chip	Area enhancement factor	NR channels separation distance (mm)	CHF (W/cm^2)	Wall superheat (°C)	HTC_{CHF} (kW/m^2°C)	CHF_{NRFC} / CHF_{plain}	HTC_{NRFC} / HTC_{plain}
Plain chip	1.0	--	128	20	65	--	--
NRFC-1	2.046	4.5	350	13.1	267	2.7	4.1
NRFC-2	2.012	3.0	285	11.0	257	2.3	4.0
NRFC-3	1.978	2.125	394	5.5	713	3.1	11.0
NRFC-4	1.944	1.6	252	14.9	168	2.0	2.6

Of particular interest is the trend showing lower wall superheats at higher heat fluxes with NRFC-3. This trend is similar to the trend in the boiling curve seen for the contoured fin [64], where the reduction in wall superheat at higher heat fluxes was attributed to the evaporation momentum force. This force increases with heat flux and dictates the bubble motion toward the center of the nucleating region. As the heat flux increases, the bubbles are driven toward the center of the nucleating region as they depart, and a strong liquid circulation pattern is established that prevents any nucleation in the feeder channels. The liquid transport in the FCs is governed by the liquid circulation set by departing bubbles. The feeder channel geometry affects the flow resistance, heat transfer coefficient to the impinging liquid and surface area available for heat transfer to the liquid. Further optimization can be achieved by varying the feeder channel dimensions. These bubble induced separate liquid-vapor pathways result in a highly efficient mechanism that is responsible for the large rise in the heat transfer coefficient to an unprecedented value of 713 kW/m^2°C, which is about 11 times the plain chip HTC and 2.7 - 4.2 times the HTC value with the other two configurations.

4.1.2.3. Effect of channel width

The nucleating region channel width and the feeder channel widths have a significant bearing on the heat transfer performance. Figure 43a and b show the pool boiling curves obtained for three NR and FC channel widths – 300 µm, 500 µm and 762 µm, respectively. These channel widths were chosen based on the ranges reported previously in literature [23,65]. The CHF comparison shown in these figures suggests that an optimal channel width exists for which the performance is significantly higher. This is in agreement with the results reported by Kandlikar [64] for a contoured fin in which a channel width of 0.5

mm resulted in a performance of 300 W/cm^2 at a wall superheat of 4.9 °C. Furthermore, the NRFC-3 configuration resulted in a HTC that was 1.1 times that of a contoured fin surface showing that this configuration was able to sustain the mechanism efficiently at higher heat fluxes.

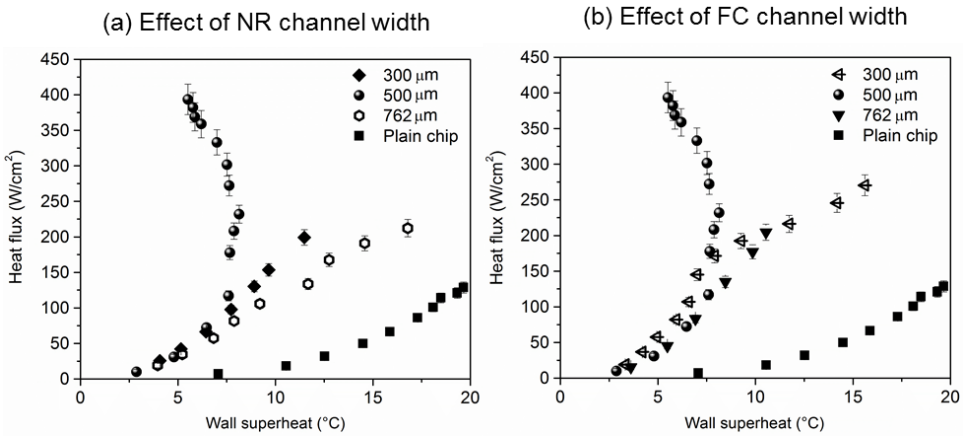

Figure 43. Pool boiling curves to study the effect of (a) NR channel width (with constant FC width = 500 μm) (b) feeder channel widths (with constant NR channel width = 500 μm).

4.1.2.4. Heat Transfer Mechanisms

The architecture of the surface was such that the FCs were able to continuously supply liquid to the NR channels. The liquid supply was heavily influenced by the FC bank width. High speed images were obtained using a Photron FASTCAM® at a high frame rate of 4000 fps and are shown in Figure 44a-f for NRFC-3. Figure 44f distinctly shows separate liquid-vapor pathways with vapor columns over the NR channel and subsequent liquid addition through the FC regions. In the videos captured at lower heat fluxes, some bubbles were seen to nucleate inside the FCs. However, these bubbles are suppressed at higher heat fluxes and provide unobstructed pathways for liquid flow. Note that the maximum wall superheat for the best performing chip was only 5.5 °C. In the NRFC-2, similar a separate

liquid-vapor pathway to NRFC- 3 was observed as seen in Figure 44h while the NRFC-4 shows bubble coalescence over the FCs blocking the liquid supply pathways.

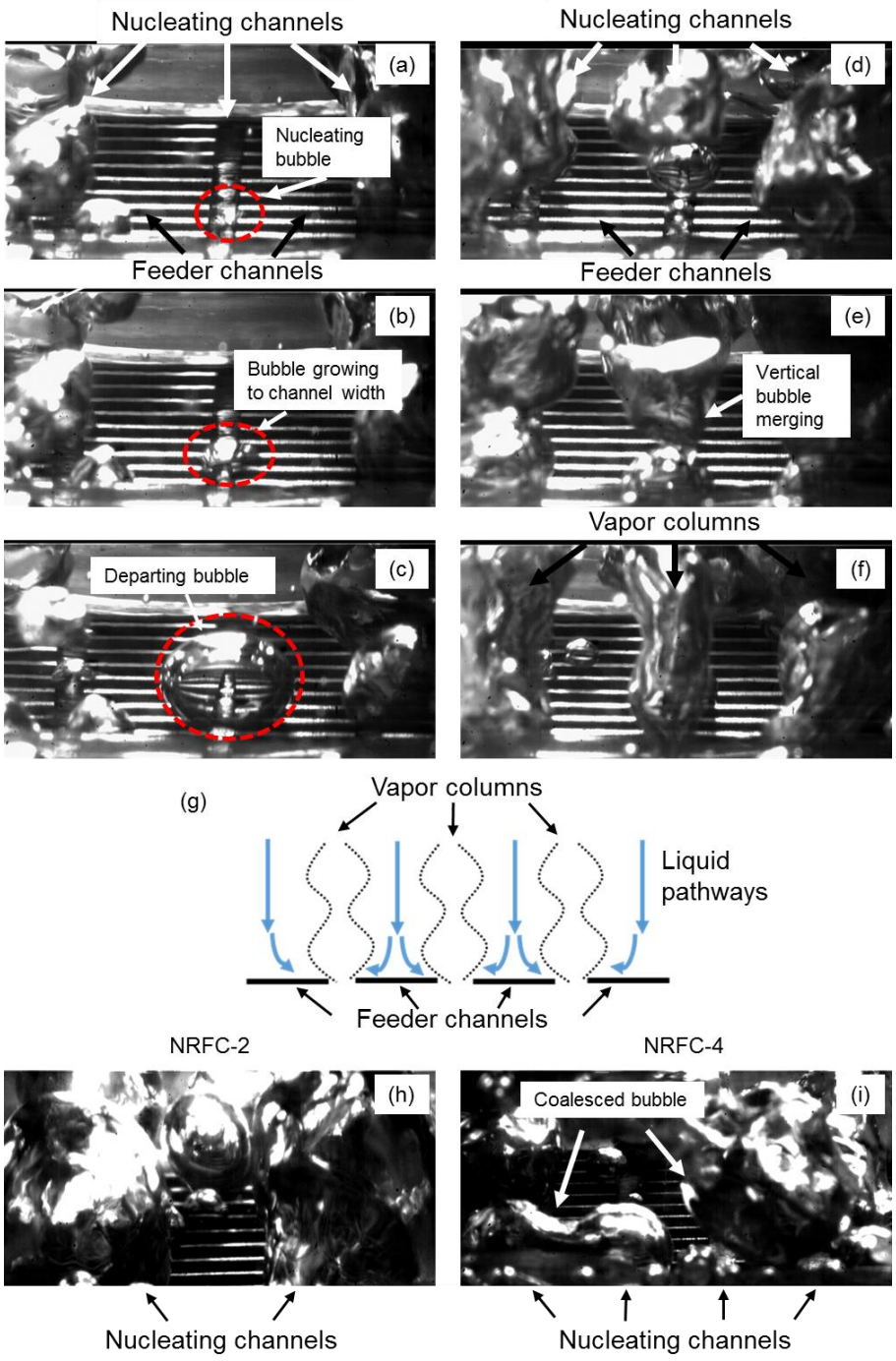

Figure 44. Bubble sequence obtained with NRFC-3 surface. (a) A bubble nucleates inside the nucleating channel region (b) Bubble growing to channel width (c) Bubble departing from the edges of the feeder channels (d) Additional nucleation sites become active in the nucleating channel (e) Bubbles coalesce in the vertical direction (f) Distinct vapor columns in the nucleating channels and liquid supply pathways through the channel regions (g) Schematic showing stable vapor columns over the NR channels with liquid supply through the FCs (h) Vapor columns over NR channels in NRFC-2 (i) Coalesced bubbles merging over the FCs in the NRFC-4 configuration.

A trend in CHF with the distance between the NRs was observed from the test surfaces investigated in this study. As mentioned previously, the bubble departure diameter obtained from the Fritz equation resulted in a value of 2.21 mm which was also in close correspondence to the critical capillary length (2.5 mm for water at 100 °C) obtained using Eq. (17).

$$\lambda_c = \sqrt{\frac{\sigma}{g(\rho_l - \rho_g)}} \tag{17}$$

NRFC-1 and NRFC-3 have NRs separated by 4.75 mm and 2.125 mm (see Figure 2) that are close integer multiples (~2 and ~1 respectively) of the bubble departure diameter (2.213 mm). These values indicate that spacing between the NR channels is dependent on the bubble departure diameter in such a way that the integer multiples of the bubble diameter enhances the pool boiling performance significantly compared to other configurations. The hydrodynamic theory using the bubble departure diameter and the capillary length explains the enhancement obtained when the FC lengths are equal to the capillary length as in the case of NRFC-3. The NRFC-1 case represents a single nucleating channel with large feeder channel lengths on its either side.

Future testing with higher integer multiples (3, 4, 5 etc.) is proposed to further validate the observed trend. However, it is demonstrated that the bubble departure diameter can be used as a guidance to develop enhanced microstructures by incorporating a network of nucleating and feeder channels. The best performance is obtained when this multiple is 1 as seen for NRFC-3. In the other two configurations, the increased flow distance in the FCs (NRFC-2) and lateral bubble coalescence (NRFC-4) makes the mechanism less efficient resulting in early CHFs.

4.1.3. Pool boiling inversion through bubble induced macroconvection

In a boiling heat transfer system, an increase in heat flux is often associated with an increase in wall superheat. However, the experimental observations for some enhanced surfaces shown in previous surfaces depicts a decrease in wall superheat at higher heat fluxes. This is termed as *boiling inversion* in this work. Figure 45a shows a graphical representation of a boiling curve with inversion along with a typical boiling curve. Other surfaces exhibiting this behavior in recent literature including surfaces developed in this thesis are summarized in Figure 45b. Kruse et al. [77] created hierarchical microstructures using a femtosecond laser and showed that the low thermal conductivity materials induce a temperature gradient within the structure. This temperature gradient results in the onset of secondary nucleation cavities at higher heat fluxes which reflects as an inversion in the boiling curve. A recent class of enhancement structures developed using separate liquid-vapor pathways also exhibits the inversion behavior. In this configuration, separate pathways are created for the vapor stream leaving the heater surface and the returning liquid, typically in the form of an impinging jet. These include a contoured fin with controlled bubble trajectory using the evaporation momentum force [64], electrodeposited porous fin with impinging liquid jets

over the channel regions [23], sintered-channels exhibiting liquid feed pathways through the fin tops (section 4.1.1.1), nanostructured bi-conductive surfaces promoting wicking [44], and a nucleating region with convective feeder channels (section 4.1.2). The focus of this paper is to explain the inversion trend on surfaces with separate liquid-vapor pathways.

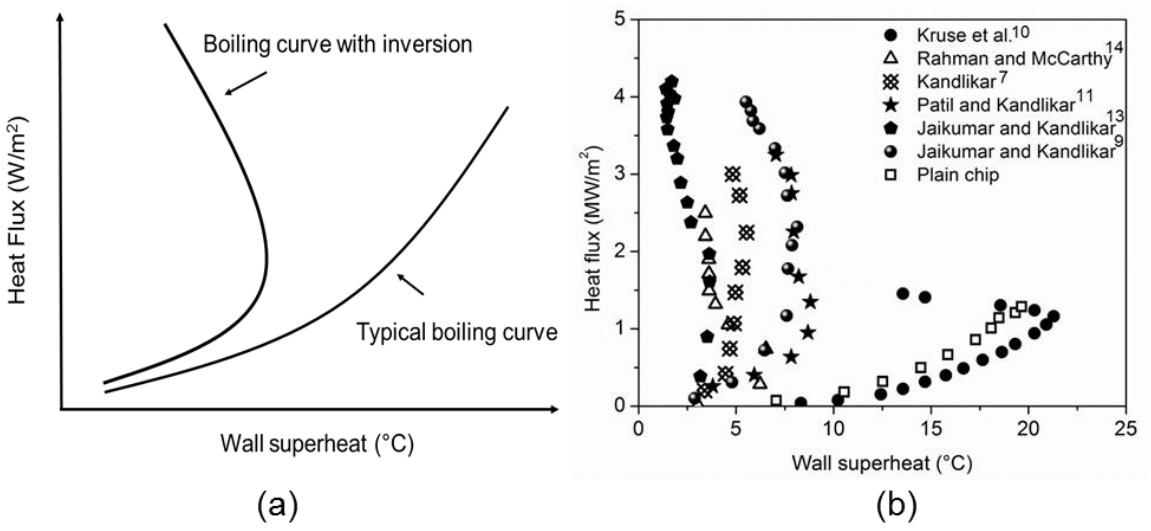

Figure 45. (a) Schematic representation of boiling curves with and without inversion, (b) summary of boiling inversion in recent literature (Kruse et al.[77] – Tall Inconel, Rahman and McCarthy[44] – Nanostructured Biconductive, Kandlikar[64] – Contoured fin, Patil and Kandlikar[23] – Electrodeposited porous fin tops, Sintered-channels, Nucleating regions with feeder channels).

4.1.3.1. Hypothesis

Macroconvection heat transfer mechanism relies on the departing bubbles inducing an impinging jet-like liquid motion on the adjacent non-boiling surface [78]. The spatially ordered motion generated by the bubbles and liquid is able to provide very high heat transfer coefficients due to thin thermal boundary layers and hydrodynamically developing flow under the impinging jet. In this enhancement configuration, distinct vapor removal and liquid supply pathways are established. As the liquid velocity increases at higher heat

fluxes, it suppresses nucleation over the non-boiling regions and provides an unimpeded path with improved heat transfer for liquid flow towards the nucleation sites. This paper presents the jet impingement over the non-boiling regions as an enhancement mechanism to explain the inversion trend on surfaces with separate liquid-vapor pathways.

To demonstrate the boiling inversion, the NRFC-3 surface is considered in the analysis as shown in Figure 46a. The feeder channels are regions dominated by macroconvective effects under an impinging liquid jet, while the bubble activity is confined to the nucleating regions. This partitioning often happens naturally due to the suppression effects of the impinging jet resulting in a self-sustained boiling configuration as demonstrated previously. The length of the feeder channel corresponded to the critical capillary length (~2.2 mm for water at 100 °C). This surface exhibited remarkable performance improvements reaching a CHF of 3.94 MW/m^2 (± 0.2 MW/m^2) at a wall superheat of 5.5 °C (±1.1 °C) with a HTC of 713 kW/m^2°C as seen previously. The liquid motion over the feeder channel occurs through jet impingement similar to that reported by Patil and Kandlikar [23]. This bubble induced liquid jet motion is amplified at higher heat fluxes due to the increase in bubble formation rates and resultant increase in liquid jet velocity.

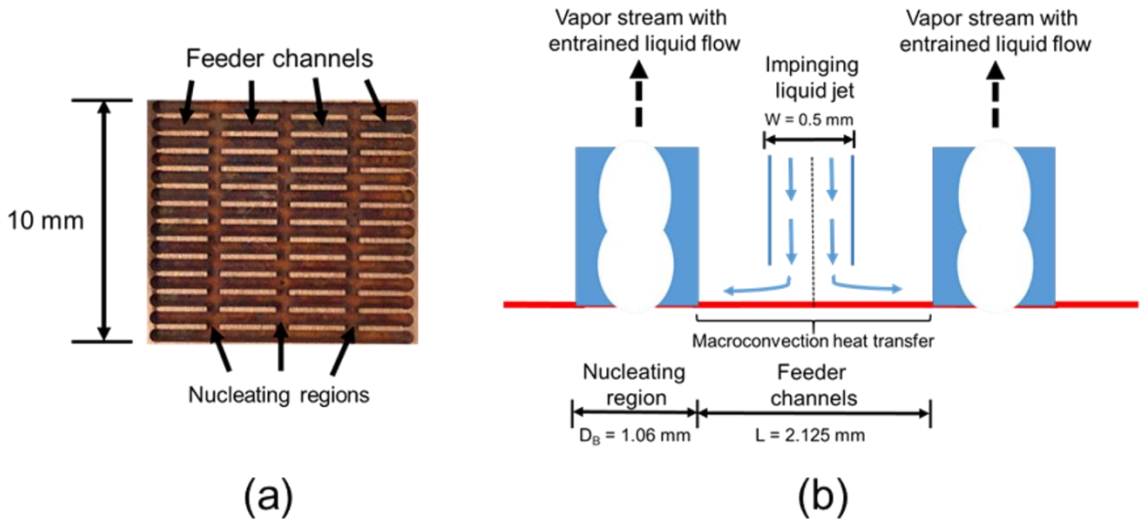

Figure 46. (a) Top view photograph of the copper chip used in the experimental test showing the feeder channels and nucleating regions. (b) Macroconvection model setup for the nucleating regions with feeder channels showing jet impingement over the feeder channels induced by liquid-stream flow over nucleating regions.

4.1.3.2. Analysis framework

The heat transfer due to macroconvective effects of liquid flow over the feeder channels is identified as the mechanism responsible for the boiling inversion at increasing heat fluxes. The macroconvective heat transfer was analyzed for the nucleating region with feeder channels as follows:

(i) Firstly, the latent heat contribution to the total heat flux was estimated based on the work conducted by Rallis and Jawurek [79].

(ii) Secondly, the void fraction (Hughmark [80]) and retained liquid volumetric flow rate over the nucleating regions were estimated for the isolated bubble (Mishima and Hibiki [81]) and coalesced bubble (Bhagawat and Ghajar [82]) regimes.

(iii) Thirdly, the macroconvection heat transfer was analyzed using a rectangular slot jet impingement heat transfer correlation (Mudawar [83]) for the two cases (isolated and coalesced bubbles).

(iv) Finally, the results are presented in terms of boiling curves depicting the predicted inversion trend using (i – iii).

4.1.3.2.1. Latent heat contribution

Since the bubble activity is confined to the nucleating regions alone, the latent heat contribution to the total heat flux is an important consideration to explain the increase in bubble formation rates at higher heat fluxes. Rallis and Jawurek [79] have demonstrated that the latent heat contribution varies linearly with the total heat flux and attains a value equal to the total heat flux at CHF. Translating this observation to the current analysis, the latent heat flux was obtained as shown in Figure 47.

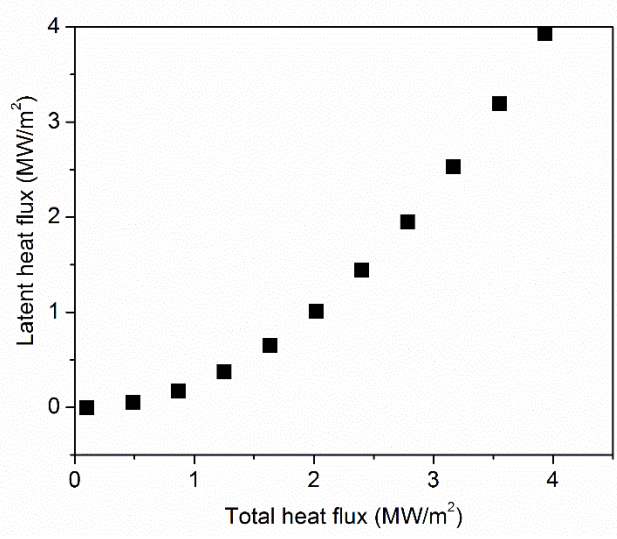

Figure 47. Latent heat flux as a function of total heat flux based on Rallis and Jawurek [79].

4.1.3.2.2. Void fraction analysis

The departing liquid-vapor stream over the nucleating region induces a liquid jet that impinges over the feeder channels. The superficial vapor velocity was calculated using the known vapor generation rate at a given heat flux, latent heat of vaporization and vapor density. The fluid properties were obtained at saturation conditions for water. The liquid velocity was modeled similar to the transient heat conduction analysis by Mikic and Rohsenow [10], where the liquid replaced the space vacated by departing bubbles. The additional volume of liquid flow entrained in the vapor-liquid stream leaving the nucleating region was estimated using the void fraction correlation proposed by Hughmark [80],

$$\alpha_G = \frac{1}{2 + \left(0.35/V_{vapor}\right)\left(\rho_l \sigma/72\right)^{1/3}} \tag{18}$$

where α_G is the gas void fraction, V_{vapor} is the vapor phase superficial velocity (m/s), ρ_l is the liquid density (kg/m^3) and σ is the liquid surface tension (N/m). At higher heat fluxes, the bubble frequency increases and the flow transitions from isolated to coalesced bubbles. Bonjour and Lallemand [84] demonstrated that the isolated bubble regime extends up to ~30% of the CHF value, while the coalesced regime (similar to annular region) was observed beyond this value. This can be viewed as a flow transition from bubbly to annular flow with increasing heat flux over the nucleating regions.

In the next step, the liquid volumetric flow rate exiting the nucleating regions in the two-phase stream was estimated for two cases: (a) bubbly flow and (b) annular flow. For the bubbly flow, the correlation proposed by Mishima and Hibiki [81] was used,

$$C_0 = 1.2 - 0.2\sqrt{\rho_G/\rho_L} \tag{19}$$

$$V_{drift} = (1 - \alpha_G)^{3/2}\sqrt{2}\,(\frac{\sigma g(\rho_L - \rho_G)}{{\rho_L}^2})^{1/4} \quad (20)$$

where C_o is the distribution parameter, V_{drift} is the drift velocity, σ is the liquid surface tension (N/m), and ρ_l and ρ_G are the liquid and vapor densities. The volumetric flow rate was then calculated using the drift flux model. The annular flow was analyzed by fitting the experimental data reported by Bhagwat and Ghajar [82] for an upward two-phase flow. The equation used to obtain the liquid velocities for annular flow is given by,

$$\frac{Liquid\ Velocity}{Gas\ Velocity} = 0.0057e^{9.246\alpha_G} \quad (21)$$

In both the cases, the void fraction calculated using eq. (18) was used. By applying a volume balance between the nucleating regions and feeder channels, the liquid velocities over the feeder channels were estimated. Subsequently, the Reynolds number in the rectangular slot jet impingement correlation of Mudawar [83] was calculated using the flow length under the jet as shown in Figure 46b.

4.1.3.2.3. Macroconvection heat transfer

The macroconvection heat transfer over the feeder channels was analyzed as a jet impingement heat transfer resulting from the single-phase flow of the returning liquid as shown in Figure 46b. In the model, the nucleating region width was equal to the experimental bubble departure diameter *(D_B)* obtained using high speed imaging at a heat flux of 0.2 MW/m^2. The single-phase convective jet impingement characteristics were analyzed the over the feeder channels,

$$Nu/_{Pr^{1/3}} = 3.06Re^{0.50} + 3.099Re^{0.664}\,[(L - W)/W]^{0.664} \quad (22)$$

where *Nu*, *Re* and *Pr* are the Nusselt number, Reynolds number and Prandtl number, respectively. This correlation captures the heat transfer from the jet impingement region (W) and the flow beyond this region (L-W) parallel to the heater surface. The jet impingement and short developing flow lengths contribute towards the macroconvection heat transfer. The jet width (W) was assumed to be effective over half the bubble departure diameter. The Nusselt number was calculated using Eq. (22).

4.1.3.2.4. Pool boiling curve

To represent the results as a pool boiling curve, the average HTC and wall superheat were calculated as follows:

$$HTC = \frac{Nuk_L}{L} \tag{23}$$

$$\Delta T_{sat} = \frac{q''_{total}}{Area\ enhancement\ factor\ \times HTC} \tag{24}$$

where ΔT_{sat}, k_L and q_{total} are the wall superheat (°C), liquid thermal conductivity (W/m-K) and the total heat flux (W/m^2), respectively. The HTC was assumed to be uniform over the microchannel surface, and hence the area enhancement factor was employed in calculating the wall superheat. The feeder channel width, height and fin width contributed to the actual enhanced area. Subsequently, the area enhancement factor was calculated as a ratio of the actual area and the projected area. The resulting area enhancement factor was equal to 1.4.

4.1.3.2.5. Manifestations of separate liquid-vapor pathways

The wall superheat obtained using eq. (24) and the total heat flux for the jet impingement flow over the feeder channels is represented as a boiling curve in Figure 48. As a comparison to the analysis, the experimental results for the enhanced chip and the plain

copper chip are also shown in this figure. The curve corresponding to the bubbly flow shows the typical boiling curve without the inversion. The horizontal dotted line at a heat flux of ~1.2 MW/m^2 shows the onset of coalesced (annular) flow [84]. The plot corresponding to the annular flow shown in Figure 48 predicts the macroconvective heat transfer over the feeder channel alone which shows a significant reduction in wall superheat at higher heat fluxes. However, a rightward shift in the curve corresponding to the annular flow heat transfer is expected due to two possible cases. Firstly, for nucleation to occur the wall superheat has to be greater than that predicted by the nucleation criterion (not shown). Therefore, a self-adjusting boiling configuration is established to overcome the reduction in superheat to promote nucleation on the surface. Secondly, the net heat transfer will be an outcome of the heat transfer over the nucleating region and feeder channels. This net effect is expected to move the curve to the right, similar to the experimental results since the heat transfer from the nucleating regions will be less than that of the heat transfer over the feeder channels. The analysis conducted here provides a theoretical explanation of the mechanisms responsible for boiling inversion.

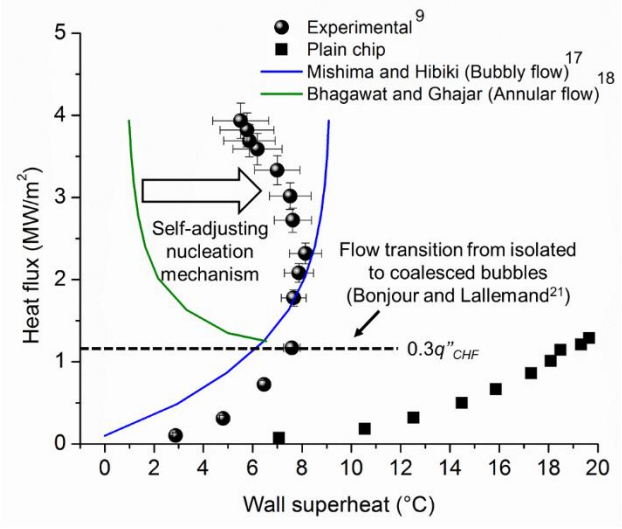

Figure 48. Boiling curve for the experimental values compared to the current model exhibiting the boiling inversion trend.

4.1.4. Interplay between Developing Flow Length and Bubble Departure Diameter During Macroconvection Enhanced Pool Boiling

Since the surfaces employing enhanced macroconvection mechanism not only result in high CHF's, but are also characterized by a steep increase in HTCs, we hypothesize that the developing flow in the mircochannels is responsible for the heat transfer enhancement. In this paper, we demonstrate the length scale effect on the efficacy of macroconvection mechanism on NRFCs. Pool boiling experiments were conducted with water and three dielectric fluids (HFE-7000, PP1, PP1C) to validate the hypothesis. For low surface tension liquids, the critical capillary length is much smaller than the observed departure bubble diameters and hence the latter is considered in the analysis.

In the current design of enhancement structures, the variation of HTC in the single-phase dominated flow in FCs is used as guidance to design the length of the channels. In a 2-D rectangular slot jet impingement configuration, the transverse flow beyond the stagnation region behaves similar to a developing flow between the wall and the free surface of the flow as seen from the developing velocity profile under an impingement jet [17]. Therefore, this configuration is similar to the flow between parallel plates, which represents the flow in the FC. The HTC corresponding to the maximum velocity (at CHF) encountered in the FC is estimated using Kays correlation [85],

$$Nu = 3.66 + \frac{0.0668\left(\frac{D_h}{l}\right)RePr}{1 + 0.04[\left(\frac{D_h}{l}\right)RePr]^{2/3}} \tag{25}$$

where, D_h is the hydraulic diameter of the microchannels (m), l is the channel flow length (m), Nu, Re, and Pr are the Nusselt number, Reynolds number, and Prandtl number,

respectively. The Reynolds number is calculated using the bubble velocity corresponding to CHF.

The HTC is then deduced by,

$$HTC = \frac{Nuk_l}{l} \tag{26}$$

where, k_l is the thermal conductivity of the liquid.

The developing flow length (L_e) for low Reynolds number flow is calculated using Chen's correlation [86],

$$\frac{L_e}{D_h} = \frac{0.79}{0.04\,Re + 1} + 0.053\,Re \tag{27}$$

where, L_e is the developing region length (m).

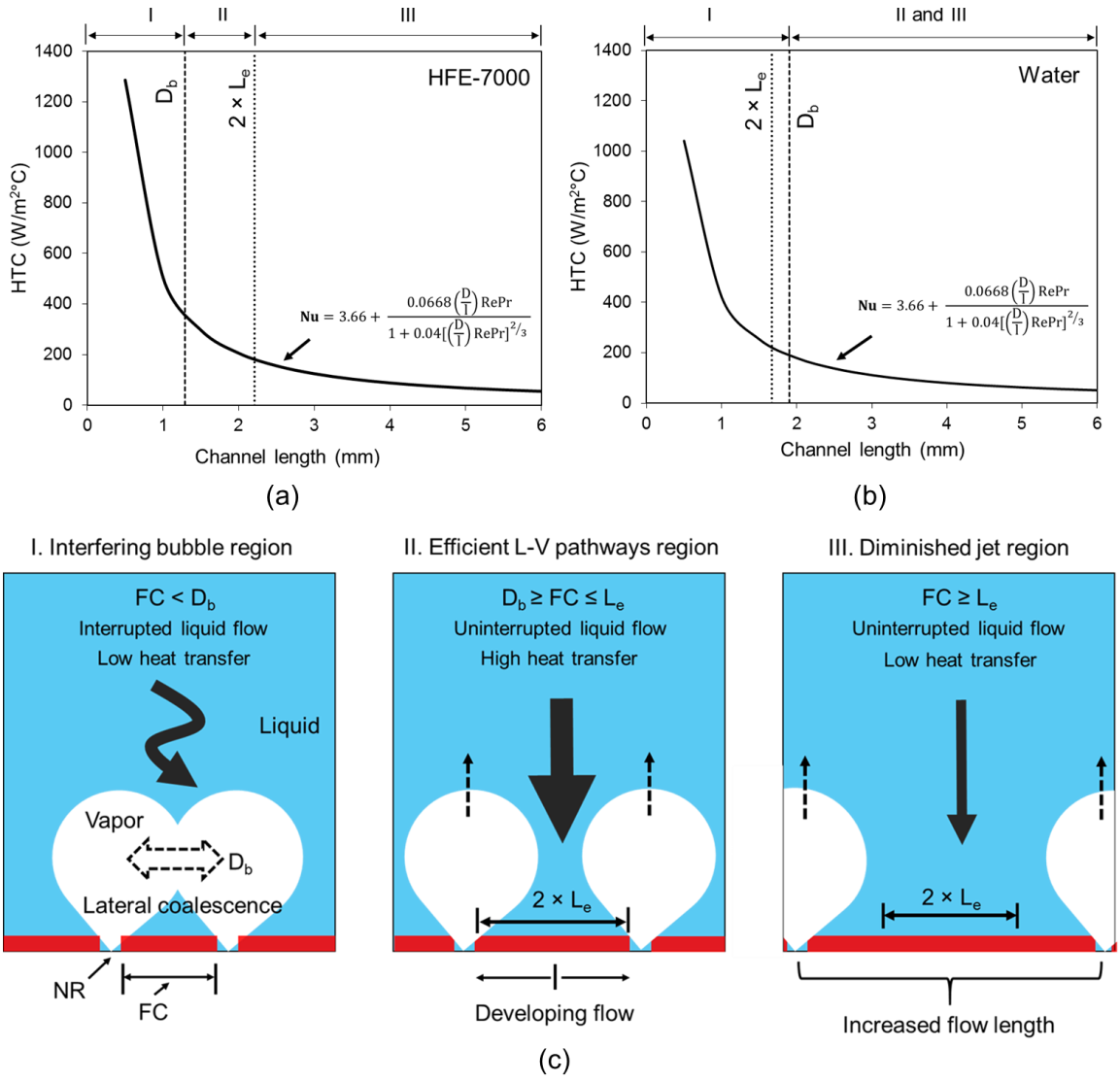

Figure 49. Variation of HTC in FCs calculated with (a) HFE-7000 or (b) water, (c) schematic representation of proposed liquid-vapor transport mechanisms based on the role of bubble departure diameter and developing flow length.

The bubble departure diameters were obtained with a high-speed camera on a plain copper chip for the three dielectric fluids and water. Figure 49(a) shows the plot of HTC and flow length in the FC for HFE-7000. The bubble departure diameters and the developing flow lengths are superimposed in the plot. The flow over the FC occurs as a jet impingement in the center (lengthwise) of channels and is assumed to be axisymmetric. Therefore, the entrance length is denoted as $2 \times L_e$ while comparing with the FC length. Three distinct

regions, demarcated by the bubble departure diameter and the developing flow length, are identified:

I. Interfering bubble region

II. Efficient L-V pathways region

III. Diminished jet region.

The three regions and the interplay mechanisms are shown as a schematic in Fig. 49(c). Region I is important as it sets the lower limit in establishing a flow field with separate liquid-vapor pathways. Heat transfer is drastically reduced due to inability of liquid to enter the FC. In region II, the lateral coalescence is overcome by adjusting the spacing such that the bubbles arising from adjacent NRs do not interfere. Consequently, there is uninterrupted flow of liquid towards the heater surface in the form of an impinging jet. Furthermore, the heat transfer during liquid travel along the FC is enhanced by the developing region effects. The cumulative benefits of uninterrupted liquid flow and shortest possible developing region liquid travel in the FC is expected to result in a marked increase in both CHF and HTC, and is therefore identified as the efficient L-V pathways region. Region III is characterized by longer FC channel lengths. As the channel length becomes larger, the developing region effect diminishes. This flow configuration becomes less effective for much larger FC lengths as the self-sustained boiling configuration is interrupted through diminished jet impingement influence in the long channels.

Two situations arise as shown in Fig. 49 (a) and (b) with HFE-7000 and water, respectively. The plot for HFE-7000 shows that the measured bubble departure diameter is lower than the developing flow length. For this case, the bubble departure diameter demarcates region I from II. For water, the bubble departure diameter is greater than the developing flow

length as shown in Fig. 49(b). The developing flow length is not seen to be critical as the $L_e < D_b$. Therefore, this arrangement is governed by D_b. Region II and III appear beyond D_b. An interesting outcome of this case with water is that smaller bubble diameters will exploit developing flow to provide a higher HTC. In any case, it is always desirable to have shortest possible channels lengths that avoid bubble interference.

Table 8. Test surfaces and performance summary with HFE-7000 and water.

Surface	**FC length (mm)**	**HFE - 7000**		
		CHF (W/cm^2)	**Wall superheat (°C)**	**$HTC_{@CHF}$ ($kW/m^2°C$)**
Plain	-	32	23	16
NRFC-2	3	35	12	30
NRFC-3	2.2	41	14	28
NRFC-4	1.6	66	11	57
NRFC-5	1.2	57	21	27
		Water		
Plain	-	128	20	65
NRFC-2	3	285	11	257
NRFC-3	2.2	394	5.5	713
NRFC-4	1.6	252	14.9	168
NRFC-3P	2.2	284	3.1	914

To validate the aforementioned mechanisms, four copper test surfaces were prepared by varying the FC lengths as listed in Table 8. The nucleating and FC widths were 500 µm, the channel depths were 400 µm, while the fin widths were 200 µm for all the test surfaces. These dimensions were selected based on the best performing NRFCs reported in the previous section. For the baseline performance evaluation, the data reported by Emery and Kandlikar [87] for the same test fluids under similar experimental conditions on a plain copper chip was used.

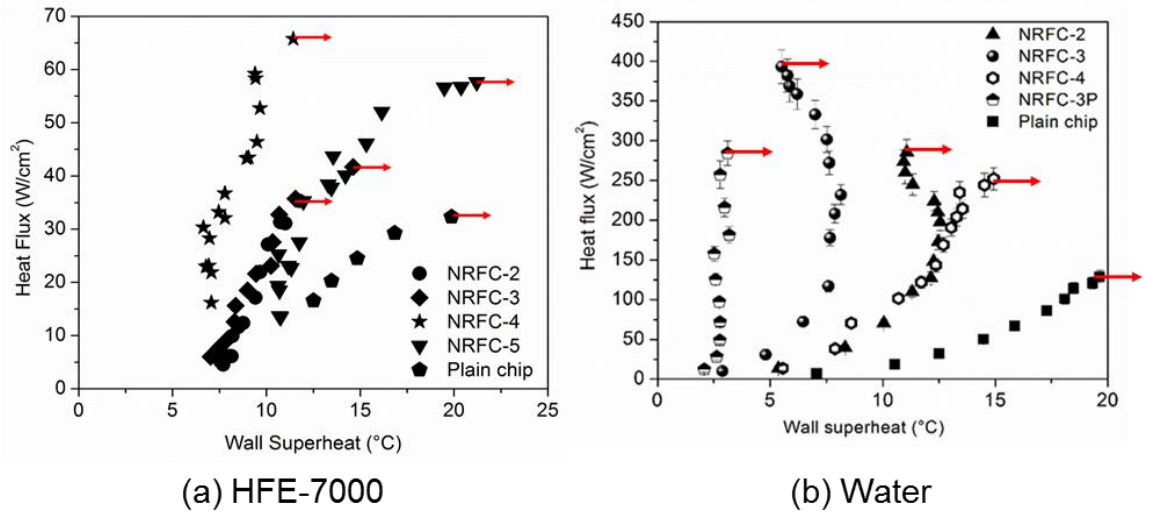

Figure 50. Pool boiling curves for NRFC surfaces with (a) HFE-7000, and (b) water at atmospheric pressure (arrows indicate CHF).

The nucleate pool boiling curves for the NRFC surfaces listed in Table 8 with HFE-7000 are shown in Figure 50(a), while the data for water is shown in Fig. 50(b). The CHF, wall superheat, and HTC at CHF with HFE-7000 and water are summarized in Table 1. All the NRFC surfaces demonstrated enhancement in both CHF and HTC when compared to the plain surface. The degree of enhancement achieved in each NRFC configuration is explained by coupling the developing flow length in the FCs and the bubble departure in the NRs.

Since the analysis combines the experimental results from multiple fluids, the normalized CHFs and HTCs are used while reporting the results in Figure 51. The CHFs are normalized by the plain baseline chip CHFs reported for each copper-dielectric fluid combination [87]. The HTCs are normalized by the HTC at CHF obtained on the plain chip. Figure 51(a) shows the variation of normalized CHF with the FC length for HFE-7000. NRFC-3 and NRFC-5 corresponds to the design of surfaces with the feeder channel length equal to the entrance length computed using Eq. (27) and the bubble departure diameter, respectively.

It is seen that NRFC-2 and NRFC-5 have lower CHF and HTC relative to NRFC-4. These two surfaces fall under region III and II, respectively. NRFC-4 is designed such that the FC length is greater than the bubble departure diameter and exploits the entrance region flow. Therefore, this configuration results in very high CHF and HTC due to self-sustained macroconvective flow over the feeder microchannels as seen in Fig. 51(a).

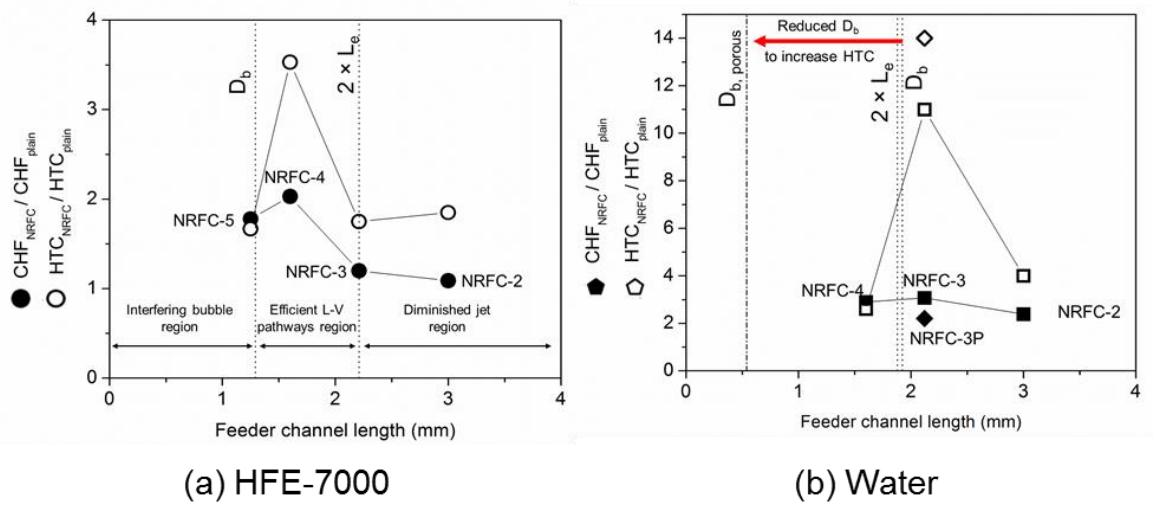

Figure 51. Normalized CHF and HTC performance for NRFC surfaces with (a) HFE-7000 and (b) water. The measured bubble departure diameter and entrance region lengths are superimposed in this plot to identify the three enhancement regions.

Figure 51(b) shows the variation of boiling performance with water. The role of bubble departure diameter is seen as the governing parameter since the $L_e < D_b$. Maximum enhancement in CHF and HTC was observed with NRFC-3, as the FC length was close to the bubble departure diameter and developing flow length. NRFC-2 and NRFC-4 fall in regions I and II respectively, hence result in relatively lower performance enhancements.

One way to further exploit the benefits of developing flow with water is to reduce the departure bubble diameter. This was accomplished by coating the nucleating regions in NRFC-3 with a 50 µm thick porous coating. This surface is referred to as NRFC-3P in Fig.

51(b). These coatings reduce the bubble departure diameter ($D_{b,\,porous}$), thereby exploiting the efficacy of the developing region flow in the channels in accordance with Fig. 51(b). This approach of reducing the D_b is effective in increasing the HTC in the channels, however the reduced D_b results in smaller volume of liquid impinging on the adjacent FCs. Consequently, the bubble induced macroconvection mechanism suffers in NRFC-3P resulting in lower CHFs as shown in Fig. 51(b). Full benefit of reduced bubble diameter can be realized by using shorter channel lengths with the porous NR regions.

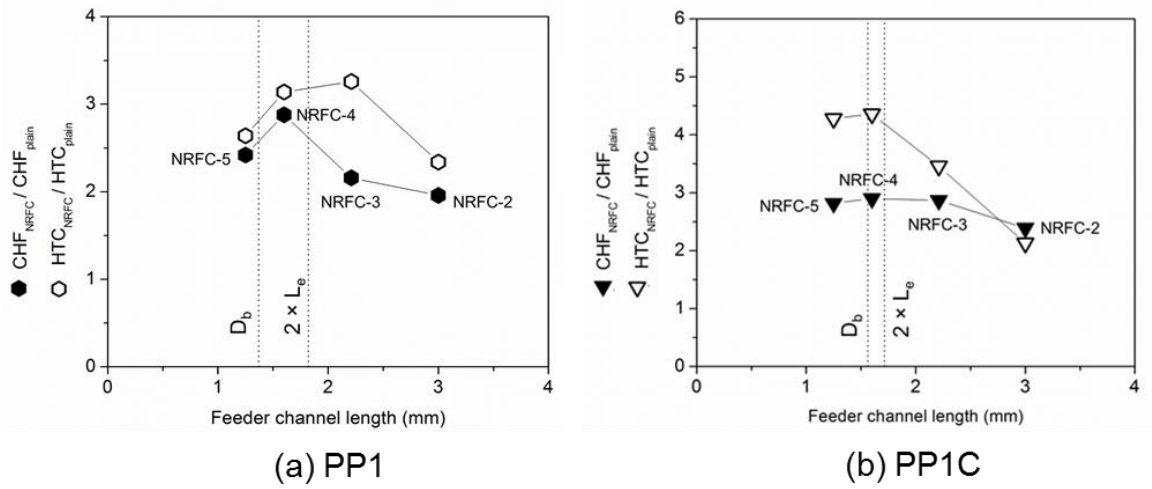

Figure 52. Performance summary with different dielectric fluids (a) PP1, and (b) PP1C.

To gain further understanding, the analysis was extended to PP1 and PP1C with the five NRFC surfaces as shown in Figure 52 (a, b). As explained previously, the maximum performance enhancement is reached in the efficient L-V pathways region (or region II), when the FC length is greater than the bubble departure diameter.

The effects of developing region flow manifests a change in the macroconvective self-sustained boiling configuration. In region III, the benefits of HTCs in the FC are significantly diminished in accordance with Figure 49(a). In this configuration, the excess flow length and lower jet velocity may also initiate undesirable nucleation in the channels

and disrupt liquid supply to the NR. This disrupts the liquid flow and consequently limits the jet impingement benefits over the feeder channels and results in a drop in the boiling performance. In the case of short feeder channel lengths, the potentially high HTCs are cannot be realized due to the interference of bubbles arising from adjacent NRs. Maximum performance enhancement utilizing the macroconvective flow is seen on surfaces where the feeder channel length overcomes the bubble coalescence and exploits the entrance region flow inside the channels. This creates a highly efficient, self-sustained configuration by disturbing the thermal and hydrodynamic boundary layers. This further results in superheating of the liquid as it approaches the NR and creating explosive bubble growth following nucleation.

4.1.5. Conclusions

In this section, a range of surfaces developed through the concept of separate liquid-vapor pathways were experimentally tested with water and other refrigerants for their pool boiling performance. The theoretical analysis conducted here supplemented the experimental values which led to the invention of a new boiling mechanism, termed as bubble induced macroconvection. Furthermore, a pool boiling curve characteristic, termed as boiling inversion, was explained through the bubble induced macroconvective jet impingement mechanism.

The summary for each enhancement type is provided as follows:

4.1.5.1. Selective enhancement coating configurations on open microchannels

An experimental study was conducted to study the heat transfer mechanisms in three heat transfer surfaces developed by selectively coating porous copper particles on open

microchannels. The configurations were identified as sintered-throughout, sintered-fin-tops, and sintered-channels. The porous coatings were deposited using a screen printing process and subsequently sintered at elevated temperatures to ensure substrate bonding. The pool boiling performance of the tested surfaces are reported in this paper. The following conclusions are drawn from this study:

1. Combining two enhancement techniques by increasing nucleation activity through porous coatings in area enhanced microchannel geometry improved the pool boiling performance significantly. This was seen by the low wall superheats and high CHF values reported here for all the configurations.

2. The effect of placement of nucleation sites over different regions of a microchannel surface on the pool boiling performance was studied. A maximum CHF of 313 W/cm^2 was obtained at a wall superheat of 7.5 °C for a sintered-throughout surface. CHF of 303 W/cm^2 and 257 W/cm^2 were obtained for sintered-channel and sintered-fin-top surfaces respectively. A maximum HTC of 565 kW/m^2°C was observed for the best performing surface (sintered-throughout) which represented a 782% enhancement over a plain chip.

3. The enhancement based on the actual surface area indicates that the heat transfer mechanism is altered since the enhancement is significantly higher than the area enhancement provided by the microchannels.

4. High speed images suggested that nucleation occurred at the location of porous coatings. Three underlying mechanisms were identified. ‘Area Augmented Enhanced Nucleation’ mechanism was responsible for the improved performance in the sintered-

throughout surface. The mechanisms responsible for liquid-vapor pathways in the sintered-fin-tops and sintered-channels were identified as 'Bubble Induced Liquid Jet Enhancement-Type-1' and 'Bubble Induced Liquid Jet Enhancement-Type-2' respectively. In Type-1, the bubbles nucleated on the fin tops with liquid flow through the channel regions whereas in Type-2 the bubbles originated in the channels with liquid flow through the fin top regions. It is concluded that the Type-2 mechanism can sustain the liquid flow better than Type-1 due to the higher temperatures in the channel walls as compared to the fin tops, and the resulting nucleation characteristics of the two surfaces. The liquid transport is governed by the chaotic liquid-vapor motion, capillary and gravity motion in all the three tested configurations.

5. In the sintered-throughout configuration, a wider channel (channel width = 762 µm) had a higher CHF than a narrower channel (channel width = 300 µm). The CHF values for the 300 µm, 500 µm and 762 µm were 241 W/cm2, 265 W/cm2 and 313 W/cm2, respectively. Maximum HTCs of 304 kW/m2°C, 410 kW/m2°C and 565 kW/m2°C were obtained for the 300 µm, 500 µm and 762 µm, respectively. The high speed images suggested that the majority of the nucleation occurred inside the channels. The driving mechanism in this configuration is the chaotic liquid-vapor motion. However, facilitating liquid pathways is critical in enhancing the CHF. Therefore a wider channel, with additional liquid pathways to feed the nucleation sites had a higher CHF and HTC compared to a narrower channel.

6. Narrower channels (300 µm) performed better than wider channels (762 µm) in the sintered-fin-top configuration. Separate liquid-vapor pathways were observed with bubbles nucleating on the fin tops and liquid supply through the channel regions by a

jet impingement-like feeding mechanism. Channel width had an important role to play as it affected the liquid transport to the nucleation sites. High speed images obtained suggested that the wider channels had a longer flow length and the liquid was unable to feed to the nucleation sites located on the fin tops. The convective mechanism in this configuration was further disrupted due to the bubbles nucleating in the channels as a result of the manufacturing process employed. The CHF values for the 300 µm, 500 µm and 762 µm channel widths were 305 W/cm^2, 272 W/cm^2 and 249 W/cm^2, respectively.

7. While analyzing the sintered-channel configuration, it was observed that the narrower channels performed better than the wider channels. A record CHF of 420 W/cm^2 at a wall superheat of 1.7 °C was observed for the 300 µm channel width test surface. This translated to an enhancement of 228% in CHF compared to a plain chip. A record HTC of 2900 kW/m^2°C was obtained with the same surface, indicating a 4361% improvement over a plain chip. The 500 µm and 762 µm channel width surfaces had a CHF of 281 W/cm^2 and 299 W/cm^2, respectively. High speed images suggested that the jet impingement on the fin tops contributed to liquid feed in to the channels. In a wide channel (762 µm), the liquid feeding mechanism is insufficient to wet the entire channel surface which led to early CHF. However, in the 300 µm wide channels, the jet impingement was sufficient to continuously wet the channel regions until the CHF was reached. The mechanism proposed for the sintered-channel configuration is expected to sustain the convective flow at higher heat fluxes making it superior to the sintered-throughout and sintered-fin tops configurations as reflected by the performance.

4.1.5.2. Nucleating region with feeder microchannels

Providing separate liquid-vapor pathways and incorporation of liquid feeder channels directing liquid flow toward the nucleating regions was seen to be very effective in enhancing the CHF and HTC. Making the distance between the two nucleating regions a multiple of departing bubble diameter was seen to be beneficial, with a multiple of 1 providing the highest performance with water. The trend of decreasing wall superheat with increasing heat flux was seen to be similar to that reported in a contoured fin which benefitted from the evaporation momentum force in directing bubble motion. A record HTC of 713 $kW/m^2°C$ was obtained at a CHF of 394 W/cm^2 and a wall superheat of 5.5 °C with NRFC-3. High speed images clearly identified the role of nucleating channels as vapor removal pathways with liquid supply through the feeder channels.

The macroconvective flow over the feeder channels results in a significant reduction in wall superheat leading to the boiling inversion observed on surfaces with separate liquid-vapor pathways as described in this paper. Increase in latent heat contribution and bubble generation rates causes a bubble induced liquid jet impingement flow over adjacent non-boiling regions. The efficacy of surfaces with separate liquid-vapor pathways through a self-sustaining boiling mechanism is demonstrated through a flow regime transition in the liquid-vapor stream over the nucleating region. The enhanced macroconvection heat transfer resulting from the impinging jet and short thermal and hydrodynamic developing flow lengths result in decreasing wall superheats with increasing heat fluxes. To sustain the nucleation under decreasing wall superheat conditions, a self-adjusting mechanism is established which provides the necessary nucleation sites by adjusting the bubble generation rate. However, the benefits from the macroconvective flow dominate the

combined effects, which reflects as the inversion in the experimental results. Additional effects due to liquid subcooling are expected to suppress nucleation over the jet impingement regions in fundamentally different ways. The latent heat contribution and the local wall superheat near CHF are key factors that are recommended for future work. This will shed further light on the localized mechanisms on different regions of the heater surface. In conclusion, the analysis conducted here indicates the role played by the bubble induced liquid jet that enhances the macroconvection heat transfer. This analysis can be utilized in tailoring surfaces targeted towards high HTCs at high heat fluxes and promoting enhanced liquid directionality towards the nucleation sites.

FC lengths shorter than the developing flow length benefit from the enhancement due to developing boundary layers over their entire length. However, FC lengths shorter than the departure bubble diameter suffer from bubble interference while FC lengths that are considerably longer than the developing flow length exhibit lower heat transfer rates in the fully developed region. The bubble interference is seen as the lower limit for the channel length. Beyond this limit, it is desirable to have the entire channel under developing flow conditions. This approach can be used in designing surfaces with separate L-V pathways such that the developing single-phase flow and the macroconvective feeder channel lengths are coupled for maximum performance enhancement.

4.2. Dual enhancement through graphene and graphene oxide (GO) coatings

The objective of this section is to identify the mechanisms responsible for the enhancements in both CHF and HTC (dual enhancement) observed with coatings comprising of graphene and graphene oxide (GO) coatings. To this effect, we carefully designed experiments to discuss the effects of *(i)* thermal conductivity of graphene films,

(ii) wettability, *(iii)* contact angle hysteresis, and *(iv)* morphological effects on nanoscale and microscale GO coatings. This section is organized such that each individual mechanism is analyzed by presenting chemical characterization of the coated structures followed by the pool boiling tests. This section is useful in determining the individual contributions of nanoscale and microscale graphene coatings and the structure-performance relationship to tailor surfaces in the quest to further increase the limits of CHF and HTC. Using surfaces developed in sections 4.3 and 4.4 as benchmark studies, a new class of enhancement structures was designed to facilitate wicking in graphene structures (section 4.6).

4.2.1. Nanoscale graphene/GO coatings

The samples for the monolayer and multilayer GO coatings (4-6% oxygen content) were developed at National Central University, Taiwan. An atmospheric pressure chemical vapor deposition (APCVD) technique was used to coat the GO on the copper test chips. The copper test chips were polished to achieve a mirror finished smooth surface. The arithmetic mean roughness (R_a) was measured using a confocal laser scanning microscope and was less than 1 μm prior to the deposition process for all the test surfaces. The details of the CVD process is described in detail in Ref. [88]. A consequence of using bulk copper substrates in the CVD process is that it introduces roughness effects arising due to thermal deformation of the bulk copper substrate. This aspect of using CVD process is extremely beneficial as it introduces a morphological change of the underlying substrate over which a conformal coating of graphene was achieved. Although previous depositions [89] of graphene or GO using this technique highlight the importance of decoupling the substrate from the layers by depositing on thin foils, this study identifies the effect of bulk copper

deformations as a potential factor in improving the boiling performance characteristics which is validated here.

4.2.1.1. Morphological characterization of nanoscale copper coated graphene/GO

Characterization of nanoscale coatings was undertaken using X-ray diffraction, Fourier Transform Infrared spectroscopy, and Raman spectroscopy.

4.2.1.1.1. X-ray diffraction

X-ray diffraction was used to probe the differences in the characteristic peaks of GRAPHENE/GO observed for mono and multilayer substrates as seen in Figure 53. The measurements showed the characteristic 2θ reflections between 6-10° that corresponds to the presence of graphene and GO. Typically, graphene and GO peaks occur in the range of ~5-12°. The peaks observed between 40-70° correspond to the copper substrate. The diffraction graphs for mono and multilayer were seen to be influenced by the variation of number of graphene layers on both the substrates and the distance between the layers in the case of multilayer samples. The presence of a small peak around 28° is attributed to the excessive oxidation of the sample from the exposure to the X-rays. The XRD pattern of mono and multilayers were analyzed around the 002 peak, and the Laue diffraction fitting function was used to determine the number of layers in the multilayer substrate [90]. The current analysis showed 3 layers on the multilayer samples. The distance between the layers in the multilayer samples is an important parameter which dictates the degree of wrinkle formations on the surface. The oxide formation in the nanoscale coatings is expected to mask the benefits of the graphene coatings. Additionally, the oxide formation hampers the heat transfer.

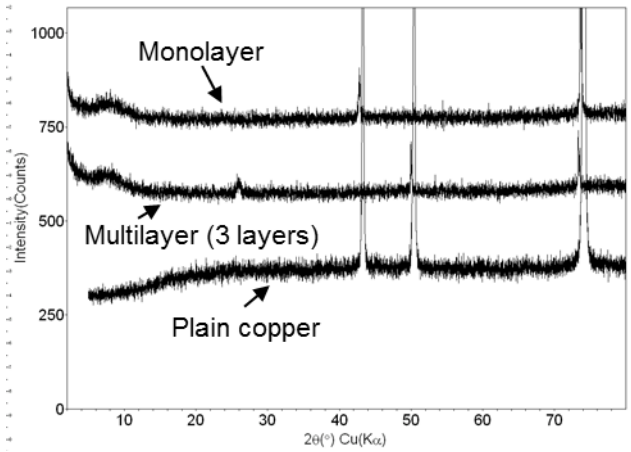

Figure 53. XRD spectrum for monolayer and multilayer coated samples.

4.2.1.1.2. Fourier transform infrared spectroscopy

Fourier transform infrared spectroscopy was employed to further confirm the presence of graphene and GO by detecting the presence of chemical bonds on the substrates. Figure 54 shows the light absorbance by the graphene molecules as a function of wavelength depicting the characteristic peaks of GO: C=O stretching vibration of carboxyl group at 1726 cm^{-1}, O-H deformation vibration resulting from C-OH at 1390 cm^{-1}, and C-O stretching vibration at 1050 cm^{-1}. The peak at 1570 cm^{-1} corresponding to the presence of aromatic rings (C=C) was also seen. The FTIR pattern for the two substrates were identical as expected due to similar molecular composition, however the high intensity peaks as seen with the multilayer sample indicate the presence of a larger number of molecules.

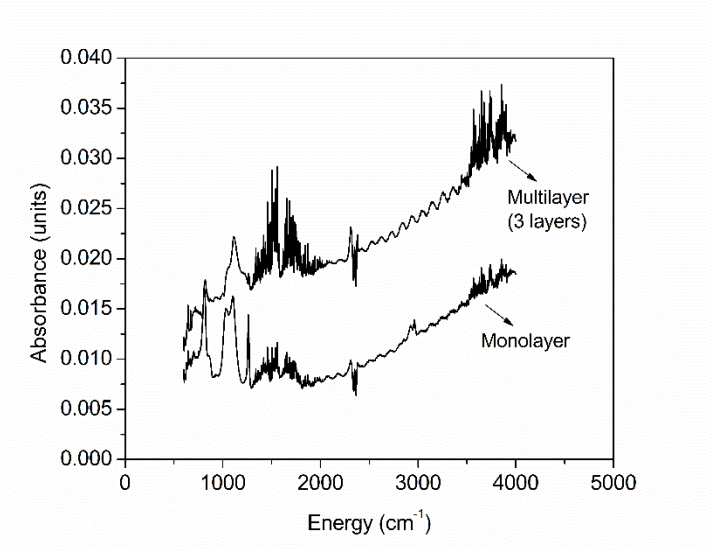

Figure 54. FTIR spectrum for monolayer and multilayer coated samples.

4.2.1.1.3. Raman spectroscopy

Raman spectroscopy was used to further quantify the number of layers for the CVD coated multilayer substrates. The laser excitation during Raman spectroscopy measurements caused a shift of the Stokes phonon energy, which resulted in three characteristic peaks for graphene: G (1580 cm^{-1}), a primary in-plane vibrational mode, a 2D peak (2690 cm^{-1}), and a different in-plane vibration, D (1350 cm^{-1}) as seen in Figure 55. The CVD deposited GO multilayer demonstrated a prominent G and 2D peak with a negligible D band indicating a relatively defect free and high quality of graphene coating. As expected, due to the lesser number of graphene layers on the substrate, the intensity of G peak for monolayer was lower than the multilayer peak. The broader 2D peak was attributed to the wrinkled graphene sheets as seen in Figure 55, which arises due to the coupling effects with the underlying copper substrate. Typically, an increase in the number of layers results in a decrease in the thermal conductivity along the z-plane. Raj et al. **[91]** have further shown that very large interlamellar spacing results in the elimination of wettability effects with

the underlying substrate. On the other hand, Rafiee et al. **[92]** have shown the influence of the underlying substrate exists for a threshold of 6 layers for copper and water wetting systems. In this context, this study highlights the importance of wettability with an increase in the number of graphene layers which manifests as a large change in the contact angle hysteresis. This change is expected to influence the microconvection and transient conduction heat transfer mechanisms.

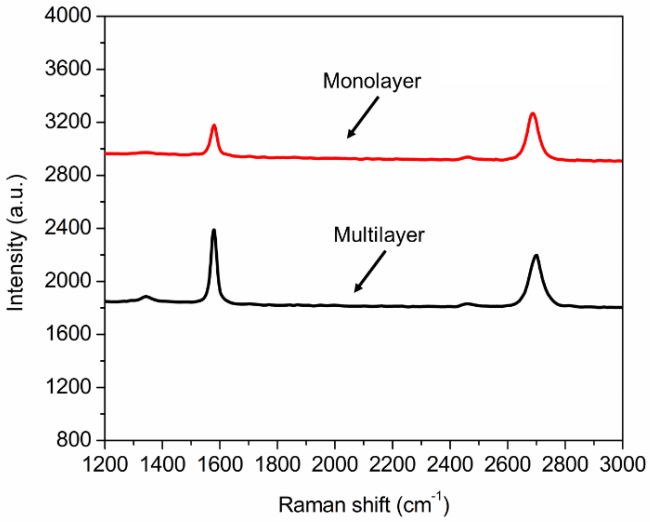

Figure 55. Raman spectrum for the monolayer and multilayer coated samples with a Horiba HR 550 confocal Raman microscope.

4.2.1.1.4. Scanning Electron Microscopy

Figure 56(a-f) indicates the Field Emission Scanning Electron Microscopy (FESEM) images obtained for the two samples. The energy dispersive X-ray spectroscopy (EDS) was also conducted to obtain the carbon-mapping on the surface (Figure 56c and f) to confirm the uniformity of graphene and GO coating. The EDS measurements were done on Bruker Quantax EDS with XFLASH 5010 detector attached to the FESEM. The images shown in Figures 56b and d were obtained at a higher magnification which reveals the location of defect sites. In the case of monolayer sample, the grain sizes are in excess of 40 µm. A

thorough characterization of the grain features is available in Ref. [88]. In the multilayer samples, the location of defect sites was greater in number and random without any observable pattern. The defect sites are an outcome of the deposition process employed and they serve as potential nucleation sites during boiling. Firstly, the thermal conductivity of the samples is related to the grain size which affects the phonon scattering. Large grains induce less scattering which results in high thermal conductivities. In this context, the monolayer sample exhibits larger grain sizes and is expected to have higher thermal conductivities. Secondly, the receding contact angles are significantly affected by the location of defects [91].

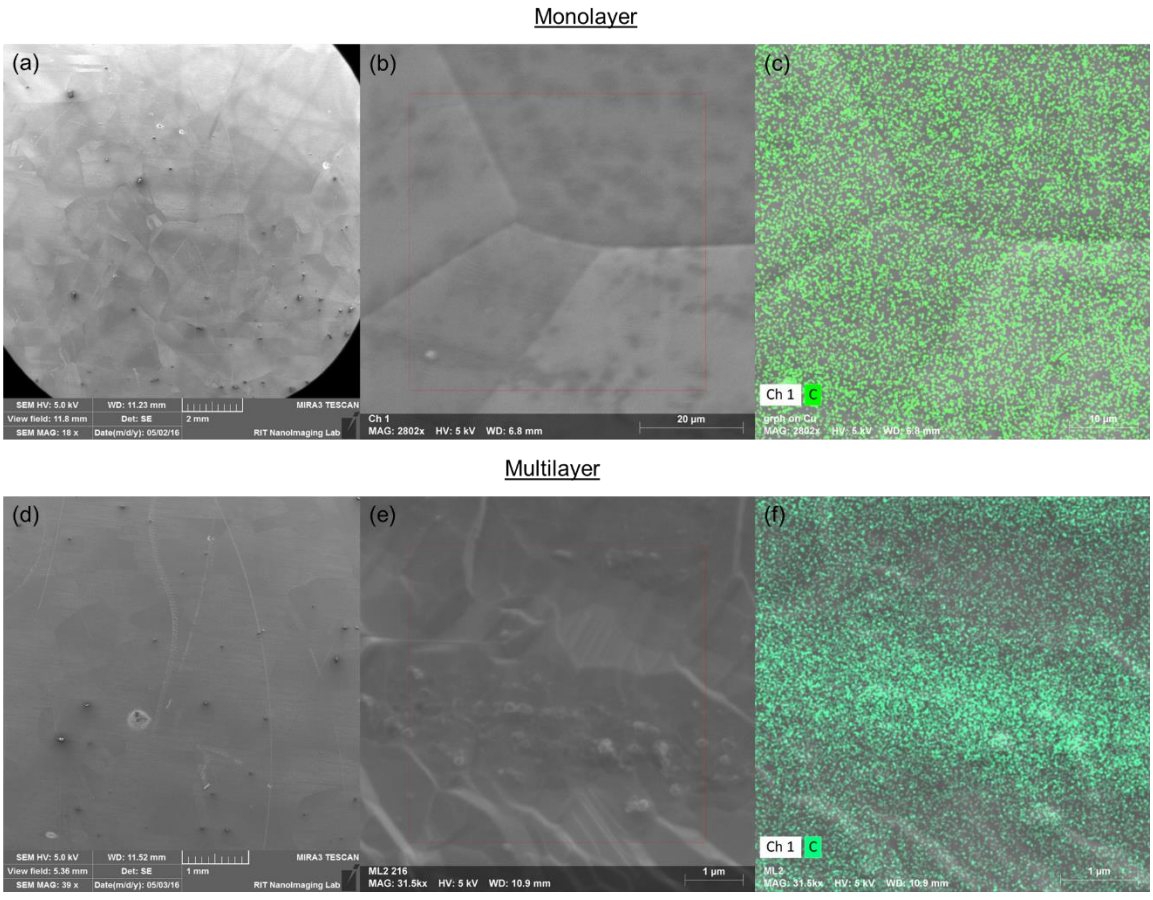

Figure 56. Field Emission SEM images of (a-c) monolayer samples and (d-f) multilayer samples. (b and e) exhibit the defect sites observed in the coating. (c and f) show carbon distribution in the coating.

4.2.1.2. Pool boiling results

The pool boiling tests were conducted on the monolayer and multilayer samples using the experimental setup described previously. The tests were conducted with distilled water at atmospheric pressure. The distilled water was degassed to eliminate the influence of non-condensable gases. The nucleate pool boiling data was obtained until CHF was reached. Figure 57 shows the pool boiling curves obtained for monolayer and multilayer sample. For enhancement comparisons, the plain baseline chip was also tested and a CHF of 128 W/cm^2 at a wall superheat of 19 °C was obtained. The CHF obtained with the plain chip is compared with the Kandlikar CHF model [71] using a receding contact angle of 43°. The results agree well with a difference of 0.7%. The monolayer and multilayer samples reached a CHF of 149 W/cm^2 and 157 W/cm^2 respectively.

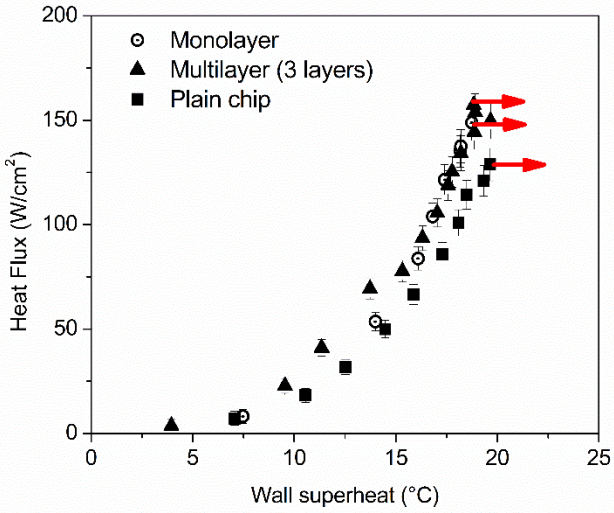

Figure 57. Pool boiling curves for (a) monolayer, (b) multilayer samples with distilled water at atmospheric pressure. The red arrows indicate CHF.

4.2.1.3. Enhancement mechanism at nanoscale

Effect of thermal conductivity:

Previous graphene based boiling studies have identified several enhancement mechanisms including thermal conductivity and wettability effects. Multiple reports [93,94] have shown that an increase in the number of layers results in a decrease in the thermal conductivity. Since we exercised control over the number of deposited layers, it is expected that the monolayer sample with the highest in-plane thermal conductivity will significantly improve the performance. Conversely, multilayer samples are expected to have lower thermal conductivities and relatively reduced performance. This is also in agreement with the FE-SEM images which show that monolayers have larger grain size, resulting in less phonon scattering (and therefore higher thermal conductivity) compared to its multilayer counterparts [93]. Furthermore Seo et al. [95] have shown that thermal conductivity can be explained by using thermal effusivity. The thermal effusivity (E) is given by,

$$E = \sqrt{\rho_h C_{ph} k_h} \tag{28}$$

where, ρ_h is the density, C_{ph} is the specific heat capacity, k_h is the thermal conductivity, and t_h is the thickness of the heater. Using theoretical values (ρ_h = 8,960 kg/m^3; C_{ph} = *376.81* J/kg; $k_{h,monolayer}$ = 5,000 W/m-K, $k_{h,multilayer}$ = 2,300 W/m-K [94]), the thermal effusivity is calculated to be 116210.45 J/m^{2}Ks$^{1/2}$ and 88120.94 J/m^{2}Ks$^{1/2}$ for the monolayer and multilayer samples, respectively. The calculated values show that the monolayer samples had a significantly higher effusivity than the multilayer samples. Therefore, the monolayer sample is expected to have a higher CHF. However as seen in Figure 57, the results show that the multilayer sample had a slightly higher CHF. Since this observed trend does not

explain the thermal conductivity effect, we eliminated thermal conductivity as an enhancement mechanism for the nanoscale coatings. This is in agreement with the conclusions drawn by Fan et al. [96] in their study.

Effect of liquid wettability:

Raj et al. [91] combined molecular dynamics simulations and experiments and showed that the advancing contact angles do not change significantly for monolayer and multilayer graphene. Large contact angle hysteresis as a result of defects on the surface were reported in their study. In this context, wettability changes have been reported previously as an enhancement mechanism for boiling with graphene colloids [62]. One of the successful CHF prediction models by Kandlikar [71] includes the effect of dynamic receding contact angle in the force-based equation to predict the CHF. Therefore, we measured the advancing and receding contact angles for the surfaces. To ensure repeatability, the average of 5 measurements was taken and this resulted in a receding contact angle value of 48.2° for the monolayer sample and 54.7° for the multilayer case. The corresponding advancing contact angles were 104° for both the samples. This is in good agreement with results reported by Raj et al. [91] who suggested that the advancing contact angle does not change with an increase in number of graphene layers. The contact angle hysteresis for the monolayer and multilayer samples were 55.8° and 49.3°, respectively. The standard deviation for all the measurements was less than 5%. The static contact angles were measured before and after the boiling tests. The measured values indicated an insignificant change in the contact angles ensuring that the surface wettability did not change after the boiling tests.

Contrary to previous reports that identify a range of contact angles varying between hydrophobic and hydrophilic wetting on the samples, here we observed a relatively small

change in the contact angles at different locations on the sample. However, contact angle hysteresis seems to play an important role in the enhancements. Although the receding contact angles are similar to that of copper-water systems (43°), the unusually large contact angle hysteresis seems to be the dominant factor in the underlying heat transfer mechanism. While measuring the static contact angles, the liquid droplet remained stable without being wicked into the coating, thereby eliminating wickability as an enhancement mechanism. This observation was consistent with previous reports where wicking was not observed [63]. In graphene and GO films that are at the nanoscale, we identify contact angle hysteresis as the enhancement mechanism. The hysteresis occurs due to the defects present on the coatings [91]. The authors postulate that the advancing and receding behavior of the liquid during bubble growth influences the contact line heat transfer and rewetting mechanisms which results in high heat transfer rates compared to a plain copper surface.

Another important consideration in this phenomenon is the interaction of the liquid with the underlying copper substrate. The consequence of depositing GO and graphene on bulk copper surfaces introduces roughness on the substrate. Rafiee et al. [92] demonstrated that the adsorption energy of water on copper coated graphene is significantly impacted by the number of layers. They further reported a threshold of 6 layers, beyond which the water droplet did not interact with the underlying substrate. Since the monolayer and multilayer samples had under 6 graphene layers, it can be considered as the case where the liquid interacted with the substrate. The interaction of the water droplet through the graphene and GO layers is expected to augment the wettability characteristics. The interlayer spacing in the case of multilayer is also expected to influence this behavior [91]. In conclusion, the grain sizes and the substrate-fluid interaction contribute to the contact angle hysteresis.

This mechanism resulted in a 17% and 22% increase in the CHF in the monolayer and multilayer samples, respectively.

4.2.2. Microscale coatings

The GO and graphene colloidal solution was prepared in an electrochemical cell in which cleaving of the graphite electrode and reduction of the resulting GO solution were carried out in a single step. An electrochemical process was employed to generate the solution in a single step using oxygen embrittlement. The cell consisted of graphite (2 cm x 2 cm; and a thickness of 0.70 cm) as the anode and the copper test chip (1.7 cm x 1.7 cm copper test section) as the cathode (Figure 58). The electrolyte consisted of carbon tetrachloride and deionized water. The percentage of carbon tetrachloride used for producing the graphene/GO solution was 10% by volume. A potential was applied between the electrodes which introduced a current density of 300 mA/cm^2. This current density was sufficient to cause the oxidation of water to produce oxygen at the graphite anode to cleave the surface into graphene. The gap between the cathode and anode was maintained at 1 mm by a Teflon spacer to hold the electrodes firmly in position. Electrical contact was established by insulated copper leads and a current meter. As a result of the process, the temperature of the bath increased from 293 K to 343 K.

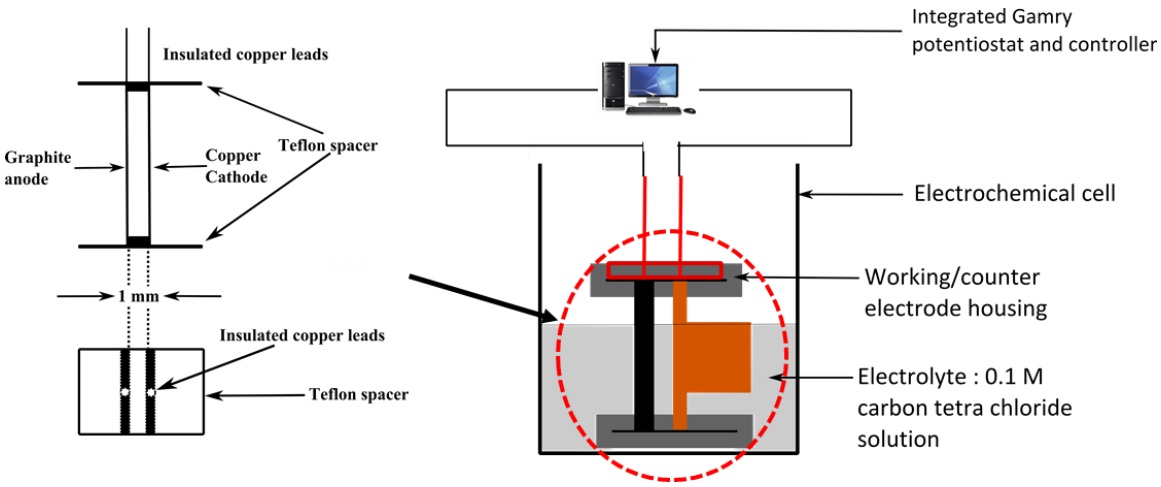

Figure 58. Electrochemical test setup assembly for the generation of GRAPHENE/GO.

4.2.2.1. Microscale surface developed

In order to generate a range of structures with different morphological features, the dip coating duration was varied between 2 and 20 minutes. A consolidated test matrix comprising of all the test surfaces used to evaluate the effect of surface features is shown in Table 9. The advancing, receding contact angles and the contact angle hysteresis measured for the surfaces is also listed in Table 9. In these samples, the number of layers are in excess of 6. Therefore, these can be considered as cases where the liquid does not interact with the copper substrate. We postulate that the primary reason for the large contact angle hysteresis is due to morphology of the different layers as a consequence of dip-coating. The CVD-GO_2min surface resulted in a non-uniform coating. The uniformity in coating is affected by the oxygen concentration in the two solutions (commercial CVD - GO and electrochemical RIT - GO solutions). The two solutions were prepared in different chemical environments which is expected to affect the adhesion characteristics on the surface.

Table 9. Test matrix with roughness values for microscale graphene coatings. R_a was measured using the surface profile analyzer and r was calculated as the ratio of the wetted area (sum of projected and additional surface area) to the projected area. The additional surface area was computed using the Keyence surface area analyzer with 3-D measurement features.

Test chip	Roughness (r)	Advancing contact angle	Receding contact angle	Contact angle hysteresis
CVD-GO_2min	Non-uniform	-	-	-
CVD-GO_5min	6.78	115.3	50.3	65.0
CVD-GO_10min	3.77	127.9	73.8	54.1
CVD-GO_20min	3.47	126.6	69.1	57.5
RIT-GO_2min	6.92	111.7	54.7	57.0
RIT-GO_5min	2.06	117.3	58.6	58.7
RIT-GO_10min	2.08	133.5	65.8	67.7
RIT-GO_20min	2.03	113.9	71.7	42.2

4.2.2.2. Morphological characterization of copper coated graphene/GO

The microscale coatings were achieved by dip-coating the copper substrates with the electrochemically generated (RIT - graphene/GO) and commercially available CVD-graphene/GO solutions. The RIT - graphene/GO solution was characterized to gain information on the size and zeta potential which is a measure of the colloidal stability of the samples. In a stable solution, the colloids remain dispersed for longer durations without forming aggregates or agglomerates that may prevent the formation of even coated layers. Visual inspection of RIT - graphene/GO solution vial showed no phase separation or agglomeration of graphene/GO particles in the vial for longer durations of time confirming the stability of the colloids. Similar to the nanoscale coatings, the compositional analysis of the two solutions were also obtained.

4.2.2.2.1. Dynamic Light Scattering

The stability and composition of RIT graphene/GO colloidal solution was investigated by

using DLS which is a widely used technique to estimate the average diameter of spherical shaped colloids. The average hydrodynamic diameter of the graphene/GO colloids were found to be 1000 nm (Figure 59). Graphene/GO colloids typically have large ratios of length to thickness in micro scale. The resultant size measurements of RIT - graphene/GO yielded convoluted results which are attributed to the lateral measurements of the graphene/GO sheets. From a general understanding of colloids, zeta potentials with absolute values larger than 30 mV can result in stable dispersions via mutual repulsion between the particles **[60,97,98]**. In the present study, the absolute zeta-potential value for the electrochemically synthesized graphene/GO oxide solution was found to be 60mV, reported as intensity-weighted z-averages based on 15 scans.

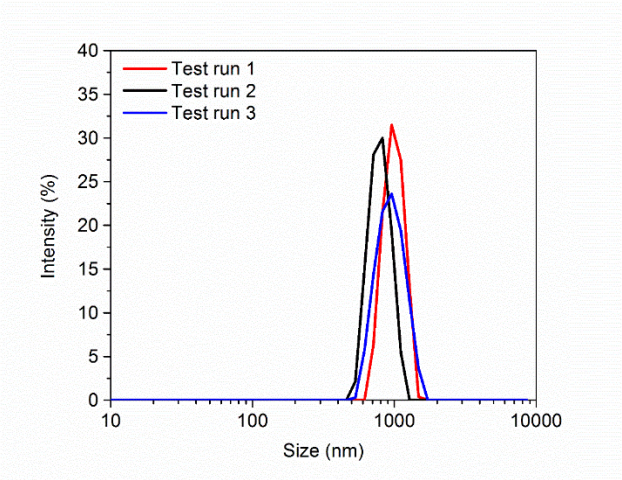

Figure 59. Graphene particle diameters measured suing DLS spectroscopy.

4.2.2.2.2. Thermogravimetry Analysis

The quantification of the composition of graphene/GO in the colloidal solution was obtained by thermogravimetric analysis by determining the loss of mass as a function of increasing temperature. The resultant thermograph shown in Figure 60 reveals the presence of both graphene/GO. The loss of mass observed at 100°C is usually associated with

removal of adsorbed water and gas molecules. The loss of mass at 200°C corresponded to the decomposition of GO, yielding CO and CO_2 as the byproducts. GO being less thermally stable, decomposes before pure graphene and is also reported **[89,99]**. The loss of mass at higher temperatures from 800° C corresponds to the remaining unstable carbon from graphene **[100]**. It is reported that complete decomposition of graphene occurs post 950°C, as seen in Figure 56. The thermogravimetric analysis confirms the chemical stability of graphene/GO coated on the copper substrates. No discernable chemical change was observed while heating between 100 – 130 °C, which replicates the temperature ranges generally observed with pool boiling studies with graphene. The percent composition by weight of GO was 12.5%.

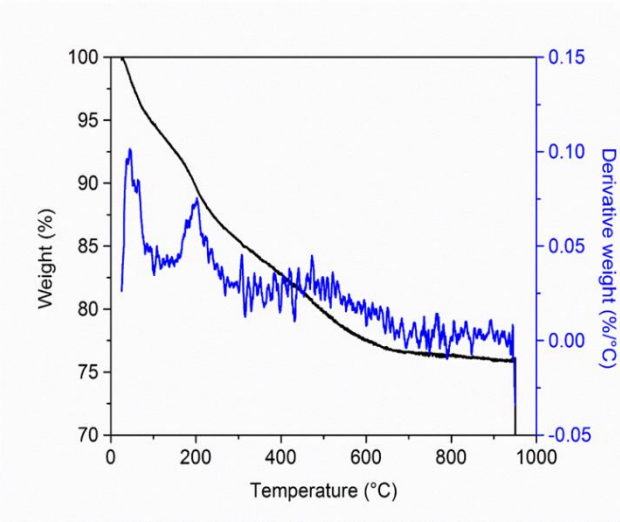

Figure 60. Thermogravimetry analysis of Graphene decomposition pattern through loss of mass.

4.2.2.2.3. Fourier Transform Infrared Spectroscopy

The FTIR spectroscopy spectrum of graphene/GO showed peaks at 3290 cm^{-1}, 1624 cm^{-1} and 1411 cm^{-1} as seen in Figure 61. The peak at 3290 cm^{-1} was attributed to O-H stretching from water. The peak was strong and it overlapped with C-H stretching at 2930 cm^{-1}. The peak at 1624 cm^{-1} was attributed to the presence of aromatic rings (C=C) and the peak at

1411 cm^{-1} was due to C-H bending. The aromatic CH_2 and C-O peaks overlap causing them to be absent in their expected locations. These results further indicate the presence of a carboxyl group in the graphene/GO coated on copper. The analysis of commercially available CVD-graphene/GO colloidal solution rendered similar size and compositional data.

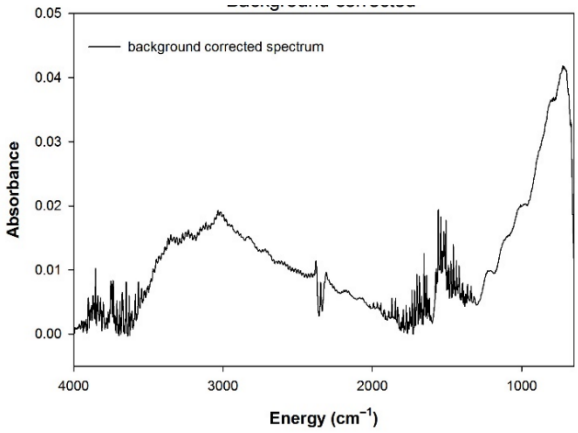

Figure 61. Fourier transform infrared spectroscopy of electrochemically produced RIT-GO solution.

4.2.2.2.4. X-Ray Diffraction

Material information on the chips was obtained using a Rigaku DMAZ-IIB XRD equipment. The graphene/GO solution was dip coated on the copper test section and allowed to dry. The XRD of the air dried sample is shown in Figure 62. GO has a characteristic two theta reflection arising from (002) plane that depends on the number of graphene layers and the distance between layers. Besides GO peaks (A, B and C), the other 2θ transitions are due to copper as reported in Joint Committee on Powder Diffraction Standards (JCPDS) Copper: data file # 04-0836.

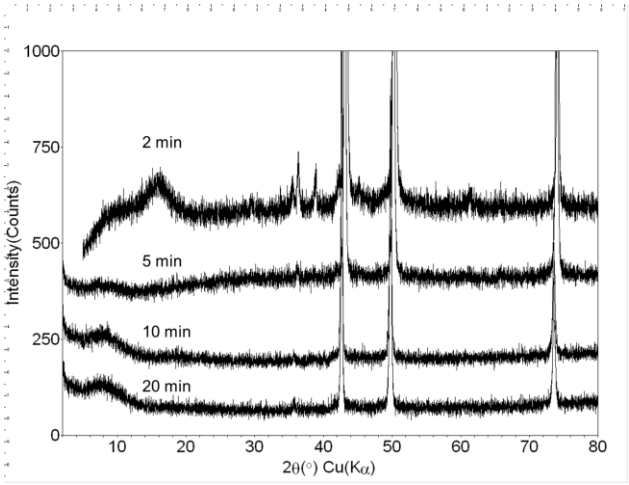

Figure 62. XRD pattern obtained on the samples.

4.2.2.2.5. Raman Spectroscopy

Raman spectroscopy data was obtained for 5, 10 and 20-min coated substrates. The Raman spectra verify the characteristic peaks of graphene/GO (1580 cm^{-1}) and a different in-plane vibration, D (1350 cm^{-1}). The 2D-bands are sensitive to the stacking order of the graphene layers along the z-axis, the disappearance of a 2D peak in Figure 63, verifies the disordering of graphene sheets also observed with XRD analysis (Figure 62). Such disordering along the z-axis is caused due to the alignment with respect to each graphene sheet and due to the presence of oxygenated functional groups due to GO in the sample. In addition to the wettability effects, the disordering is beneficial as it creates crevices or gaps on the surface which can act as potential nucleation sites.

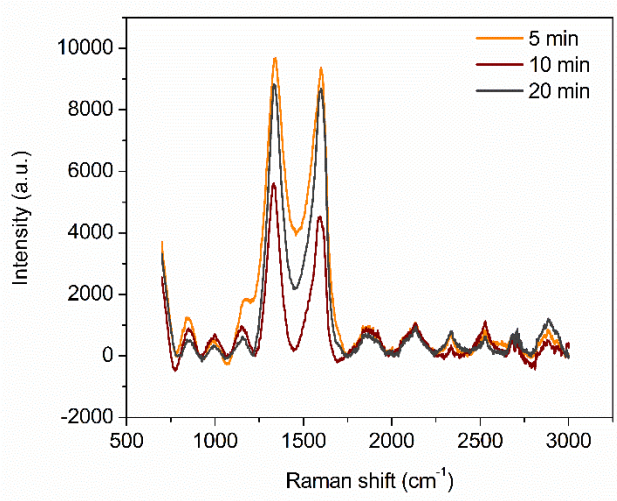

Figure 63. Raman spectroscopy on the electrochemically generated samples.

4.2.2.2.6. Scanning Electron Microscopy

Figure 64 summarizes the various morphologies of the RIT graphene/GO oxide coatings on the copper test section achieved for different dip-coating durations. The substrate with the shortest coating duration of 2-min exhibited mixed morphology which comprised of flakes and granule-like structures extended on the copper substrate, as seen in Figure 64. Further observation at higher magnification and 70° stage tilt (Figure 60a) showed the presence of ridges that are approximately 11 µm tall. The ridges are shown to act as liquid reservoir slabs through which the microlayer evaporation is enhanced. The microlayer increases the nucleation activity on the surface and hence the heat flux dissipation. Additionally, these type of structures create roughness and wettability changes at the microscale. In the case of 5, 10 and 20-min coated substrates (Figure 60b-d) the granule like structures were seen predominantly and with increased coating durations, a tighter packing of these granules were observed. These tighter packings appear as a laminated film which is expected to deteriorate the heat transfer performance due to lack of morphological features. This trend was confirmed by the low CHF values reported for longer dip-coating

durations as reported in the previous sections. Figure 64d represents the image obtained for 20-min coated substrates generated by tilting the microscope stage to 70 indicating that the shorter granular structures (less than 1μm in height) result in a smoother surface profile. This was also corroborated by the surface roughness measurements (R_a) that were conducted using a confocal laser scanning microscope. The average surface roughness measured for the shorter coating duration was ~10 μm, while it was less than 1 μm for the longer coating duration.

A number of reports have shown the importance of morphology to the pool boiling performance. Typically in the microscale coatings, the morphology appears as roughness structures with a range of multiscale cavities. A closer examination of the SEM results show that the longer dip-coating duration resulted in tighter packing of the graphene/GO coatings which creates a smooth laminated film lacking roughness features which results in lower CHFs. The shorter coating duration results in distinct ridge microstructures which are capable of trapping a thin liquid film that promotes bubble formation.

Figure 64 also illustrates the SEM-EDS analysis of carbon, oxygen and copper elements that were present on the substrates coated at various time durations. The copper is from the underlying substrate, while the oxygen is due to oxidation of the sample. A decrease in intensity is depictive of copper from ~10,000 counts to 8,500 counts for 10-min and 20-min coated samples respectively, whereas the intensity of carbon peak for 5-min coated substrate was observed to be slightly higher than 10 and 20-min coated. This difference in intensities of copper and carbon peaks probably stem from the presence of taller graphene ridges that could have been more easily detected by the electron beam than the flatter carbon structures.

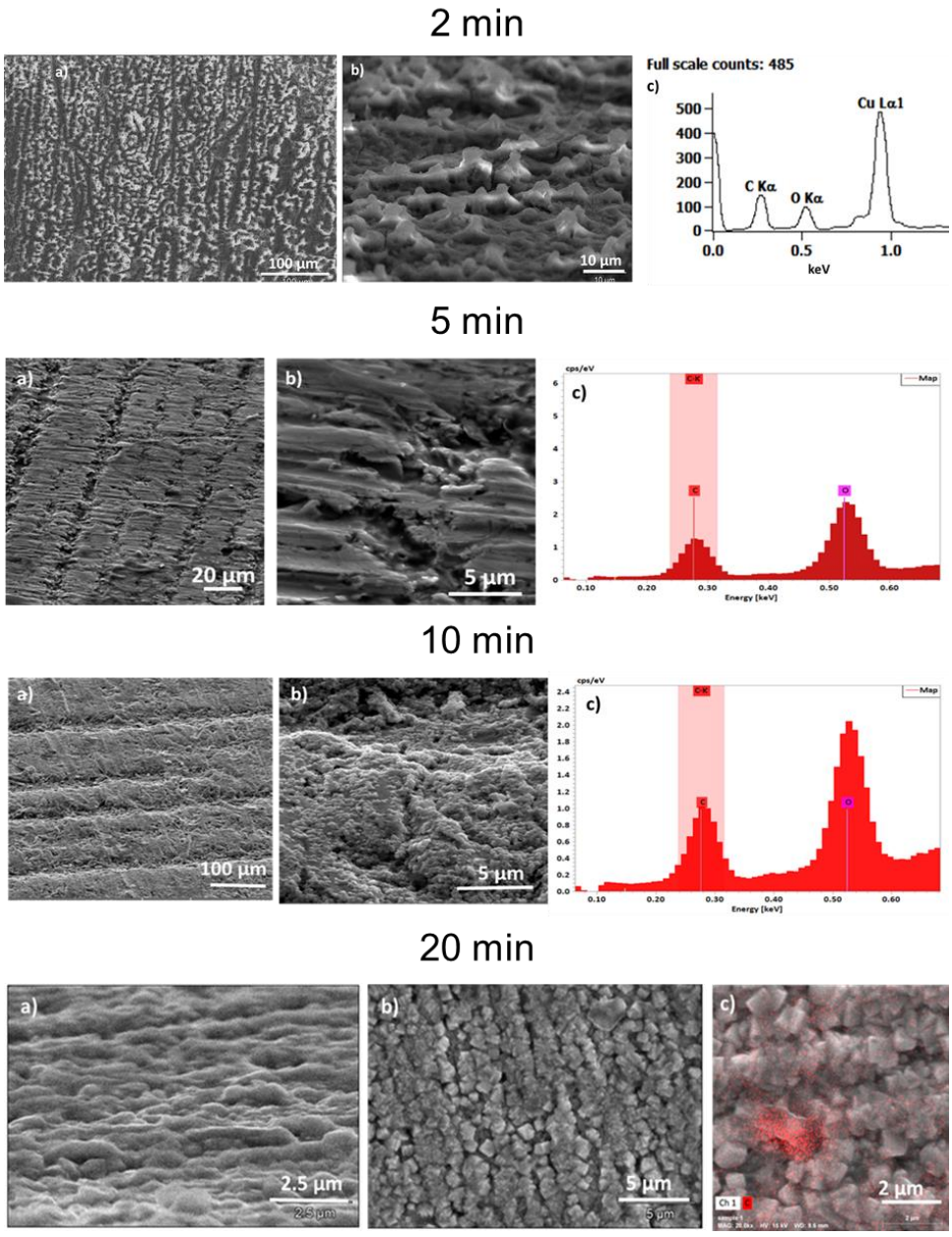

Figure 64. SEM images of the samples with their corresponding EDX analysis.

4.2.2.3. Pool Boiling Results with microscale coatings

Figure 65a shows the pool boiling curves obtained with GO/graphene surfaces. Chip 1 reached a CHF of 182 W/cm^2 at a wall superheat of 19 °C. This translated to an enhancement of 42% in CHF compared to a plain chip. Chip 2 had a CHF of 128 W/cm^2 while chip 3 and 4 had CHF of 124 W/cm^2. The CHF of chip 2, 3 and 4 are very close to

the baseline chip indicating that the dip coating process resulted in multiple layers of graphene and GO being deposited. Closer examination of the results revealed that thinner coatings performed better than thicker coatings.

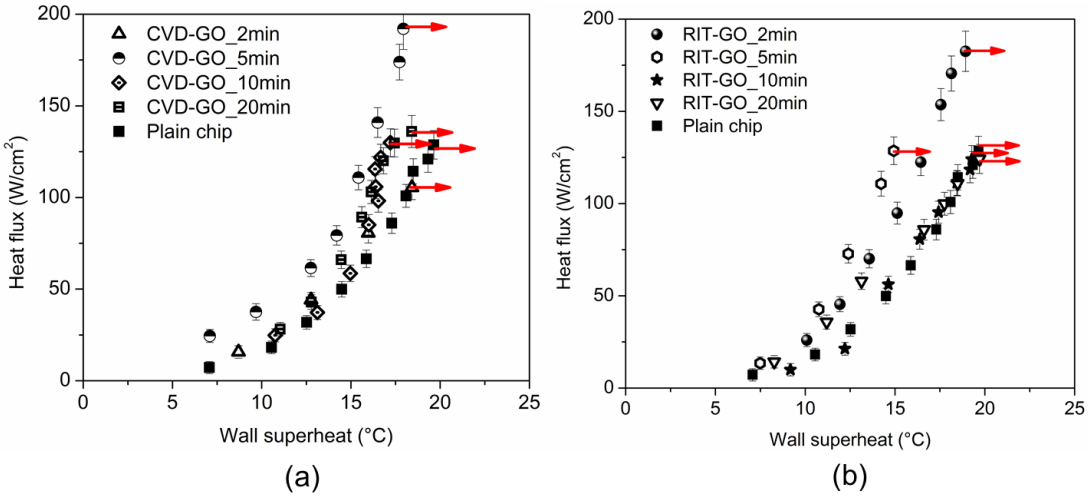

Figure 65. Pool boiling curve for (a) CVD solution, (b) RIT solution with distilled water at atmospheric pressure. The red arrows indicate CHF.

Figure 65b shows the pool boiling curves for the commercial CVD-GO solution. CVD-GO_2min had non-uniform coating and reached a CHF of 100 W/cm^2. CVD-GO_5min reached a CHF of 192 W/cm^2 which was the highest performing surface in the tested matrix. CVD-GO_10min and CVD-GO_20min reached a CHF of 129 W/cm^2 and 136 W/cm^2, respectively, which were comparable to that of a plain chip. The HTC values at CHF for CVD-GO_2min, CVD-GO_5min, CVD-GO_10min and CVD-GO_20min were 57 kW/m^2°C, 107 kW/m^2°C, 75 kW/m^2°C and 73 kW/m^2°C, respectively. To compare the results, the pool boiling curves obtained with RIT-GO solution as shown in Figure 65(b). The boiling curve obtained with RIT-GO shows that the highest CHF was observed with the RIT-GO_2min coating. Dip coating for a duration of 2 minutes with RIT-GO solution

yielded uniform coatings which was confirmed by observing under the confocal laser scanning microscope.

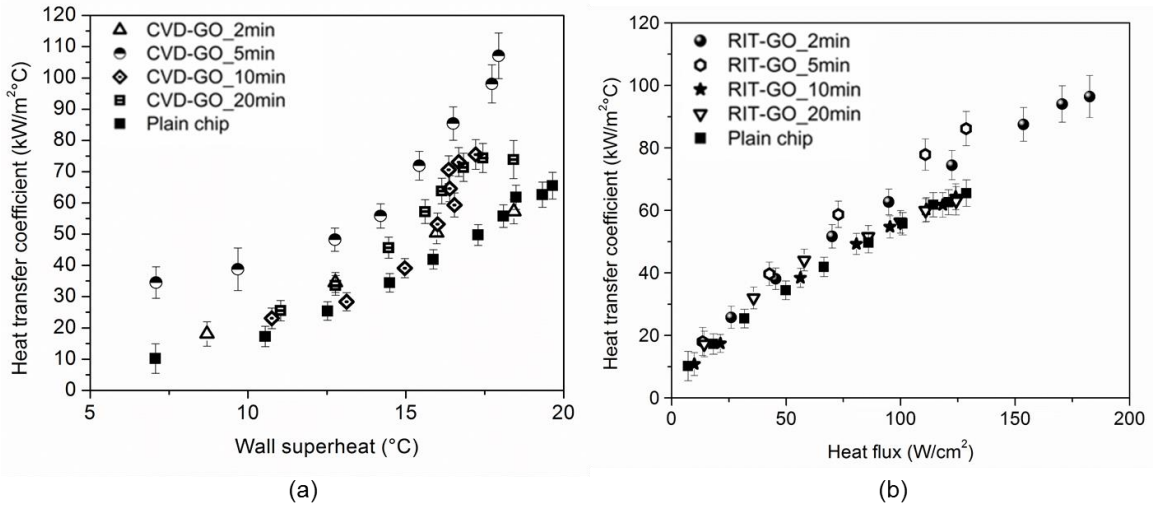

Figure 66. Heat transfer performance of RIT graphene/GO and CVD graphene/GO.

Figure 66b shows the heat transfer performance plot where the HTC is plotted against the heat flux. The capability of a surface to efficiently dissipate heat can be established from this plot. The general trend indicated that HTC increased with wall superheat. The shorter coating durations exhibiting uniform coatings and ridge morphologies, resulted in higher CHF and HTCs.

4.2.2.4. Enhancement mechanisms at Microscale

Effect of roughness

The effect of large contact angle hysteresis is apparent in the case of dip-coated surfaces and is in the similar range observed with the nanoscale coatings (monolayer and multilayer samples). However, since the contact angle hysteresis is due to the morphology of different layers on the sample and the pool boiling performance is different, we identify morphology-induced mechanisms as the contributing mechanisms. Furthermore, the

performance characteristics for the nanoscale coatings were significantly different from the microscale cases. Therefore, we directed our analysis towards surface features on the coatings through two mechanistic explanations *(i)* roughness effects, and *(ii)* microlayer evaporation since liquid wettability did not explain the enhancement entirely. The currently established trends in literature suggests that an increase in roughness is expected to increase the CHF [101]. The Kandlikar model [71] was modified to include the effect of roughness of the heater surface [101]. The equation used to predict the CHF based on roughness augmented structures is given by,

$$q''_{CHF} = K \times h_{fg}\rho_g^{1/2}\left[\sigma_{lv}g\left(\rho_l - \rho_g\right)\right]^{1/4} \tag{29}$$

where,

$$K = \left(\frac{1+cos\beta}{16}\right)\left[\frac{2(1+\alpha)}{\pi(1+cos\beta)} + \frac{\pi}{4}(1+cos\beta)cos\varphi\right]^{1/2} \tag{30}$$

and,

$$\alpha = rcos\beta \tag{31}$$

The additional term (1+ α) in Eq. (29) was added by Chu et al. [101] to account for the surface roughness effect in the Kandlikar model. The roughness parameter (*r*) was calculated as the ratio of wetted area to the projected area. The model proposed by Chu et al. [101] was successfully extended to non-uniform roughness coatings here. Figure 67 shows the variation of CHF with respect to the roughness. The model developed by Chu et al. [101] is also shown (dotted line) in the plot. This model clearly captures the trend observed in the samples tested here where an increase in the roughness is shown to increase the CHF. The model successfully predicts the CHF for the longer dip-coating duration (5-20 min) samples. In the cases of shorter coating durations, the experimental data markers are clear outliers when compared to that predicted by the model. Therefore, it can be said

that roughness is one of the promoters for the enhancement but additional mechanisms were further responsible for the enhancement observed in short coating duration samples.

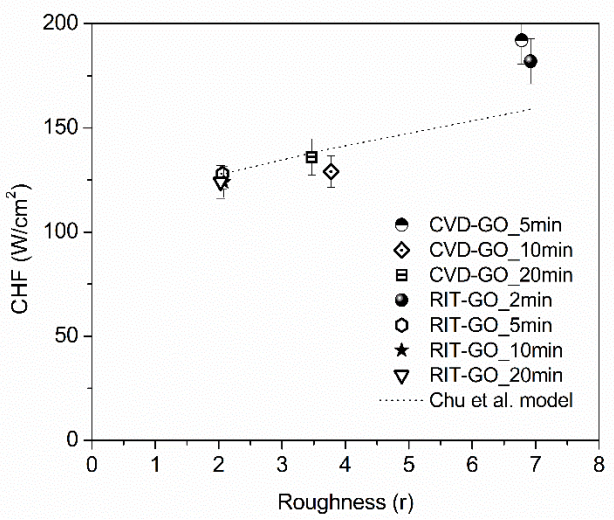

Figure 67. Effect of roughness on CHF for the samples developed in this study and comparison with the roughness CHF model by Chu et al. [101].

To evaluate the mechanism further, a careful examination of the surface features was conducted using a TESCAN Field Emission Mira III LMU SEM. Figure 68 shows the SEM images for short (< 5 min) and long coating (5-20 min) durations. In the case of coating durations between 5-20 min (Figure 68c and d), the roughness values are low and in some cases (RIT-GO_20min and CVD-GO_20min) lower than that of the roughness of underlying copper. This indicated that the cavities contributing to the roughness on the copper were filled resulting in a *smooth, laminated film* on dip coating for longer durations. The terms smooth and laminated arise due to the low roughness and low CHF values reported for these surfaces. For the shorter coating durations (<5 min), the surface effect is more pronounced where randomly distributed ridges are observed as shown in Figure 68a & b. The structures with the ridges result in the highest performances. Therefore, we directed our study towards analyzing the coatings as ridge microstructures.

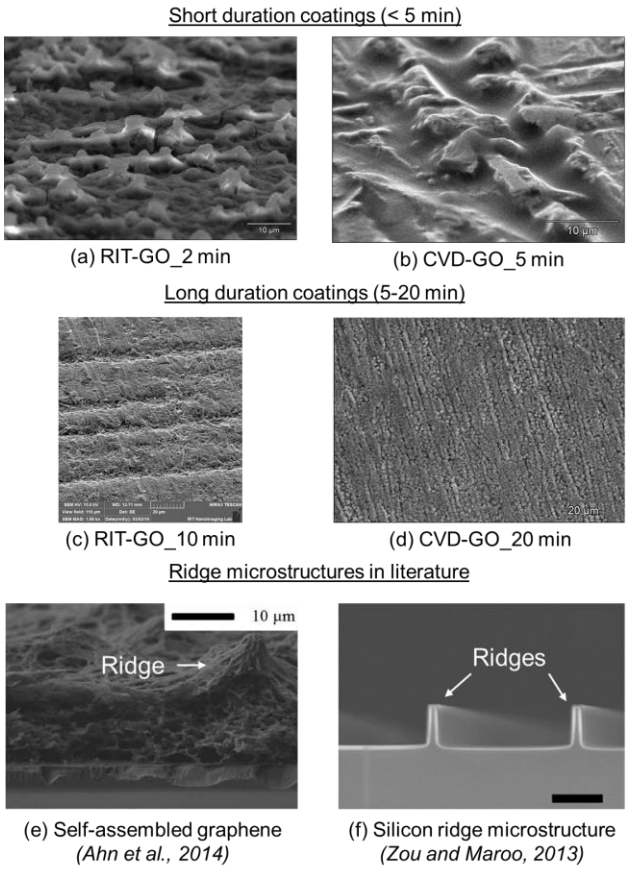

Figure 68. SEM images of (a) RIT-GO_2min, (b) CVD-GO_5min, (c) RIT-GO_10 min, and (d) CVD-GO_20 min (d) ridge microstructures as a consequence of self-assembled graphene during nanofluid boiling [62], and (e) ridge microstructures fabricated by Zou and Maroo [46].

Enhanced microlayer evaporation

The microlayer is a thin liquid film that forms underneath a growing bubble. Recently, Zou and Maroo [46] employed ridges as an enhancement structure and demonstrated that the fragmentation of the microlayer in the form of discrete ridges resulted in additional evaporation of the microlayer liquid film underneath the bubble. This caused an increase in bubble growth rate leading to an increase in CHF values which was confirmed by an analytical model. Additionally, they also demonstrated that an enhancement in CHF was achieved when the microlayer thickness was less than the ridge heights which enabled partitioning of the microlayer into slabs.

The receding contact angles measured on the dip coated surfaces were also between 45°-50° and did not contribute to the enhancement as mentioned earlier. This pointed towards enhanced microlayer evaporation due to ridges as seen from the SEM images. The consequence of a ridge microstructure is the early evaporation of the partitioned microlayers and increased bubble growth rates [46].

For the RIT-GO_5min surface, the interplay between the ridge heights and spacing results in partial enhancement, similar to that proposed by Zou et al. [47]. This translates as an enhancement in HTC in this surface. To evaluate the effect of microlayer evaporation further, an isolated bubble was analyzed from nucleation to departure at low heat flux values (<15 W/cm^2) on the best performing dip coated samples (RIT_2min and CVD_5min). Here we focused on the inertial bubble growth. Due to availability of microlayer, we postulate that the inertial region will be affected by the fragmentation of the microlayer as demonstrated by Zou and Maroo [46]. A Photron FASTCAM® high speed camera was used to obtain images. Figure 69 shows a plot of the variation of bubble radius with time for the best performing chips with dip-coating on copper substrates with *(i)* CVD-GO, *(ii)* RIT-GO solutions, and (iii) a plain chip, obtained at a wall superheat of 5-6°C. In addition, the bubble radius predicted using Mikic et al. [11] model is also plotted.

As seen in the plot, the enhancement due to microlayer is apparent in the case of CVD-GO_5min and RIT-GO_2min which showed large bubble sizes (hence larger volume and growth rates) compared to that of a plain chip (Mikic's model [37]). This effect can be attributed to the ridge microstructures which resulted in partitioning of microlayer. This indicated enhanced evaporation from microlayer due to the partitioning induced by the ridges at the bubble base. A second-order polynomial fit was established for the data

markers representing CVD-GO_5min and a plain chip which suggested that during the initial phase (0.2-0.6 ms), the bubble growth rate on the dip coated samples is almost twice than that on a plain chip.

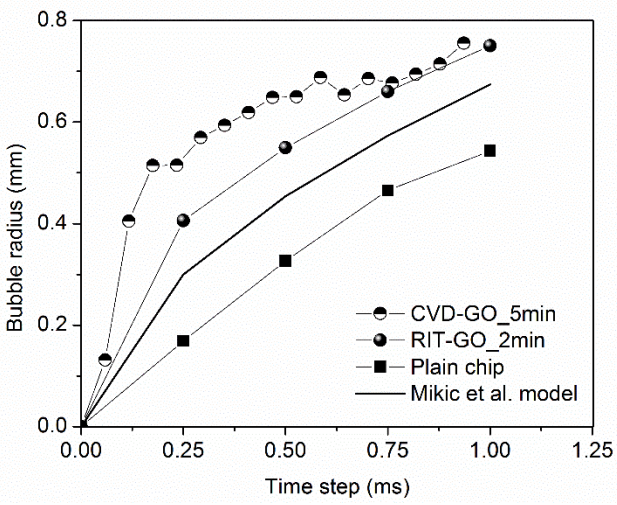

Figure 69. Bubble growth rate for the best performing surfaces compared with Mikic et al. model [11].

Preliminary estimation of fragmented microlayer contribution to total heat flux

The contribution from microlayer mechanism to the total heat transfer has been estimated by previous researchers to be in the range 15-25 percent, e.g. [8,102]. Moghaddam and Kiger [8] estimated that the microlayer contribution at CHF was approximately 18 percent of the total heat flux, based on his experiments. Utaka et al. [103] performed a series of experiments with water and ethanol to determine the microlayer thickness based on the radial distance from the nucleation site. Therefore, for the measured bubble departure radius (0.8 mm) in this study, the maximum microlayer thickness was estimated to be 3 μm (extracted from Figure 14 in Ref. [103]). We estimated the scale of enhancement due to ridge partitioning to be influenced by the extra microlayer volume available for

evaporation. This extra volume depends on the ridge heights. The scaled heat flux can be calculated as follows,

$$q''_{microlayer\ partioning} = q''_{plain\ chip} - 0.18 \times q''_{plain\ chip} + 0.18 \times q''_{plain\ chip} \times \left(\frac{ridge\ height}{intial\ microlayer\ thickness\ on\ a\ plain\ chip}\right) \quad (32)$$

In the above equation, the microlayer contribution was assumed to be 18 percent and the ridge heights were estimated to be ~11 µm from the SEM (Figure 68a-b) images. The CHF estimated using this equation was 181 W/cm^2 which agrees well with CHF obtained with CVD-GO_5min (192 W/cm^2) and RIT-GO_2min (182 W/cm^2). Further understanding of the mechanism is required to develop a comprehensive model.

4.3. Summary and conclusions of enhancement with nanoscale and microscale graphene/GO coatings

The CHF obtained for nanoscale (mono and three layered substrates) and microscale coatings obtained via dip coating of electrochemically generated and commercially available graphene/GO solutions are summarized in Figure 70. In case of monolayer and multilayer (3 layers) coating the resultant CHF enhancements were found to be 149 W/cm^2 and 157 W/cm^2 respectively which was ~20% more than that of plain copper chip (128 W/cm^2). The microscale coatings with shortest coating time of 2-min rendered a CHF enhancement of 182 W/cm^2 which was ~45% as compared to a plain copper chip. The variation in the CHF values for different graphene coated substrates and enhancements in case of microscale coatings are attributed to the surface features arising from roughness modifications, enhanced microlayer evaporation, and wettability effects. The enhancement observed with nanoscale coatings was attributed to the liquid wettability and larger contact

angle hysteresis that plays a pivotal role in the case of coatings comprising of few layer graphene sheets that lack microscale roughness features. The microscale coatings contributed to a variety of morphologies of varying thickness (or heights) as illustrated in Figure 68. As discussed previously, the 2-min dip-coating of electrochemically generated RIT - graphene/GO substrate delivered taller ridge-like structures that extended on the copper surface creating a rough surface profile as compared to longer duration coated samples. The enhancement in CHF for 2-min coated samples is attributed to the combined effects of contact angle hysteresis, roughness and enhanced microlayer evaporation as supported by the heat transfer analysis investigation using optical and microscopy techniques in addition to correlating with models as demonstrated.

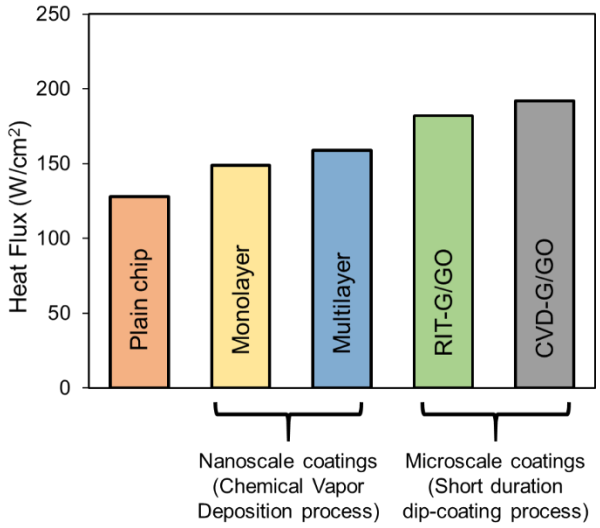

Figure 70. Summary of enhancements obtained through nanoscale and microscale coatings.

The chemical characterization results are linked to the pool boiling enhancement mechanisms. A key finding of this work is the difference in the morphologies and the mechanisms that determine the varying pool-boiling performances of multiscale substrates as summarized in Table 10. This table illustrates the benefits of the monolayer, multilayer,

and dip-coated samples that can be exploited for pool boiling enhancement. Based on the characterization data provided in the present work, it is concluded that the nanoscale coatings benefit from wettability changes and additional nucleation sites, while the microscale coatings were influenced by the multiscale roughness features and ridge microstructures.

Table 10. Summary of property-structure-characterization to the boiling performance enhancements on graphene structures.

Surface	XRD	TGA	FTIR	Raman	SEM	Enhancement mechanisms
Monolayer	--	Chemically stable in the boiling temperature ranges	Presence of carboxyl and aromatic compounds influencing local wettability	High intensity G peak due to presence of wrinkles	Wrinkle sheets through thermal deformation of the underlying copper substrate	Large contact angle hysteresis due to wrinkled sheets
Multilayer	Interlayer distance controls the degree of wrinkle formation	Chemically stable in the boiling temperature ranges	Presence of chemical compounds (carboxyl, aromatic rings, etc.) influences local wettability	Three layers with broad 2D peak indicating stacking disorder	Wrinkle sheets with disordered layers	Wettability affects through large contact angle hysteresis Additional nucleation sites from stacking disorder
Long duration dip-coating	Broad peaks comprising of densely packed carbon	Chemically stable between 100- 130 °C	Carboxyl and aromatic rings influence local wettability	Parallel and perpendicular alignment of carbon material	Tightly packed granules appearing as a Laminated film	Lacks morphological features that contribute to the enhancement

Short duration dip-coating	Broad peaks due to disordered carbon materials	Chemically stable between 100- 130 °C	--	Morphological features induced by disordering of layers	Ridges microstructures	Multiscale roughness features Ridges act as water retaining slabs for enhanced microlayer evaporation

4.4. Microscale morphological effects of copper-GO coatings on the pool boiling characteristics

Enhanced pool boiling heat transfer, with simultaneous increase in both critical heat flux (CHF) and heat transfer coefficient (HTC), is desired to improve overall system efficiency and reduce equipment size and cost. This section focuses on different techniques associated with generating enhancement structures based on their ability to enhance HTC, CHF or both. Specific microscale morphologies were generated with copper and GO coatings using (a) screen-printing and (b) electrodeposition techniques. The main understandings of the enhancement mechanisms achieved with nanoscale and microscale graphene/GO is incorporated here.

4.4.1. Concept and hypothesis

In this work, we categorize the boiling characteristics based on the increase in CHF and decrease in wall superheats (Figure 71). Three distinct boiling characteristics identified here are

1. *Type-I:* In this type, the surfaces exhibit a decrease in wall superheat without significant increase in CHF. The CHFs obtained on these surfaces are similar to that on the baseline surface.

2. *Type-II:* In this type, the surfaces exhibit an increase in CHF without significant reduction in wall superheats. The wall superheats obtained on these surfaces are similar to that on the baseline surface.
3. *Type-III*: In this type, the surfaces exhibit an increase in CHF with a simultaneous decrease in wall superheats. These type of surfaces are extremely beneficial as they offer increased operating ranges as well as efficient heat transfer.

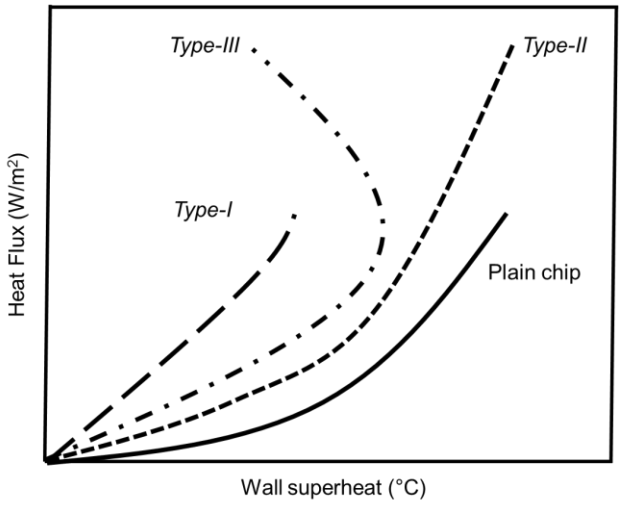

Figure 71. Schematic representation of the three boiling characteristics identified in this study. Type-I: Reduced wall superheat (increase in HTC), Type-II: Increased CHF without reduction in wall superheat, and Type-III: Increased CHF with reduction in wall superheat (increase in HTC) at higher heat fluxes.

Controlled experiments were conducted to demonstrate the three boiling characteristics identified in Figure 71. Increasing evaporation rates from the microlayer under a bubble has been found to increase the boiling performance by [47,104,105]. This can be achieved by increasing the microlayer volume under a growing bubble [24,46]. Wick structures utilize the irregularly shaped matrix around curved interfaces to contain the extra volume for evaporation. These structures significantly increase the CHF by preventing dry-out

condition due to liquid retention in the wick structure. On the other hand, non-wicking graphene coatings have shown to increase CHF by wettability changes and microlayer partitioning mechanisms. Therefore, the current work focuses on combining porous structures with graphene coatings to demonstrate the three boiling characteristics identified through morphology-driven effects. Typical graphene-based coatings are considered to be non-wicking. However, additional dynamics of the wick structure such as the mixed wettability of GO and copper is expected to significantly alter the performance characteristics and is evaluated in this paper.

4.4.2. Surface preparation and methods

The heat transfer surfaces were prepared by combining copper and GO coatings using two coating techniques: *(i)* screen printing, and *(ii)* electrodeposition. Sintered [35,106] and electrodeposited [107] porous copper particles are shown to increase the nucleation site density and wickability by enhancing thin film evaporation. A combination of microscale surface morphologies using copper and graphene coatings are generated here and their pool boiling performance with distilled water at atmospheric pressure is investigated. The details of the coating techniques are described next.

4.4.2.1. Screen printing

Screen printing is a widely used technique employed in the industry to create uniform coatings between 5-50 μm. In this study, the GO solution was mixed with copper particles to create a paste. The GO solution was prepared using a simple electrochemical liquid exfoliation technique using an oxygen embrittlement liquid-exfoliation technique [108]. The average hydrodynamic diameter of the GO colloids were found to be 1000 nm using Dynamic light scattering (DLS) instrument. Hydrodynamic diameter was measured by

placing 1 mL of sample in 10 x 10 x 45 mm quartz cuvettes with 120 s equilibration time. The average hydrodynamic diameters were based on 11 scans and three measurement cycles. The chemical stability of the coatings was confirmed using Energy Dispersive Spectroscopy (EDS) data. The presence of carbide, which is indicative of any reactions with the copper substrate, was not observed in the samples.

Table 11. Test matrix developed with a screen-printing technique.

Test chip	% GO (by mass)	Contact angles		
		Receding	Advancing	Hysteresis
Plain chip	-	43	100	57
SP-1	0.2	13.5	69.8	56.3
SP-2	0.4	10.6	81.8	71.2
SP-3	0.6	18.3	117.8	99.5
SP-4	1.0	18.4	118.5	100.1

The GO was combined with the copper particles (mean particle size = 15 μm) commercially obtained from 3M. Four test chips (SP-1 – SP-4) were generated by varying the amount of GO in the coatings while keeping the amount of copper constant on all the surfaces. A paste was created by adding a commercially available screen printing binder (Nazdar 9627) and subsequently mixing it using a micromixer (Thinky® micromixer). The amount of binder added was constant in all the cases. The coating thickness was measured using a confocal laser scanning microscope at the edge location of the test chip separating the coated and non-coated regions. To exercise close control over the coating thickness, a single-pass screen printing process was used similar to the previous studies in Chapter 5. The coating thickness was ~35 ± 3 μm for all the surfaces. Substrate bonding was achieved using a sintering process similar to that reported previously. The sintering temperature was 800 °C for a duration of two hours in an inert Helium atmosphere. An intermediate step in the sintering process was introduced to eliminate the binder from the coatings. This was

achieved by holding the single-zone furnace temperature at 450 °C for a duration of 1 hour. The Fourier Transform Infrared Spectroscopy (FTIR) results presented in Figure 68 confirm the elimination of other materials from the coatings and is described in detail later. The static, advancing and receding contact angles and contact angle hysteresis for these surfaces are shown in Table 10.

4.4.2.2. Electrodeposition

Electrodeposition is a simple technique which involves ion reduction at cathode by passing direct current through the solution. Patil and Kandlikar [23,107] used a two-step electrodeposition technique to coat porous copper particles on a copper substrate. A similar arrangement was used in this study. Copper and graphite electrodes formed the cathode and anode, respectively. The electrolyte consisted of 0.8M copper sulphate solution and 1.5M sulfuric acid. GO solution was subsequently added to the bath. Two electrochemical methods were employed (a) galvanostatic – constant current density, and (b) chronoamperometry – constant potential. The evolution of hydrogen bubbles during the process is shown to create dense porous matrices. The hydrogen bubbles serve as template structures. In the galvanostatic process, the volumetric composition of GO was varied between 1-2.5% in the bath to generate the test surfaces (GS-1 - 4). A two-step deposition process involving deposition for 15 s, and substrate bonding for 2400 s was employed. This results in a coating thickness of ~45 ± 4 μm for the samples generated using this technique. For the chronoamperometric process, the deposition time was varied between 500-1500 s which resulted in a coating thickness of 40 ± 6 μm. A summary of the test surfaces and their respective contact angles and hysteresis is shown in Table 12.

Table 12. Test matrix and surface details developed using electrodeposition techniques (chronoamperometry and galvanostatic).

Electrochemical method	Test chip	% GO (by volume)	Deposition time (s)	Contact angles		
				Receding	Advancing	Hysteresis
	Plain chip	-	-	43	100	57
Galvanostatic (GS)	GS-1	0.5	Step-1: 15 Step-2: 2400	22.4	58.1	35.6
	GS-2	1		14.3	36.4	22.1
	GS-3	1.5		13	33.6	20.6
	GS-4	2.5		13.5	42.6	29.1
Chronoamperometry (CA)	CA-1	2.5	500	48.5	125.6	77.1
	CA-2		1000	35	95.4	60.4
	CA-3		1200	32.4	87	54.6

4.4.3. Chemical characterization of heat transfer surfaces

4.4.3.1. FTIR

A Fourier transform infrared (FTIR) spectroscopy (Shimadzu IR Prestige 21) was used to confirm the presence of GO on the substrate. Figure 72 shows the absorption peaks arising from the molecular vibrations of functional groups associated with the coatings. The plot represents the light absorbance by the molecules as a function of wavelength. The characteristic peaks of C=O including stretching vibration of carboxyl group at 1726 cm^{-1}, O-H deformation vibration resulting from C-OH at 1390 cm^{-1}, and C-O stretching vibration at 1032 cm^{-1} was observed here. The peak at 1570 cm^{-1} corresponding to the presence of aromatic rings (C=C) is also seen. The broad peak between 3400-3100 cm^{-1} is attributed to O-H stretching from water vapor. The C=C, C=O, C-OH peaks confirm the presence of GO on the surface.

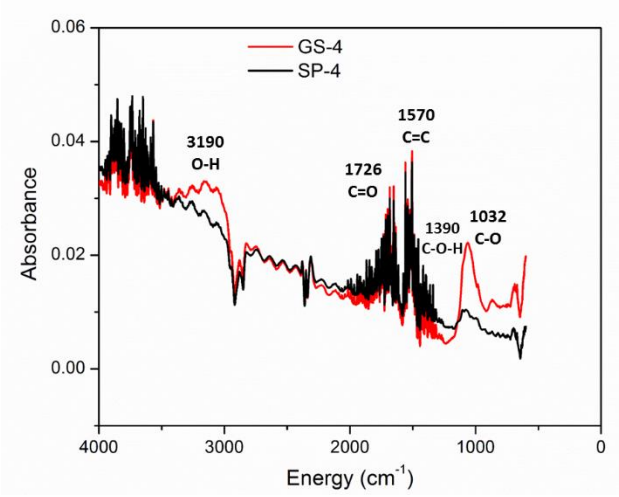

Figure 72. FTIR spectrum for the screen-printing and electrodeposition samples.

4.4.3.2. Contact angles

The effect of contact angle on the pool boiling CHF was modeled by Kandlikar [26] in his CHF equation. Numerous graphene based studies [95,109] have also highlighted that the wettability played a significant role in the performance. Therefore, the advancing and receding contact angles were measured on the developed surfaces. Raj et al. [91] have shown that the advancing contact angles are a true representation of the surface wettability on graphene structures. The receding contact angles are dominated by variations caused due to surface defects. In this study, the porosity created by the coatings is expected to amplify the effects due to defects. Therefore, the advancing contact angle and contact angle hysteresis, defined as the difference between the advancing and receding contact angles, are used to compare the surface wettability effects.

Comparison of advancing contact angles:

In the screen-printed (SP-1 – SP-4) copper-graphene surfaces, the advancing contact angles lie between 60 – 120°. Also an increasing trend in the advancing contact angles with GO composition is seen (see Table 12). The advancing contact angles in the

chronoamperometry cases were between 87-126°. In the case of galvanostatic electrodeposited samples, the advancing contact angles are lower than 60°. In this data set, the contact angle decreases with an increase in graphene composition. The microscale morphology is postulated to have a significant bearing on the contact angles as seen by the relatively low contact angles with the galvanostatic samples which is discussed in detail later.

4.4.4. Pool boiling results and discussions

Pool boiling performance of all the test surfaces shown in Tables 11 and 12 were investigated. The primary objective of this study was to study the effect of combining porous coatings and graphene in a systematic manner. To serve as a baseline, a plain copper chip was also tested. It resulted in a CHF, and HTC at CHF, of 128 W/cm^2 and 65 kW/m^2°C, respectively. Additionally, a plain copper surface coated with porous copper (without GO) under similar conditions was also experimentally tested. This resulted in a CHF of 140 W/cm^2, 140 W/cm^2 and 122 W/cm^2 for screen-printed, chronoamperometry and galvanostatic coating techniques, respectively. The corresponding wall superheats at CHF were 9 °C, 11 °C and 18 °C, respectively.

4.4.4.1. Pool boiling tests on screen-printed surfaces – Type-I enhancement

Figure 73a shows the pool boiling curves for the chips prepared using screen-printing. The coatings consisted of sintered-copper and GO. The amount of GO was varied from 0.2% - 1%. The CHF, defined as the upper nucleate boiling limit, was similar to that of a plain chip for all the tests surfaces investigated here. A drastic reduction in the wall superheat is observed for all the surfaces investigated. The wall superheats reported for the test chips were less than 10 °C.

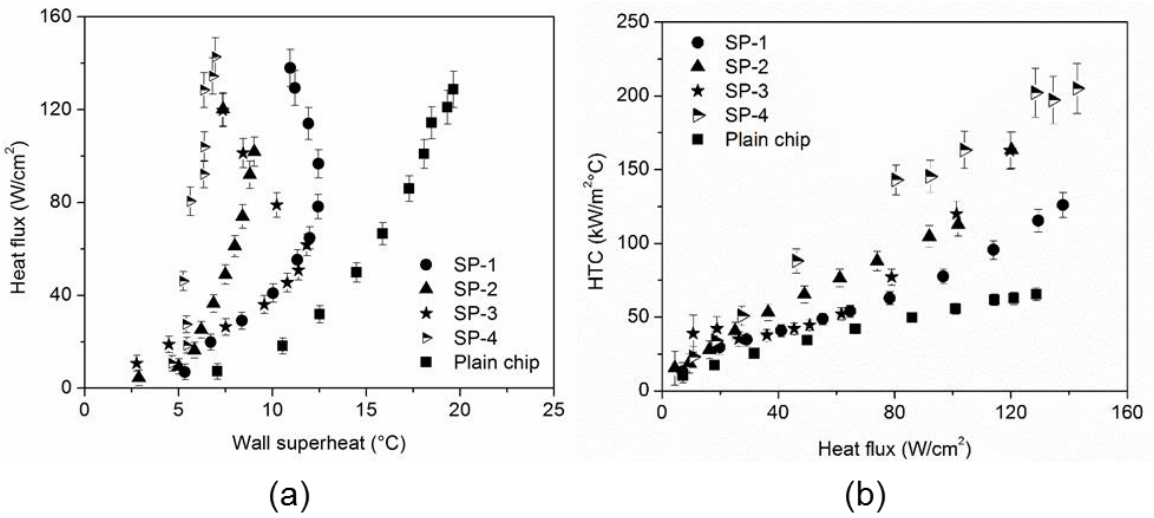

Figure 73. (a) Pool boiling results for SP-1 - 4 with distilled water at atmospheric pressure. (b) Heat transfer performance curves for the screen-printed samples (SP-1 - 4).

Figure 73b shows the variation of HTC with heat flux for all the samples. The heat dissipation capability of a surface can be understood from this plot. The trend indicated that the HTC increases with an increase in heat flux. At CHF, a maximum HTC of 194 kW/m^2°C was obtained with the SP-4 coated surface. This HTC translates to an enhancement of ~200% increase in HTC when compared to a plain chip. Chip SP-1, SP-2 and SP-3 had HTC's of 126 kW/m^2°C, 163 kW/m^2°C and 164 kW/m^2°C, respectively.

4.4.4.1.1. CHF enhancement – Effect of wicking

Wickability of a surface is shown to be responsible for the enhancement in CHF on wicking structures [24]. The wicking rates of each surface was measured by visualizing the dynamic spreading behavior of a drop placed on these surfaces. The volumetric change in a liquid droplet of a fixed volume was captured for a duration of ~75 s using a VCA Optima goniometer. Figure 74 summarizes the wicking rates obtained with the screen-printed copper-GO (SP-1 – SP-4) test surfaces. In this dataset (SP-1 – SP-4), the coatings exhibit

poor wickability as seen by the low volume of liquid wicked into the coatings. A sintered-copper porous coating without GO results in a wicking rate of 0.99 mm/s, which is significantly higher than that observed on SP-1 – SP-4. This correlates well with the CHFs obtained from these samples which are similar to that of a plain chip (~128 W/cm^2). Although, previous studies have indicated high wickability with sintered-copper coatings [35], the addition of GO seems to significantly alter this behavior as demonstrated here. Since the CHF is similar to a plain chip, the contact angle change for SP 1- 4 cannot explain the reduction in wall superheats. Therefore, we identify alternate mechanism to influence the enhancement in these surfaces.

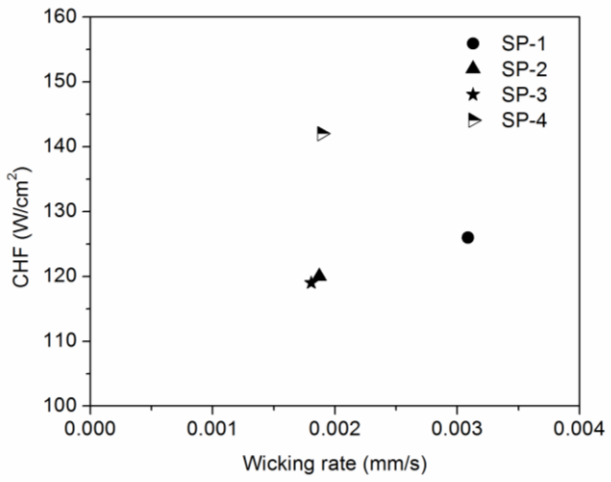

Figure 74. Wicking rates obtained with the screen-printed samples. These surfaces exhibit poor wickability.

4.4.4.1.2. Reduction in wall superheats – Effect of additional nucleation sites

The irregular porous matrix of the coatings results in a range of cavity sizes on these coatings. The model proposed by Hsu [2] determines the cavity sizes that nucleate at different wall superheats.

$$Dmax, Dmin = \frac{\delta_t C_2}{C_1} \frac{\Delta T_w}{\Delta T_w + \Delta T_{sub}} \times \left[1 \pm \sqrt{1 - \frac{8 C_1 \sigma T_{sat} (\Delta T_w + \Delta T_{sub})}{\rho_v h_{fg} \delta_t (T_w)^2}}\right] \quad (33)$$

where C_1 = 1 + cosθ and C_2 = sinθ. The application of Hsu's model [2] to the results will be able to estimate the cavity sizes that nucleate at the point where the curve begins to shift to the left at higher heat fluxes. Figure 75 (a and b) shows the minimum and maximum cavity diameters for the contact angles corresponding to each surface for the range of wall superheats observed here. The plot shows that the potential nucleation cavity diameters for the surfaces: 25 µm – 1.9 µm for SP-1, 19 µm – 1.4 µm for SP-2, 33 µm – 2.4 µm for SP-3 and 34 µm – 2.8 µm for SP-4 estimated using Eq. (33). A HTC of 6000 W/m^2°C was used assuming a linear thermal boundary layer while calculating the boundary layer thickness in each sample. Kruse et al. [77] showed that temperature gradient induced by microstructure height also plays a critical role in the range of cavity sizes that become available for nucleation. Furthermore, they stated that low thermal conductivity materials introduce large thermal gradients which are beneficial in reducing wall superheats at higher heat fluxes.

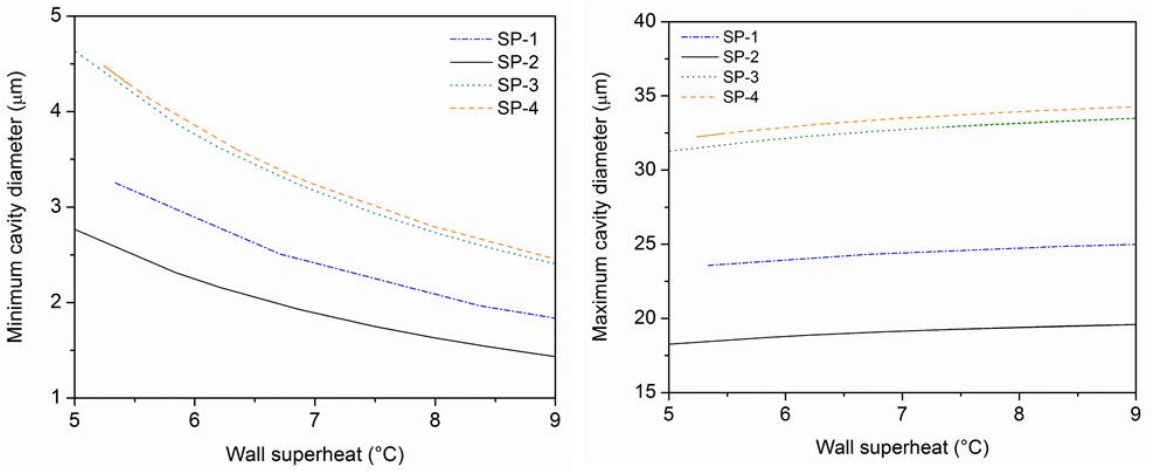

(a) (b)

Figure 75. (a) Maximum cavity diameter and (b) minimum cavity diameter for the samples as a function of wall superheat using Hsu's model [2]. At higher wall superheats, smaller cavities begin to nucleate which forms the basis of enhancement on these surfaces.

The scanning laser confocal images shown in Figure 76 illustrates the range of cavity sizes available for nucleation on the SP-1 – SP-4 surfaces. The images were obtained using a Keyence laser confocal microscope using a 10X magnification lens with an approximate working distance of 25 mm. These cavity sizes are within the range corresponding to each test surface. Furthermore, the coating thickness (~35 μm) induces a temperature gradient which promotes nucleation from smaller cavities along the feature height at higher wall superheats. At the point where the curve begins to shift to the left, the effects arising from additional cavities is amplified. Consequently, the HTC increases significantly due to the increased contribution from the rapid nucleation activity.

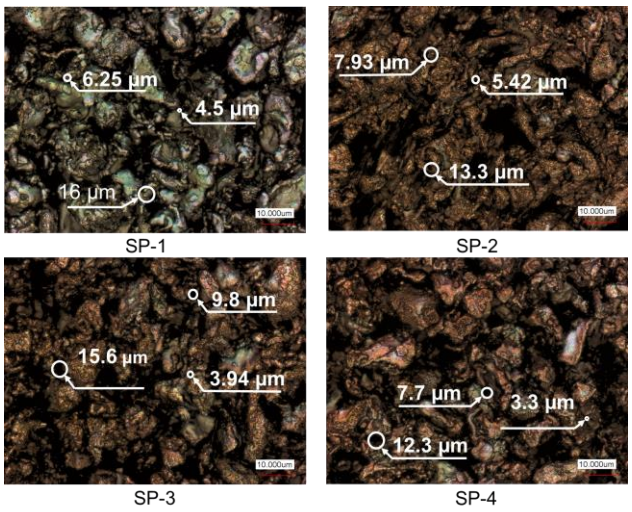

Figure 76. Confocal laser scanning images showing range of cavities available for nucleation in the samples. These cavities fall within the range established using Hsu's criterion and nucleate when superheat conditions are met.

The effect of deposition through screen-printing results in a typical sintered-morphology with a range of cavity sizes 1-30 μm. While the addition of graphene has shown to alter the

contact angles in these copper-GO porous coatings, the effect of wicking is also significantly diminished inside the features. It is postulated here that the GO encapsulates the porous copper thereby inhibiting liquid to be wicked into the coatings. Figures 77a and b shows the morphological features on the SP-4 surface examined on a JSM-6400V scanning electron microscope (SEM) at an accelerating voltage of 15 kV. A typical sintered-morphology was observed on these surfaces. Figures 77c shows the SEM image obtained at 5000X on which the elemental analysis was conducted. Figure 77d show the elemental analysis which confirms the presence of carbon, oxygen and copper in the coatings.

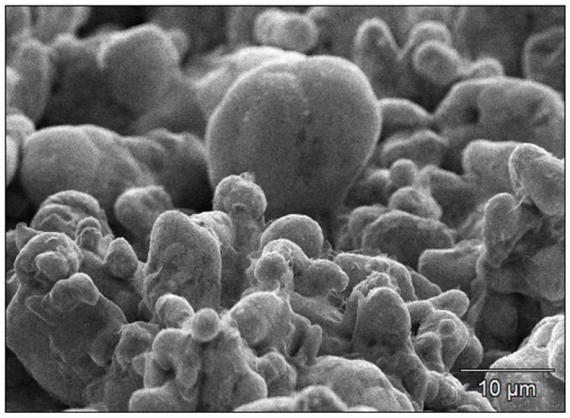

(a)

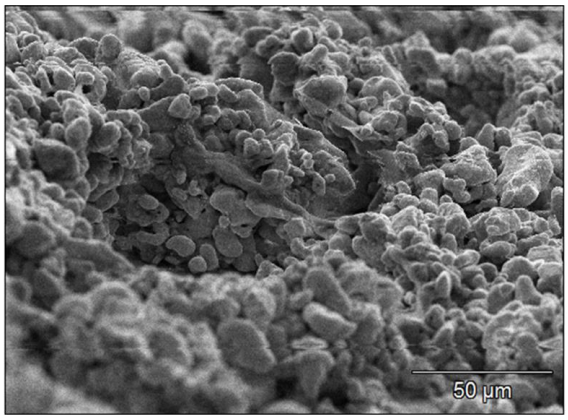

(b)

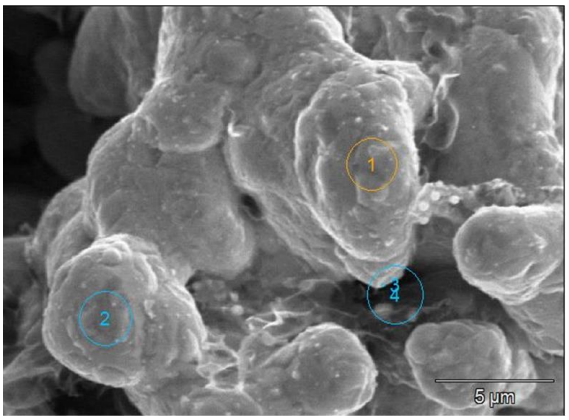

(c)

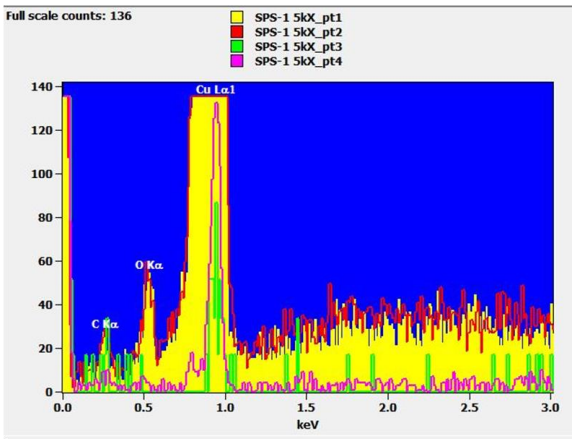

(d)

Figure 77. SEM images of the coated samples at (a) 2 kX, 66° tilt (b) 600X (c) 5 kX magnification (d) elemental analysis. These images confirm the deposition of copper and carbon as seen by the intensity signals in (d).

The enhancement mechanism in these structures is primarily due to increased nucleation activity. The range of cavity sizes available for nucleation both in the planar and along the coating thickness is identified as the main contributing mechanism for the increase in HTC. This causes the boiling curve to shift to the left owing to the rapid nucleation activity. On the other hand, the wicking rates in these coatings are small indicating that liquid retention in the wick structure did not contribute to the enhancement. This is evident from the low CHF values observed for these samples.

4.4.4.2. Chronoamperometry electrodeposition process – Type-II enhancement

Figure 78 shows the pool boiling results obtained with GO-copper samples CA-1, CA-2 and CA-3 prepared using the chronoamperometry electrodeposition process (see Table 12). In this data set, the deposition time was varied between 500-1500 seconds to create three test surfaces. A maximum CHF of 216 W/cm^2 was achieved with the surface corresponding to the shortest coating duration (500 s). The CA-2 and CA-3 surfaces reached a CHF of 176 W/cm^2 and 188 W/cm^2, respectively. The wall superheats in these surfaces were similar to that on a plain copper chip. The HTC at CHF for the samples CA-1, CA-2 and CA-3 were 86 kW/m^2°C, 60 kW/m^2°C and 78 kW/m^2°C, respectively.

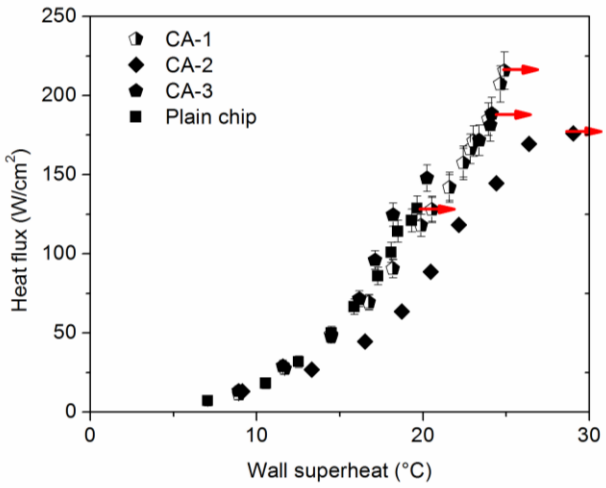

Figure 78. Pool boiling results obtained with CA-1-3 with distilled water at atmospheric pressure.

4.4.4.2.1. CHF enhancement – Effect of contact angles

The surfaces prepared under this category show a well-strung morphology unlike the sintered-morphology seen with SP 1-4. Therefore, the authors postulate that the CHF enhancement is dependent on the dynamic contact angles which dictate the wettability on the surface. The surfaces here exhibit high CHFs which are attributed to the change in the advancing contact angles influenced by the roughness on the surface. Hierarchical microstructures are shown to manipulate the surface forces holding the contact line due to its large effective contact length on these surfaces [110]. The arithmetic mean roughness, R_a, values for CA-1, 2 and 3 were 13.7 µm, 8.93 µm and 12.33 µm, respectively. The corresponding CHF values were 216 W/cm^2, 176 W/cm^2 and 188 W/cm^2, respectively. The plain chip had a R_a and CHF values of 1.1 µm and 128 W/cm^2, respectively. Therefore, roughness augmented wettability was identified as the driving mechanism here similar to Chu et al. [110].

4.4.4.2.2. Type II: Heat transfer enhancement mechanism

The surfaces (CA-1, CA-2 and CA-3) tested here exhibit an increase in CHF without a reduction in wall superheat. These surfaces benefit from large advancing contact angles which significantly increase the CHF. Figure 79 shows the SEM images obtained on the surface. The image indicates that the deposition resulted in a hierarchical matrix of copper decorated with graphene. In such an arrangement, the roughness augmented wettability is amplified as the contact angles are significantly influenced by the hierarchical structures similar to that reported by Chu et al. [110]. Therefore, it can be concluded that *Type-II* structures benefit from roughness augmented wettability, but the absence of rapid nucleation activity at high heat fluxes due to the morphology induced effects causes the wall superheats to increase. Further examination of the test surfaces and additional experiments are warranted to confirm the mechanism in this category.

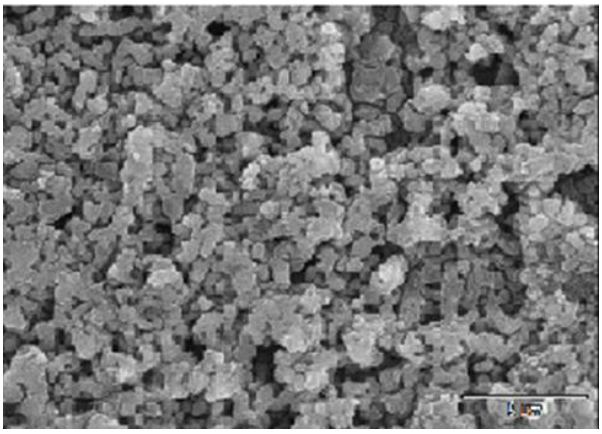

Figure 79. SEM images depicting well-strung features on CA-1.

4.4.4.3. Galvanostatic electrodeposition process – Type-III enhancement

Figure 80a shows the pool boiling curves obtained with the GS1-4. The GO composition in these samples was varied between 0.5-2.5 percent by volume. The deposition was carried out in a carefully designed electrochemical cell using a galvanostatic method as discussed

previously. GS-1, GS-2 and GS-3 reached a CHF of 135 W/cm^2, 169 W/cm^2 and 194 W/cm^2, respectively. A CHF of 220 W/cm^2 was obtained with GS-4 corresponding to the sample with the maximum GO composition of 2.5 percent. To the best of the authors' knowledge, this is currently the highest reported CHF with GO-based coatings. Contrary to the results reported with screen-printed samples (SP-1-4), the test surfaces in this data set resulted in an increase in CHF with a simultaneous reduction in wall superheat at higher heat fluxes.

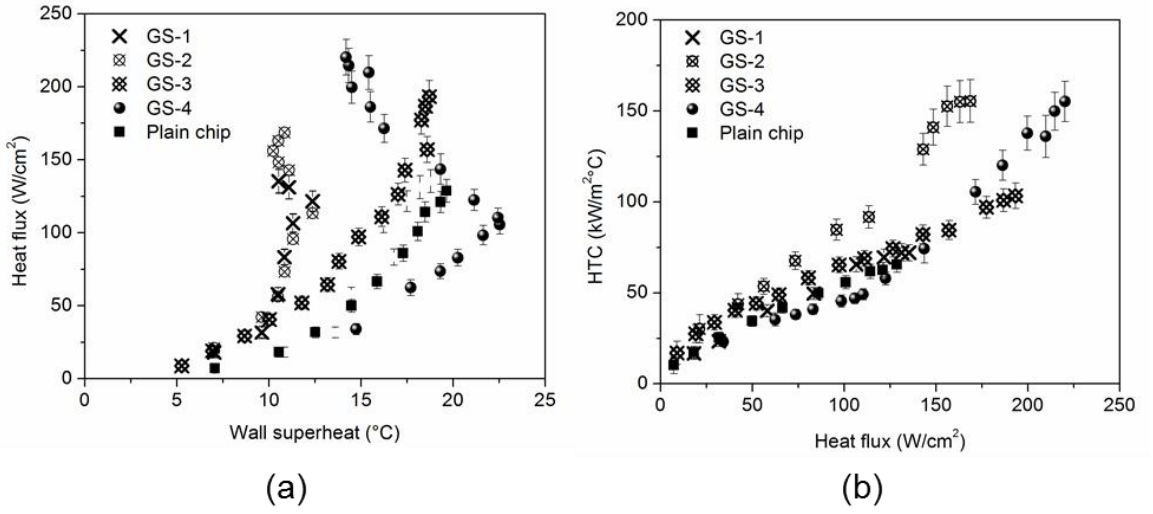

Figure 80. (a) Pool boiling results obtained with distilled water at atmospheric pressure with GS-1 - 4. (b) Heat transfer performance curves.

Figure 80b shows the HTC plots obtained for the surfaces prepared using the galvanostatic process. In these samples, a significant increase in HTC in addition to a CHF increase was observed. A maximum HTC of 72 kW/m^2°C, 155 kW/m^2°C, 103 kW/m^2°C and 155 kW/m^2°C at CHF was achieved with GS-1, GS-2, GS-3 and GS-4, respectively. The trend in the investigated surfaces suggest that the CHF increased with an increase in the GO concentration.

4.4.4.3.1. CHF enhancement – Wickability of the surface

The wicking rates play a significant role in enhancing the CHF. Rahman et al. [24] demonstrated this effect by introducing a dimensionless parameter, wicking number (*Wi*), which directly correlated to the increase in CHF using bio-templated structures. The enhancement in CHF is attributed to the increase in liquid retention in the wick structure which promotes evaporation. Figure 81 shows the variation of CHF with the (1 + *Wi)* for the surfaces investigated here. It must be noted that the wicking rate in the two studies were computed using different methods. The wicking number is calculated using Eq.(34) as described by Rahman et al. [24].

$$Wi = \frac{V_o'' \rho_l}{{\rho_v}^{1/2} \left[\sigma g (\rho_l - \rho_v)\right]^{1/4}} \tag{34}$$

Where,

V_o'' is the wicking rate (m/s), ρ_l and ρ_v are the liquid and vapor densities (kg/m^3), g is the acceleration due to gravity (m/s^2) and σ is the surface tension force (N/m). The wicked volume (mm^3/s) is estimated as the droplet volume change over time using a VCA Optima goniometer. The wicking rate (mm/s) is calculated by normalizing the wicked volume over the droplet impingement area. This method offers a simple technique to characterize wickability on moderate and low wicking structures.

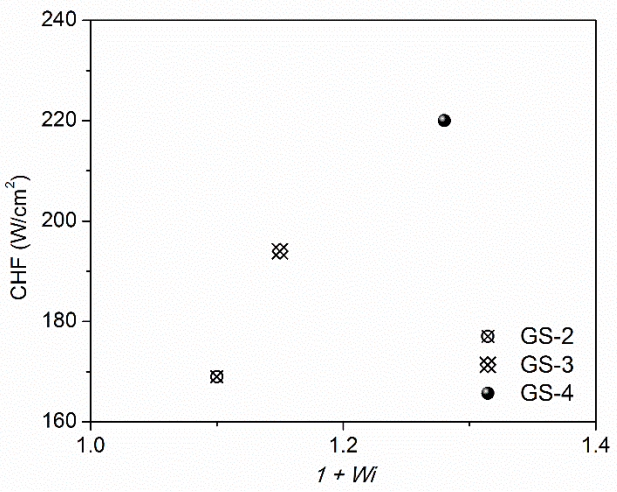

Figure 81. CHF trend as a function of wicking number (Wi). High Wi represents a surface with high wickability contributing to increase in CHF.

It is noted from Figure 81 that the CHF increases with an increase in the wicking number. The application of the CHF model proposed by Rahman et al. [24] predicts a CHF of less than 150 W/cm^2 which is less than the experimental values obtained in this data set. Therefore, we recognize that additional mechanisms were further responsible for the enhancement.

4.4.4.3.2. Additional nucleation sites and microlayer partitioning mechanisms

In the samples investigated here (GS-1 through GS-4), the HTC is significantly increased due to the low wall superheats at relatively higher heat fluxes. This behaviour is similar to that observed with the screen-printed samples (SP-1 through SP-4) but with a substantial increase in CHF. GS-1 exhibits a similar effect to the screen-printed samples where the CHF is similar to that observed on a plain chip. Therefore, this surface can be categorized under *Type-I* enhancement. Similarly, GS-3 can be classified under *Type-II* enhancement. GS-2 and GS-4, in addition to wicking, have increased nucleation sites that are activated under suitable superheat conditions and contribute towards decreasing the wall superheat.

The mechanism for such a trend is attributed to the range of cavity sizes available for nucleation as discussed previously. The nucleation activity is further promoted by the enhanced evaporation through microlayer partitioning mechanisms. Maroo's group introduced this mechanism by fabricating silicon ridges in the nano/microscale [46,47]. The microlayer is a thin liquid film that forms underneath a growing bubble. By employing ridges, Zou and Maroo [46,47] demonstrated that the microlayer gets partitioned which results in additional liquid volume available for evaporation. Through analytical models, they demonstrated that this behavior results in increased bubble volume and frequencies.

4.4.4.3.3. Type-III: Heat transfer enhancement mechanism

The enhancements in CHF and HTC are due to the relative effects of wicking and additional nucleation sites. The microscale morphology of the samples play a critical role in enhancing wicking and promoting nucleation. Figure 82 shows the SEM images of the test surface (GS-4). The unique morphology obtained with these samples shows the clear separation of copper and GO sheets deposited through the process. The copper appears as dendritic structures as confirmed by the SEM images obtained (see Figure 82b), which is similar to that reported by Patil and Kandlikar [107]. GO seems to get deposited as sheets underlying the dendritic copper features. These features seem to promote wicking through the copper-dendrites and nucleation through the underlying GO sheets. The nucleation activity increases due to microlayer partitioning mechanisms, as demonstrated by Zou and Maroo [46]. The microlayer partitioning increases bubble growth rates and frequency. This arrangement results in an increase in both CHF and HTC under *Type-III* characteristics demonstrated here.

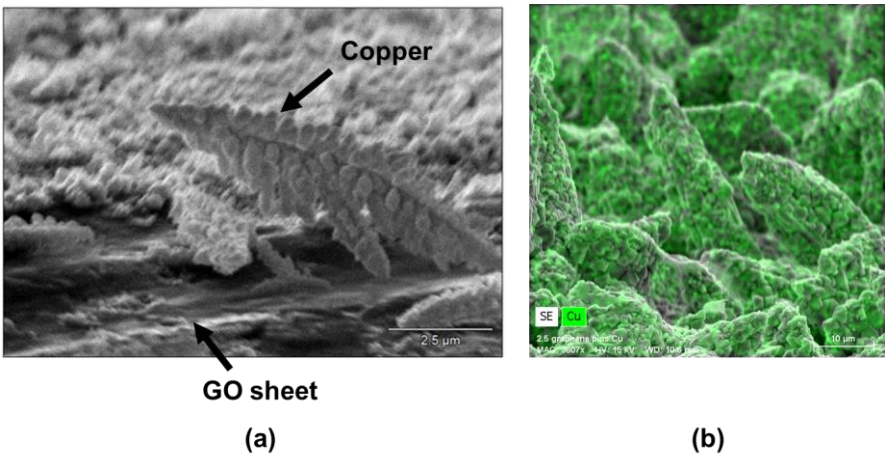

Figure 82. SEM images of the electrodeposited surface using galvanostatic method. (a) Dendritic copper structures with underlying GO sheets at 10 kX, 70° tilt, (b) Energy dispersive X-ray spectroscopy (EDS) showing copper mapping confirming dendritic structures were made of copper.

The effect of additional nucleation sites and wicking seems to be the main contributing mechanisms in *Type-III* enhancement. This is attributed to the competing nature of the two mechanisms induced by the coatings. Further studies are warranted to explain the relative merits of the two mechanisms in a unified model.

4.5. Conclusions

A detailed experimental study was conducted using screen-printing and electrodeposition techniques to demonstrate the three boiling characteristics. A combination of copper and GO was used to develop the corresponding heat transfer surfaces. FTIR, SEM and confocal laser scanning images were obtained to further understand the microscale morphologies. The pool boiling results were obtained with distilled water at atmospheric pressure. The following conclusions were drawn from this study.

i. Type-I boiling characteristic results in a significant reduction in the wall superheat without an increase in CHF when compared to a plain surface. Four surfaces (SP-1 –

SP-4) were generated using a screen-printing technique. The GO composition in the surfaces was varied between 0.2-1% by mass of the copper composition in the matrix. The lowest wall superheat of 7 °C was observed with SP-2 and SP-3 test surfaces. A typical sintered-morphology was observed using SEM images. The rapid nucleation activity contributed to the enhancement in Type-I boiling enhancement as a consequence of the available nucleation sites.

ii. A chronoamperometry electrodeposition technique was used to generate three surfaces (CA-1 – CA-3) to demonstrate Type-II boiling characteristics. In this category, a significant increase in CHF without a reduction in the wall superheat was observed. The deposition duration was varied between 500 – 1500 s to create unique morphologies. The SEM images indicated a hierarchical matrix which influenced the liquid wettability through roughness augmentation. These surfaces do not show the curve shifting to the left at higher heat fluxes. A maximum CHF of 216 W/cm^2 which translated to an enhancement of 69% was obtained with the surface (CA-1) corresponding to the shortest coating duration (500 s) when compared to a plain surface.

iii. In Type-III, an increase in CHF is accompanied with a decrease in wall superheats at higher heat fluxes. A galvanostatic technique with GO composition of 0.5 – 2.5% (by volume) was used to generate four surfaces (GS-1 – GS-4) in this data-set. The electrodeposition technique seems to create separated depositions of dendritic copper and GO sheet structures. The wicking enabled dendritic structures to enhance the CHF while the underlying GO sheets promote nucleation characteristics through microlayer partitioning mechanisms. A CHF enhancement of 72% and wall superheat reduction

of 43% was obtained with the surface corresponding to the maximum GO concentration.

4.6. Enhancement through coupled motion of contact line on chemically inhomogeneous surfaces

Introducing chemical inhomogeneities at nanoscale induces a local change in dynamic contact angles which alters the CL characteristics. Nanoscale chemically inhomogeneous surfaces comprising of gold, palladium and nickel were generated on copper substrates to demonstrate the underlying CL dynamics. The spatial variations of chemical constituents were mapped using elemental display SEM images. Further, the coupled and stick-slip motion was confirmed for a sliding water droplet on these surfaces, and then applied in studying the pool boiling bubble dynamics of a single bubble from nucleation to departure.

4.6.1. Hypothesis

Tanner's law (Eqn. 36) describes the dependence of the hydrodynamic factors influencing liquid travel with the dynamic contact angle. In this context, the capillary number as a function of viscosity (μ), surface tension (σ) and CL velocity (V) is used to represent the hydrodynamic effects as:

$$Ca = \frac{V\mu}{\sigma} \tag{35}$$

which is related to the dynamic contact angle,

$$\theta_D^3 = (const)Ca \tag{36}$$

A manifestation of this effect can be translated to surfaces with nanoscale chemical inhomogeneity or surfaces comprising of nanoscale area fractions of different chemical

constituents. On these surfaces, the local change in dynamic contact angles along the CL due to variation in chemical composition is capable of altering the stick-slip motion. This altered CL motion is hypothesized to increase the CL velocity in accordance with Tanner's law (Eqn. 36). On a surface lacking chemical inhomogeneities, the typical stick-shift motion is expected to adversely affect the CL velocity due to increased pinning effects.

An experimental setup was devised to validate the hypothesis using a contact angle goniometer, distilled water and a high speed camera. A plain copper test section was used as the control while another copper test section sputter-coated with gold and palladium served as the surface comprising of chemical inhomogeneities. The surfaces were held at an angle on a leveled stage for the droplets to slide. A motor controlled system was employed to inject 5 µl liquid droplet on the surface while simultaneously capturing high speed videos at 4000 fps. Figure 83 shows the measured distance of the advancing liquid front and its corresponding CL motion profile for the plain and chemically inhomogeneous surfaces. In the case of a plain surface, the CL motion reveals a clear pinning event, and subsequent interface motion (slip) between the pinning events. This is further confirmed by the high speed images shown in the figure as insets. Consequently, the CL advances in a non-continuous or staggered motion. The chemically inhomogeneous surface reveals a smooth motion of the CL as confirmed by the measured distance and high speed images. This smooth and continuous motion was termed as coupled jumps by Decker and Garof [54]. Following their terminology, this smooth and continuous interface motion on nanoscale inhomogeneous surfaces is referred to as the coupled CL motion. The change in dynamic contact angles along the CL due to chemical inhomogeneities present on the surface drives the CL motion.

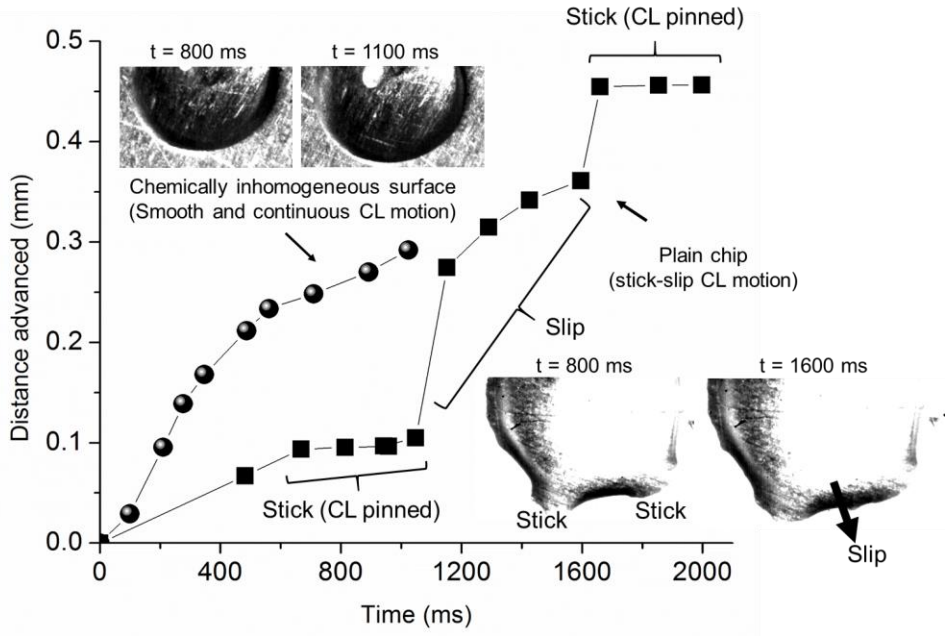

Figure 83. Distance advanced by the liquid over time for (a) plain chip showing stick-slip motion, and (b) gold and palladium surface showing coupled CL motion. (Insets) High speed images of the CL motion obtained using a Photron FASTCAM® at 4000 fps.

The CL speed [111], contact angle [112] and the nature of its motion are of significant interest in boiling heat transfer. Continual demand for higher system efficiency to reduce cost, improve reliability and increase safety drives methods to enhance the boiling performance characteristics [113–115]. At the heart of any boiling system is a single bubble which undergoes nucleation, growth and departure [11]. During this cycle, referred to as the ebullition cycle, heat is transferred through microconvection, microlayer evaporation, and transient conduction mechanisms [8,13]. The rapid motion of the liquid-vapor interface disturbs the thermal boundary layer in its immediate vicinity which induces microconvection enhancement [116]. Microlayer evaporation occurs when a thin liquid film trapped underneath a growing bubble aids in evaporation promoting bubble growth [7]. The transient conduction occurs as the bubble interface retracts, causing the advancing liquid to sweep over the heater surface at the bubble base [13]. Exploitation of these

underlying mechanisms through micro/nanoscale surface enhancements can deliver remarkable improvements in the performance limits as shown in Chapter 2. The addition of surface structures has been reported to provide a variety of enhancement levels.

The heat transfer due to the CL motion is significantly higher than the bulk heat transfer as indicated in multiple reports [56,57]. The absence of stick-slip motion on a chemically inhomogeneous surface formed the basis of designing surfaces to improve the CL heat transfer. A chemical inhomogeneity is introduced on the surface due to compositional gradients during the deposition process. These inhomogeneities are typically neglected in microscale features, however their effects are more pronounced in the CL region as demonstrated here. This study provides a framework to enhance boiling heat transfer at the nanoscale by improving the CL characteristics.

4.6.2. Sample preparation

Plain and nanoscale chemically heterogeneous copper chips, 17 mm square were used similar to previous studies. The chemical coatings were applied on a central area of 1 cm^2. This area was polished to achieve a smooth surface finish. In addition to polishing, a careful cleaning process with isopropyl alcohol and subsequent rinsing with deionized water was done on all the test chips. The measured arithmetic mean roughness on these samples was 1.1 ± 0.2 μm.

Sputter coating and electroplating techniques were devised to deposit the desired coatings on the surface. For sputter coating, a solution comprising of gold and palladium was evenly sputtered on the surface in an argon atmosphere. An electroplating process was employed to deposit layers of gold and nickel on the surface. A Casewell Plug and Plate®

electroplating equipment was used in the experiments. This technique employs a stainless steel wick wand to transfer the solution uniformly over the surface. The aforementioned test section formed one of the electrodes, while the wick wand dipped in the desired solution formed the other electrode. A 4.5 V-DC was applied to initiate the plating process. A single stroke across the surface formed a coated layer. To generate uniform coatings with acceptable surface coverage, the number of strokes was increased. Gold-1 and gold-2 surfaces comprised of 10 and 100 strokes, respectively. The nickel and gold surfaces were developed by mixing equal proportions (by vol.) of gold and nickel solutions and subsequently electroplating the surfaces under similar conditions.

Gold-1 and gold-2 surfaces were generated by varying the number of electrochemical strokes. Figure 84(a1 and a2) shows the schematic representation of staggered and continuous CL motions with the plain and chemically inhomogeneous surfaces, respectively. Figure 84b shows the scanning electron microscope and elemental display images on the prepared samples. The chemical inhomogeneity due to compositional changes (b1 and b3), imperfect surface coverage (b2) and defect-induced changes (b4) were captured in these images.

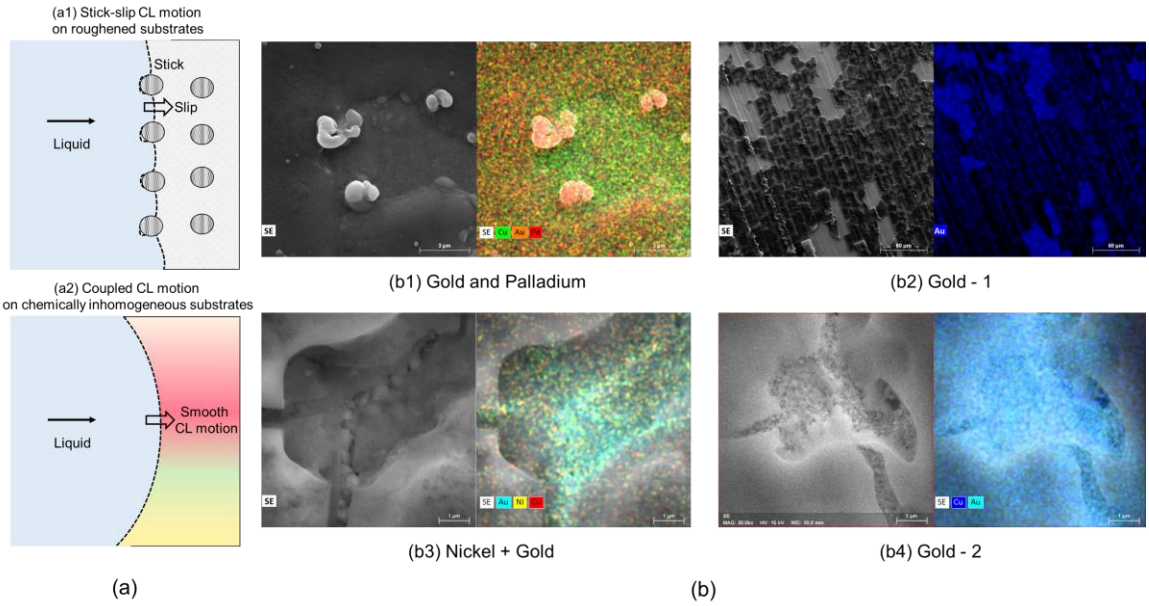

Figure 84. (a) Schematic representation of stick-slip motion (a1) and coupled CL motion (a2). (b) Scanning electron microscope and elemental display mapping images on gold and palladium (b1), gold-1(b2), nickel and gold (b3), gold-2 (b4) samples. The images show the existence of a compositional change which drives the CL motion on the surface.

The advancing and receding contact angles were measured during the bubble cycle time using high speed images obtained during the boiling tests. The arithmetic mean roughness of the chemically enhanced coatings was obtained through a Keyence® laser confocal microscope and is summarized in Table 13. The repeatability of the contact angle and roughness measurements was confirmed by conducting over 10 measurements on each test surface. The values show good agreement with maximum standard deviation in contact angle and roughness being ±2° and ±0.5 µm, respectively. In addition to the contact angle and roughness measurements, wickability tests were conducted on the samples using a video contact angle goniometer. In all the tests conducted here, the droplet attained its static contact angle without showing any further spreading behavior.

Table 13. Contact angle and roughness values on the fabricated samples. The contact angles were determined from high speed images obtained at 4000 fps using a Photron FASTCAM® camera. The arithmetic mean roughness (R_a) was obtained using a Keyence laser scanning microscope using a 10X magnification lens.

Surface	Contact Angle		Roughness, μm
	Advancing	Receding	
Plain chip	67.5	40.2	1.1
Gold and palladium	59.5	39.9	0.94
Gold-1	45	30.2	1.34
Gold-2	44.3	41.7	0.87
Nickel and gold	50.5	40.4	0.93

4.6.3. Role of heat transfer mechanisms

Fundamental heat transfer mechanisms in boiling centers around rewetting mechanisms to improve the nucleation and heat transfer characteristics [102,117]. Primary enhancements that have been identified to affect the CL dynamics are the roughness modification by increasing the CL length and liquid spreading through increased wicking. The lack of microscale roughness features and wicking (spreading) behavior indicates that another mechanism was responsible for the enhancement in the tested samples.

The complex and chaotic nature of bubbles at higher heat fluxes impedes the ability to visualize close to the heater surface. Therefore, several earlier experimental and theoretical studies have based their work on explaining the observed mechanisms using visualization at lower heat fluxes, and hypothesizing similar liquid-vapor transport to occur at higher heat fluxes [76,114]. Another approach undertaken by researchers is to capture a single bubble from nucleation to departure on the heater surface through which the heat transfer mechanisms can be analyzed [8,13]. During this process, heat transfer can be effectively partitioned as from microlayer evaporation and transient conduction mechanisms. To this

effect, an isolated individual nucleating bubble in saturated water was analyzed through high speed imaging. A Photron FASTCAM was used to capture videos at 4000 fps. A thorough calibration procedure was undertaken prior to capturing the videos.

Figure 85a shows the high-speed image sequence obtained on a plain surface under saturated boiling conditions. Characteristic CL motion can be identified for the plain chip and the chemically enhanced surface in accordance with the hypothesis described previously. The image sequence shows that a bubble nucleating on a plain chip undergoes two pinning events during its advancing motion. The motion of the CL occurs in a typical stick-slip fashion. In this motion, the CL remains pinned at defects, while the interface between the pinning sites advances the CL due to built-up inertia. This type of pinning event was seen to be absent on the chemically enhanced surface. The bubble base diameter measured on the plain chip was compared with that obtained on a chemically enhanced surface (Figure 85b) which shows a continuous CL motion. The CL in such an arrangement seems to occur smoothly which is referred to as a coupled motion (without stick-slip) in this work.

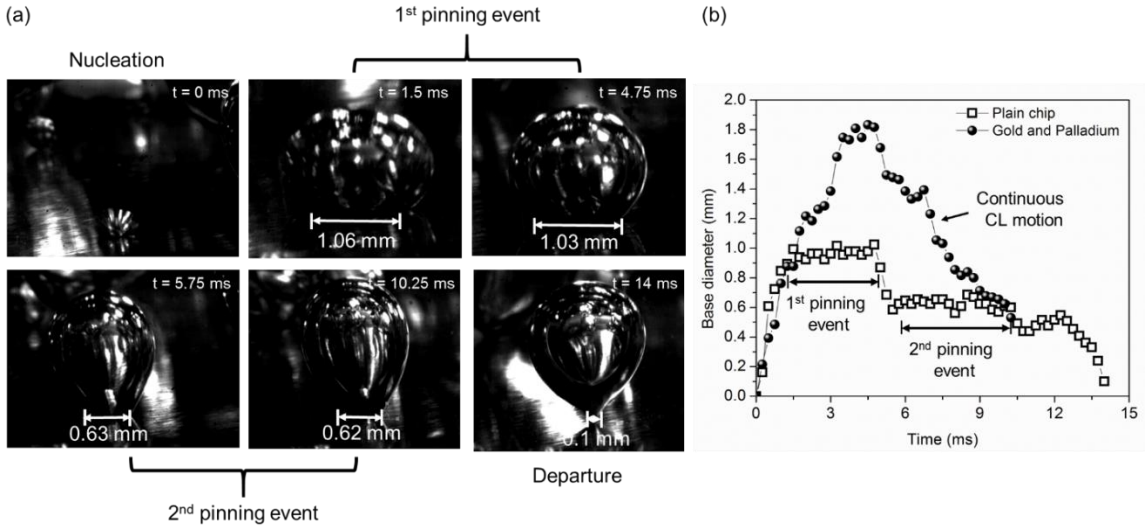

Figure 85. (a) High speed image sequence of a single bubble from nucleation to departure. This image sequence shows the two pinning events encountered by the bubble during its advancing motion. (b) Measured bubble base diameter motion for a plain chip and a chemically enhanced surface.

4.6.3.1. Effect of bubble base diameter on microlayer evaporation

The base diameter of each bubble on all the surfaces was measured over its cycle time at a heat flux of ~20 W/cm^2. To ensure repeatable data, four isolated bubbles were analyzed on each surface and showed good agreement with each other. Figure 86 shows the measured diameter for the plain chip and the chemically enhanced surfaces. Several key observations were derived from this figure. Firstly, the CL motion on the plain surface revealed a staggered motion during its initial receding and subsequent advancing motion. This suggested that the CL motion suffers pinning and de-pinning (moving) events during its cycle time. Secondly, the CL motion on the chemically enhanced surface shows a continuous (coupled) motion lacking any pinning events. This effect was attributed to the presence of chemical constituents on the surface. Thirdly, the maximum base diameter observed for each surface is an important consideration for the microlayer heat transfer contribution.

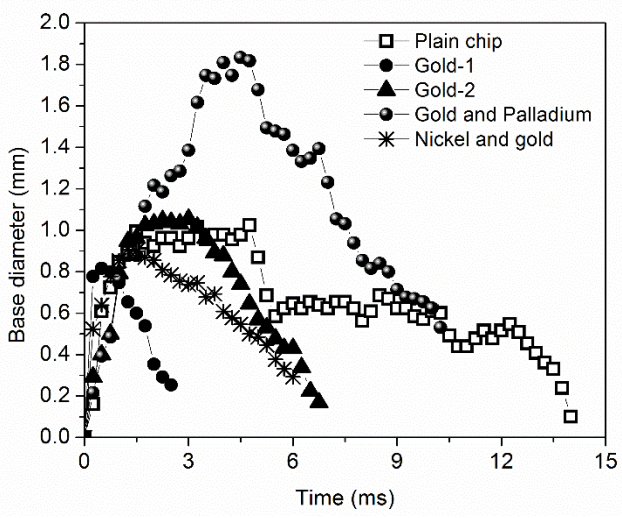

Figure 86. Bubble base diameter from nucleation to departure for the samples investigated in this study. The bubble base radius was obtained after a calibration procedure before capturing the high-speed images. The initial motion till a surface attains maximum base diameter is the receding motion (or bubble growing), while the latter is the advancing (or bubble detaching) motion.

Microlayer evaporation occurs when a thin liquid film is trapped under a growing bubble. Evaporation of this thin film leads to a substantial increase in the bubble growth rate [47]. The total energy from the microlayer can be estimated by analyzing (i) the heat transfer from the wall during the microlayer event, and (ii) the initial sensible energy of the microlayer [8]. The thickness of the microlayer contributes to the total heat transferred during the process. Since, the microlayer thickness typically measured are in the microscale (less than 10 µm), the temperature profile within this layer is expected to be linear. The total microlayer heat transferred over the bubble cycle time can be estimated using

$$\dot{Q_{ME}} = \frac{\rho_l V_{\delta o} h_{lv}}{t} \tag{37}$$

where, $\dot{Q}_{ME}$ is the heat transferred from the microlayer, ρ_l, $V_{\delta o}$, h_{lv} and t are the liquid density, volume of the microlayer, latent heat and time, respectively.

In analyzing the microlayer contribution, the maximum base diameter was used to calculate the volume of the microlayer film under the bubble. Utaka et al. [103] conducted a series of experiments using an interferometry technique to estimate the microlayer thickness. Using their work as guidance, the microlayer thickness based on the radial position from the nucleation site was estimated for each surface as listed in Table 14. A linear line fit on the experimental data by Utaka et al. [103] was established in arriving at the microlayer thickness corresponding to the maximum bubble base diameter. The width span of this microlayer on the surface was assumed to be equal to the maximum base diameter attained on each surface (see Figure 86). The microlayer heat transfer over the bubble cycle time was obtained using Eq. (34) as shown in Figure 87. The microlayer heat transfer is analyzed as a function of the maximum base diameter and the bubble cycle time. The coupled motion of the CL increases the contribution from the microlayer by either increasing the bubble base diameter (gold and palladium) or by decreasing the bubble cycle time (gold-1, gold-2, and nickel and gold). Effectively, a high microlayer volume results in significantly higher evaporation rates as seen in the figure. A plain surface undergoing a stick-slip CL motion on the other hand increases the bubble cycle time and decreases the maximum diameter which cumulatively reduces the contribution from microlayer evaporation.

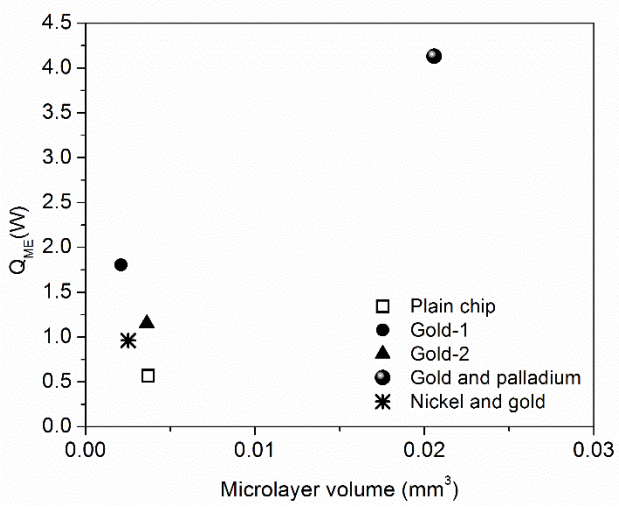

Figure 87. Microlayer volume and heat transfer from the microlayer under a bubble for the samples investigated here.

4.6.3.2. Effect of contact line velocity on transient conduction heat transfer

Transient conduction occurs as the CL sweeps over the heater surface during the advancing motion of the liquid. This motion creates the cold bulk liquid to quench the heater surface resulting in a cooling effect. The origin of this mechanism can be traced to Mikic et al. [11] where the displaced volume of the bubble was assumed to be replaced by the liquid front instantaneously. Through advanced sensor based instrumentation techniques, Demiray and Kim [13] demonstrated that the liquid front advanced gradually over the heater surface. The expression for surface heat flux per unit length can be estimated using,

$$\dot{Q}_{TC} = \int_0^x \frac{k\Delta T}{\sqrt{\pi \alpha_l x}}\, dx \tag{38}$$

where, $\dot{Q}_{TC}$ is the heat transferred through transient conduction, k is the thermal conductivity, α_l is the thermal diffusivity, and x is the distance traveled by the CL.

Recent developments through controlled two-phase experimentation techniques [8,58] suggest that the initial receding motion of the liquid increases the dry-spot region and drives the superheated liquid layer away from the dry-spot, thereby resulting in a lower heat transfer. On the other hand, it is shown that the advancing motion contributes efficiently by causing a gradual quenching of the region as the bubble departs which results in 3X heat transfer when compared to its receding motion [58]. Furthermore, a number of reports [8,13,102] have suggested that the microlayer contributes ~15-25% of the total heat transfer and is expected to remain constant over the entire heat flux range. Therefore, we attribute a significant enhancement to occur through the transient conduction mechanism. Integrating Eq. (38) and transferring into time coordinates yields the following equation

$$\dot{Q}_{TC} = \frac{k\Delta T}{\sqrt{\pi \alpha_l}} v\sqrt{t_{adv.}} \tag{39}$$

The CL velocity *(v)* and the gradual wetting time *(t_{adv})* is seen as critical parameters in explaining the degree of enhancement between the tested surfaces. Demiray and Kim [13] established that the heat transfer varied as the square root of the time during the advancing liquid motion. The CL velocity was deduced from 82 during its advancing motion since the heat transfer during this period was shown to be significantly higher than its receding motion [58]. For a plain surface, the effective CL velocity is significantly reduced due to the pinning event. The chemically enhanced surfaces demonstrate a higher CL velocity. Table 14 summarizes the heat transfer obtained by solving Eq. (37) and Eq. (39).

Table 14. Summary of heat transfer from microlayer and transient conduction mechanisms with CL velocity.

Surface	Microlayer thickness, μm	$\dot{Q}_{ME}$ (W)	CL velocity (m/s)	t_{adv} (ms)	$\dot{Q}_{TC}$ (W)
Plain chip	4.4	0.56	0.08	2	1.20
Gold and palladium	7.9	4.12	0.19	5.75	4.79
Gold-1	3.5	3.71	0.28	2	3.72
Gold-2	4.4	1.15	0.23	3.25	4.03
Nickel and gold	3.9	0.96	0.13	4.25	1.54

4.6.4. Pool boiling results

Pool boiling experiments were conducted with degassed and distilled water at atmospheric pressure. Degassing was achieved by continuously boiling the liquid prior to conducting the boiling tests. Figure 88 shows the pool boiling curves obtained with heat flux on the Y-axis and wall superheat on the X-axis. As a baseline for enhancement comparisons, the plain surface was tested for its boiling performance. This surface reached a CHF of 128 W/cm^2 at a wall superheat of 20°C. A maximum CHF of 220 W/cm^2 was obtained with the sputter coated sample comprising of gold and palladium. A CHF of 143 W/cm^2 was obtained with the nickel and gold surface, while a CHF of 155 W/cm^2 and 177 W/cm^2 was obtained with the gold-1 and gold-2 surfaces, respectively. The wall superheats were similar for all the surfaces.

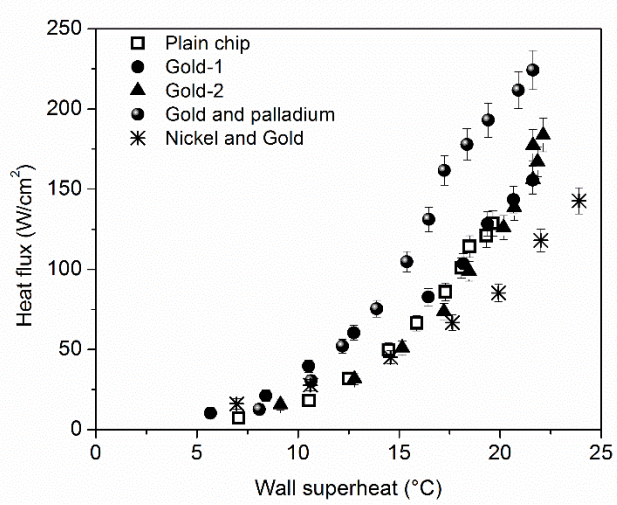

Figure 88. Pool boiling tests on the prepared samples with distilled water at atmospheric pressure.

4.6.5. Enhancement mechanism

The CL velocity during its advancing motion is shown to be critical on surfaces at the nanoscale with enhanced coatings. Therefore, the product of CL velocity and gradual surface coverage time obtained previously is plotted against the normalized experimental CHF values as shown in Figure 89a. The normalized CHF refers to the CHF on the chemically inhomogeneous surface divided by the CHF on a plain copper surface. This figure shows that an increase in the velocity is seen to increase with CHF. This leads to heat transfer enhancement by two important mechanisms: (a) the CL velocity affects the transient conduction contribution which is identified as the significant contributor for the enhanced performance characteristics on chemically enhanced nanoscale surfaces, and (b) lack of pinning events due to chemically induced inhomogeneity drives the CL motion on these surfaces through a change in the local dynamic contact angles. These attributes contribute to increased nucleation and rewetting characteristics on the surfaces. At higher heat fluxes, boiling becomes fully developed and a large number of nucleation sites become active. Therefore the boiling characteristics are captured through the bubble frequency in

the analysis to explain the CHF enhancement. Figure 85b shows the increase in bubble frequency as a function of the transient conduction parameters, namely CL velocity and liquid advancing time. A higher CL velocity results in the faster growth and departure of the bubble contributing to increased bubble frequency as seen in the figure.

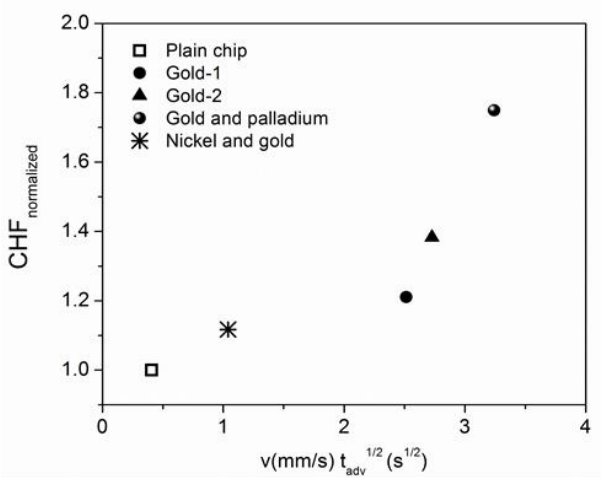
Plain chip
Gold-1
Gold-2
Gold and palladium
Nickel and gold
CHF normalized
v(mm/s) t adv 1/2 (s 1/2)

(a)

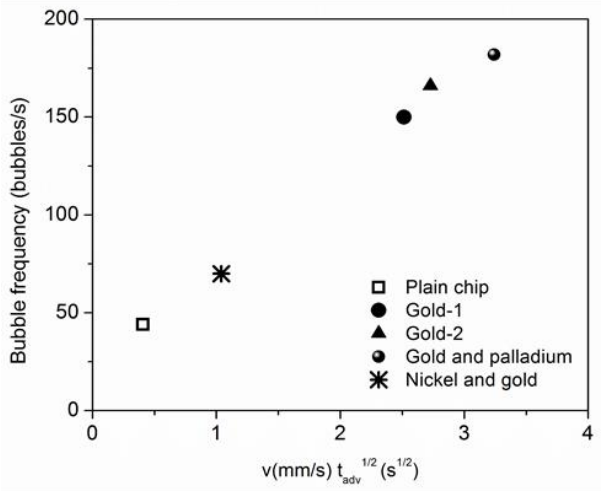
Plain chip
Gold-1
Gold-2
Gold and palladium
Nickel and gold
Bubble frequency (bubbles/s)
v(mm/s) t adv 1/2 (s 1/2)

(b)

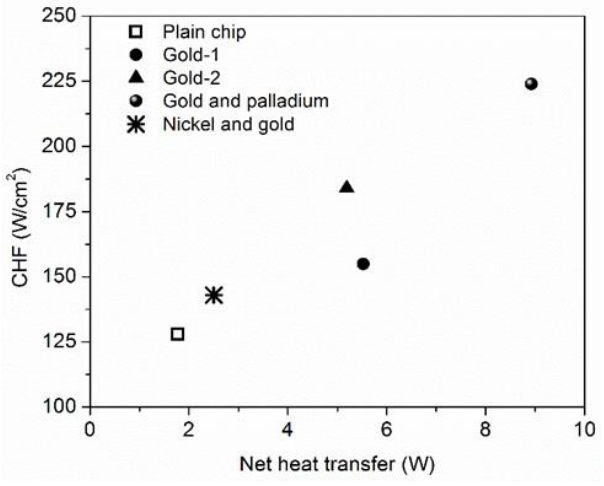
Plain chip
Gold-1
Gold-2
Gold and palladium
Nickel and gold
CHF (W/cm2)
Net heat transfer (W)

(c)

Figure 89. (a) Effect of transient conduction (represented by the advancing liquid velocity) and time on the normalized CHF enhancement. The CHF was normalized over the plain copper surface without chemical inhomogeneity. (b) Experimentally measured bubble frequency as a function of transient conduction parameters (CL velocity and advancing liquid front time). (c) Net heat transfer (microlayer evaporation and transient conduction) from a single bubble on the experimentally obtained CHF.

The net heat transfer to each bubble from microlayer evaporation and transient conduction are plotted against the CHF values obtained experimentally, as shown in Figure 89c. The microlayer span is effective over the maximum base diameter that a bubble grows over on different surfaces. The pinning event experienced by the plain chip reduced the CL velocity which diminishes the effect from transient conduction mechanisms. The chemically enhanced surfaces experienced a continuous motion of the CL without any pinning events, and therefore these surfaces experienced a higher heat transfer from the transient conduction mechanisms. Figure 89(c) confirms the above observations showing that a chemically enhanced surface with higher CL velocity and microlayer evaporation shows significantly higher CHF compared to the plain uncoated surface.

The analysis presented here supports a mechanism in which the CL moves smoothly over a chemically inhomogeneous surface. This effect is amplified when microscale features are absent, and therefore the surface chemistry effects are seen to drive the CL motion. The compositional change due to inhomogeneity induces a local wettability change along the CL in accordance with Tanner's law.

4.7. Conclusions

The motion of the CL was analyzed for surfaces developed with chemical inhomogeneities. Carefully designed experiments demonstrate the motion of the CL to occur in a coupled

fashion on these surfaces which is shown to be influenced by the CL velocity. The coupled motion of CLs is recognized as an important mechanism for enhancement in boiling heat transfer. Therefore, a range of surfaces with different chemical compositions were created and their pool boiling performance characteristics were evaluated. An isolated bubble from nucleation to departure revealed that the plain chip suffered multiple pinning events during the ebullition cycle, resulting in degraded heat transfer performance. The surfaces developed through chemical inhomogeneities depicted a coupled motion of the CL resulting in higher heat transfer. Furthermore, the CL velocity was shown to correlate almost linearly with an increase in CHF and bubble frequency, thereby increasing the total contribution from the microlayer evaporation and transient conduction mechanisms when compared to a plain chip. This study shows that the enhancement mechanism at the nanoscale is affected by the compositional gradient to drive the CL over the surface. Therefore, designing nanoscale surfaces with compositional and wettability transitions will be beneficial in further improving the performance.

Chapter 5

5. Summary

5.1 Major Accomplishments

Thermal management has emerged as a critical consideration in the design of the next generation of electronic devices and the electronics packaging architecture. The advent of cloud computing and the ever-increasing demand for faster and more reliable devices has presented new challenges in the thermal management of electronics. The large pressure drops and fluid temperature differences in single phase cooling strategies have been unable to deliver the cooling performance requirements in an energy efficient and inexpensive manner. Pool boiling systems are simple without the use of complex header configurations and flow regulating pumps. Often, the pool boiling performance is limited by the inability of liquid to wet the prime heater surface due to increased counter-flow resistance offered by the departing/rising bubbles. With this background, the goal of this research work was to develop passive heat transfer surfaces to limit the counter-flow resistance. This was achieved by designing and fabricating a range of surfaces developed through the concept of separate liquid-vapor pathways, enhanced microlayer evaporation in graphene coatings, and improved contact line motion on nanoscale chemically heterogeneous surfaces for a simultaneous increase in CHF and HTC.

The main contributions from this work are summarized below:

i. Open microchannels enhanced with selectively located porous coatings (sintered throughout, sintered-fin-tops and sintered-channels) and feeder microchannels resulted in the simultaneous enhancement in both the CHF and HTC. The simultaneous enhancement was achieved with both water and dielectric fluids (HFE

7000, FC-87, PP1 and PP1C). Notably, the sintered-channels reached a CHF of 420 W/cm^2 at a wall superheat of 1.7 °C which translated to an unprecedented CHF of 2.9 $MW/m^2°C$. The NRFC-3 surface reached a CHF of 394 W/cm^2 at a wall superheat of 5.5 °C with a HTC of 713 $kW/m^2°C$.

ii. Mechanistic examination through high speed imaging at 4,000 – 10,000 fps revealed separate liquid-vapor pathways as the enhancement mechanism which was shown to be pronounced outside the influence region of the bubble. Porous coatings enforced bubble nucleation, while the uncoated microchannel regions served as liquid supply pathways. In the NRFC surfaces, bubbles were confined to the nucleating regions, while feeder microchannels improved the liquid directionality. The interplay mechanisms at low and high heat fluxes, and the geometrical trends were identified for the enhanced configurations with both water and dielectric fluids. This led to the invention of enhanced macroconvection heat transfer mechanism, as coined by Kandlikar [9]. This mechanism was capable of creating a self-sustained boiling configuration through confined nucleating regions, and the region between them for enhanced single-phase jet impingement flow. This mechanistic understanding was used to explain a new pool boiling curve, termed as boiling inversion, characteristic to surfaces developed under this category.

iii. Material characterization of graphene and graphene oxide coated surfaces led to the understanding of a structure-property relationship which was exploited at the nanoscale and microscale. Contact angle hysteresis, roughness and enhanced microlayer evaporation were identified as the enhancement mechanisms. Surfaces were then tailored to facilitate wicking in graphene through a sintering and

electrochemical technique. This resulted in a simultaneous enhancement in both CHF and HTC through graphene promoted nucleation activity and dendritic copper propelled capillary rewetting pathways. Notable enhancements include a CHF of 220 W/cm^2 with a HTC of 155 $kW/m^2°C$, depicting a pool boiling inversion with copper.

iv. At the nanoscale, chemically heterogeneous surfaces were developed to alter the contact line motion on the heater surfaces. The contact line velocity was shown to be influential in improving the contributions from the microlayer and transient conduction mechanisms. A maximum CHF of 226 W/cm^2 was achieved with a coating of < 1µm.

v. The important findings and data generated in the experimental testing were summarized in 15 journal articles, 1 patent application and disseminated at 8 conference proceedings.

5.2 Future Recommendations

In this work, the efficacy of surfaces developed through the concept of separate liquid-vapor pathways and enhanced macroconvection heat transfer mechanisms (selectively coated open microchannels and NRFCs) to reduce the counter-flow resistance have been demonstrated. This concept was exploited to increase the CHF and HTC to unprecedented values. Additionally, the role of wicking, microlayer evaporation and transient conduction to simultaneously increase CHF and HTC on graphene and chemically heterogeneous surfaces was shown through experimental and theoretical work. Some relevant suggestions for the future work are discussed here:

Performance metrics: The quest to create energy efficient and safe cooling systems enforces the need for high heat flux dissipation at low wall superheats in pool boiling systems. It is desirable to develop surfaces in pool boiling with flux dissipation in excess of 1 kW/cm^2 and wall superheats less than 10 °C in the near future. The mechanistic tool described in this work provides a pathway to enhance both CHF and HTC. Porous, graphene, CNT and chemical coatings have demonstrated the ability to alter the bubble dynamics and rewetting pathways. Strategic implementation of these enhancements with the macroconvective flow field is expected to further bolster the performance. On surfaces with graphene, copper interlaced graphene has shown tremendous performance enhancement levels. Further refinement in the electrochemical parameters is suggested to develop unique morphologies to increase the CHF and HTC.

Experimental parameters: The experimental tests were conducted under atmospheric pressure in the current work. A number of applications (space, refrigeration, cryogenics, etc.) demand different operating pressures as system design. Alternatively, the degree of

subcooling can also alter the single-phase jet impingement flow. To facilitate the current concept in these applications, it is essential to generate experimental data to ascertain the efficacy of separate liquid-vapor pathways, and macroconvective heat transfer at different operating pressures and degrees of subcooling. The test surfaces developed with graphene and other chemical coatings were not tested with refrigerants and other dielectric fluids. Therefore, experimental testing with other refrigerants will shed light on the parametric trends and further geometrical refinement opportunities for a specific fluid-surface combination.

Hysteresis and aging studies: The adverse environmental conditions encountered in various applications requires a thorough study of the hysteresis effects due to varying operating heat flux ranges. In addition, the aging characteristics and mechanical degradation of the samples due to fluid contamination, fouling and the chaotic nature of boiling will be helpful for its realization in practical applications.

Theoretical model / CHF prediction: Since the arrangement of liquid-vapor flow fields are confined to specific regions on the heater surface, it is possible to develop a hydrodynamic model to explain the stability of the column and the influence of macroconvective jet impingement to predict the CHF. This method will be highly beneficial in understanding the parameters contributing to the enhancement, the associated forces and the underlying mechanism to further refine specific parameters in this configuration. Additionally, understanding the fluid dynamics property groups (Reynolds number, Prandtl number, etc.) and their effect on the microscale geometry is suggested for further exploitation of the macroconvection mechanism. This will aid in developing a

unified representation of the fluid dynamics and heat transfer mechanism on surfaces with separate liquid-vapor pathways.

Numerical work: Simulating two-phase flow with similar experimental conditions in the macroconvective arrangement could lead to valuable information regarding bubble motion, local heat flux levels, velocity and pressure contours in the macroconvective field. This will be helpful in quantitatively estimating the liquid-vapor velocities in the vicinity of the heater surface.

5.3 Societal Context

The work conducted here has relevance in numerous two-phase heat transfer applications. The mechanistic understanding in the thesis work primarily caters to the electronics cooling industry, but can also be applied to the refrigeration, process, air-conditioning, desalination, nuclear and cryogenic industries. The main goal in this work was to extend the limits of pool boiling CHF and HTC. In the electronics cooling industry, this results in a wider operating range with increased efficiency of heat transfer. These improved performance metrics enable compaction and allows for the packing of a larger number of electronic components, both at the component level and system level. The outcome of this work will lead to advancements in electronics packaging architecture, which will enable faster and more reliable future electronic devices. The heat sink to fluid thermal resistance is significantly reduced due to the high HTCs as a result of enhanced macroconvection through separate liquid-vapor pathways. An example of reduced convective thermal resistance using the sintered-fin-top surfaces (Chapter 4(a), section 4.1.1.6) and FC-87 is shown in Figure 86.

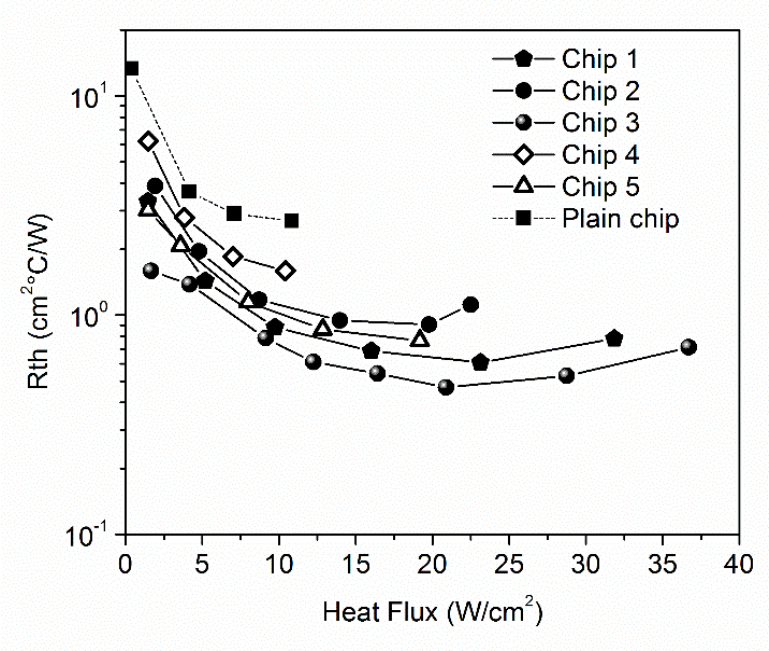

Figure 90. Measured variation of convective thermal resistance with heat flux for sintered-fin tops test chips with FC-87.

Similarly, flooded evaporators in refrigeration systems exclusively employ pool boiling heat transfer on the external surface. Increasing CHF allows for a large volumetric heat transfer rate, compact evaporators and lower refrigerant inventory. The refrigerant-side resistances are dominant, and therefore increasing the HTC is of prime importance to increase the boiling energy efficiency. The separate-liquid vapor pathways was successfully implemented on tubular surfaces as demonstrated by Raghupathi et al. [59]. Using the circumferential temperature variation as a guidance, a bubble diverter was inserted at the bottom of the tube to mitigate bubble agglomeration. Figure 91(a-d) shows the bubble being diverted away from the fin through EMF, creating an efficient liquid circulation in the region. Figure 91(e) shows the heat transfer performance of the diverter tube compared to a plain tube with water as the working fluid.

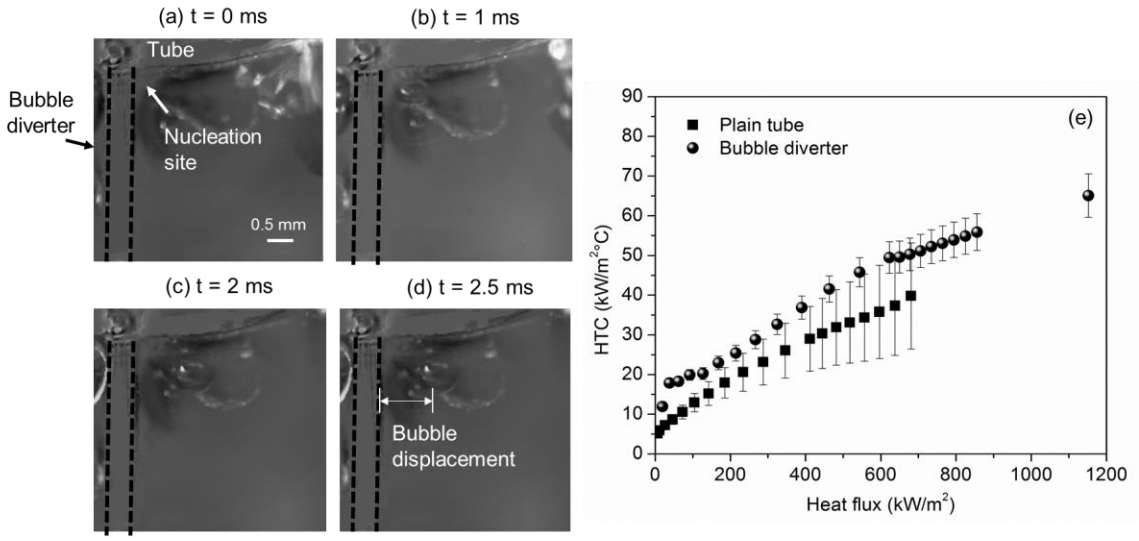

Figure 91. Bubble displacement captured using high speed imaging at 4000 fps. Bubble nucleation is shown in (a), and displacement from the fin is shown in (b)–(d). (e) HTC vs heat flux for the plain tube and the tube with a bubble diverter.

6. References

[1] Hsu, Y. Y., and Graham, R. W., 1961, "Analytical and Experimental Study of Thermal Boundary Layer and Ebullition Cycle in Nucleate Boiling," Natl. Aeronaut. Space Adm., Tech. Note, Washington, [D.C.], p. 43.

[2] Hsu, Y. Y., 1961, "On Size Range of Active Nucleation Cavities on Heating Surface," *ASME Meeting WA-177, Nov 26-Dec 1 1961*, American Society of Mechanical Engineers (ASME), p. 7.

[3] Kandlikar, S. G., and Spiesman, P. H., 1998, "Effect of Surface Finish on Flow Boiling Heat Transfer," *Proceedings of the 1998 ASME International Mechanical Engineering Congress and Exposition, November 15, 1998 - November 20, 1998*, ASME, pp. 157–163.

[4] Kandlikar, S. G., Shoji, M., and Dhir, V. K., 1999, *Handbook of Phase Change: Boiling and Condensation*, Taylor & Francis.

[5] "The Measurement of Rapid Surface Temperature Fluctuations during Nucleate Boiling of Water - Moore - 1961 - AIChE Journal - Wiley Online Library" [Online]. Available: http://onlinelibrary.wiley.com/doi/10.1002/aic.690070418/abstract.

[6] Hendricks, R. C., and Sharp, R. R., 1964, "Initiation of Cooling due to Bubble Growth on a Heating Surface." Natl. Aeronaut. Space Adm., Tech. Note, Washington, [D.C.], D-2290.

[7] Cooper, M. G., and Lloyd, A. J. P., 1969, "The Microlayer in Nucleate Pool Boiling," Int. J. Heat Mass Transf., **12**(8), pp. 895–913.

[8] Moghaddam, S., and Kiger, K., 2009, “Physical Mechanisms of Heat Transfer during Single Bubble Nucleate Boiling of FC-72 under Saturation Conditions. II: Theoretical Analysis,” Int. J. Heat Mass Transf., **52**(5–6), pp. 1295–1303.

[9] Kandlikar, S. G., 2017, “Enhanced Macroconvection Mechanism With Separate Liquid–Vapor Pathways to Improve Pool Boiling Performance,” J. Heat Transf., **139**(5), p. 051501.

[10] Mikic, B. B., and Rohsenow, W. M., 1969, “A New Correlation of Pool-Boiling Data Including the Effect of Heating Surface Characteristics,” J. Heat Transf., **91**(2), pp. 245–250.

[11] Mikic, B. B., Rohsenow, W. M., and Griffith, P., 1970, “On Bubble Growth Rates,” Int. J. Heat Mass Transf., **13**(4), pp. 657–666.

[12] Han, C.-Y., 1962, “The Mechanism of Heat Transfer in Nucleate Pool Boiling,” Technical report - Heat Transfer Laboratory, no. 19. Massachusetts Institute of Technology.

[13] Demiray, F., and Kim, J., 2004, “Microscale Heat Transfer Measurements during Pool Boiling of FC-72: Effect of Subcooling,” Int. J. Heat Mass Transf., **47**(14), pp. 3257–3268.

[14] Nukiyama, S., 1934, “Maximum and Minimum Values of Heat Transmitted from Metal to Boiling Water under Atmospheric Pressure,” Soc. Mech. Eng. Jpn. -- J., **37**(206), pp. 367–374.

[15] Moore, G. E., and others, 1998, “Cramming More Components onto Integrated Circuits,” Proc. IEEE, **86**(1), pp. 82–85.

[16] Alkharabsheh, S., Fernandes, J., Gebrehiwot, B., Agonafer, D., Ghose, K., Ortega, A., Joshi, Y., and Sammakia, B., 2015, "A Brief Overview of Recent Developments in Thermal Management in Data Centers," J. Electron. Packag., **137**(4), pp. 040801-040801-19.

[17] Frank P. Incropera, Theodore L. Bergman, Adrienne S. Lavine, and David P. DeWitt, *Fundamentals of Heat and Mass Transfer*, John Wiley & Sons, 2011.

[18] Chang, J. Y., and You, S. M., 1997, "Enhanced Boiling Heat Transfer from Micro-Porous Cylindrical Surfaces in Saturated FC-87 and R-123," J. Heat Transf.-Trans. Asme, **119**(2), pp. 319–325.

[19] "Manufacturing Energy Consumption Survey (MECS) - Data - U.S. Energy Information Administration (EIA)" [Online]. Available: https://www.eia.gov/consumption/manufacturing/data/2010/#r5. [Accessed: 25-Oct-2017].

[20] 2016, "EIA - Electricity Data" [Online]. Available: https://www.eia.gov/electricity/monthly/epm_table_grapher.cfm?t=epmt_5_03. [Accessed: 24-Aug-2016].

[21] Tonner, J. B., Hinge, S., and Legorreta, C., 2001, "Plates—the next Breakthrough in Thermal Desalination," Desalination, **134**(1), pp. 205–211.

[22] Yao, Z., Lu, Y.-W., and Kandlikar, S. G., 2011, "Direct Growth of Copper Nanowires on a Substrate for Boiling Applications," IET Micro Nano Lett., **6**(7), pp. 563–566.

[23] Patil, C. M., and Kandlikar, S. G., 2014, “Pool Boiling Enhancement through Microporous Coatings Selectively Electrodeposited on Fin Tops of Open Microchannels,” Int. J. Heat Mass Transf., **79**, pp. 816–828.

[24] Rahman, M. M., Ölçeroğlu, E., and McCarthy, M., 2014, “Role of Wickability on the Critical Heat Flux of Structured Superhydrophilic Surfaces,” Langmuir, **30**(37), pp. 11225–11234.

[25] Betz, A. R., Xu, J., Qiu, H., and Attinger, D., 2010, “Do Surfaces with Mixed Hydrophilic and Hydrophobic Areas Enhance Pool Boiling?,” Appl. Phys. Lett., **97**(14), pp. 141909-141909–3.

[26] Kandlikar, S. G., 2001, “A Theoretical Model to Predict Pool Boiling CHF Incorporating Effects of Contact Angle and Orientation,” J. Heat Transf., **123**(6), p. 1071.

[27] Pastuszko, R., and Piasecka, M., 2012, “Pool Boiling on Surfaces with Mini-Fins and Micro-Cavities,” 6th Eur. Therm. Sci. Conf. Eurotherm 2012, **395**, p. 012137.

[28] Pastuszko, R., 2013, “Pool Boiling on Rectangular Fins with Tunnel-Pore Structure,” Efm12 - Exp. Fluid Mech. 2012, **45**.

[29] Rainey, K. N., You, S. M., and Lee, S., 2003, “Effect of Pressure, Subcooling, and Dissolved Gas on Pool Boiling Heat Transfer from Microporous, Square Pin-Finned Surfaces in FC-72,” Int. J. Heat Mass Transf., **46**(1), pp. 23–35.

[30] Guglielmini, G., Misale, M., and Schenone, C., 2002, “Boiling of Saturated FC-72 on Square Pin Fin Arrays,” Int. J. Therm. Sci., **41**(7), pp. 599–608.

[31] Patil, C. M., and Kandlikar, S. G., 2014, “Review of the Manufacturing Techniques for Porous Surfaces Used in Enhanced Pool Boiling,” Heat Transf. Eng., **35**(10), pp. 887–902.

[32] Nakayama, W., Daikoku, T., Kuwahara, H., and Nakajima, T., 1980, “Dynamic Model of Enhanced Boiling Heat Transfer on Porous Surfaces—Part I: Experimental Investigation,” J. Heat Transf., **102**(3), pp. 445–450.

[33] Nakayama, W., Daikoku, T., Kuwahara, H., and Nakajima, T., 1980, “Dynamic Model of Enhanced Boiling Heat Transfer on Porous Surfaces—Part II: Analytical Modeling,” J. Heat Transf., **102**(3), pp. 451–456.

[34] WEBB, R. L., 1983, “Nucleate Boiling on Porous Coated Surfaces,” Heat Transf. Eng., **4**(3–4), pp. 71–82.

[35] Li, C., and Peterson, G. P., 2007, “Parametric Study of Pool Boiling on Horizontal Highly Conductive Microporous Coated Surfaces,” J. Heat Transf., **129**(11), p. 1465.

[36] Afgan, N., Stefanovic, M., Jovanovic, L., and Pislar, V., 1973, “Determination of the Statistical Characteristics of Temperature Fluctuation in Pool Boiling,” Int. J. Heat Mass Transf., **16**(2), pp. 249–56.

[37] Bergles, A. E., and Chyu, M. C., 1981, “Characteristics of Nucleate Pool Boiling from Porous Metallic Coatings,” Adv. Enhanc. Heat Transf.-1981 ASME HTD, **18**, pp. 61–71.

[38] Mudawar, I., and Anderson, T. M., “Microelectronic Cooling by Enhanced Pool Boiling of a Dielectric Fluorocarbon Liquid,” Trans. ASME, **111**, pp. 752–759.

[39] Liter, S. G., and Kaviany, M., 2001, "Pool-Boiling CHF Enhancement by Modulated Porous-Layer Coating: Theory and Experiment," Int. J. Heat Mass Transf., **44**(22), pp. 4287–4311.

[40] Li, C. H., and Peterson, G. P., 2010, "Experimental Study of Enhanced Nucleate Boiling Heat Transfer on Uniform and Modulated Porous Structures," Front. Heat Mass Transf., **1**(2).

[41] Li, C. H., Li, T., Hodgins, P., Hunter, C. N., Voevodin, A. A., Jones, J. G., and Peterson, G. P., 2011, "Comparison Study of Liquid Replenishing Impacts on Critical Heat Flux and Heat Transfer Coefficient of Nucleate Pool Boiling on Multiscale Modulated Porous Structures," Int. J. Heat Mass Transf., **54**(15–16), pp. 3146–3155.

[42] Mori, S., and Okuyama, K., 2009, "Enhancement of the Critical Heat Flux in Saturated Pool Boiling Using Honeycomb Porous Media," Int. J. Multiph. Flow, **35**(10), pp. 946–951.

[43] Bai, L., Zhang, L., Lin, G., and Peterson, G. P., 2016, "Pool Boiling with High Heat Flux Enabled by a Porous Artery Structure," Appl. Phys. Lett., **108**(23), p. 233901.

[44] Rahman, M. M., and McCarthy, M., 2016, "Boiling Enhancement on Nanostructured Surfaces with Engineered Variations in Wettability and Thermal Conductivity," Heat Transf. Eng., Vol. 38, Iss. 14-15.

[45] Ahn, H. S., Lee, C., Kim, H., Jo, H., Kang, S., Kim, J., Shin, J., and Kim, M. H., 2010, "Pool Boiling CHF Enhancement by Micro/Nanoscale Modification of Zircaloy-4 Surface," Nucl. Eng. Des., **240**(10), pp. 3350–3360.

[46] Zou, A., and Maroo, S. C., 2013, "Critical Height of Micro/Nano Structures for Pool Boiling Heat Transfer Enhancement," Appl. Phys. Lett., **103**(22), p. 221602.

[47] Zou, A., Singh, D. P., and Maroo, S. C., 2016, "Early-Evaporation of Microlayer for Boiling Heat Transfer Enhancement," Langmuir, 32 (42), pp 10808-10814.

[48] Berg, J. C., 2010, *An Introduction to Interfaces & Colloids: The Bridge to Nanoscience*, World Scientific.

[49] Oliver, J. F., and Mason, S. G., 1977, "Microspreading Studies on Rough Surfaces by Scanning Electron Microscopy," J. Colloid Interface Sci., **60**(3), pp. 480–487.

[50] Oliver, J. P., Huh, C., and Mason, S. G., 1980, "An Experimental Study of Some Effects of Solid Surface Roughness on Wetting," Colloids Surf., **1**(1), pp. 79–104.

[51] Johnson, R. E., Dettre, R. H., and Brandreth, D. A., 1977, "Dynamic Contact Angles and Contact Angle Hysteresis," J. Colloid Interface Sci., **62**(2), pp. 205–212.

[52] Cassie, A. B. D., and Baxter, S., 1944, "Wettability of Porous Surfaces," Trans. Faraday Soc., **40**, pp. 546–551.

[53] Brochard, F., 1989, "Motions of Droplets on Solid Surfaces Induced by Chemical or Thermal Gradients," langmuir, **5**(2), pp. 432–438.

[54] Decker, E. L., and Garoff, S., 1997, "Contact Line Structure and Dynamics on Surfaces with Contact Angle Hysteresis," Langmuir, **13**(23), pp. 6321–6332.

[55] Varagnolo, S., Ferraro, D., Fantinel, P., Pierno, M., Mistura, G., Amati, G., Biferale, L., and Sbragaglia, M., 2013, "Stick-Slip Sliding of Water Drops on Chemically Heterogeneous Surfaces," Phys. Rev. Lett., **111**(6), p. 066101.

[56] Wayner, P. C., Kao, Y. K., and LaCroix, L. V., 1976, "The Interline Heat-Transfer Coefficient of an Evaporating Wetting Film," Int. J. Heat Mass Transf., **19**(5), pp. 487–492.

[57] Panchamgam, S. S., Chatterjee, A., Plawsky, J. L., and Wayner, P. C., 2008, "Comprehensive Experimental and Theoretical Study of Fluid Flow and Heat Transfer in a Microscopic Evaporating Meniscus in a Miniature Heat Exchanger," Int. J. Heat Mass Transf., **51**(21), pp. 5368–5379.

[58] Kunkelmann, C., Ibrahem, K., Schweizer, N., Herbert, S., Stephan, P., and Gambaryan-Roisman, T., 2012, "The Effect of Three-Phase Contact Line Speed on Local Evaporative Heat Transfer: Experimental and Numerical Investigations," Int. J. Heat Mass Transf., **55**(7), pp. 1896–1904.

[59] Raghupathi, P. A., and Kandlikar, S. G., 2017, "Pool Boiling Enhancement through Contact Line Augmentation," Appl. Phys. Lett., **110**(20), p. 204101.

[60] Ahn, H. S., Kim, J. M., and Kim, M. H., 2013, "Experimental Study of the Effect of a Reduced Graphene Oxide Coating on Critical Heat Flux Enhancement," Int. J. Heat Mass Transf., **60**, pp. 763–771.

[61] Kim, J. M., Kim, T., Kim, J., Kim, M. H., and Ahn, H. S., 2014, "Effect of a Graphene Oxide Coating Layer on Critical Heat Flux Enhancement under Pool Boiling," Int. J. Heat Mass Transf., **77**, pp. 919–927.

[62] Ho Seon Ahn, Ji Min Kim, Kaviany, M., and Moo Hwan Kim, 2014, "Pool Boiling Experiments in Reduced Graphene Oxide Colloids. Part I - Boiling Characteristics," Int. J. Heat Mass Transf., **74**, pp. 501–12.

[63] Park, S. D., Lee, S. W., Kang, S., Bang, I. C., Kim, J. H., Shin, H. S., Lee, D. W., and Lee, D. W., 2010, "Effects of Nanofluids Containing Graphene/Graphene-Oxide Nanosheets on Critical Heat Flux," Appl. Phys. Lett., **97**(2), p. 023103.

[64] Kandlikar, S. G., 2013, "Controlling Bubble Motion over Heated Surface through Evaporation Momentum Force to Enhance Pool Boiling Heat Transfer," Appl. Phys. Lett., **102**(5), p. 051611 (5 pp.).

[65] Cooke, D., and Kandlikar, S. G., 2012, "Effect of Open Microchannel Geometry on Pool Boiling Enhancement," Int. J. Heat Mass Transf., **55**(4), pp. 1004–13.

[66] Cooke, D., and Kandlikar, S. G., 2011, "Pool Boiling Heat Transfer and Bubble Dynamics Over Plain and Enhanced Microchannels," J. Heat Transf., **133**(5), p. 052902 (9 pp.).

[67] "Http://Www.dupont.com/Content/Dam/Dupont/Products-and-Services/Membranes-and-Films/Polyimde-Films/Documents/DEC-Kapton-Summary-of-Properties.pdf."

[68] Kalani, A., and Kandlikar, S. G., 2013, "Enhanced Pool Boiling with Ethanol at Subatmospheric Pressures for Electronics Cooling," J. Heat Transf., **135**(11).

[69] Kalani, A., and Kandlikar, S. G., 2014, "Evaluation of Pressure Drop Performance during Enhanced Flow Boiling in Open Microchannels with Tapered Manifolds," J. Heat Transf., **136**(5).

[70] "1" OFHC COPPER PLATE C101 - Online Metal Store" [Online]. Available: http://www.onlinemetals.com/merchant.cfm?pid=13032&step=4&showunits=inches&id=966&top_cat=8. [Accessed: 24-Oct-2017].

[71] Kandlikar, S. G., 2001, "A Theoretical Model to Predict Pool Boiling CHF Incorporating Effects of Contact Angle and Orientation," J. Heat Transf., **123**(6), pp. 1071–1079.

[72] Liu, F., 2016, A Study of Sintered Copper Porous Surfaces for Pool Boiling Enhancement, MS Thesis, Rochester Institute of Technology.

[73] Patil, C. M., and Kandlikar, S. G., 2014, "Pool Boiling Enhancement through Microporous Coatings Selectively Electrodeposited on Fin Tops of Open Microchannels," Int. J. Heat Mass Transf., **79**, pp. 816–828.

[74] Forrest, E., Williamson, E., Buongiorno, J., Hu, L.-W., Rubner, M., and Cohen, R., 2010, "Augmentation of Nucleate Boiling Heat Transfer and Critical Heat Flux Using Nanoparticle Thin-Film Coatings," Int. J. Heat Mass Transf., **53**(1–3), pp. 58–67.

[75] Chang, J. Y., and You, S. M., 1997, "Enhanced Boiling Heat Transfer from Microporous Surfaces: Effects of a Coating Composition and Method," Int. J. Heat Mass Transf., **40**(18), pp. 4449–4460.

[76] Jaikumar, A., and Kandlikar, S. G., 2015, "Enhanced Pool Boiling Heat Transfer Mechanisms for Selectively Sintered Open Microchannels," Int. J. Heat Mass Transf., **88**, pp. 652–661.

[77] Kruse, C., Tsubaki, A., Zuhlke, C., Anderson, T., Alexander, D., Gogos, G., and Ndao, S., 2016, "Secondary Pool Boiling Effects," Appl. Phys. Lett., **108**(5), p. 051602.

[78] Kandlikar, S. G., 2016, "Enhanced Macro-Convection Mechanism with Separate Liquid-Vapor Pathways to Improve Pool Boiling Performance," J. Heat Transf.

[79] Rallis, C. J., and Jawurek, H. H., 1964, “Latent Heat Transport in Saturated Nucleate Boiling,” Int. J. Heat Mass Transf., **7**(10), pp. 1051–1068.

[80] Hughmark, G. A., 1967, “Holdup and Mass Transfer in Bubble Columns,” Ind. Eng. Chem. Process Des. Dev., **6**(2), pp. 218–220.

[81] Mishima, K., and Hibiki, T., 1996, “Some Characteristics of Air-Water Two-Phase Flow in Small Diameter Vertical Tubes,” Int. J. Multiph. Flow, **22**(4), pp. 703–712.

[82] Bhagwat, S. M., and Ghajar, A. J., 2012, “Similarities and Differences in the Flow Patterns and Void Fraction in Vertical Upward and Downward Two Phase Flow,” Exp. Therm. Fluid Sci., **39**, pp. 213–227.

[83] Mudawar, I., 1990, “Cooling of a Multichip Electronic Iodyle by Leans of Confined Two-Dimensional Jets of Dielectric Liquid,” J. Heat Transf., **112**, p. 891.

[84] Bonjour, J., and Lallemand, M., 1998, “Flow Patterns during Boiling in a Narrow Space between Two Vertical Surfaces,” Int. J. Multiph. Flow, **24**(6), pp. 947–960.

[85] Kays, W. M., and others, 1953, Numerical Solutions for Laminar Flow Heat Transfer in Circular Tubes, Office of Naval Research, United States, 47 pages.

[86] Chen, R.-Y., 1973, “Flow in the Entrance Region at Low Reynolds Numbers,” J. Fluids Eng., **95**(1), pp. 153–158.

[87] Emery, T. S., and Kandlikar, S. G., 2017, “Pool Boiling with Four Non-Ozone Depleting Refrigerants and Comparison with Previously Established Correlations,” Exp. Therm. Fluid Sci., **85**, pp. 132–139.

[88] Chen, Y.-M., He, S.-M., Huang, C.-H., Huang, C.-C., Shih, W.-P., Chu, C.-L., Kong, J., Li, J., and Su, C.-Y., 2016, “Ultra-Large Suspended Graphene as a Highly Elastic Membrane for Capacitive Pressure Sensors,” Nanoscale, **8**(6), pp. 3555–3564.

[89] Singh, B. P., Jena, B. K., Bhattacharjee, S., and Besra, L., 2013, "Development of Oxidation and Corrosion Resistance Hydrophobic Graphene Oxide-Polymer Composite Coating on Copper," Surf. Coat. Technol., **232**, pp. 475–481.

[90] Andonovic, B., Ademi, A., Grozdanov, A., Paunović, P., and Dimitrov, A. T., 2015, "Enhanced Model for Determining the Number of Graphene Layers and Their Distribution from X-Ray Diffraction Data," Beilstein J. Nanotechnol., **6**(1), pp. 2113–2122.

[91] Raj, R., Maroo, S. C., and Wang, E. N., 2013, "Wettability of Graphene," Nano Lett., **13**(4), pp. 1509–1515.

[92] Rafiee, J., Xi Mi, Gullapalli, H., Thomas, A. V., Yavari, F., Yunfeng Shi, Ajayan, P. M., and Koratkar, N. A., 2012, "Wetting Transparency of Graphene," Nat. Mater., **11**(3), pp. 217–22.

[93] Balandin, A. A., Ghosh, S., Bao, W., Calizo, I., Teweldebrhan, D., Miao, F., and Lau, C. N., 2008, "Superior Thermal Conductivity of Single-Layer Graphene," Nano Lett., **8**(3), pp. 902–907.

[94] Yan, Z., Nika, D. L., and Balandin, A. A., 2015, "Review of Thermal Properties of Graphene and Few-Layer Graphene: Applications in Electronics," Mesoscale and Nanoscale Physics, Cond-Mat, IET Circuits, Devices and Systems, 9, 4.

[95] Seo, H., Chu, J. H., Kwon, S.-Y., and Bang, I. C., 2015, "Pool Boiling CHF of Reduced Graphene Oxide, Graphene, and SiC-Coated Surfaces under Highly Wettable FC-72," Int. J. Heat Mass Transf., **82**, pp. 490–502.

[96] Fan, L.-W., Li, J.-Q., Li, D.-Y., Zhang, L., Yu, Z.-T., and Cen, K.-F., 2015, "The Effect of Concentration on Transient Pool Boiling Heat Transfer of Graphene-Based Aqueous Nanofluids," Int. J. Therm. Sci., **91**, pp. 83–95.

[97] Li, D., Mueller, M. B., Gilje, S., Kaner, R. B., and Wallace, G. G., 2008, "Processable Aqueous Dispersions of Graphene Nanosheets," Nat. Nanotechnol., **3**(2), pp. 101–105.

[98] Heltzel, A., Mishra, C., Ruoff, R. S., and Fleming, A., 2012, "Analysis of an Ultrathin Graphite-Based Compact Heat Exchanger," Heat Transf. Eng., **33**(11), pp. 947–956.

[99] Loryuenyong, V., Totepvimarn, K., Eimburanapravat, P., Boonchompoo, W., Buasri, A., Loryuenyong, V., Totepvimarn, K., Eimburanapravat, P., Boonchompoo, W., and Buasri, A., 2013, "Preparation and Characterization of Reduced Graphene Oxide Sheets via Water-Based Exfoliation and Reduction Methods, Preparation and Characterization of Reduced Graphene Oxide Sheets via Water-Based Exfoliation and Reduction Methods," Adv. Mater. Sci. Eng. Adv. Mater. Sci. Eng., 2013, p. e923403.

[100] Hassan, H. M. A., Abdelsayed, V., Khder, A. E. R. S., AbouZeid, K. M., Terner, J., El-Shall, M. S., Al-Resayes, S. I., and El-Azhary, A. A., 2009, "Microwave Synthesis of Graphene Sheets Supporting Metal Nanocrystals in Aqueous and Organic Media," J. Mater. Chem., **19**(23), p. 3832.

[101] Chu, K.-H., Enright, R., and Wang, E. N., 2012, "Structured Surfaces for Enhanced Pool Boiling Heat Transfer," Appl. Phys. Lett., **100**(24), pp. 241603-241603–4.

[102] Kim, J., 2009, “Review of Nucleate Pool Boiling Bubble Heat Transfer Mechanisms,” Int. J. Multiph. Flow, **35**(12), pp. 1067–1076.

[103] Utaka, Y., Kashiwabara, Y., and Ozaki, M., 2013, “Microlayer Structure in Nucleate Boiling of Water and Ethanol at Atmospheric Pressure,” Int. J. Heat Mass Transf., **57**(1), pp. 222–230.

[104] Kandlikar, S., 2016, “Enhanced Macro-Convection Mechanism with Separate Liquid-Vapor Pathways to Improve Pool Boiling Performance,” Journal of Heat Transfer.

[105] Maroo, S. C., 2016, “Origin of Surface-Driven Passive Liquid Flows,” Langmuir, **32**(34), pp. 8593–8597.

[106] WEBB, R. L., 1981, “Nucleate Boiling on Porous Coated Surfaces,” Heat Transf. Eng., **4**(3–4), pp. 71–82.

[107] Patil, C. M., Santhanam, K. S. V., and Kandlikar, S. G., 2014, “Development of a Two-Step Electrodeposition Process for Enhancing Pool Boiling,” Int. J. Heat Mass Transf., **79**, pp. 989–1001.

[108] Santhanam, V., Kalathur, S., Kandlikar, S. G., Mejia, V., and Yue, Y., 2016, Electrochemical Process for Producing Graphene, Graphene Oxide, Metal Composites, and Coated Substrates, US 20160017502 A1.

[109] Ahn, H. S., Kim, J. M., Kaviany, M., and Kim, M. H., 2014, “Pool Boiling Experiments in Reduced Graphene Oxide Colloids Part II–Behavior after the CHF, and Boiling Hysteresis,” Int. J. Heat Mass Transf., **78**, pp. 224–231.

[110] Chu, K.-H., Joung, Y. S., Enright, R., Buie, C. R., and Wang, E. N., 2013, "Hierarchically Structured Surfaces for Boiling Critical Heat Flux Enhancement," Appl. Phys. Lett., **102**(15), p. 151602.

[111] Mukherjee, A., and Kandlikar, S. G., 2007, "Numerical Study of Single Bubbles with Dynamic Contact Angle during Nucleate Pool Boiling," Int. J. Heat Mass Transf., **50**(1), pp. 127–138.

[112] Kandlikar, S. G., and Steinke, M. E., 2002, "Contact Angles and Interface Behavior during Rapid Evaporation of Liquid on a Heated Surface," Int. J. Heat Mass Transf., **45**(18), pp. 3771–3780.

[113] Cho, H. J., Preston, D. J., Zhu, Y., and Wang, E. N., 2016, "Nanoengineered Materials for Liquid–vapour Phase-Change Heat Transfer," Nat. Rev. Mater., **2**, p. 16092.

[114] Mahamudur Rahman, M., Pollack, J., and McCarthy, M., 2015, "Increasing Boiling Heat Transfer Using Low Conductivity Materials," Sci. Rep., **5**, p. 13145.

[115] O'Hanley, H., Coyle, C., Buongiorno, J., McKrell, T., Lin-Wen Hu, Rubner, M., and Cohen, R., 2013, "Separate Effects of Surface Roughness, Wettability, and Porosity on the Boiling Critical Heat Flux," Appl. Phys. Lett., **103**(2), p. 024102 (5 pp.).

[116] Forster, H. K., and Zuber, N., 1955, "Dynamics of Vapor Bubbles and Boiling Heat Transfer," AIChE J., **1**(4), pp. 531–535.

[117] Kim, S. J., Bang, I. C., Buongiorno, J., and Hu, L. W., 2007, "Surface Wettability Change during Pool Boiling of Nanofluids and Its Effect on Critical Heat Flux," Int. J. Heat Mass Transf., **50**(19–20), pp. 4105–4116.

7.1 Appendix I - Thermocouple Calibration

The thermocouples used in the experimental studies, namely T_1, T_2 and T_3 were calibrated using the OMEGA Hot Point® Dry Block Probe cell. The set point temperature were varied between 25 °C and 200 °C. This range was selected as it encompasses the boiling temperature test ranges. Figure 92 shows the calibration data for the top (T_1) thermocouple. A linear line fit was established to estimate the slope and intercept of the line. These values were added as numeric constants in LabVIEW to estimate the real time temperatures accurately. The R^2 value is also shown in this plot which shows a good linear line fit. Similar procedures were followed with the T2 and T3 thermocouples. The uncertainty in the precision values was equal to ±0.1 °C which was incorporated in the uncertainty analysis.

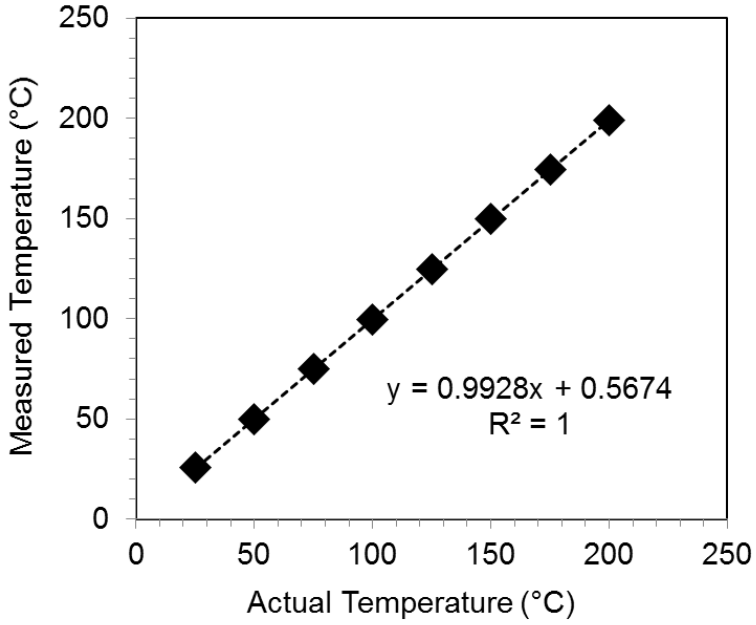

Figure 92. Thermocouple calibration of temperature T_1.

7.2 Appendix II - Heat Loss Study

The design of the test chip and its assembly in the garolite casing demands area outside the boiling surface which results in heat loss to the ambient air due to natural convection. A heat loss study was performed experimentally in which a fiberglass insulation is made to cover the boiling surface and a single phase test is run in air to calculate the heat loss. The heat loss is plotted against the difference in temperature between the surface and ambient air. A linear line fit equation is established and the corrected heat flux is computed.

$$q''_{corrected} = q''_{corrected} - q''_{Heat\ loss} \tag{40}$$

Figure 93 below shows the plot of the heat loss to ambient air during the testing procedure.

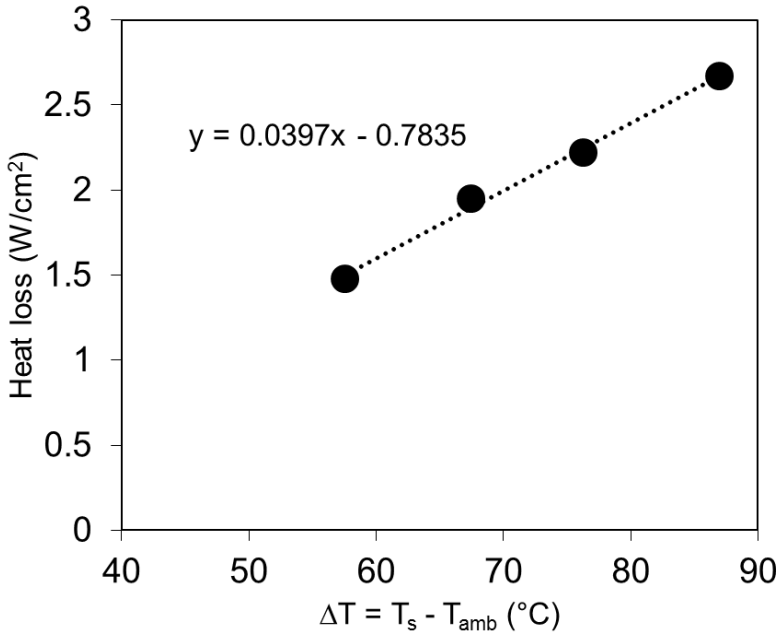

Figure 93. Heat loss to ambient air.

7.3 Appendix – III - Chemical Characterization Equipment

Table 15. Chemical characterization equipment's and faculty collaborator at RIT.

Test	Equipment	Faculty collaborator
X-ray diffraction	Rigaku DMAZ-IIB X-Ray Diffractometer	Dr. Surendra Gupta
FTIR spectroscopy	Shimadzu, IR Prestige 21	Dr. Anju Gupta
Raman Spectroscopy	Jobin Yvon Horriba LabRAM HR Raman Spectroscope	Dr. Anju Gupta
SEM	TESCAN Field Emission Mira III LMU	Dr. Anju Gupta
DLS	Malvern Instruments Zetasizer Nano ZS	Dr. Anju Gupta
TGA	TA Instruments Q500 Thermogravimetric analyzer	Dr. Anju Gupta

7.4 Appendix IV - Error Propagation – Derivation of Uncertainties

The derivation of the uncertainty equations shown in Section 3.3 (Chapter 3) is shown below.

7.4.1 Heat Flux Uncertainty Derivation

The relation for heat flux, measured from the three heater block thermocouples, is computed from Eqns. (10) and (11) in Chapter 3 (section 3.1), and shown below in Eqn. (38)

$$q'' = -k_{Cu}\left(\frac{3T_1 - 4T_2 + T_3}{2\Delta d}\right) \tag{41}$$

The variables in Eqn. (41) are substituted into the error propagation equation, as shown in Eqn. (42) and Eqn. (43) below.

$$\frac{U_{q"}}{q"} = \sqrt{\sum_{i=1}^{n}\left(\frac{\partial q"}{\partial \sigma_i}U_{\sigma_i}\right)^2} \tag{42}$$

$$\frac{U_{q"}}{q"} = \sqrt{\frac{\left(\frac{\partial q"}{\partial k_{Cu}}U_{k_{Cu}}\right)^2 + \left(\frac{\partial q"}{\partial \Delta d}U_{\Delta d}\right)^2 + \left(\frac{\partial q"}{\partial T_1}U_{T_1}\right)^2 + \left(\frac{\partial q"}{\partial T_2}U_{T_2}\right)^2 + \left(\frac{\partial q"}{\partial T_3}U_{T_3}\right)^2}{q"^2}} \tag{43}$$

It will be useful for the derivation to define a variable α defined as shown in Eqn. (44).

$$\alpha = 3T_1 - 4T_2 + T_3 \tag{44}$$

This will simplify the derivations that follow. The sensitivity coefficients for each variable, which are expressed as partial derivatives of the equation (function p in Eqn. 15) with respect to the individual variables of interest (variables a_i in Eqn. 15), are evaluated individually. The expressions are then rewritten in terms of the function of interest, q", as shown in Eqns. (45-49).

$$\frac{\partial q"}{\partial k_{Cu}} = -\frac{\alpha}{2\Delta d} = \frac{q"}{k_{Cu}} \tag{45}$$

$$\frac{\partial q"}{\partial \Delta x} = -k_{Cu}\frac{\alpha}{-2\Delta d^2} = -\frac{q"}{\Delta d} \tag{46}$$

$$\frac{\partial q"}{\partial T_1} = -k_{Cu}\frac{3}{2\Delta d} = \frac{3q"}{\alpha} \tag{47}$$

$$\frac{\partial q"}{\partial T_2} = -k_{Cu}\frac{-4}{2\Delta d} = -\frac{4q"}{\alpha} \tag{48}$$

$$\frac{\partial q"}{\partial T_3} = \frac{-k_{Cu}}{2\Delta d} = \frac{q"}{\alpha} \tag{49}$$

The terms in Eqns. (45-49) are substituted back into Eqn. (43) to obtain the following.

$$\frac{U_{q"}}{q"} = \sqrt{\frac{\left(\frac{q"}{k_{Cu}}U_{k_{Cu}}\right)^2 + \left(-\frac{q"}{\Delta d}U_{\Delta d}\right)^2 + \left(\frac{3q"}{\alpha}U_{T_1}\right)^2 + \left(-\frac{4q"}{\alpha}U_{T_2}\right)^2 + \left(\frac{q"}{\alpha}U_{T_3}\right)^2}{q"^2}} \quad (50)$$

The squared terms in each of the parentheses in the numerator of Eqn. (50) are expanded in Eqn. (47).

$$\frac{U_{q"}}{q"} = \sqrt{\frac{\frac{q"^2}{k_{Cu}^2}U_{k_{Cu}}^2 + \frac{q"^2}{\Delta x^2}U_{\Delta x}^2 + \frac{9q"^2}{\alpha^2}U_{T_1}^2 + \frac{16q"^2}{\alpha^2}U_{T_2}^2 + \frac{q"^2}{\alpha^2}U_{T_3}^2}{q"^2}} \quad (51)$$

This allows all q"^{2} terms in the numerator to cancel with the denominator, thus yielding the final expression in Eqn. (14), which is reproduced below in Eqn. (52).

$$\frac{U_{q"}}{q"} = \sqrt{\frac{{U_{k_{Cu}}}^2}{k_{Cu}^2} + \frac{{U_d}^2}{\Delta d^2} + \frac{9{U_{T_1}}^2}{\alpha^2} + \frac{16{U_{T_2}}^2}{\alpha^2} + \frac{{U_{T_3}}^2}{\alpha^2}} \quad (52)$$

7.4.2 Chip Surface Temperature Uncertainty Derivation

The relation for wall temperature is calculated from the heat flux over the projected area, taking into account the thermal resistance of copper, and the distance between the top thermocouple and the surface, as is shown in Eqn. (12) in Section 4. While the uncertainty in surface temperature is expected to be quite low, mathematical rigor dictates it is required in order to compute the uncertainty in heat transfer coefficient.

The variables are substituted into the error propagation equation (Eqn. 14), as shown in Eqn. (49) and Eqn. (50) below.

$$\frac{U_{T_s}}{T_s} = \sqrt{\sum_{i=1}^{n}\left(\frac{\partial T_s}{\partial \sigma_i}U_{\mathrm{ai}}\right)^2} \quad (53)$$

$$\frac{U_{T_s}}{T_s} = \sqrt{\frac{\left(\frac{\partial T_s}{\partial T_1} U_{T_1}\right)^2 + \left(\frac{\partial T_s}{\partial q"} U_{q"}\right)^2 + \left(\frac{\partial T_s}{\partial d_1} U_{d_1}\right)^2 + \left(\frac{\partial T_s}{\partial k_{Cu}} U_{k_{Cu}}\right)^2}{T_s^2}} \tag{54}$$

The sensitivity coefficients for each variable are evaluated individually below. The expressions are then rewritten in terms of the function of interest, T_s, as shown in Eqns. (55-58).

$$\frac{\partial T_s}{\partial T_1} = 1 - 0 = 1 = \frac{T_s}{T_s} \tag{55}$$

$$\frac{\partial T_s}{\partial q"} = 0 - 1\left(\frac{d_1}{k_{Cu}}\right) = -\left(\frac{d_1}{k_{Cu}}\right)\left(\frac{T_s}{T_s}\right) \tag{56}$$

$$\frac{\partial T_s}{\partial d_1} = -\frac{q"}{k_{Cu}} = -\frac{q"}{k_{Cu}}\left(\frac{T_s}{T_s}\right) \tag{57}$$

$$\frac{\partial T_s}{\partial k_{Cu}} = -q"d_1 = -q"d_1\left(\frac{T_s}{T_s}\right) \tag{58}$$

The terms in Eqns. (51-54) are substituted back into Eqn. (50) to obtain the following expression.

$$\frac{U_{T_s}}{T_s} = \sqrt{\frac{\left(\frac{T_s}{T_s} U_{T_1}\right)^2 + \left(-\left(\frac{d_1}{k_{Cu}}\right)\left(\frac{T_s}{T_s}\right) U_{q"}\right)^2 + \left(-\frac{q"}{k_{Cu}}\left(\frac{T_s}{T_s}\right) U_{d_1}\right)^2 + \left(-q"d_1\left(\frac{T_s}{T_s}\right) U_{k_{Cu}}\right)^2}{T_s^2}} \tag{59}$$

The squared terms in each of the parentheses in the numerator of Eqn. (59) are expanded in Eqn. (60).

$$\frac{U_{T_s}}{T_s} = \sqrt{\frac{\frac{T_s^2}{T_s^2} U_{T_1}^2 + \frac{d_1^2}{k_{Cu}^2}\frac{T_s^2}{T_s^2} U_{q"}^2 + \frac{q"^2}{k_{Cu}^2}\frac{T_s^2}{T_s^2} U_{d_1}^2 + q"^2 d_1^2 \frac{T_s^2}{T_s^2} U_{k_{Cu}}^2}{T_s^2}} \tag{60}$$

This allows all q''^2 terms in the numerator to cancel with the denominator, thus yielding the final expression shown in Eqn. (61).

$$\frac{U_{T_s}}{T_s} = \sqrt{\frac{U_{T_1}^2}{T_s^2} + \frac{U_{q''}^2 d_1^2}{k_{Cu}^2 T_s^2} + \frac{U_{d_1}^2 q''^2}{k_{Cu}^2 T_s^2} + \frac{U_{k_{Cu}}^2 q''^2 d_1^2}{T_s^2}} \tag{61}$$

7.4.3 Heat Transfer Coefficient Uncertainty Derivation

The relation for heat transfer coefficient is evaluated by substituting the parameters into the error propagation equation, as shown in Eqn. (62) and (63) below.

$$\frac{\mathrm{U_h}}{\mathrm{h}} = \sqrt{\sum_{\mathrm{i=1}}^{\mathrm{n}} \left(\frac{\partial \mathrm{h}}{\partial \sigma_\mathrm{i}} \mathrm{U}_{\sigma_\mathrm{i}}\right)^2} \tag{62}$$

$$\frac{\mathrm{U_h}}{\mathrm{h}} = \sqrt{\frac{\left(\frac{\partial \mathrm{h}}{\partial \mathrm{q''}} \mathrm{U}_{\mathrm{q''}}\right)^2 + \left(\frac{\partial \mathrm{h}}{\partial \mathrm{T_s}} \mathrm{U}_{\mathrm{T_s}}\right)^2 + \left(\frac{\partial \mathrm{h}}{\partial \mathrm{T_{sat}}} \mathrm{U}_{\mathrm{T_{sat}}}\right)^2}{\mathrm{h}^2}} \tag{63}$$

The sensitivity coefficients for each variable are evaluated individually. The expressions are then rewritten in terms of the function of interest, h, as shown in Eqns. (64-66).

$$\frac{\partial h}{\partial q''} = \frac{1}{T_s - T_{sat}} = \frac{h}{q''} \tag{64}$$

$$\frac{\partial h}{\partial T_s} = -\frac{q}{(T_s - T_{sat})^2} = -\frac{h}{(T_s - T_{sat})} \tag{65}$$

$$\frac{\partial h}{\partial T_{sat}} = \frac{q}{(T_s - T_{sat})^2} = \frac{h}{(T_s - T_{sat})} \tag{66}$$

The terms in Eqns. (64-66) are substituted to obtain the following.

$$\frac{U_h}{h} = \sqrt{\frac{\left(\frac{h}{q"}U_{q"}\right)^2 + \left(-\frac{h}{(T_s - T_{sat})}U_{T_s}\right)^2 + \left(\frac{h}{(T_s - T_{sat})}U_{T_{sat}}\right)^2}{h^2}} \tag{67}$$

The squared terms in each of the parentheses in the numerator of Eqn. (67) are expanded in Eqn. (68).

$$\frac{U_h}{h} = \sqrt{\frac{\frac{h^2 U_{q"}^2}{q"^2} + \frac{h^2 U_{T_s}^2}{(T_s - T_{sat})^2} + \frac{h^2 U_{T_{sat}}^2}{(T_s - T_{sat})^2}}{h^2}} \tag{68}$$

This allows all h^2 terms in the numerator to cancel with the denominator, thus yielding the final expression in Eqn. (9), which is reproduced below in Eqn. (69).

$$\frac{U_h}{h} = \sqrt{\frac{U_{q"}^2}{q"^2} + \frac{U_{T_s}^2}{\Delta T_{sat}^2} + \frac{U_{T_{sat}}^2}{\Delta T_{sat}^2}} \tag{69}$$

7.5 Publication List

7.5.1 Journal Papers

1. **Jaikumar, A.,** and Kandlikar, S. G., 2015, "Enhanced pool boiling heat transfer mechanisms for selectively sintered open microchannels," Int. J. Heat Mass Transf., 88, pp. 652–661.
2. **Jaikumar, A.,** and Kandlikar, S. G., 2015, "Enhanced Pool Boiling For Electronics Cooling Using Porous Fin Tops on Open Microchannels With FC-87," Appl. Therm. Eng. Vol. 91, pp. 426-433.
3. **Jaikumar, A.,** and Kandlikar, S. G., 2016, "Ultra-high pool boiling performance and effect of channel width with selectively coated open microchannels," Int. J. Heat Mass Transf., 95, pp. 795–805.
4. Protich, Z., Santhanam, K. S. V., **Jaikumar, A.,** Kandlikar, S. G., and Wong, P., 2016, "Electrochemical Deposition of Copper in Graphene Quantum Dot Bath: Pool Boiling Enhancement," J. Electrochem. Soc., 163(6), pp. E166–E172.
5. **Jaikumar, A.,** and Kandlikar, S. G., 2016, "Pool boiling enhancement through bubble induced convective liquid flow in feeder microchannels," *Appl. Phys. Lett.*, 108(4), p. 041604.
6. **Jaikumar, A.,** Kandlikar, S. G., and Gupta, A., 2016, "Pool Boiling Enhancement through Graphene and Graphene Oxide Coatings," Heat Transf. Eng., 38 (14-15), 1274-1284.
7. **Jaikumar, A.,** Gupta, A., Kandlikar, S. G., Yang, C.-Y., and Su, C.-Y., 2017, "Scale Effects of Graphene and Graphene Oxide Coatings on Pool Boiling Enhancement Mechanisms," Int. J. Heat Mass Transf., 109, pp. 357–366.
8. **Jaikumar, A.,** and Kandlikar, S. G., 2017, "Pool boiling inversion through bubble induced macroconvection," Appl. Phys. Lett., 110 (9), 094107.
9. **Jaikumar, A.,** Kandlikar, S. G., and Gupta, A., 2017, "Microscale Morphology Effects of Copper-Graphene Oxide Coatings on Pool Boiling Characteristics," Journal of Heat Transfer, 139 (11), 111509.
10. Ragupathi, P., Joshi, I., **Jaikumar, A.,** Emery, T., Kandlikar, S. G., 2017, "Bubble induced flow field modulation for pool boiling enhancement over a tubular surface," *Appl. Phys. Lett.,* 110 (25), 251603.
11. Gupta, A., **Jaikumar, A.**, Kandlikar, S. G., Layman, A., Rishi, A., 2017, "A multiscale morphological insight into graphene based coatings for pool-boiling applications," Heat Transf., Published online http://dx.doi.org/10.1080/01457632.2017.1366228.
12. **Jaikumar, A.,** and Kandlikar, S. G., 2017, "Coupled Motion of Contact Line on Nanoscale Chemically Heterogeneous Surfaces for Improved Bubble Dynamics in Boiling," Scientific Reports 7, Nature Publications, p.g. 15691.
13. **Featured article** - SG Kandlikar, **A Jaikumar**, 2015, "Enhanced pool boiling using separate liquid-vapor pathways for cooling high heat flux electronics devices," *Electronicscooling.com* - Focused on Thermal Management, TIMs, Fans, Heat Sinks, CFD Software, December edition.

7.5.2 Conference Papers

1. **Jaikumar, A.,** Santhanam, K. S. ., Kandlikar, S. G., Raya, I. B. ., and Raghupathi, Electrochemical Deposition of Copper on Graphene with A High Heat Transfer Coefficient, ECS Transactions, 66 (30) 55-64 (2015).
2. **Jaikumar, A.,** and Kandlikar, S., "Effect Of Channel Width On Pool Boiling Enhancement Of Open Microchannels With Selective Sintered Porous Coatings." Proceedings of the ASME 2015 13th International Conference on Nanochannels, Microchannels, and Minichannels INTERPACKICNMM2015 July 8-12, 2015, California, USA.
3. **Jaikumar, A**, Kandlikar, S.G., Gupta., A, 2016, "Dip Coating of Electrochemically generated graphene and graphene oxide coatings to enhance pool boiling performance," Proceedings of the ASME 14th International Conference in Nanochannels Microchannels Minichannels HTFEICNMM2016 Conference, July 10-14, Washington DC, 2016.
4. Gupta, A, **Jaikumar, A**, Kandlikar, "Characterization of Effects of Systematically Increased Graphene Dip coating Durations on the Surface Morphology," AIChE Annual Meeting, October 2016.
5. Gupta A, **Jaikumar, A**, Kandlikar, S, "Pool Boiling Enhancement through Graphene and Graphene Oxide Coatings," International Workshop on New Understanding in Nanoscale/Microscale Phase Change Phenomena, Norwegian University of Science and Technology, Trondheim, Norway, 2016.
6. **Jaikumar, A.**, and Kandlikar, S., "Pool Boiling Inversion on Surfaces With Separate Liquid-Vapor Pathways And Enhanced Macroconvection Mechanisms." Proceedings of the ASME 2017 15th International Conference on Nanochannels, Microchannels, and Minichannels ICNMM2017 August 27-31, 2017, Massachusetts, USA.
7. **Jaikumar, A.,** and Kandlikar, S., "Microcavity Augmented Pool Boiling Surfaces For Enhanced Heat Transfer" The 28th International Symposium on Transport Phenomena 22-24 September 2017, Peradeniya, Sri Lanka.

7.5.3 Posters

1. **Jaikumar, A.**, and Kandlikar, S., "Effect Of Channel Width On Pool Boiling Enhancement Of Open Microchannels With Selective Sintered Porous Coatings." Proceedings of the ASME 2015 13th International Conference on Nanochannels, Microchannels, and Minichannels INTERPACKICNMM2015 July 8-12, 2015, California, USA.
2. **Jaikumar, A**, Kandlikar, S.G., Gupta., A, 2016, "Dip Coating of Electrochemically generated graphene and graphene oxide coatings to enhance pool boiling performance," Proceedings of the ASME 14th International Conference in Nanochannels Microchannels Minichannels HTFEICNMM2016 Conference, July 10-14, Washington DC, 2016.
3. **Jaikumar, A.**, and Kandlikar, S., "Next generation of enhancement surfaces with separate liquid-vapor pathways" Gordon Research Conference, Galveston, Texas, January 8-13, 2017.